Geofluids

Water Migration and Protection in Underground Mining

Lead Guest Editor: Gangwei FAN
Guest Editors: Cheng-guo Zhang, Dongsheng Zhang, and Mingwei Chen

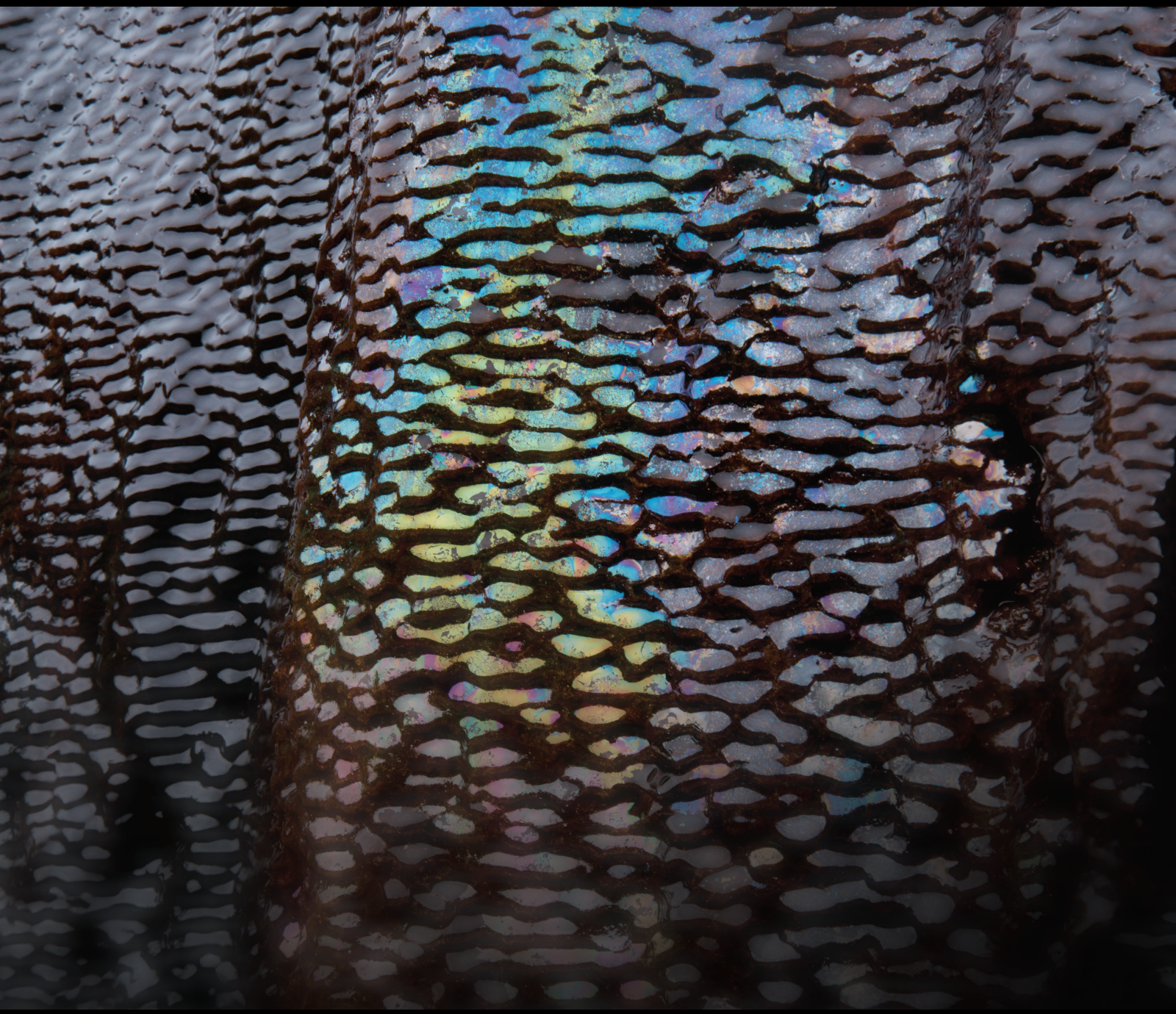

Water Migration and Protection in Underground Mining

Geofluids

Water Migration and Protection in Underground Mining

Lead Guest Editor: Gangwei FAN
Guest Editors: Cheng-guo Zhang, Dongsheng Zhang, and Mingwei Chen

Chief Editor

Associate Editors

Academic Editors

Contents

Hindawi
Geofluids
Volume 2022, Article ID 3067983, 11 pages
https://doi.org/10.1155/2022/3067983

Research Article

Defects and Improvement of Predicting Mine Water Inflow by Virtual Large Diameter Well Method

Zhimin Xu[1,2] **Tianci Chen**[1] **Jianfeng Li**[3] **Yajun Sun**[1,2] **Chenghang Zhang**[4] **Ge Chen**[1] **Yating Gao**[1] **and Ye He**[3]

[1]*China University of Mining and Technology, School of Resources and Geosciences, Xuzhou 221116, China*
[2]*Fundamental Research Laboratory for Mine Water Hazards Prevention and Controlling Technology, Xuzhou 221116, China*
[3]*Xuzhou Coal Mining Group, Xuzhou 221007, China*
[4]*Sun Yat-Sen University, School of Earth Science and Engineering, Zhuhai 519082, China*

Correspondence should be addressed to Zhimin Xu; xuzhimin@cumt.edu.cn

Received 9 March 2022; Accepted 3 September 2022; Published 22 September 2022

Academic Editor: Jun Dong

In order to prevent the occurrence of water inrush accidents, it is particularly important to predict the mine water inrush, especially the accurate prediction of the mine water inflow in the coal mining process. Mine water inflow is caused by mining disturbance, groundwater flows into mining panels along the mining-induced fissures, and a depression cone of water table is formed in certain range around the mining sites. Mining panel is usually regarded as an irregular "virtual large diameter well" so as to calculate mine water inflow in China. However, in the mining process, the area, shape, and cross section of goafs are constantly changing, so is the water inflow. Therefore, the central position and influence radius of the "virtual large diameter well" in the spatial and temporal distribution are in a dynamic process of continuous movement and expansion, rather than being confined to a static position. This paper firstly analyzes the formation mechanism of coal mine roof water inflow and the errors and defects in the calculation of mine water inflow by virtual large diameter well (VLDWM). Then, based on the theory of steady flow and combined with the dynamic change process of goaf area and depression cone of water table during mining activities, this paper proposes an improved method and puts forward a concept of dynamic virtual large diameter well (DVLDWM) and establishes a theoretical model of the central position and influence radius of the "mining large diameter well" moving forward. The first (periodic) caving step is taken as the calculation unit and generalized as the "dynamic large diameter well," which is used to calculate the dynamic water inflow in the process of mine advancing. Taking the No.7208 mining panel in Zhangshuanglou Coalmine in Xuzhou City, Jiangsu Province, as the study area, the mine water inflow was calculated dynamically by using the DVLDWM. The results show that the mine water inflow calculated is similar to the actual mine water inflow of the No.7208 mining panel observed, thus proving the reliability and credibility of the DVLDWM.

1. Introduction

China is one of the world's largest mining economies and the number, scale, and difficulty of China's mine water problems are unique. Compared with those of other countries, the coal mining areas in China are characterized by complex hydrogeological conditions and various mining depths [1, 2], and the roof and floor rocks of coal seams are greatly affected by the groundwater from the confined sandstone aquifer, loose sandy and soil aquifer, limestone-karst aquifer and goafs water [3, 4]. Water inrush accidents not only lead to heavy casualties and property losses, but also the increasing cost of mine water treatment in coal mines [5–7]. According to the data released by the State Coal Mine Safety Supervision Bureau, 1027 water inrush accidents occurred in coal mines from 2000 to 2021, resulting in 4390 deaths. In 2021, a total amount of 7.3 billion m^3 mine water from aquifer and mining activities was formed, and more than 10 billion CNY was used to prevent, control, treat, and rehabilitate mine water [8]. In this case, it is particularly important to explore a method of predicting mine water inflow so as to prevent the occurrence of mine water

inrush accidents [9, 10], especially with regard to how to enhance the accurate prediction of mine water inflow in mining panel [11, 12].

Many researches have been carried out on the prediction method of mine water inflow, including water balance method, hydro-geological analogy method, correlation analysis method, numerical method, and conventional analytical method [13–17]. Miladinovic et al. used a multiple linear regression model to simulate the situation of mine water flowing into the mine and conducted short-term prediction of mine water inflow [18]. Wu et al. proposed the variable weight model (VWM) to evaluate the hydrodynamic process of groundwater inflow [19]. Yao et al. analysed the change of mine water inrush by establishing a numerical model of the roof fracture and seepage development law [20]. Sun et al. used Visual Modflow software and numerical simulation method to evaluate the flow field of karst water under large-scale mining conditions [21]. Surinaidu et al. established a numerical model of groundwater flow based on finite difference and predicted ground-water inflow at different stages of mine advancement [22].

Darcy's Law [23], which was obtained through seepage column experiments by Darcy in 1856, has led to the transition of hydrogeology from qualitative descriptions to quantitative calculations, and it is an important milestone in the history of hydrogeology. Seven years later, Dupuit established the Dupuit steady flow model based on Darcy's Law and derived the steady flow formula known as the Dupuit formula [24]. Thiem [25] extended the Dupuit model to a horizontal infinite aquifer using an approximate hypothesis and thus established the Thiem model. Generally, when the principle of the Dupuit model and the Thiem model is used to calculate mine water inflow in China, it is called the virtual large diameter well method (Figure 1). After a long period of water gushing, relatively steady flow field with goaf as the discharge point is formed in the mining panel. At this time, the groundwater runoff basically meets the steady runoff condition, which can be regarded as steady runoff flow field. On this basis, the VLDWM regards the complex system as steady runoff discharge system with the central large well, and the irregular pit system as the area of the large well, and summarizes a complex geological condition as homogeneous strata of the same medium. Then, the water inflow of the large diameter well can be regarded as the water inflow of the whole mining area [26, 27]. Accordingly, the Dupuit steady flow equation can be used to predict the water inflow of the mining area. In recent years, some scholars have optimized the calculation parameters, aquifer conditions, and influence radius of the VLDWM [28] or revised the formula according to real water inflow, but the theoretical equations for the evolution of dynamic water inflow is not presented yet, for its changing process is fuzzy [29, 30].

On the ground of analyzing basic theories, assumptions and calculation errors of the existing calculation methods of mine water inflow and groundwater flow field, this paper exploratorily puts forward the scientific concept and calculation principle of dynamic virtual large diameter well method (DVLDWM). Then, the DVLDWM was utilized to calculate water inflow at the No.7208 mining panel of Zhangshuanglou Coalmine and reveal the dynamic water inflow process of the Quaternary bottom gravel aquifer of the coal mine roof in the study area. The calculation results were also compared with the traditional the VLDWM and the actual mine water inflow observed in the No.7208 mining panel, which could be applied to verify that the DVLDWM is reliable for the calculation of dynamic water inflow during the mining process.

2. Study Area

Zhangshuanglou Coalmine is located in Pei County, 79 km away from Xuzhou City to the northwest, Jiangsu Province, China. As is shown in Figure 2, it is located in the range of the Yellow River alluvial plain, with the geomorphology being relatively flat. The weather conditions of the Zhangshuanglou Coalmine belong to the south temperate Huanghuai region-monsoon continental climate, with the annual average temperature and precipitation being 13.8 °C and 811.7 mm, respectively. The maximum and minimum of annual precipitation are 1178.9 mm (1977) and 550 mm (1968), respectively. The Dasha River passes through the study area from north to south, with Xupei River in the east and Fengpei River in the south. The frozen soil depth is 19 cm, with an average of 12 cm.

There are no faults, collapse columns, and other structures in the No.7208 mining panel, so mining activities has no in situ stress effect. Moreover, the mining panel is located in the shallow part of the mining area, and there is no impact of rock burst.

3. Theories and Methods

3.1. Formation Mechanism of Mine Roof Water Inflow. The example of water inflow from coal seam roof rocks is shown in this paper. When the coal seam is to be mined out, the roof rock collapse and fracture development would occur consequently [31]. The rock collapse and fracture zones can be divided into three stages in the mining panel, and the phenomenon lasts through the whole mining period from the formation of panel to the first weighting, periodic pressure stage, and the end of mining [31].

The area of the goaf is small, and its surrounding rock bears less but relatively concentrated stress from the upper rock mass when the first weighting occurs above the roof of mining panel [32]. At the beginning, the mining influence of coal seam is weak, which is mainly manifested in concentrated stress and caving rock stratum; and the range of rock movement, deformation, cracking, and collapse is small, so the panel water inflow is relatively small. After entering the periodic pressure stage, the roof rock mass collapses downward, further developing fractures upward, and the upper rock stratum bends and sinks until all the coal seams are mined out. The water conducted fissure zone of stable roof will be formed in the roof rock stratum of the stope and the coal seam. When the fracture zone connects the roof aquifer of coal seam with the mining panel, the groundwater

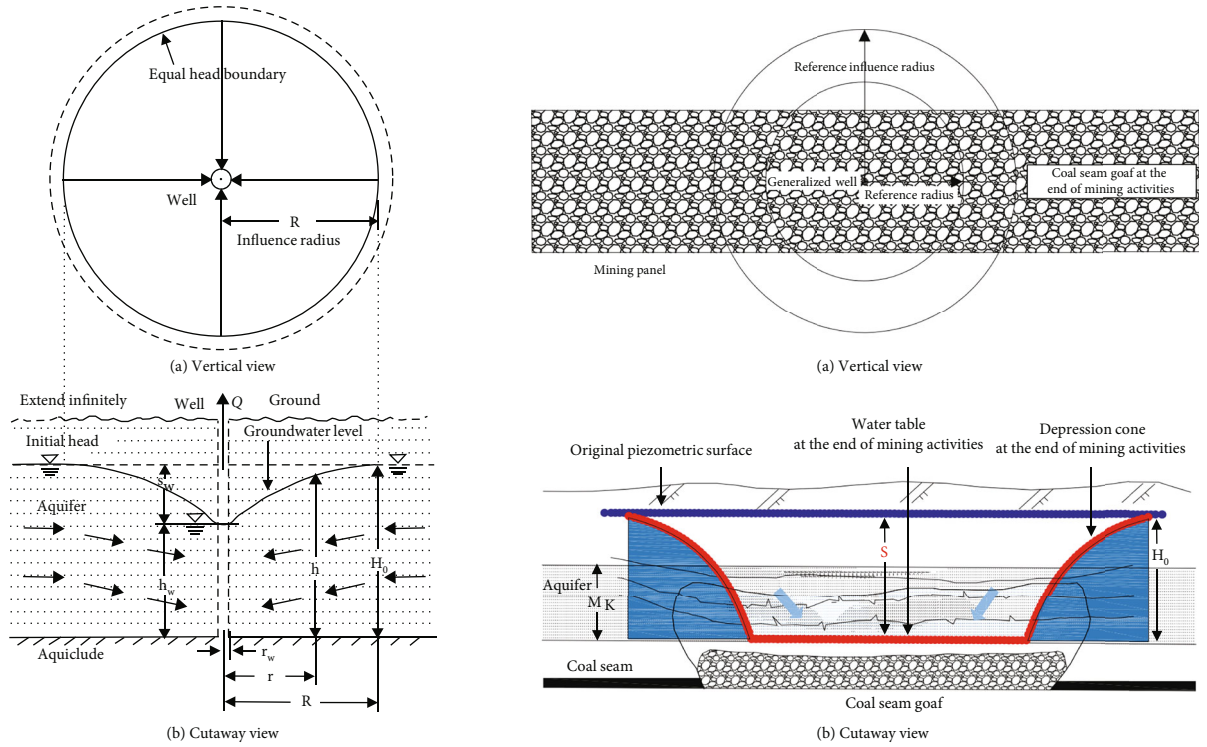

FIGURE 1: Schematic diagram of Thiem model and VLDWM.

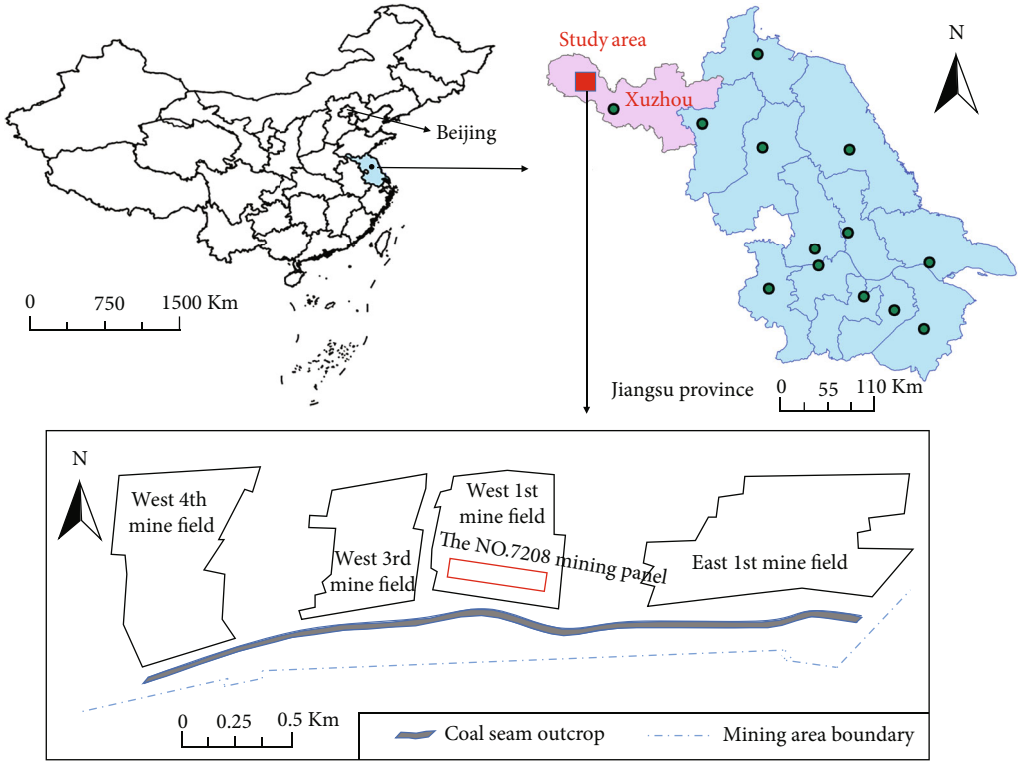

FIGURE 2: Location of the study area.

in the aquifer flows into the goaf, roadway, and mining system along the mining fissures to form mine water inflow, as shown in Figure 3.

3.2. Theoretical Defects of VLDWM. The theoretical formula of steady flow has strict assumptions, which makes it unadaptable to the complex actual hydrogeological

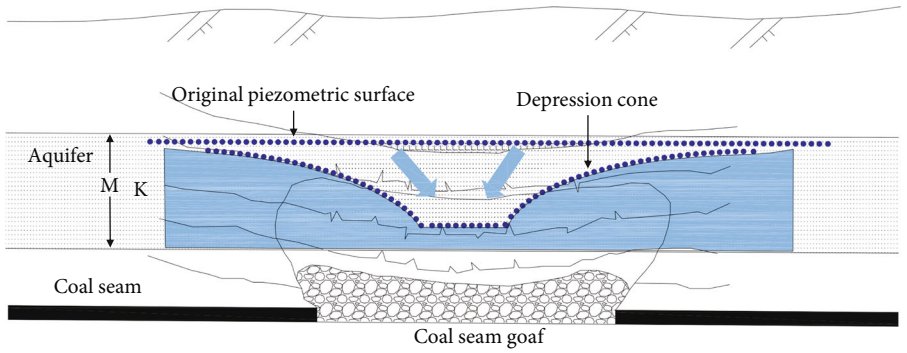

Figure 3: Formation mechanism of mine roof water inflow.

Table 1: Generalization of large diameter wells with different sketches.

Plane figure of mine pit		r_0 expression	Explanation
S	Long strip	$r_0 = S/4 = 0.25S$	S is length, Only when width/length $\rightarrow 0$ is used
b, a	Rectangle	$r_0 = \eta(a + b/4)$	a and b are the rectangular side lengths; η can be seen in Table 2
a	Square	$r_0 = 0.59a$	a is the edge length of square

conditions. The generalized hydrogeological conditions of the mining area are usually named as "hydrogeological conceptual model" [33], which is the qualitative description of the groundwater system movement in mining area. "Virtual large diameter well" is in nature a hydrogeological conceptual model. In order to apply the theoretical formula of steady flow, it is necessary to reasonably summarize and simplify the hydrogeological conditions of the mining area, without distorting the original conditions in certain range.

A depression cone with a certain shape centered on the goaf area is to be formed around the mine site when the mine water drainage is conducted, which is similar to the formation of a depression cone of water table around the pumping well. Therefore, the distribution range of the panel goaf area can be assumed to be an ideal large diameter well.

It is assumed that the circular section area of the large diameter well is equivalent to the area of the goaf area distribution. Therefore, the equation of groundwater dynamics can be directly used to calculate the water inflow of mining panel, and the calculation equation for confined aquifer is used:

$$Q = 2.73K\frac{MS}{\lg R_0 - \lg r_0}, \quad (1)$$

$$R = 10S\sqrt{K}, \quad (2)$$

$$R_0 = R + r_0, \quad (3)$$

Table 2: The relationship between b/a and η.

b/a	0	0.20	0.40	0.60	0.80	1.00
η	1.00	1.12	1.14	1.16	1.18	1.18

where Q denotes the water inflow of the mining panel (m^3/s); K is the hydraulic conductivity (m/s); M refers to the thickness of aquifer (m); S is the water table drawdown caused by mine water drainage (m); R_0 stands for the reference influence radius (m); r_0 is the reference radius (m); and R denotes the influence radius (m).

It should be noted that the variable R is only related to the water table drawdown and hydraulic conductivity. R depends on the shape and sketch of the goaf area of mining panel η [34]. The calculation methods of large diameter well and reference radius with different profiles are shown in Tables 1 and 2.

Based on the steady well flow theory, the VLDWM generalizes the whole mining panel into a "large diameter well," and the predicted mine water inflow refers to the flow formed when the water flow reaches an approximately steady state at the end of the mining panel. This theory does not consider the transition of large well flow from steady flow to transient flow, and the way and time of releasing water stored in the aquifer to the mining panel. In fact, the mining process in the mining panel (or mining area) is a

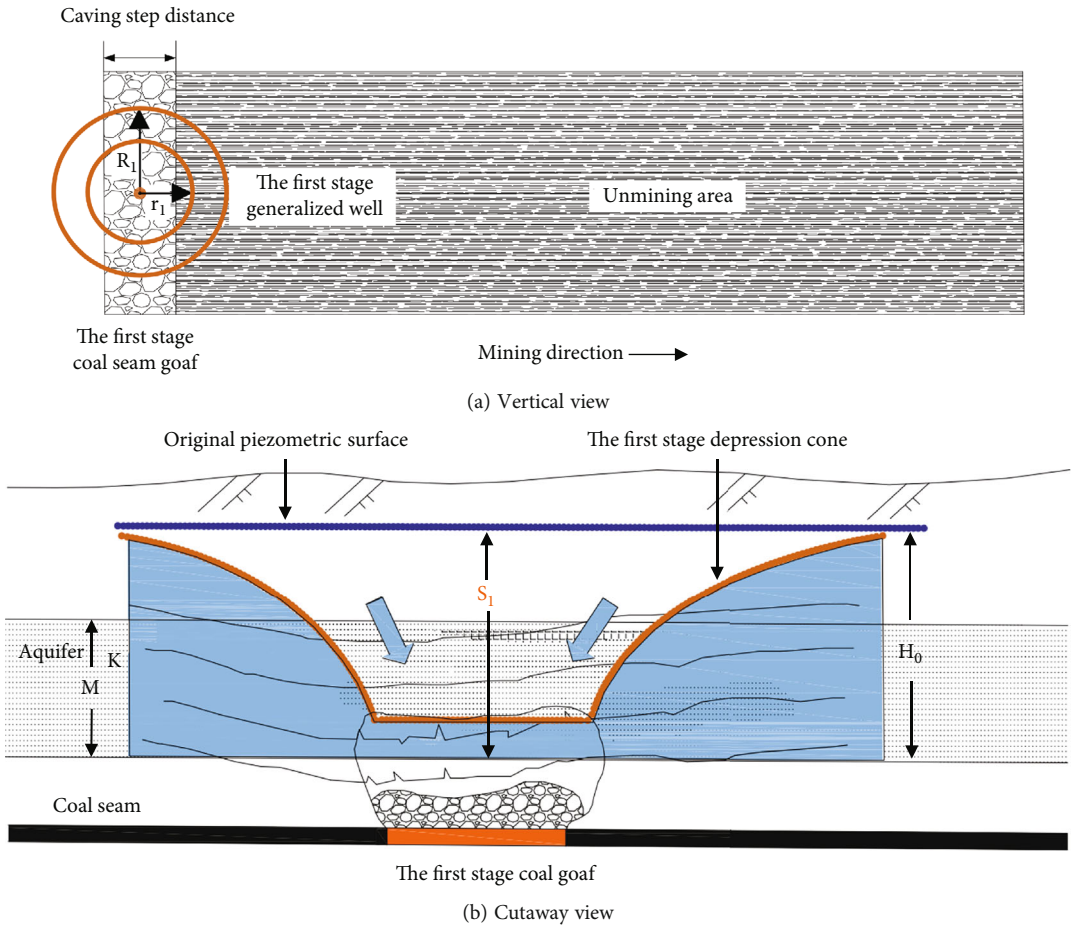

Figure 4: The first stage of the depression cone.

step-by-step process, which does not form the goaf at once. In fact, at the beginning of mining activities, the affected area by mining is small, the water flow section is limited, and the water inrush quantity is relatively little. Therefore, using conventional the VLDWM to calculate water inflow often leads to larger results, even exceeding the warning magnitude.

3.3. The Improved Method of VLDWM. Groundwater flow in mine area is transient, because it is not only affected by seasonal climate changes, but the mining activities. Groundwater often forms transient flow centered on the goaf when the depression cone becomes larger during the mining process. Transient flow theory displays better practicability because it can describe the whole process of groundwater moving to goaf. However, there still exists the steady flow condition in the process of mining activities. For example, the aquifer has abundant supply water, or the mine water inflow and supply are approximately equal in the early stage of mining activities.

In field experiments, the area and shape of the goaf are constantly changing, and water flow section is also constantly increasing with the continuous advancement of the mining panel. Accordingly, depression cone is expanding, and water inflow is also increasing. The central position and influence radius of "large diameter well" in spatial and temporal distribution is in a dynamic change process of continuous movement and expansion, rather than being confined to a static position. Besides, since steady flow formula does not contain time variables, the transient flow theory should be used so as to understand the dynamic change process of mine water inrush.

Based on the theory of steady flow and combined with the dynamic change process of goaf area and depression cone in the mining process, the concept and method of the DVLDWM are proposed. On this basis, the theoretical model is established of the central position and influence radius of "mining large diameter well" which moves forward continuously. With this improved method, the initial (periodic) collapse step is taken as the calculation unit, and the "mining large diameter well" is generalized as "dynamic large diameter well" so that the dynamic mine water inflow advancing with the mining panel can be calculated more accurately.

4. Discussion and Results

4.1. Calculation Principle and Method of the DVLDWM. Assumption: The aquifer is an infinite boundary, and the infinite distance is a constant head boundary. With the excavation of the mining panel, the local water table in the goaf will drop [35–38].

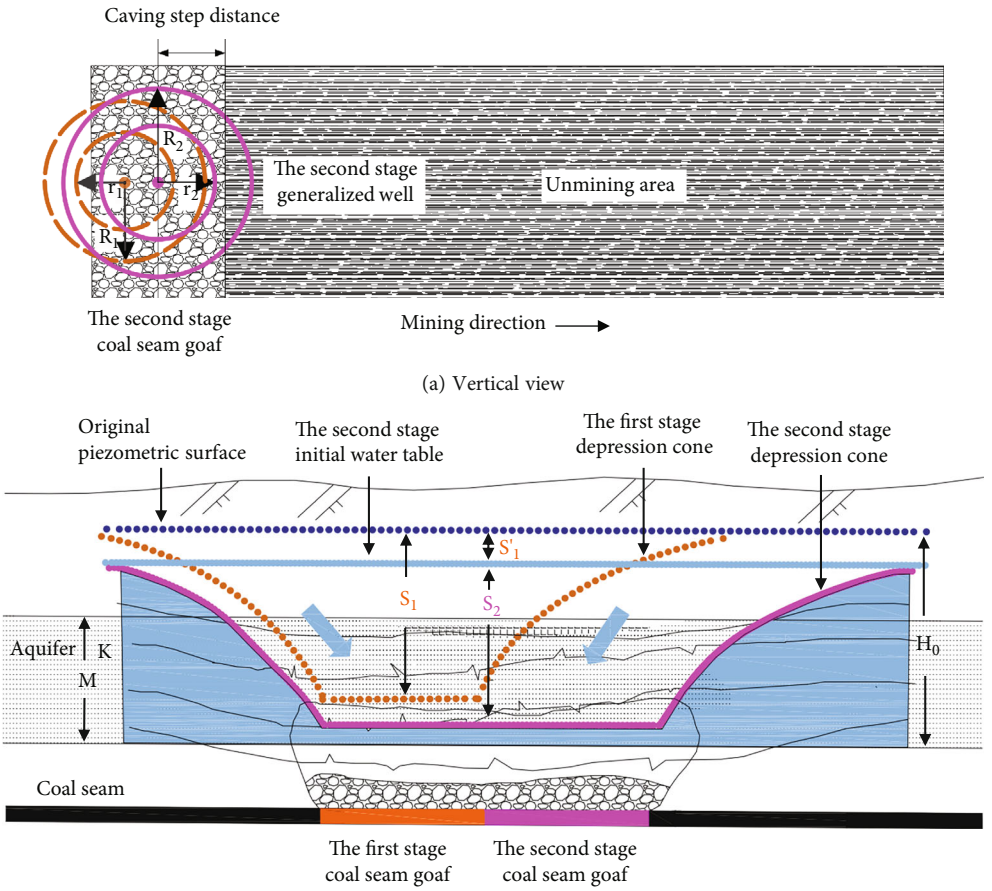

Figure 5: The second stage of the depression cone.

In the first stage, the first collapse and the aquifer form the first depression cone during the excavation of the mining panel (as shown in Figure 4). The confined aquifer calculation formula is used to calculate the water inflow Q_1 of the mining panel at the end of the first stage:

$$Q_1 = 2.73K\frac{MS_1}{\lg R_1 - \lg r_1}, \tag{4}$$

$$R_1 = 10S_1\sqrt{K} + r_1, \tag{5}$$

where Q_1 denotes the water inflow of the mining panel at the end of the first stage (m^3/s); H_0 means the initial water table of the aquifer (m); K refers to the hydraulic conductivity (m/s); M is the thickness of aquifer (m); S_1 stands for the water table drawdown caused by mine drainage in the first stage (m); R_1 denotes the reference influence radius of the first stage (m); and r_1 means the reference radius of the first stage (m).

(1) The drawdown in the first stage (S_1): The traditional VLDWM is used to predict the mine water inflow [39, 40], and the depression cone is usually taken from the roof to the floor of the aquifer. However, the aquifer water table is difficult to drain to the floor, and the maximum depression cone value will change with the excavation of the mining panel in field processing, especially in western China. Therefore, it is assumed that the first stage drops $S_1 = \lambda H_0$ and λ can be obtained by the following two methods:

(a) When the first stage of mining is completed, the approximate theoretical formula of transient flow (Jacob's formula) is used to calculate the flow at the center of the "generalized-well" of the mining panel. To be specific, the drawdown of the water table is observed through the long observation hole in the aquifer adjacent to the mining panel; and then the water inflow in the center of "large diameter well" in the first stage can be obtained by the following formula:

$$Q' = \frac{S_r T}{0.183 \lg\left(2.25Tt_1/r_1^2\mu^*\right)}, \tag{6}$$

where Q' denotes the water inflow in the center of "large diameter well" in the first stage

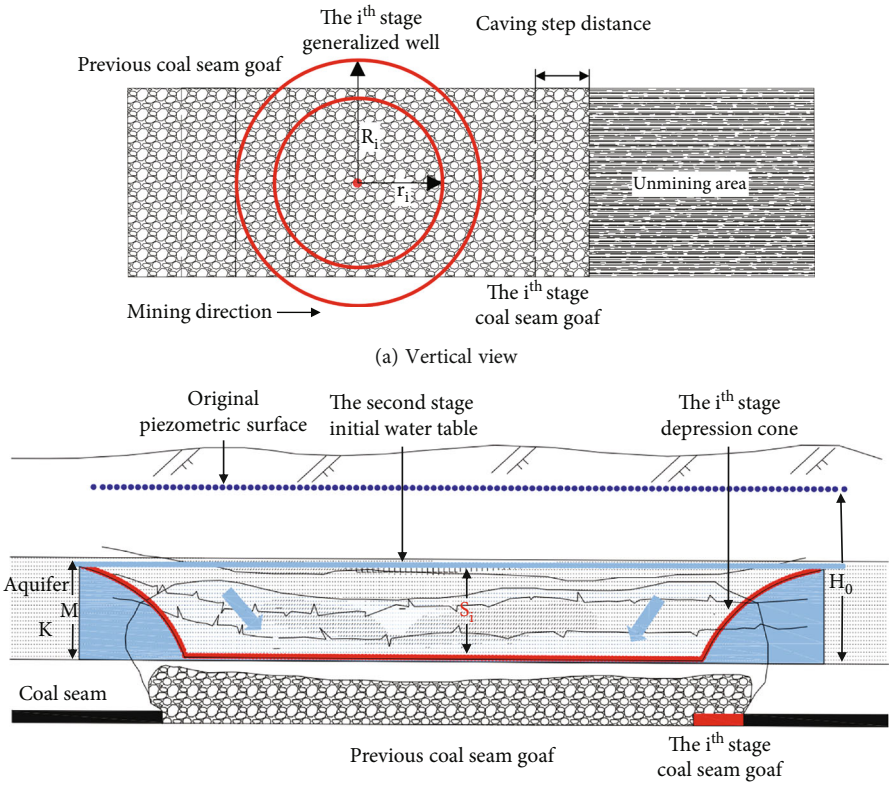

FIGURE 6: The i^th stage of the depression cone.

calculated from observation logging (m^3/s); S_r means the drawdown of observation well (m); T refers to transmissivity (m^2/s); t_1 means the time required for the first stage of mining (s); r_1 is the distance from observation point to well center (m); and μ^* denotes coefficient of storage (dimensionless).

According to the flow rate at the center of the "generalized-well" in mining panel, the water table drawdown of the aquifer at the center of the "generalized-well" can be reversely deduced by using the confined aquifer formula of the Dupuit's law, and then λ can be obtained:

$$Q' = \frac{2.73KMS_1}{\lg\left(10S_1\sqrt{K} + r_1\right) - \lg r_1}, \quad (7)$$

$$\lambda = S_1/H_0. \quad (8)$$

(b) According to the existing mine water inflow caused by the initial collapse of mining panel, the drawdown of aquifer water table at the center of "generalized-well" can be deduced by using the Dupuit's law confined aquifer formula, and then $\lambda = S_1/H_0$ can be obtained

(2) Initial water table of aquifer (H_0): The natural water table elevation of confined aquifer within the water-conducting fracture zone of coal seam roof is based on coal seam floor

(3) Hydraulic conductivity (K): The hydraulic conductivity value is calculated according to the steady flow Dupuit's law formula based on the test data of pumping (draining) water from boreholes in field tests

(4) Aquifer thickness (M): It refers to the accumulated thickness of aquifer within the water-conducting fracture zone of coal roof

(5) Substitute influence radius of the first stage (R_1): It is obtained according to the "generalized-well" after the first collapse of the mining panel

(6) Reference radius of the first stage (r_1): It is obtained by the generalization of "large diameter well" contour after the first collapse of the mining panel

In the second stage, the depression cone expands, and the drawdown decreases compared with that in the first

stage (Figure 5). The drawdown formed by the mine inflow generated in the first stage is used to push back the "initial" water table in the center of the "large diameter well" before the end of the second stage and the periodic collapse. The drawdown formed here by the mine water inflow in the first stage can be calculated by Jacob's formula of the approximate theory of transient flow:

$$S_1' = \frac{0.183Q_1}{T} \lg \frac{2.25Tt_1}{r_1^2\mu^*}, \tag{9}$$

where S_1' means the actual drawdown of water table caused by mine water inflow in the first stage (m); Q_1 denotes the water inflow in the first stage (m^3/s); T means transmissivity (m^2/s); t_1 refers to the time required for the first stage of mining (s); r_1 stands for the reference radius of the first stage (m); and μ^* means coefficient of storage (dimensionless).

The water table drawdown in the second stage (S_2): The water inflow Q_2 at the end of the second stage and after the cycle collapse can be obtained by repeating the calculation of mine water inflow with the following formulas:

$$S_2 = \lambda\left(H_0\text{-}S_1'\right), \tag{10}$$

$$Q_2 = 2.73K\frac{MS_2}{\lg R_2 - \lg r_2}, \tag{11}$$

$$R_2 = 10S_2\sqrt{K} + \mathrm{r}_2, \tag{12}$$

where Q_2 means the water inflow of mining panel at the end of the second stage and backward cycle collapse (m^3/s); H_0 denotes the initial water table of aquifer (m); S_2 means the water table drawdown caused by mine drainage in the second stage (m); R_2 refers to the reference influence radius of the second stage (m); and r_2 means the reference radius of the second stage (m).

With the continuous advance of the mining panel, when the water table of the aquifer decreases below the roof (Figure 6), the following equation shall be adopted to calculate the water inflow of the mining panel:

$$Q_\mathrm{i} = 1.366K\frac{(2H - M)M - \mathrm{h}^2}{\lg R_i - \lg r_i}, \tag{13}$$

where Q_i means the water inflow of mining panel after the first stage is over and the cycle collapses (m^3/s); R_i denotes the substitute influence radius (m) in the i^{th} stage; and R_i means the reference radius (m) in the i^{th} stage.

The caving step is introduced as the calculation unit to calculate the mine water inflow by stages during the mining process. Then, repeat the similar calculations until the end.

The mining scope and influence radius ("large diameter well" radius) gradually expand during the mining process, and a new depression cone and water table drawdown will be formed in each mining stage. The DVLDWM for mine water inflow calculation is based on the new initial water table formed by the drainage of aquifer by previous mining stage, which greatly corrects the error of mine water inflow calculated by the traditional VLDWM. The key point of the DVLDWM is that the water table and the influence radius caused by coal mining, which are used to calculate the mine water inflow, will both be affected by the previous stage.

Table 3: Comparison between the DVLDWM calculation and actual observed results.

The excavated distance of the mining panel (m)	Mine water inflow (m^3/h)	
	Calculation results	Actual observed results
15	5.19	3.1
30	5.41	3.5
45	5.91	3.4
60	6.43	4.0
75	6.92	4.8
90	7.42	6.9
105	8.50	8.4
120	8.28	7.0
135	8.78	8.5
150	9.16	8.7
165	10.43	8.4
180	10.79	7.0
195	11.17	10.1
210	11.62	11.1
225	12.07	10.4
…	…	…
390	18.65	16.2
405	19.11	24.8
420	19.58	19.1
435	19.88	19.3
450	20.36	19.1
465	20.83	19.0
480	21.29	21.0

Generally, both the VLDWM and the DVLDWM are based on the theory of steady flow to predict mine water inflow. The difference is that the VLDWM can only calculate the total mine water inflow when the mining-induced aquifer reaches steady state at the end of the mining process in a panel, and then, the changes of the water table and the influence radius in each stage during the mining process were not considered. However, the above defects are totally considered in the DVLDWM, and a great improvement is achieved.

4.2. Case Comparison and Superiority Analysis. Both methods are employed to calculate the water inflow of the target mining panel in the study area. The NO.7208 mining panel is 105 m in width and 480 m in length. The length for periodic roof weighting is 15 m. Moreover, M (aquifer thickness) = 14 m, K (hydraulic conductivity) = 0.0033 m/s,

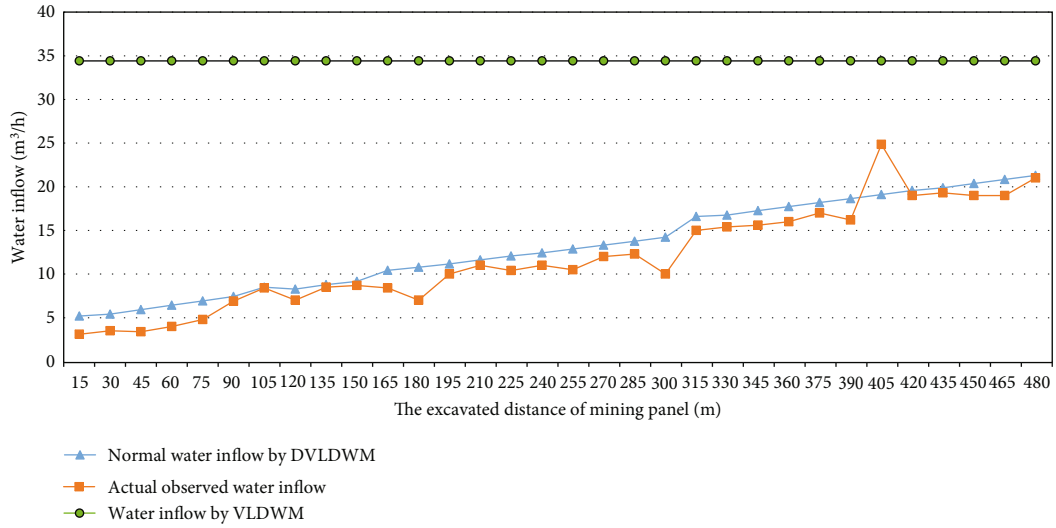

FIGURE 7: Prediction of water inflow variation curve of the mining panel by two methods and actual observed water inflow.

μ^* (coefficient of storage) = 1.8×10^{-4}, T (transmissivity) = 0.0467 m^2/s, and H_0 (initial water table) = 150 m.

(1) According to traditional VLDWM:

$$Q = 2.73K\frac{MS}{\lg R - \lg r}, \tag{14}$$

$$R = 10S\sqrt{K} + r. \tag{15}$$

The mining panel water inflow is $Q = 34.4\ m^3/h$ ($0.00956\ m^3/s$).

(2) In the light of DVLDWM, the dynamic change of water inflow during the whole mining process of the NO.7208 mining panel is confirmed. Besides, the λ values can be calculated as 1/10, 1/6, and 1/3, respectively, by using the observed water inflow during the real mining process of the mining panel. The calculation results and their change trends are shown in Table 3 and Figure 7

The observed water inflow during the mining process of the panel is about 3-10 m^3/h (0.000833-0.002778 m^3/s) in the initial stage, 15 m^3/h (0.004167 m^3/s) in the middle stage, and at most 21 m^3/h (0.005833 m^3/s) in the later stage. The calculation results obtained by DVLDWM are consistent with the actual mine water inflow, which proves that the calculation theory, method, and results of the DVLDWM are more reliable than before.

Summarily, the results obtained by the VLDWM are obviously larger than the observed ones, and the DVLDWM results are closer to the observed ones. Moreover, the calculation accuracy of mine water inflow by using the DVLDWM is greatly improved compared with that of the traditional VLDWM. In this sense, the DVLDWM achieves the goal of dynamically predicting the mine water inflow finally. These are also the innovative aspects of this paper.

5. Conclusions

(1) It is particularly important to predict the mine water inrush for preventing the occurrence of water inrush accidents, especially the accurate prediction of the mine water inflow in the coal mining process. In this paper, the defects of the widely used VLDWM were analyzed. We improved the VLDWM based on the actual water inflow principles during mining processes, and a calculation method of water inflow quantity with higher accuracy was named as DVLDWM

(2) The DVLDWM proposed in this paper for mine water inflow calculation is based on the new initial water table formed by the drainage of aquifer by previous mining stage, which greatly corrects the error of mine water inflow calculated by the traditional VLDWM. The key point of the DVLDWM is that the water table and the influence radius caused by coal mining, which are used to calculate the mine water inflow, will both be affected by the previous stage. Generally, the defects of the VLDWM are totally considered in the DVLDWM and a great improvement is achieved

(3) According to the principle and calculation of the DVLDWM, and combined with the groundwater inflow observed at the NO.7208 mining panel in the study area, the λ values in the first, middle, and later stage are calculated, and the water inflow in each stage of the mining panel advancement is dynamically presented. Compared with the calculation results obtained by the traditional VLDWM, the calculation results of DVLDWM greatly reduce

the calculation error and are consistent with the actual observation records of mine water inflow in the mining panel. The quantitative comparison result proves that the calculation principle of the DVLDWM displays higher reliability than the traditional VLDWM

Data Availability

The (data type) data used to support the findings of this study are included within the article.

Conflicts of Interest

There is no conflict of interest regarding the publication of this paper.

Acknowledgments

This research was supported by the National Science Foundation of China (42172272), the National Key Research and Development Program of China (2019YFC1805400), the Fundamental Research Funds for the Central Universities (2020ZDPY0201), and the National Science Foundation of Jiangsu Province (BK20210524).

References

[1] Y. Zhang, L. Gao, W. Yang et al., "Hydro-geological conditions and mine inflow water forecast of the Western Long Beach in Junggar Coalfield," *Energy Procedia*, vol. 16, pp. 915–920, 2012.

[2] Q. Liu, Y. Sun, Z. Xu, and G. Xu, "Application of the comprehensive identification model in analyzing the source of water inrush," *Arabian Journal of Geosciences*, vol. 11, no. 9, p. 189, 2018.

[3] C. Newman, Z. Agioutantis, and G. B. Leon, "Assessment of potential impacts to surface and subsurface water bodies due to longwall mining," *International Journal of Mining Science and Technology*, vol. 27, no. 1, pp. 57–64, 2017.

[4] S. Li, C. Ma, R. Liu et al., "Super-absorbent swellable polymer as grouting material for treatment of karst water inrush," *International Journal of Mining Science and Technology*, vol. 31, no. 5, pp. 753–763, 2021.

[5] D. Kuscer, "Hydrological regime of the water inrush into the Kotredez Coal Mine (Slovenia, Yugoslavia)," *Mine Water and the Environment*, vol. 10, no. 1, pp. 93–101, 1991.

[6] K. Polak, K. Różkowski, and P. Czaja, "Causes and effects of uncontrolled water inrush into a decommissioned mine shaft," *Mine Water and the Environment*, vol. 35, no. 2, pp. 128–135, 2016.

[7] R. N. Singh and A. S. Atkins, "Application of idealised analytical techniques for prediction of mine water inflow," *Mining Science and Technology*, vol. 2, no. 2, pp. 131–138, 1985.

[8] X. Wang, Z. Xu, Y. Sun, J. Zheng, C. Zhang, and Z. Duan, "Construction of multi-factor identification model for real-time monitoring and early warning of mine water inrush," *International Journal of Mining Science and Technology*, vol. 31, no. 5, pp. 853–866, 2021.

[9] B. Yang, W. Sui, and L. Duan, "Risk assessment of water inrush in an underground coal mine based on GIS and fuzzy set theory," *Mine Water and the Environment*, vol. 36, no. 4, pp. 617–627, 2017.

[10] Q. Wu, S. Fan, W. Zhou, and S. Liu, "Application of the analytic hierarchy process to assessment of water inrush: a case study for the no. 17 coal seam in the Sanhejian Coal Mine, China," *Mine Water and the Environment*, vol. 32, no. 3, pp. 229–238, 2013.

[11] Q. Wu, W. Zhou, J. Wang, and S. Xie, "Prediction of groundwater inrush into coal mines from aquifers underlying the coal seams in China: vulnerability index method and its construction," *Environmental Geology*, vol. 56, no. 2, pp. 245–254, 2008.

[12] K. S. More, C. Wolkersdorfer, N. Kang, and A. S. Elmaghraby, "Automated measurement systems in mine water management and mine workings - a review of potential methods," *Water Resources and Industry*, vol. 24, article 100136, 2020.

[13] P. Bukowski, "Evaluation of water hazard in hard coal mines in changing conditions of functioning of mining industry in Upper Silesian coal basin–USCB (Poland)," *Archives of Mining Sciences*, vol. 60, no. 2, pp. 455–475, 2015.

[14] R. N. Singh and A. S. Atkins, "Analytical techniques for the estimation of mine water inflow :," *International Journal of Rock Mechanics and Mining Sciences & Geomechanics Abstracts*, vol. 23, no. 2, p. 41, 1986.

[15] X. Guo and X. Ma, "Mine water discharge prediction based on least squares support vector machines," *Mining Science and Technology (China)*, vol. 20, no. 5, pp. 738–742, 2010.

[16] F. Marinelli and W. L. Niccoli, "Simple analytical equations for estimating ground water inflow to a mine pit," *Ground Water*, vol. 38, no. 2, pp. 311–314, 2000.

[17] X. Ni, W. Chen, Z. Li, and X. Gao, "Reconstruction of different scales of pore-fractures network of coal reservoir and its permeability prediction with Monte Carlo method," *International Journal of Mining Science and Technology*, vol. 27, no. 4, pp. 693–699, 2017.

[18] B. Miladinovic, V. R. Vakanjac, D. Bukumirovic, V. Dragisic, and B. Vakanjac, "Simulation of mine water inflow: case study of the Štavalj coal mine (Southwestern Serbia)," *Archives of Mining Sciences*, vol. 60, no. 4, pp. 955–969, 2015.

[19] Q. Wu, B. Li, and Y. Chen, "Vulnerability assessment of groundwater inrush from underlying aquifers based on variable weight model and its application," *Water Resources Management*, vol. 30, no. 10, pp. 3331–3345, 2016.

[20] B. Yao, H. Bai, and B. Zhang, "Numerical simulation on the risk of roof water inrush in Wuyang Coal Mine," *International Journal of Mining Science and Technology*, vol. 22, no. 2, pp. 273–277, 2012.

[21] W. Sun, Q. Wu, H. Liu, and J. Jiao, "Prediction and assessment of the disturbances of the coal mining in Kailuan to karst groundwater system," *Physics and Chemistry of the Earth*, vol. 89-90, pp. 136–144, 2015.

[22] L. Surinaidu, V. V. S. Gurunadha Rao, N. Srinivasa Rao, and S. Srinu, "Hydrogeological and groundwater modeling studies to estimate the groundwater inflows into the coal Mines at different mine development stages using MODFLOW, Andhra Pradesh, India," *Water Resources and Industry*, vol. 7-8, pp. 49–65, 2014.

[23] H. Darcy, *Les Fontaines Publiques de la Ville de Dijon [the Public Fountains of the City of Dijon]*, Victor Dalmont, Paris, 1856.

[24] J. Dupuit, *Etudes Théoriques et Pratiques sur le Mouvement des Eaux dans les Canaux Découverts et à Travers les Terrains Perméables [Theoretical and Practical Studies on the Movement of Water in Open Channels and Permeable Ground]*, Dunod, Paris, 1863.

[25] G. A. Thiem, *Hydrologische Methoden*, Gebhardt, Leipzig, 1906.

[26] C. Wu, X. Wu, G. Zhu, and C. Qian, "Predicting mine water inflow and groundwater levels for coal mining operations in the Pangpangta coalfield, China," *Environment and Earth Science*, vol. 78, no. 5, p. 130, 2019.

[27] K. Zhang, B. Cao, G. Lin, and M. Zhao, "Using multiple methods to predict mine water inflow in the Pingdingshan no. 10 coal mine, China," *Mine Water and the Environment*, vol. 36, no. 1, pp. 154–160, 2017.

[28] Y. Yang, J. Yuan, and S. Chen, "R/S analysis and its application in the forecast of mine inflows," *Journal of China University of Mining and Technology*, vol. 16, no. 4, pp. 425–428, 2006.

[29] R. Gao, H. Yan, F. Ju, X. Mei, and X. Wang, "Influential factors and control of water inrush in a coal seam as the main aquifer," *International Journal of Mining Science and Technology*, vol. 28, no. 2, pp. 187–193, 2018.

[30] Q. Wu, Y. Du, H. Xu, Y. Zhao, X. Zhang, and Y. Yao, "Finding the earliest arrival path through a time-varying network for evacuation planning of mine water inrush," *Safety Science*, vol. 130, p. 104836, 2020.

[31] S. E. Minkoff, C. M. Stone, S. Bryant, M. Peszynska, and M. F. Wheeler, "Coupled fluid flow and geomechanical deformation modeling," *Journal of Petroleum Science and Engineering*, vol. 38, no. 1-2, pp. 37–56, 2003.

[32] A. Gudmundsson, S. S. Berg, K. B. Lyslo, and E. Skurtveit, "Fracture networks and fluid transport in active fault zones," *Journal of Structural Geology*, vol. 23, no. 2-3, pp. 343–353, 2001.

[33] M. R. Islam, D. Hayashi, and A. B. Kamruzzaman, "Finite element modeling of stress distributions and problems for multi-slice longwall mining in Bangladesh, with special reference to the Barapukuria coal mine," *International Journal of Coal Geology*, vol. 78, no. 2, pp. 91–109, 2009.

[34] P. Wycisk, T. Hubert, W. Gossel, and C. Neumann, "High-resolution 3D spatial modelling of complex geological structures for an environmental risk assessment of abundant mining and industrial megasites," *Computers & Geosciences*, vol. 35, no. 1, pp. 165–182, 2009.

[35] S. Zheng, J. Chen, H. Liu, Y. Hu, and Y. Sun, *Special Hydrogeology*, China University of Mining and Technology Press, Xuzhou, 1999.

[36] L. Lianchong, Y. Tianhong, L. Zhengzhao, Z. Wancheng, and T. Chunan, "Numerical investigation of groundwater outbursts near faults in underground coal mines," *International Journal of Coal Geology*, vol. 85, no. 3-4, pp. 276–288, 2011.

[37] J. G. McLellan, N. H. S. Oliver, and P. M. Schaubs, "Fluid flow in extensional environments; numerical modelling with an application to Hamersley iron ores," *Journal of Structural Geology*, vol. 26, no. 6-7, pp. 1157–1171, 2004.

[38] L. Bateson, F. Cigna, D. Boon, and A. Sowter, "The application of the Intermittent SBAS (ISBAS) InSAR method to the South Wales Coalfield, UK," *International Journal of Applied Earth Observation and Geoinformation*, vol. 34, pp. 249–257, 2015.

[39] H. J. Henriksen, L. Troldborg, P. Nyegaard, T. O. Sonnenborg, J. C. Refsgaard, and B. Madsen, "Methodology for construction, calibration and validation of a national hydrological model for Denmark," *Journal of Hydrology*, vol. 280, no. 1-4, pp. 52–71, 2003.

[40] X. Tao, J. Ma, and W. Zeng, "Treatment effect investigation of underground continuous impervious curtain application in water-rich strata," *International Journal of Mining Science and Technology*, vol. 25, no. 6, pp. 975–981, 2015.

Hindawi
Geofluids
Volume 2022, Article ID 8471638, 13 pages
https://doi.org/10.1155/2022/8471638

Research Article

Research on the Characteristics of Coal Bump and Monitoring and Early Warning in Hujiahe Coal Mine

Fei Yu,[1] **Tong Zhang**,[2,3] **and Zhen Wei**[1,3]

[1]*School of Mining Engineering, Anhui University of Science and Technology, Huainan, 232001 Anhui, China*
[2]*Institute of Energy, Hefei Comprehensive National Science Center, Anhui, Hefei 230031, China*
[3]*State Key Laboratory of Mining Response and Disaster Prevention and Control in Deep Coal Mines, Anhui University of Science and Technology, Huainan, 232001 Anhui, China*

Correspondence should be addressed to Tong Zhang; 1099731996@qq.com

Received 25 January 2022; Revised 1 June 2022; Accepted 22 June 2022; Published 8 August 2022

Academic Editor: Gangwei Fan

Under the high intensity mining disturbance, coal bump is easily triggered by the sudden release of large amount of elastic energy contained in the coal body, which seriously affects coal mine safety production. Triaxial experiments were used to study the damage characteristics of coal samples subjected to loading at the 401103 working face of Hujiahe coal mine, and the critical value of peak strength of coal samples was investigated. Based on the characteristics of the mechanical damage behavior of coal samples obtained from the triaxial experiment, the statistics of the occurrence of coal bump events at the 401103 working face were conducted through numerical simulation and field monitoring to study the areas that need to be focused on prevention and control, with a view to providing basic research for deep coal mining. The results show the following: (1) the strength of coal samples is "weakened" by stress loading, and the fracture penetrates the coal body interface leading to the formation of tensile-shear damage of coal samples. The value of the damage variable for the coal sample in the initial damage stage is 0; at the damage stabilization stage, the values of damage variables were derived to be located at 0.03~0.14. The bearing capacity of the coal sample decreases rapidly during the accelerated development period. (2) According to the simulation and field monitoring, it is known that 0~100 m in front of the coal mining face belongs to the key monitoring area. (3) With the advancement of the working face, different coal pillar widths have obvious effects on the vertical stress, and stress increase and decrease zones appear on both sides of the coal column, and the peak stress shows the characteristics of increasing first and then decreasing with the advancement of the working face. The width of the working face has a great influence on the change of vertical stress. When the sensitivity of the vertical stress to the width of the working face increases, the stress concentration phenomenon will occur, and a large amount of elastic energy gathered in the coal body is suddenly released to induce coal bump.

1. Introduction

With the rapid development of China's economy, energy demand has increased dramatically; in situ multistress environment, a large amount of elastic energy is contained in the coal body; and to a certain extent, the sudden release of elastic energy aggravates the destruction of the coal body, which leads to the instability of the coal-rock system-induced coal bump events that gradually increased. Therefore, it is important to study the mechanical damage mechanism of coal damage and the prevention of key coal bump areas through numerical simulation and field monitoring. Coal bump, characterized by the dynamic vibration and rock-mass spallation, is directly correlated to the geological structure, in situ stress, and lithology. Due to the nonlinearity and mortal threat of the coal bump, numerous efforts and research interest have been focused on the mechanism and trigger factors [1–6].

For the complex nonlinear and dynamic mechanic properties, coal bump is regarded as a discontinuous problem, and a comprehensive method, including theoretical derivation, field measurement, and numerical simulation, was employed [7, 8]. The mining geometry and surrounding rock mass properties influence the concentration and

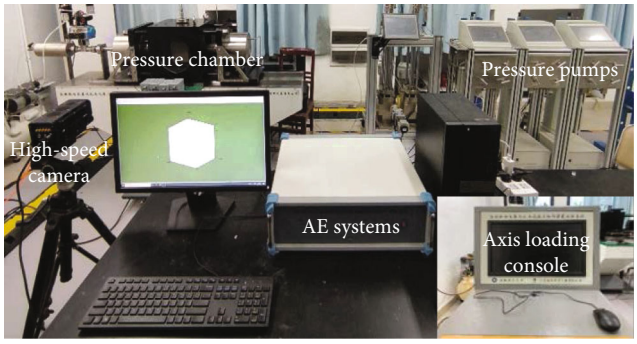

Figure 1: Three-axis dynamic and static loading experimental system.

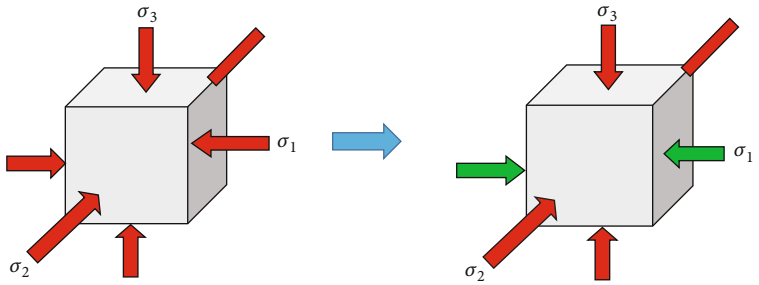

Figure 2: Loading and unloading 3D schematic (path 1).

instability of the elastic energy [9, 10]. The theoretical and numerical models, including "strength theory," "stiffness theory," and "energy theory" which are named "rock burst basic theory," were developed for the coal bump judgment and prediction [11]. Considering the influence of the geology and geomechanics, Thom [12] and Henley [13] developed a catastrophe theory for the prediction of the coal bump. Regarding the roof and the coal pillar as a testing machine and coal specimen system, Pan and Zhang [14] established a cusp catastrophe model. Using the catastrophe theory, Qin et al. [15] and Xu et al. [16] studied the instability mechanisms of the coal-pillar-and-roof system.

The static stress, seismic activity, or acoustic emission (AE) is the source of rock bursts and support damage [17]. Monitoring method, including EME, AE, electric charge, and microseismic (MS) monitoring as well as seismic velocity tomography, is the most popular method for monitoring and predicting the coal bump. Assuming the rock burst is caused by static and dynamic load superposition, He et al. [4] proposed the microseismic and electromagnetic coupling method for coal bump assessment. According to Lu and Dou [18], the relationship between the vertical stress gradient, seismic, and EME signals at the Sanhejian mine was investigated and a positive correlation was found between the number of seismic events, the vertical stress concentration factor, and the strength of the EME signal and the borehole [19]; it was concluded that microseismic monitoring systems were widely installed in deep mine, and the model calibration process, considering AE or microseismic source location and source parameter, was a challenge.

Most of the above studies on the characteristics of damage mechanical behavior of coal samples and the law of acoustic

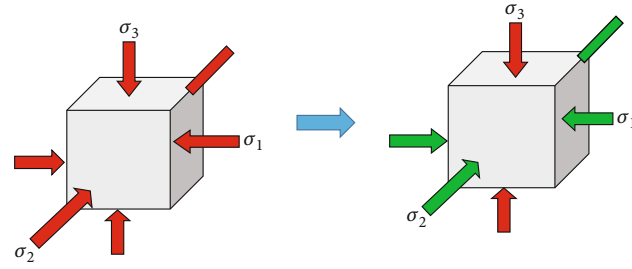

Figure 3: Loading and unloading 3D schematic (path 2).

emission signals are based on theoretical studies or numerical simulations, which have a single research means and deviations in the research results under the inversion of real geological conditions, and the determination of coal rock dynamic hazards and impact propensity is a macroscopic study based on field monitoring, and there are fewer studies on the damage mechanical characteristics of coal samples under different unloading stress paths in the true triaxial. To address the above problems, this paper designs experiments on the damage characteristics of coal samples under three different unloading stress paths using the true triaxial experimental system with Hujiahe coal mine engineering geology as the research background and investigates the peak damage strength of coal samples. Based on the experimental study, numerical simulation and field monitoring methods were used to analyze the key monitoring areas where coal bump occurred in Hujiahe coal mine and the effects of dynamic and static loading stress on the sensitivity of coal pillars and working face width.

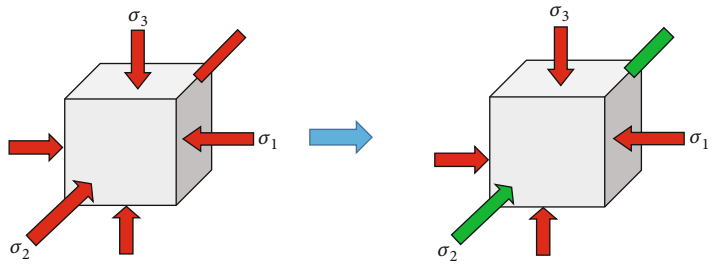

Figure 4: Loading and unloading 3D schematic (path 3).

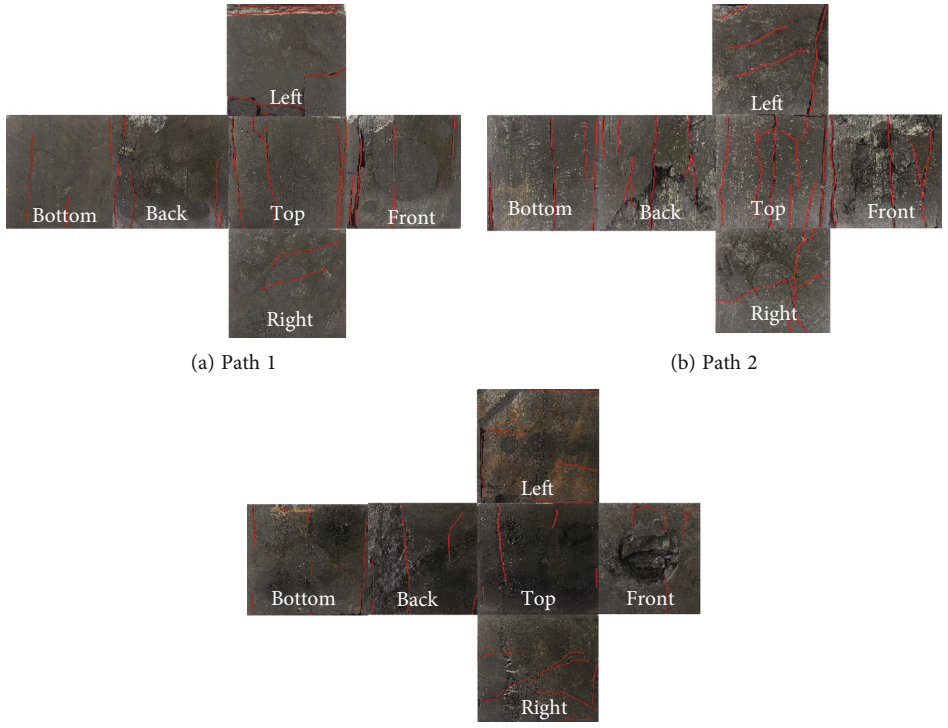

(a) Path 1

(b) Path 2

(c) Path 3

Figure 5: Deformation and damage characteristics of coal bodies in different paths.

2. Triaxial Experiment

2.1. Experimental Equipment. To study the mechanical damage behaviour, acoustic emission characteristics and coal bump mechanism of coal samples, the experiment uses the "three-axis dynamic and static loading experimental system." The experimental device can realize independent loading of three directions. The system consists of an acoustic emission monitoring system, a high-speed camera, an axial loading console, a pressure chamber, and a pressure pump, as shown in Figure 1.

2.2. Experimental Steps. Three excavation scenarios are often used in the mining process of Hujiahe coal mine: one is excavation along one side of the coal body, another is excavation along two symmetrical faces of the coal body, and another is excavation along two adjacent faces of the coal body. Therefore, the three stress paths in this paper correspond to the above three scenarios, respectively. In the three-dimensional diagram, $\sigma_1(X)$ indicates the minimum principal strain; $\sigma_2(Y)$ indicates the maximum principal strain; $\sigma_3(Z)$ indicates the intermediate principal strain; the red arrow indicates the loading direction, and the green arrow indicates the unloading direction.

Path 1: from Figure 2, first load the stress in three directions to the initial balance. Subsequently, the $\sigma_3(Z)$ direction was loaded. The $\sigma_1(X)$ direction was unloaded to 0 MPa after stabilization for 2 minutes.

Path 2: from Figure 3, first load the stress in three directions to the initial balance. Subsequently, the $\sigma_3(Z)$ direction was loaded. After stabilizing for 2 minutes, $\sigma_1(X)$ and $\sigma_2(Y)$ are simultaneously unloaded to 0 MPa.

Path 3: from Figure 4, first load the stress in three directions to the initial balance. Subsequently, the $\sigma_3(Z)$ direction was loaded. After stabilizing for 2 minutes, the $\sigma_2(X)$ direction was unloaded to 0 MPa.

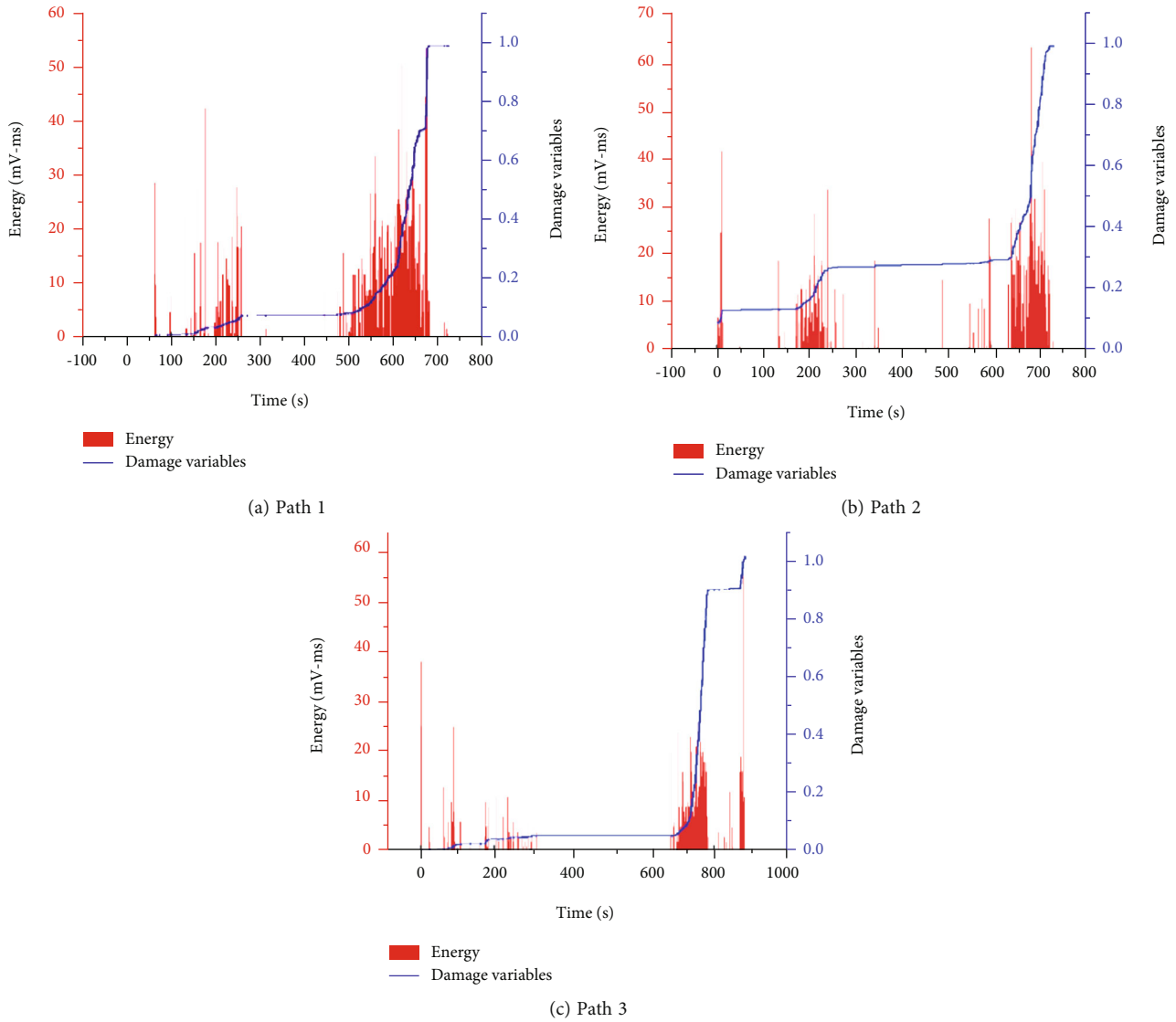

Figure 6: Diagram of AE energy and damage variables of coal body loaded under different stress paths.

2.3. Analysis of Experimental Results

2.3.1. Analysis of Damage Characteristics of Coal Samples. Analysis of coal body damage characteristics by 3 different stress paths was conducted.

In path 1, there are two macroscopic cracks on each of the front and back surfaces, less density of cracks on the left and right surfaces, and four macroscopic cracks on the top surface, as shown in Figure5(a).

In path 2, the fracture density of the front and back surfaces is larger relative to the fracture density of the path 1 test, with a total of 12 macroscopic fractures through the specimen, a smaller fracture density on the left surface, an annular fracture on the right surface, and a total of 12 macroscopic fractures through the specimen on the top and bottom surfaces as well as misalignment friction of coal powder particles inside the specimen, with the specimen in tensile-shear damage, as in Figure 5(b).

In path 3, stress concentration occurs on the front surface and three macroscopic fractures through the back surface, two macroscopic fracture on the right surface, fewer cracks on the top and bottom surfaces, as shown in Figure 5(c).

2.3.2. Acoustic Emission Response Characteristics. From Figure 6, it is concluded that in the three different stress paths, looking at the whole process of coal sample damage by loading, when the coal sample has a large rupture produced, the acoustic emission will show a sudden increase [20, 21]. In path 2, the increase of acoustic emission energy is not necessarily continuous but may also be jumping, which indicates that the energy release presents a scattered distribution when unloading two directions, and the stress is carried by two directions separately; the final energy release in each direction is smaller; in path 1 and path 3, the increase of acoustic emission energy basically presents as intensive and continuous, which indicates that the

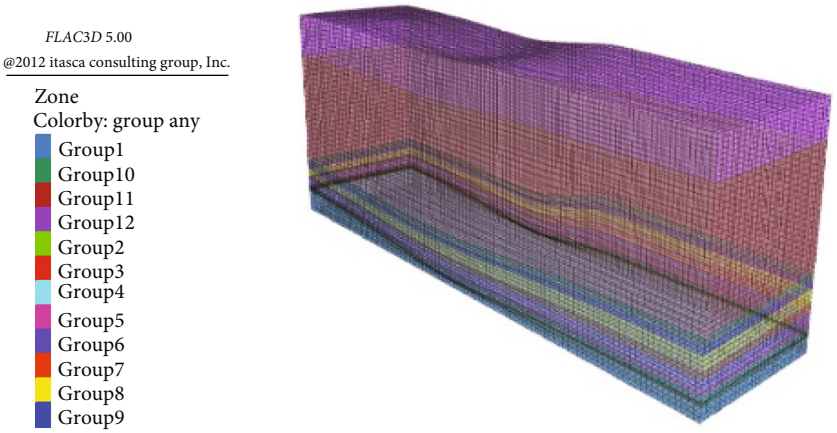

Figure 7: Modeling of the geology.

Table 1: Geometry and mechanical parameters of coal and rock.

Rock properties	Thickness (m)	Modulus of elasticity (GPa)	Poisson ratio	Cohesive strength (MPa)	Internal friction angle (°)	Tensile strength (MPa)
Sand shale	60	6.10	0.12	4.5	27	1.76
Sandstone	60	6.36	0.14	3.23	25	3.90
Mud stone	60	1.86	0.13	5.67	32	1.54
Fine sandstone	12	6.34	0.11	6.21	29	2.79
Silt stone	5	2.32	0.10	5.13	25	1.92
Coal	23	0.81	0.02	5.43	20	2.13
Silt stone	100	2.46	0.11	2.45	31	1.63

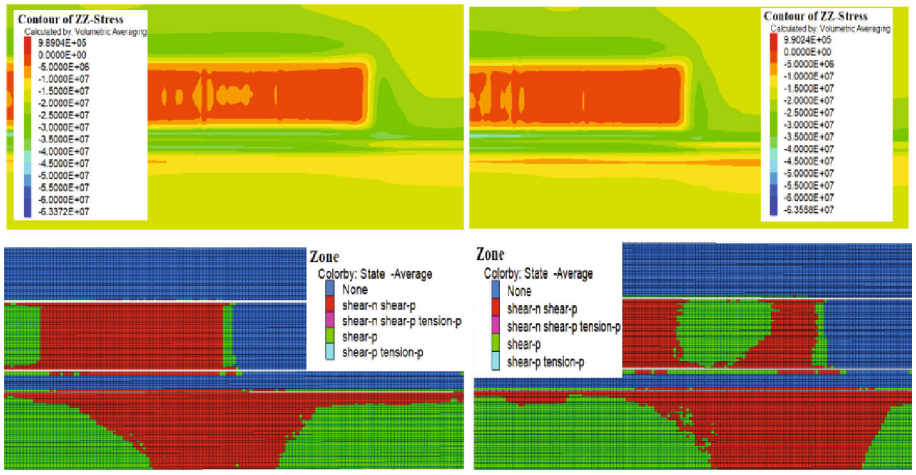

Figure 8: Evolution characteristics of the static stress and rock damage.

stress is borne by only one direction when unloading one direction; the final energy release is larger.

Damage to the coal body has gone through roughly 3 stages as follows.

During the initial damage stage, there is internal pore compressing of the coal sample in the initial stress and no fracture expansion; the internal structure of the coal sample is in a stable state; thus, the value of damage variable in the initial damage stage is 0.

In the damage stabilization stage, the pore space inside the coal sample changes to form tiny fissures due to the continuous loading of stress, and the fissures in the coal sample gradually stabilize and develop under the action of stress, with damage variable values reaching 0.03~0.14.

During the accelerated development stage, the value of the damage variable increases in 90° increments. As the fractures develop rapidly and extend throughout the coal sample during stress loading, the load bearing capacity of the sample

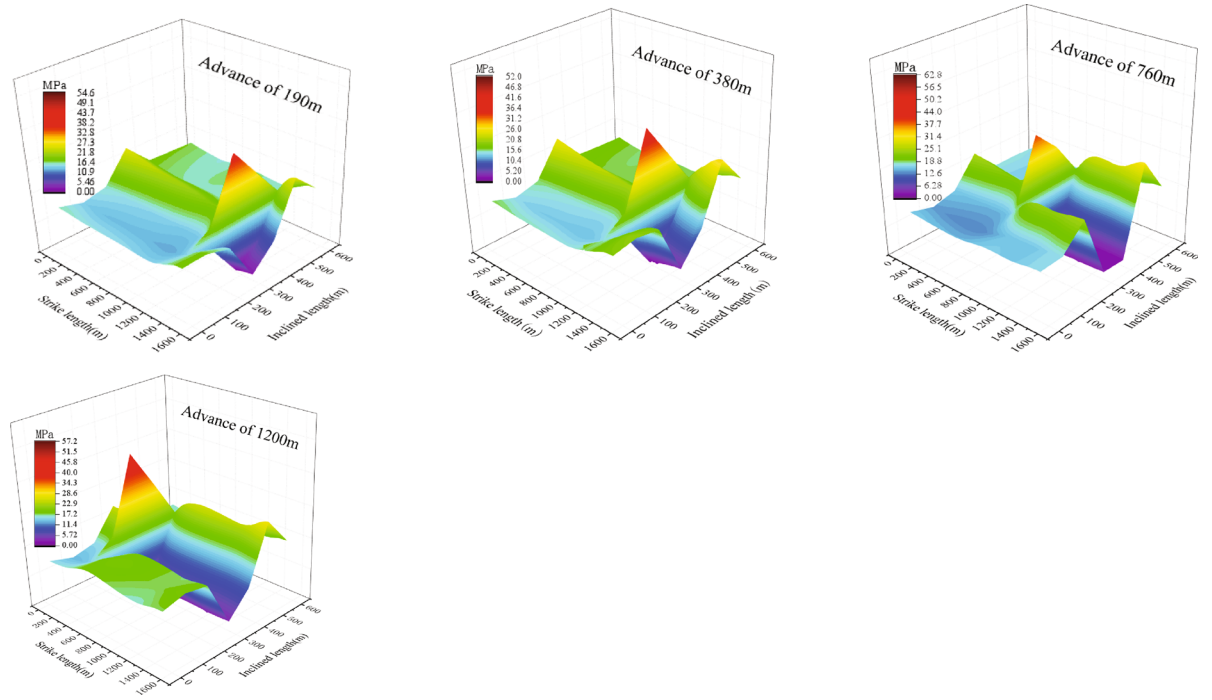

(a)

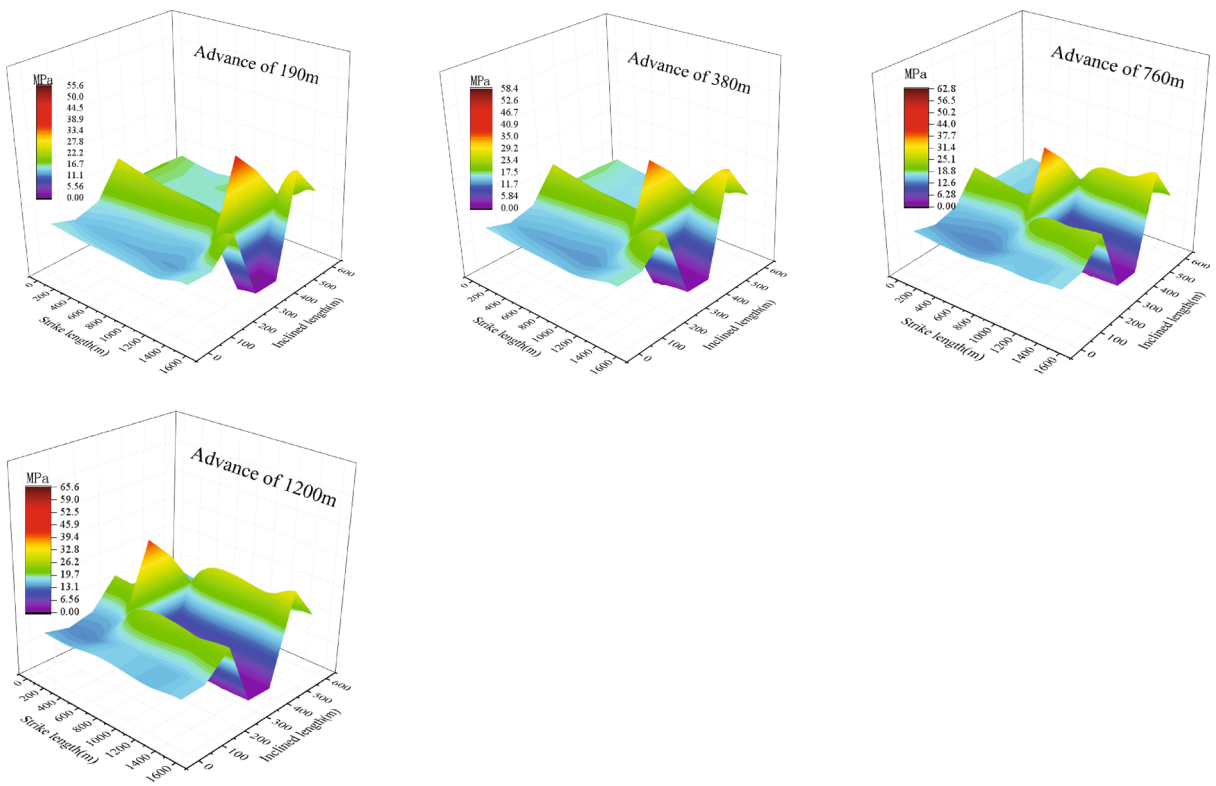

(b)

Figure 9: Continued.

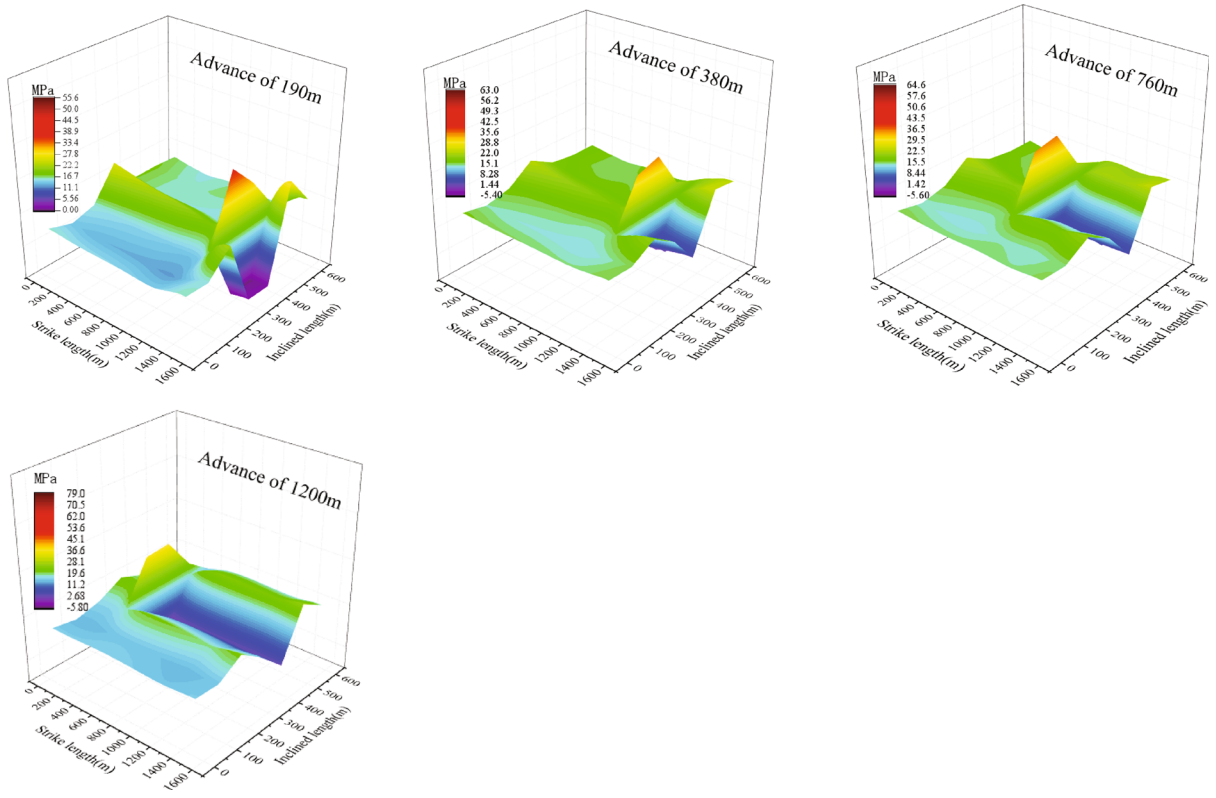

(c)

Figure 9: Vertical stress evolution for different pillar widths: (a) 5 m, (b) 25 m, and (c) 70 m.

weakens, the damage variable increases sharply, and the sample is completely destroyed.

3. Modeling of the Panel #401103

3.1. Geological Model. Hujiahe coal mine is located in Changwu County District, Xianyang City, Shaanxi Province, China, and is a typical coal bump coal mine. In order to accurately probe the area to be focused on in engineering applications, numerical simulation should be performed to restore the geological structure of coal#4. Coal #4 is the main coal seam with an average depth of 680 m, inclination of 5°, and thickness of 23 m.

In order to accurately describe the change of surrounding rock stress field and fracture field under the influence of mine activity, the simulation was conducted. In detail, a real geological model with a dimension of 1449 m × 606 m × 753 m (length × width × high) was established based on the lithology boreholes. The boundaries were constrained with a free roof, as shown in Figure 7. The geometry and mechanical parameters employed in the model are shown in Table 1.

3.2. Characteristic and Evolution of Static Stress of Surrounding Rock Mass. In order to accurately probe the area to be focused on in engineering applications, the mining process of the 401103 working face was first numerically simulated, as shown in Figure 8.Within 190~1200 m in front of the mining face, due to the large deformation of the roadway and effect of shear force, the stress is concentrated and the coal bump may occur. The region behind the mining face was damaged by shear and stretch under the effect of concentrated stress. The coal pillar-side stress concentration significantly increased with the advance of the mining face. The evolution characteristics of stress field and fracture field of the panel #401103 indicate that stress concentrations occur at the coal pillars and the gob in the range of 0~100 m in front of the working face, and there is a higher risk of coal bump in the roadway near the 401102 working face.

3.3. Effect of Coal Pillar Width. The coal mining was conducted under the condition of 5 m, 25 m, and 70 m coal pillar in mining geology. Figure 9 indicates that the vertical stress was characterized with increase and decrease in cloud picture, with the advance of the working face. The maximum vertical stress of the working face was 39.8 MPa and 35.8 MPa, respectively, for the coal pillar of 5 m and 25 m. For coal pillar of 70 m, the peak value of the mining face was 33.8 MPa to 35.1 MPa. As a result, the vertical stress decreased with the increase of the coal pillar width.

After coal mining, the stress concentration zone was presented ahead of the mining face, and the release stress zone was located in the gob. From Figure 10, it can be concluded that during the advance of the working face from 190 m to 760 m, the sensitivity of vertical stress to pillar width increases; when the working face advances 1200 m, the sensitivity of vertical stress to pillar width decreases.

With the advance of the working face, different coal pillar widths have a significant effect on the vertical stress and both

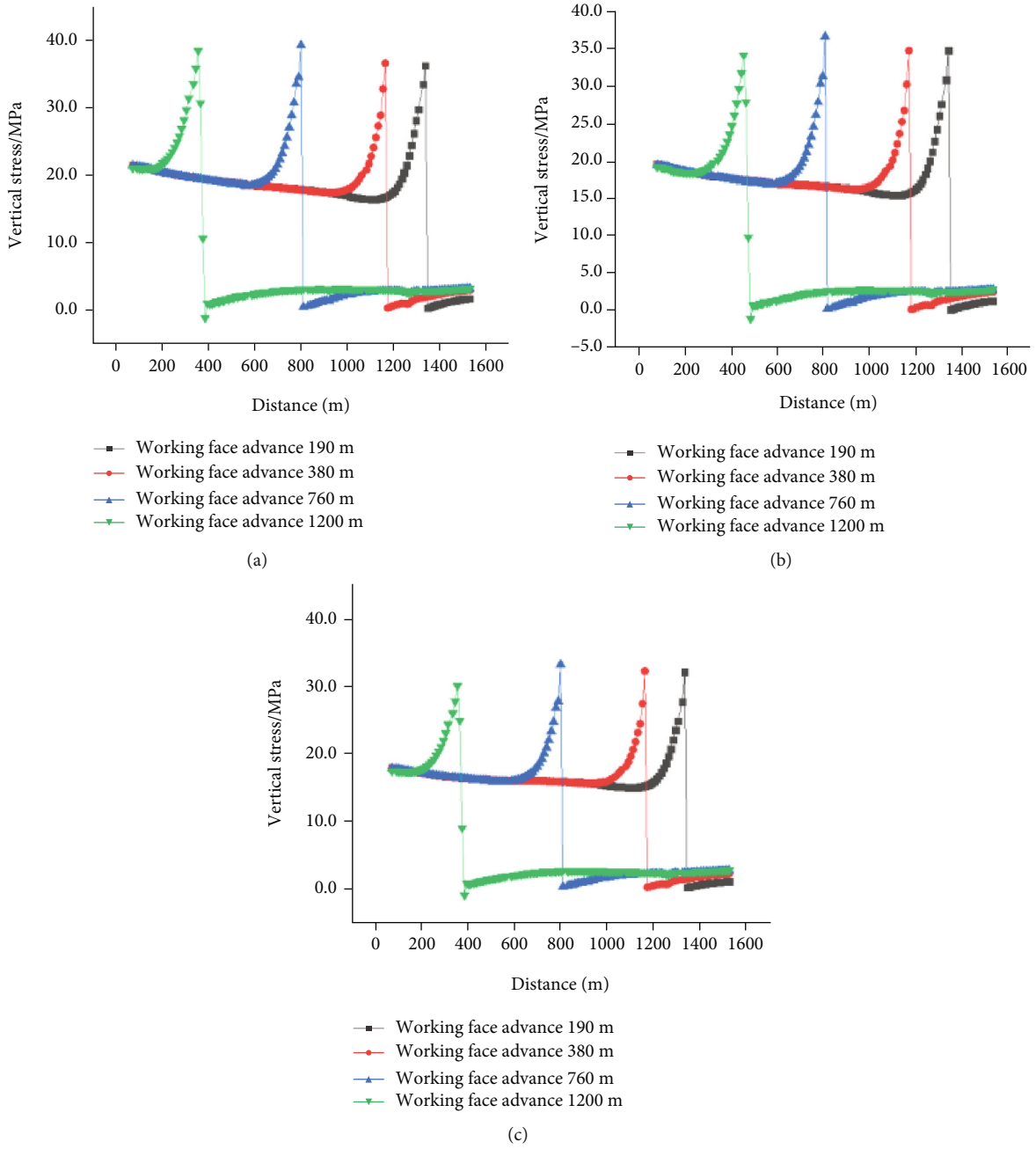

Figure 10: Vertical stress change in different pillar widths: (a) 5 m; (b) 25 m; (c) 70 m.

sides of the pillar show stress increase and decrease zones, and the peak stress shows that it increases first and then decreases with the advance of the working face. Finally, with the increase of the width of coal pillar from 5 m to 70 m, the peak of the vertical stress maintained stable and the morphology presented parallel distribution, as shown in Figure 10.

Figure 10 illustrates that the working face is advanced from 190 m to 760 m, the vertical stress shows a rising trend, and the stability was obtained after 760 m. The curve of stress peak was opposite to that of the pillar width in trend, with the increase of the pillar width from 5 m to 70 m and with the peak value decreasing from 39 MPa to 32 MPa.

3.4. Effect of Mining Face Width. In Figure 11, for the 250 m width of the working face, the vertical stress reached 39 MPa as the working face was advanced to 1200 m. The vertical stress reached 40 MPa as the mining face was advanced to 760 m. The vertical stress reaches 38 MPa and 37 MPa as the mining face was advanced to 380 m and 190 m. By contrast, for the 300 m width of the mining face, the vertical stress reaches 44 MPa as the mining face was advanced to 1200 m. The vertical stress reached 45 MPa as the mining face was advanced to 760 m. The vertical stress reached 39 MPa and 38 MPa as the mining face was advanced to 380 m and 190 m. Meanwhile, at the 350 m width of the mining face, the vertical stress reached

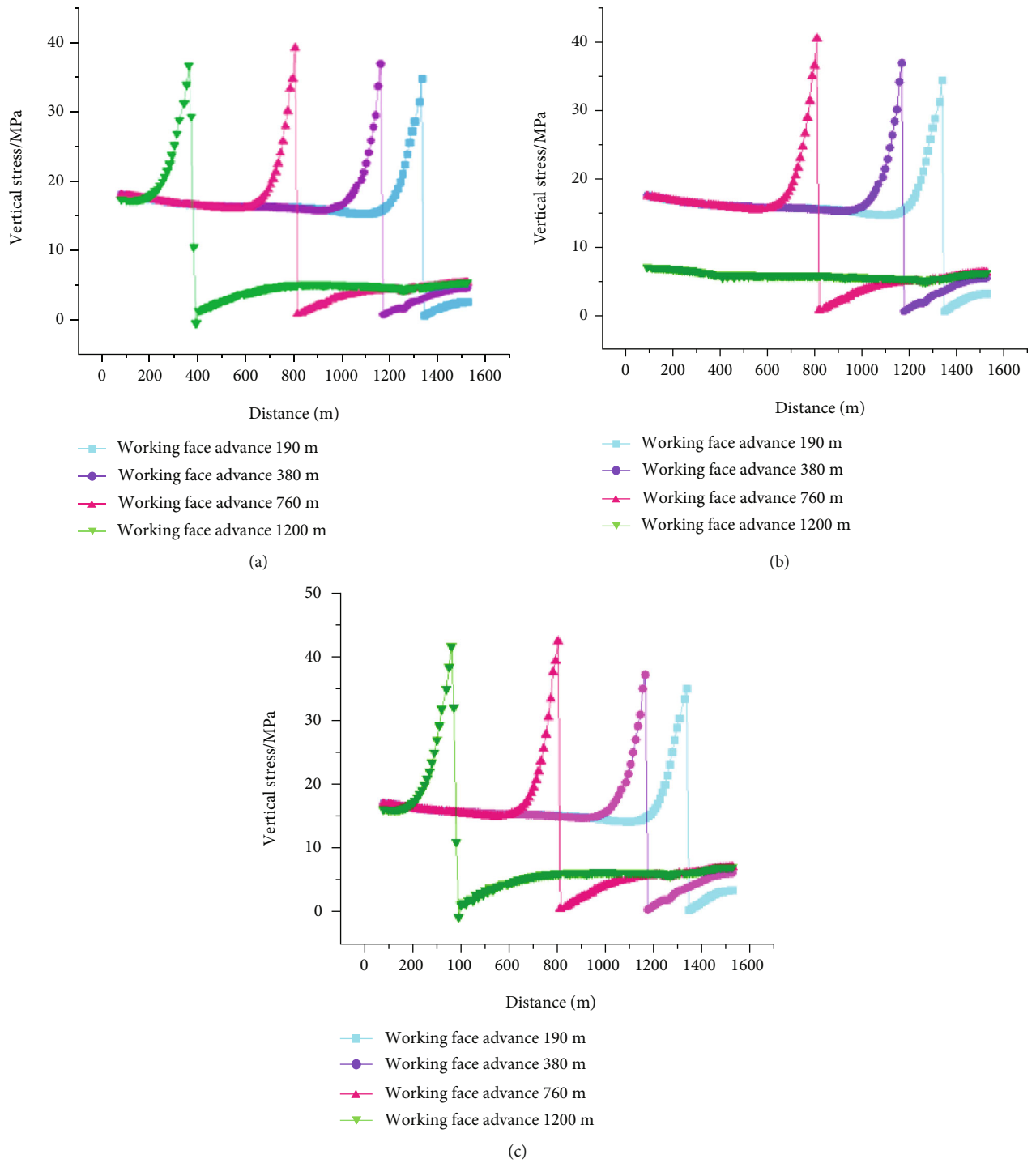

Figure 11: Vertical stress change in different working face widths: (a) 250 m, (b) 300 m, and (c) 350 m.

15 MPa as the working face advanced 1200 m. The vertical stress reached 42 MPa as the mining face was advanced to 760 m. The vertical stress reached 39 MPa and 38 MPa as the working face was advanced to 380 m and 190 m, respectively.

In Figure 11, with the advance of the working face, the stress increase zone and the reduction zone appeared on both sides of the coal pillar. The width of the working face has a significant effect on the vertical stress evolution. When the sensitivity of vertical stress to working face width increases, stress concentration phenomenon occurs, and the sudden release of a large amount of elastic energy accumulated in the coal body will lead to coal bump.

4. Coal Bump Theory Analysis

4.1. Coal Bump Theory Analysis. In Figure 12, a model of coal bump occurring at the coal pillar and working face caused by dynamic and static coupled stresses has been established based

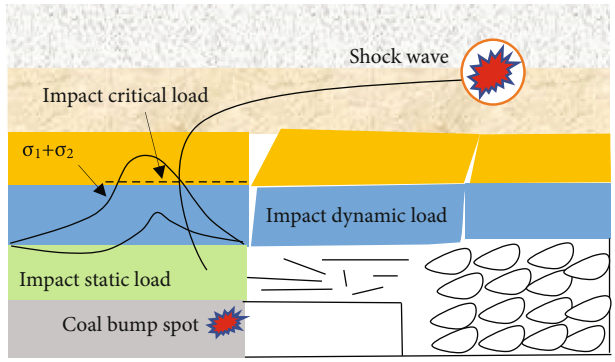

Figure 12: The coal bump model is due to the superposition of dynamic and static loads (σ_d and σ_s represent the static and dynamic stress, respectively, and $\sigma_d + \sigma_s$ represent the superposition of dynamic and static loads stress).

Table 2: Summary of peak intensity of 3 sets of coal samples.

Group	Paths	Peak intensity (MPa)	Average intensity (MPa)	Critical stress of coal bump (MPa)
1	1	17.26	15.26	15.7
	2	13.21		
	3	15.32		
2	1	12.45	14.02	
	2	17.39		
	3	12.24		
3	1	19.20	17.77	
	2	15.10		
	3	19.00		

on extensive research [22–24]. Classical coal bump mechanisms can be divided into two categories, one characterized by high static stress concentrations in the coal pillar and the other caused by dynamic stresses or shock waves due to rock movement at a considerable distance from the working face.

Different widths of coal pillars and working surfaces have significant effects on the sensitivity to vertical stress. The wider the coal pillar, the vertical stress decreases significantly. The wider the working face, the lower the vertical stress tends to be as the working face advances. Coal seams are subjected to certain static stresses due to gravity, tectonic stresses, and stresses caused by mining activities, while many factors cause shock waves during the mining process, such as hard top breaking, coal seam rupture, and blasting [25, 26]. These shock waves are transmitted to the perimeter of the mine or road and exert dynamic stresses on the coal or rock mass [27]. The total stress is an integration of static and dynamic stress, and the coal bump will certainly occur when the total stress exceeds the minimum critical value of coal bump.

4.2. Coal Bump Mechanism. Peak intensity is the mechanism of induced coal bump; different stress path is one of the factors affecting the occurrence of coal bump, both of which are the discriminatory criteria for induced rock bursts. Due to the influence of the internal structure of the coal samples, the peak intensity of the stress paths is significantly different. The mean value of peak intensity of the three groups lies within the 15.7 MPa. It can be shown that the higher the peak intensity, the greater the damage intensity, and when the average intensity range is exceeded, it will trigger the coal bump, as shown in Table 2.

The paper uses true triaxial experiments to study the destabilization of the coal rock system caused by coal sample damage, which is a high static load stress effect. Static energy concentration is a key factor causing coal bump; the higher the concentration of stress, the higher the probability of coal bump. In order to accurately describe this phenomenon, the study of the occurrence of coal bump mechanism can be described as follows:

$$\sigma_1 + \sigma_2 \geq \sigma_k, \tag{1}$$

where σ_1 represents the initial static stress of the coal body; σ_2 represents the dynamic stress caused by coal body damage; and σ_k represents the critical stress of coal bump.

From the true triaxial experiments, it is known that the critical stress σ_k coal bump is located in the 15.7 MPa; when the sum of the static stress and the dynamic stress caused by coal body damage is greater than 15.7 MPa, the coal rock system instability is triggered by coal bump.

5. On-Site Monitoring

5.1. Field Monitoring. Based on the characteristics of acoustic emission signals from the above experiments and the key monitoring areas obtained from numerical simulation

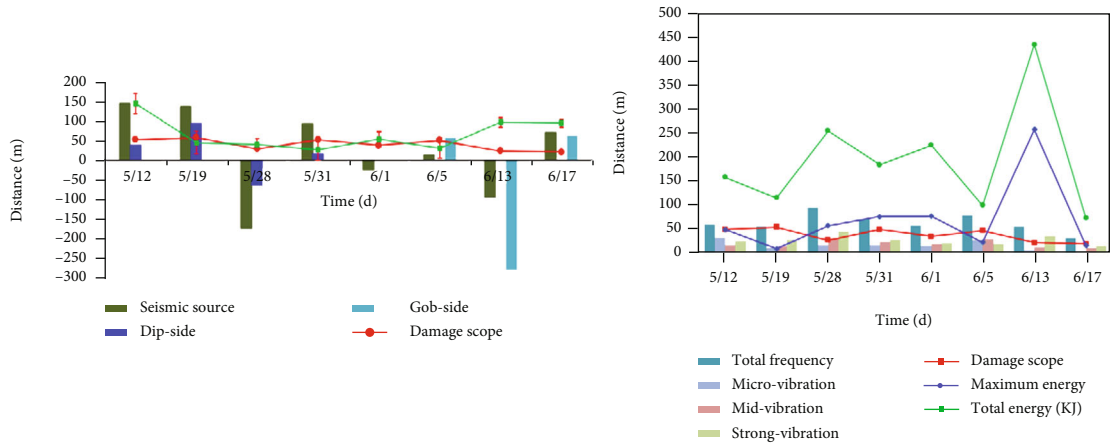

Figure 13: Rock burst event statistics.

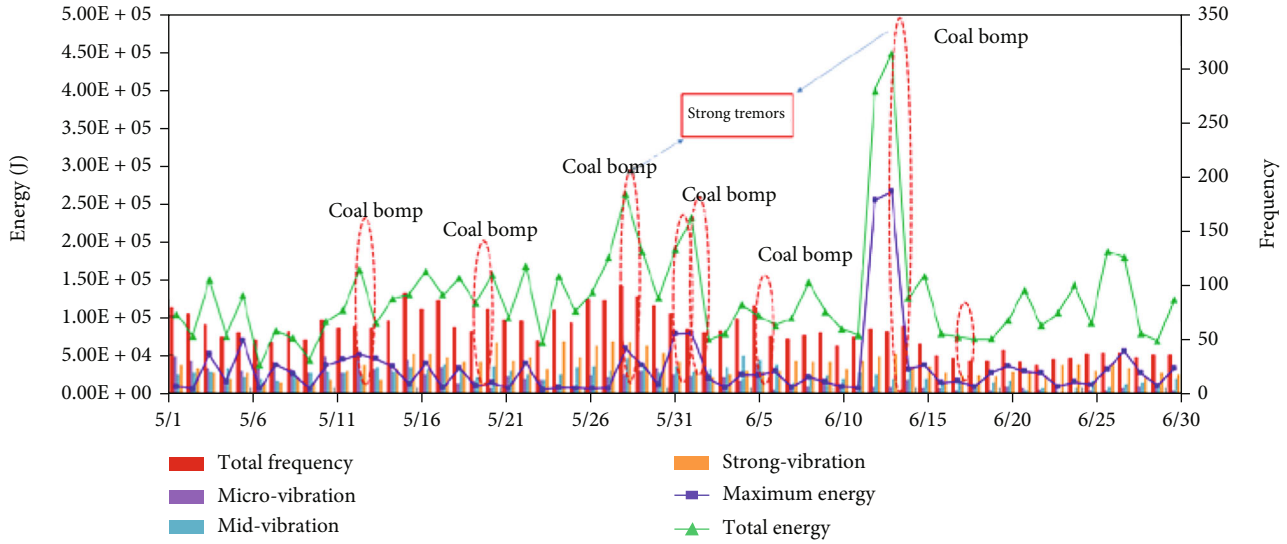

Figure 14: Time series of the tremors before the occurrence of rock bursts.

analysis, the electromagnetic emission (EME) method is used to reveal the microseismic law of coal bump occurring at the 401103 working face. The specific monitoring produce is shown below: three field recorder scones were placed at the mining face side along the ventilation roadway with an interval of 30~50 m; one field recorder scone was placed at the mining face side along the haulage roadway with an interval of 30 m to display the vibration of the surrounding rock of the mining face and roadway.

5.2. In-Site Energy Condition. During the mining process, the dynamic energy characterized by "coal bump" sound, local roadway caving and bottom drum, anchor (rope) off, and belt frame and rib spalling was frequently presented in the panel of #401103. Based on the electromagnetic emission (EME) monitoring system, the relationship between vibration energy and rock bursts frequency is investigated [28]. A total of 8 times coal bump occurred during the excavation of panel #401103, as shown in Figure 13 From May 12 to June 17, the microvibration, midvibration, strong vibration, damage scope, maximum energy, total energy, and the relationship between coal bump were observed. The maximum energy of 250 KJ ahead of the working face at 100 m and microvibration energy less than 50 KJ were obtained. The same phenomenon for midvibration and strong vibration occurred. A smoothing trend of damage scope was obtained. With the dynamic change of the damage scope, the location of coal bump also changed. The distance between the coal bump and the seismic source was approximately 50 m, as shown in Figure 13.

The coal bump mainly occurred at 100 m ahead of the mining face in the ventilation roadway. Vertical stress was mainly produced at the scope of 0~100 m ahead of the mining face associated with a 0~50 m damage region ahead of the mining face. At the same time, the frequent microvibration and midvibration can also lead to the occurrence of coal bump.

5.3. Response of the Mining Face. Figure 14 shows that the time series of the energy, vibration, and frequency were monitored by the EME system in the #401103 working face from May 1 to June 30. The total frequency showed slight fluctuation, indicating that the fracture did not get steady

in the coal body. The midvibration was activated, and at the same time, the accumulated energy was released inadequately, respectively; the energy concentration increased easily to the critical value and was released suddenly at one time, resulting in a serious rock bursts. The vibration activities during May 1 to June 30 demonstrated basically similar rules. From May 1 to June 30, the total energy almost remained at more than 2×10^5 J or less than 2×10^5 J. The coal bumps occurring on June 13 and 14 were characterized by a higher energy release, compared to the coal bumps occurring on May12, May 19, May 28, May 31, and June 1.

The total energy exhibited a "rise trend" during the 3 days, and occurrence probability of coal bump was high. After the coal bump, the EME and microvibration monitoring index remained at a relatively low level for several days, as the accumulated energy almost released, as shown in Figure 14.

In Figure 14, the frequency of tremors and total energy presented similar pattern to each other; as a result, there was no time for the energy to concentrate, and each impact was not enough to cause a catastrophe in the rock burst disaster. This provides a guide to the prevention of coal bump in high stress areas, facilitating the dissipation of energy in the control, and at the same time, this allows the effect of stress to be assessed.

Figure 14 describes the time series of the tremors before the occurrence of rock bursts. The microseismic signals were weak, and precursors were not obvious before the occurrence of the rock burst because the breakage of roof strata was prone to occur abruptly. The fracture of this stratum will cause strong dynamic stresses. As a result, the dynamic stresses generated by the fracture of the strata instantly feed high stresses into the coal and rock in the vicinity of the roadway, triggering rock bursts when the stresses reach the critical strength of the coal and rock [29]. The laws obtained from the field monitoring are well coupled with the basic experiments and numerical simulations.

6. Conclusions

(1) The acoustic emission shows signs of a sudden increase in stage when the coal sample appears to rupture. The increase in acoustic emission energy is not necessarily continuous

(2) Stress concentrations occur at the coal pillars and the gob in the range of 0~100 m in front of the working face, and there is a higher risk of coal bump in the roadway near the 401102 working face

(3) It is known that the critical stress σ_k coal bump is located in the 15.7 MPa; when the sum of the static stress and the dynamic stress caused by coal body damage is greater than 15.7 MPa, the coal rock system instability is triggered by coal bump

(4) The coal bump mainly occurred at 100 m ahead of the mining face in the ventilation roadway, the maximum energy up to 250 KJ

Data Availability

The data used to support the findings of this study are included within the article.

Conflicts of Interest

The authors declare no conflict of interest.

Acknowledgments

This work was supported by the Institute of Energy, Hefei Comprehensive National Science Center, under Grant No. 21KZS216; Postgraduate Innovation Fund, Anhui University of Science and Technology (2020CX2015); Open Fund of State Key Laboratory of Water Resource Protection and Utilization in Coal Mining (GJNY-18-73.7); National Youth Science Foundation (No. 51904011); Natural Science Foundation of Anhui Province (No. 1908085QE183); Anhui University Scientific Research Foundation (No. QN2018108); and Independent Research fund of the State Key Laboratory of Mining Response and Disaster Prevention and Control in Deep Coal Mines, Anhui University of Science and Technology (SKLMRDPC19ZZ05).

References

[1] H. Wang, B. A. Poulsen, B. Shen, S. Xue, and Y. Jiang, "The influence of roadway backfill on the coal pillar strength by numericalinvestigation," *International Journal of Rock Mechanics & Mining Sciences*, vol. 48, no. 3, pp. 443–450, 2011.

[2] K. Bo-Hyun, K. L. Mark, and H. E. Lawson, "Applying robust design to study the effects of stratigraphic characteristics on brittle failure and bump potential in a coal mine," in *36th Ground Control Conference*, 2017.

[3] B. María, D. Aguado, and C. González, "Influence of the stress state in a coal bump-prone deep coalbed: a case study," *International Journal of Rock Mechanics & Mining Sciences*, vol. 46, no. 2, pp. 333–345, 2009.

[4] X. Y. Li and Y. M. Li, "The instability mechanics of surrounding rock-coal mass system in longwall face and the prevention of pressure bumps," *Journal of Coal Science & Engineering (China)*, no. 1, pp. 47–50, 2003.

[5] S. Qin, "Instability leading to rock bursts and nonlinear evolutionary mechanisms for coal-pillar-and-roof system," *Journal of Engineering Geology*, vol. 13, no. 4, pp. 437–446, 2005.

[6] L. M. Dou, Z. L. Mu, Z. L. Li, A. Y. Cao, and S. Y. Gong, "Research progress of monitoring, forecasting, and prevention of rockburst in underground coal mining in China," *International Journal of Coal Science & Technology*, vol. 1, no. 3, pp. 278–288, 2014.

[7] M. D. G. Salamon, "Keynote address: some applications of geomechanical modeling and related research," in *Rock burst and Seismicity in Mines, Proceedings of the 3rd International Symposium*, pp. 279–309, Balkema, Rotterdam, 1993.

[8] P. K. Kaiser, "Observational modeling approach for design of underground excavations," in *Proceedings of International Workshop on Observational Method of Constructions of Large Underground Caverns in Difficult Ground Conditions*, pp. 1–7, Tokyo, 1995.

[9] C. A. Tang, *Catastrophe in Rock Unstable Failure (in Chinese)*, China Coal Industry Publishing House, Beijing, 1993.

[10] J. A. Wang and H. D. Park, "Comprehensive prediction of rockburst based on analysis of strain energy in rocks," *Tunnelling and Underground Space Technology*, vol. 16, no. 1, pp. 49–57, 2001.

[11] L. M. Dou, C. P. Lu, Z. L. Mu, and M. S. Gao, "Prevention and forecasting of rock burst hazards in coal mines," *Mining Science and Technology*, vol. 19, no. 5, pp. 585–591, 2009.

[12] R. Thom and Stabilite´ Structurelle, *Morphoge'ne'se*, Benjamin, New York, 1972.

[13] S. Henley, "Catastrophe theory models in geology," *Journal of the International Association for Mathematical Geology*, vol. 8, no. 6, pp. 649–655, 1976.

[14] Y. S. Pan and M. T. Zhang, "Analysis on the physical process of rock bursts by catastrophe theory (in Chinese)," *Jiang Fuxin Mining Institution*, vol. 11, no. 1, pp. 12–18, 1992.

[15] S. Q. Qin, Z. Y. Zhang, and S. T. Wang, *An Introduction to Nonlinear Engineering Geology*, Southwest University Press of Transportation, Chengdu, PR China, 1993.

[16] Z. H. Xu, X. H. Xu, and C. A. Tang, "Analysis of a cusp catastrophe bump of coal pillar under hard rocks," *Journal China Coal Society*, vol. 20, no. 5, pp. 191–485, 1995.

[17] P. K. Kaiser and C. A. Tang, "Numerical simulation of damage accumulation and seismic energy release during brittle rock failure–part II: rib pillar collapse," *International Journal of Rock Mechanics & Mining Sciences & Geomechanics Abstracts*, vol. 35, no. 2, pp. 123–134, 1998.

[18] C. P. Lu and L. M. Dou, "The relationship between vertical stress gradient, seismic, and electromagnetic emission signals at Sanhejian coal mine, China," *International Journal of Rock Mechanics & Mining Sciences*, vol. 70, pp. 90–100, 2014.

[19] P. K. Kaiser, D. D. Tannant, and D. R. McCreath, "Support of tunnels in burst-prone ground," in *Proceedings of 8th International Congress on Rock Mechanisms*, vol. 2, pp. 471–477, Tokyo, 1995.

[20] Y. Xue, J. Liu, P. G. Ranjith, Z. Zhang, F. Gao, and S. Wang, "Experimental investigation on the nonlinear characteristics of energy evolution and failure characteristics of coal under different gas pressures," *Bulletin of Engineering Geology and the Environment*, vol. 81, no. 1, p. 38, 2022.

[21] P. Hou, Y. Xue, F. Gao et al., "Effect of liquid nitrogen cooling on mechanical characteristics and fracture morphology of layer coal under Brazilian splitting test," *International Journal of Rock Mechanics and Mining Sciences*, vol. 151, article 105026, 2022.

[22] Y. S. Yang, S. J. Wei, and D. M. Zhang, "Influence of rock burst and other disasters on stability of surrounding rock of roadway," *Geotechnical and Geological Engineering*, vol. 36, no. 3, pp. 1767–1777, 2018.

[23] H. W. Zhang, E. Derek, and Z. J. Wan, "Failure response of composite rock-coal samples," *Geomechanics and Geophysics for Geo-Energy and Geo-Resources*, vol. 4, no. 2, pp. 175–192, 2018.

[24] Y. Y. Pu, A. Derek, and H. W. Xu, "A principal component analysis/fuzzy comprehensive evaluation for rockburst potential in kimberlite," *Pure and Applied Geophysics*, vol. 175, no. 6, pp. 2141–2151, 2018.

[25] X. J. Hao, W. S. Du, and Y. X. Zhao, "Dynamic tensile behaviour and crack propagation of coal under coupled static-dynamic loading," *International Journal of Mining Science and Technology*, vol. 30, no. 5, pp. 659–668, 2020.

[26] X. J. Hao, Y. N. Wei, and K. Yang, "Anisotropy of crack initiation strength and damage strength of coal reservoirs," *Petroleum Exploration and Development*, vol. 48, no. 1, pp. 243–255, 2021.

[27] J. F. Lou, F. Q. Gao, J. H. Yang et al., "Characteristics of evolution of mining-induced stress field in the longwall panel: insights from physical modeling," *International Journal of Coal Science and Technology*, vol. 8, no. 5, pp. 938–955, 2021.

[28] H. Hu, D. Ldc, and D. Sgb, "Microseismic and electromagnetic coupling method for coal bump risk assessment based on dynamic static energy principles," *Safety Science*, vol. 114, pp. 30–39, 2019.

[29] G. Wang, S. Gong, L. Dou, W. Cai, X. Yuan, and C. Fan, "Rockburst mechanism and control in coal seam with both syncline and hard strata," *Safety Science*, vol. 115, pp. 320–328, 2019.

Hindawi
Geofluids
Volume 2022, Article ID 2794446, 13 pages
https://doi.org/10.1155/2022/2794446

Research Article

Relationship between Permeability Coefficient and Fractal Dimension of Pore in Ionic Rare Earth Magnesium Salt Leaching Ore

Dan Wang[1], **Yunzhang Rao**[1], **Liang Shi**[1,2], **Wei Xu**[3] and **Tao Huang**[1]

[1]*School of Resources and Environmental Engineering, Jiangxi University of Science and Technology, Ganzhou 341000, China*
[2]*School of Resources and Architectural Engineering, Gannan University of Science and Technology, Ganzhou 341000, China*
[3]*The Seventh Geological Brigade of Jiangxi Bureau of Geology, Ganzhou 341000, China*

Correspondence should be addressed to Yunzhang Rao; raoyunzhang@jxust.edu.cn

Received 26 January 2022; Revised 27 May 2022; Accepted 2 July 2022; Published 16 July 2022

Academic Editor: Mingwei Chen

The change of permeability coefficient of ionic rare earth ore is one of the most important factors causing the uncontrollable flow of leaching solution, and the variation of pore structure of the ore body has a great influence on the permeability coefficient. The research on the evolution of the relationship between pore structure and permeability coefficient of ionic rare earths is of great significance for controlling water and soil pollution and improving the leaching rate of rare earths. In this paper, the column leaching test of ionic rare earth was carried out to study the evolution of the relationship between pore structure and permeability coefficient. In the process of $MgSO_4$ solution and deionized water leaching, the T_2 spectrum and inversion image at each time were obtained by nuclear magnetic resonance (NMR). Based on the fractal theory, the pore structure change of the inversion image was quantitatively analysed, and the permeability coefficient of samples at each time of different leaching agents was calculated by using supercritical Dubinin-Redushckevich (SDR) model to analyse the nuclear magnetic resonance T_2 spectrum. The results show that in $MgSO_4$ solution, the permeability coefficient of the sample changes significantly, and the growth rate of pore fractal dimension remains large. By discussing the evolution law of pore fractal dimension and seepage characteristics of ionic rare earth, the mathematical relationship between permeability coefficient and pore fractal dimension of mineral soil samples at different depths is fitted by polynomial function.

1. Introduction

Ionic rare earth ore in southern China mainly occurs in clay minerals of the weathered granite layer in the form of hydrated cations or hydroxyl hydrated cations [1], and the content of medium and heavy rare earth elements is relatively high, so it is of great value. At present, in situ leaching technology is widely applied to extract effectively rare earth ions from soil. Compared with pool leaching, heap leaching, and other mining technologies [2], in situ leaching technology has the advantages of higher efficiency, lower cost, and more environmental friendly. However, in the process of in situ leaching, a large amount of leaching solution is injected into the ore body through the injection wells and the pore distribution in the ore body changes in real time, leading to the change of ore body permeability [3]. The result shows that the shape of pore channels and the state of their communication paths control the permeability of ore body. With the increase of porosity in ore body, the more channels and the better connectivity, the better the permeability of ore soil, which is beneficial to the infiltration and diffusion of leaching solution in the ore soil layer. Then, the larger the surface area of the leaching reaction, the larger the leaching reaction rate [4]. Hence, it is of great significance to study

Figure 1: Sampling site of ore soil at different depths.

the relationship between ore body pore structure and permeability coefficient in the process of ionic rare earth in situ leaching [5].

According to the interaction between hydrogen protons in the sample and the external magnetic field, the hydrogen proton information is obtained by nuclear magnetic resonance (NMR) technology. NMR is extensively used in porosity measurement and microstructure studies of rock and soil for its three-dimensional, accurate, and nondestructive advantages. Some scholars have explored the relationship between the microstructure of soil particle pores and seepage characteristics by using NMR and electron microscope scanning technology [6]. Under different water content, Dong et al. [7] studied the change rule of soil pore water storage forms based on NMR, and the influence of dry-wet cycle on soil permeability was evaluated. The results showed that in the process of soil wetting, pore water mainly exists in the form of gravity water, and the permeability of soil is proportional to the 6th power of cycle time within 4 cycles. Based on NMR analysis technology, Yang et al. [8] explored the development law of soil permeability of saturated clay in hydrochemical environment and revealed the influence of salt solution concentration on clay permeability by testing the soil pore structure in salt solutions with different concentration. Altunbay et al. [9] studied the relationship between saturation distribution and permeability of rock mass in the longitudinal sections of samples through analysing NMR data. Ausbrooks [10] and other scholars applied the mercury injection method to explore carbonate reservoirs by NMR and found that the pore distribution has a great impact on the permeability coefficient of rock mass. Nakashima and Kikuchi [11] proposed to construct NMR T_2 map to reflect the fracture porosity and permeability coefficient by establishing one-dimensional model. Wu et al. [12] applied NMR to detect the spatial structure and velocity between ore body particles in agar deposits under saturated water condition and obtained velocity field images at three different velocity rates, results showed that the fitting curve diameter of the pore equivalent distribution follows Gaussian distribution, and the velocity distribution in holes is parabolic.

The term fractal was first proposed and used by Mandelbrot. In mathematics, fractal has a strict definition. The so-called fractal refers to the set whose Hausdorff dimension D_h is strictly greater than its topological dimension D_t. Nowadays, the application of fractal has penetrated various disciplines and developed continuously [13]. This is mainly because fractal can express complex objects that cannot be described quantitatively or is difficult to be described quantitatively in a more convenient quantitative method. Relevant studies include the relationship between the fractal dimension of metal fracture and material properties, the relationship between the fractal dimension of rock joint or rock fracture and rock mechanical properties, the relationship between the fractal dimension of pore media and permeability characteristics, etc. In addition, researches also involve the fractal dimension of root form, chemical reaction interface, and soil pores [14]. In practical research, the physical information of the research object can be recorded through various ways, including various graphic image results, for example, photos captured by camera or scanner, micrographs taken by optical microscope or scanning electron microscope, IR images taken by infrared camera, and images obtained by CT technology, AFM technology, and remote sensing technology, even including measurement curves. As these obtained graphics and images contain a lot of physical information of the research object, they are important carriers for us to calculate the fractal dimension. With the development of information processing technology and computer technology, a large number of graphics and images are obtained in the form of digital image, or can be transformed into digital image, which is a two-dimensional matrix represented by a series of binary numbers (0 and 1) after sampling and quantization, has the characteristics of quantization and discretization. Therefore, it has its own characteristics in the calculation of fractal dimension.

Physical fractals in nature often show some randomness and scale, that is, they only show fractal characteristics in a specific scale range from the perspective of statistics [15]. Therefore, there are different ways to define fractal dimension, including Hausdorff dimension D_h, information dimension D_i, similarity dimension D_s, correlation dimension D_g, capacity dimension D_c, spectral dimension D_p, and Lyapunov dimension D_l. For different research objects, different description methods can be used to calculate their fractal dimension.

In general, it is very complicated to determine the Hausdorff dimension D_h of fractals, which restricts its application in practical problems [16]. For fractals with strict self-similarity, it can be proved that the Hausdorff dimension D_h

Table 1: Density of ore samples.

Ore soil depth	Sample number	Volume/cm^3	Mass/g	Natural density/(g/cm^3)	Mean natural density/(g/cm^3)	Mean dry density/(g/cm^3)
3 m	1	50.0	68.51	1.37	1.38	1.26
	2	50.0	67.85	1.36		
	3	50.0	70.38	1.41		
4 m	1	50.0	64.36	1.29	1.29	1.13
	2	50.0	65.47	1.31		
	3	50.0	63.65	1.27		
5 m	1	50.0	78.31	1.56	1.52	1.33
	2	50.0	75.62	1.51		
	3	50.0	74.23	1.48		

Table 2: Particle size percentage content of ore samples at different depths.

Ore soil depth	Particle diameter/mm					
	>5	2.5~5	1~2.5	0.5~1	0.075~0.5	<0.075
3 m	15.8%	32.2%	16.6%	16.2%	10.9%	8.3%
4 m	12.4%	37.3%	18.4%	16.2%	10.8%	4.9%
5 m	10.3%	31.6%	17.6%	18.2%	16.2%	6.1%

is equal to the similarity dimension D_s and the similarity dimension, which is easy to calculate normally, and can be calculated according to the following formula, where N is the number of similarity elements, and r is the similarity ratio of similarity elements.

$$Ds = \frac{\ln N}{\ln (1/r)}. \tag{1}$$

For many fractals, both Hausdorff dimension and similarity dimension are difficult to be calculated, so many equivalent or approximate dimension definitions are proposed. Considering that the image is a surface surrounded by various curves, such as pores and sections, box-counting dimension D_f can be used [17]. Box-counting dimension is a better method to calculate the fractal dimension of two-dimensional image. There are a series of equivalent definitions of boxed dimension, and the approximate calculation method of boxed dimension is the following formula, where N is the number of δ net cubes intersecting F.

$$D_f = \lim_{k \longrightarrow \infty} \frac{\ln N(F)}{\ln \delta}. \tag{2}$$

Currently, a large amount of research on the relationship between pore microstructure and seepage characteristics of soil particles has been done by using NMR and SEM techniques, yet the pore structure analysis and evolution of rare earth ore in leaching process need to be further investigated. Based on the above, the permeability coefficient of mineral soil at different leaching time was calculated by SDR model. In this paper, the pore fractal dimension was introduced using fractal theory, the change of pore structure was described quantitatively, and the evolution of the relationship between pore structure change and seepage characteristics of ionic rare earth mineral soil was discussed.

Table 3: Porosity and pore ratio of ore samples at different depths.

Ore soil depth	3/m	4/m	5/m
Porosity (n)	0.47	0.52	0.45
Pore ratio (e)	1.05	1.25	1.01

Figure 2: Rare earth samples at different depths.

2. Materials and Methods

2.1. Materials. To truly simulate the in situ leaching situation of mines, Luoyang shovel with a diameter of 160 mm was

Figure 3: Low field NMR.

used in this site soil borrowing, after planning the surface humic layer, drilled with Luoyang shovel to 0.5 m for sampling. For every 1 m drilling, we took undisturbed soil samples of fully weathered layers 3 m, 4 m, and 5 m away from the topsoil with a ring knife, took 3 samples at the same depth, a total of 9 samples were taken, and took protective measures to prevent excessive evaporation of water in the subsequent transportation process of soil samples, which would affect the determination of physical properties of undisturbed soil. The excess loose soil of the same depth was packed and brought back in woven bags and marked on the outside of the bags, see Figure 1 for the sampling site of mineral soil.

The mineral soil in this area is generally clayey soil. In this test, the density of samples with different depths was tested by ring knife method. The density measurement results are shown in Table 1. Samples with different depths were screened by sieving method, and the apertures of the sieves were superimposed from large to small, which were 5 mm, 2 mm, 1 mm, 0.5 mm, 0.25 mm, 0.1 mm, and 0.075 mm, respectively, see Tables 2 and 3 for particle size distribution, porosity, and void ratio of samples with different depths.

Based on the difference of physical and chemical properties of undisturbed soils, the soil samples were divided into three groups: A, B, and C according to the height of soil from the surface. Among them, groups A, B, and C represent the ore soil 3 m, 4 m, and 5 m away from the surface, respectively. During the column leaching experiment, to ensure that the sample to be tested was located in the effective detection area of the NMR instrument, mineral soil was added into the acrylic tube in layers and tamped. In addition, each layer of soil sample was treated by surface scratching to prevent the stratification effect of ore soil due to the seepage of leaching solution. A qualitative filter paper and a permeable stone were placed in turn at the bottom of the acrylic tube so that the leaching solution could not only flow out of the system but also prevented the loss of sample microparticles [18]. Finally, the remolded soil sample with diameter-height ratio of 44 mm: 60 mm was obtained, as shown in Figure 2. Furthermore, two samples were set up in each group. One sample was leached with 2% MgSO4 solution (A1, B1, and C1), and the other was leached with deionized water (A2, B2, and C2).

2.2. Experimental Apparatus and Scheme. In this experiment, a MesoMR23-060H-I NMR [19] apparatus was applied. It is mainly composed of magnet, magnet resonance spectrometer, data processing, and image reconstruction (Figure 3). And the relevant parameters are as shown in Table 4. After the sample was put into the instrument for detection, the nuclear magnetic resonance instrument would scan the image of the sample profile, compare it with the preset parameter model, and inversed the image inside the soil column at this time.

To investigate the relationship between permeability coefficient and pore fractal dimension of ion-adsorbed rare earth in $MgSO_4$ solution leaching, column leaching experiments were carried out. The column leaching experiment system consists of a beaker, liquid infusion pipe, and an object stage (Figure 4). The whole leaching procedure is as follows:

(1) After a large number of laboratory experiments and production practices in mining enterprises, the 2% $MgSO_4$ solution was used to leach ore, and the recovery rate can reach 99.7%. In addition, the other ions in the solution could be greatly reduced. Hence, 2% $MgSO_4$ solution was used for column leaching in this experiment. The $MgSO_4$ solution used in the experiment was purchased from local chemical plants

(2) One end of the infusion pipe was inserted into the beaker, and the other end was suspended above the sample. The infusion rate was adjusted to 3 mL/min

Table 4: Technical parameters and test parameters of low field NMR.

Instrument parameters				Test parameters			
Resonant frequency	23.316/MHz	Pulse width P90	18/us	RF delay D3	80/us	Repeated sampling times NS	4
Coil diameter	60/mm	Pulse width P180	36/μs	Sampling duration TR	1000/ms	Scan times	32
Magnet strength	0.52/T	Sampling point TD	266424	Analog gain RG1	20	Echo interval	0.2/ms
Magnet temperature	32/°C	Sampling frequency SW	200/kHz	Numerical gain RG2	3	Echo count	4000

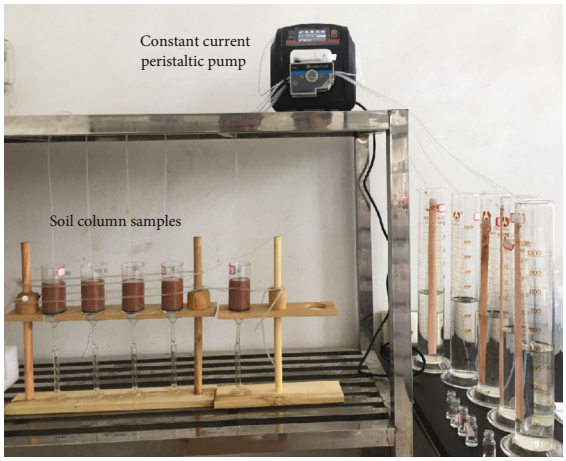

Figure 4: Indoor leaching device.

and turned on the switch of the infusion set. The concentration of RE^{3+} in the leaching solution was analysed by sampling at intervals to judge the leaching process

(3) The samples were put into NMR instrument every one hour for pore structure detection and inversion imaging. Then, the samples were put back into the solution to continue leaching. When the concentration of RE^{3+} in the leaching solution is very low or almost undetectable, it is believed that all rare earth in the samples have been leached and stopped during the column leaching experiment

3. Results and Discussion

3.1. Calculation of Permeability Coefficient. In a pulse environment with a certain frequency, the hydrogen nucleus in the sample absorbs electromagnetic waves with a specific frequency and transitions from low energy state to a high energy state. Then, the magnetization vector deviates from an equilibrium state, the process of the hydrogen nucleus recovering from an unequilibrium state to an equilibrium state is called a relaxation process, and the duration of the process is the relaxation time [20]. Based on the principle, two types of permeability coefficient calculation models are proposed: (1) Coates model, which is suitable for laminar flow of water or hydrocarbons; (2) average T_2 model, which is suitable for water-bearing pore system. According to the

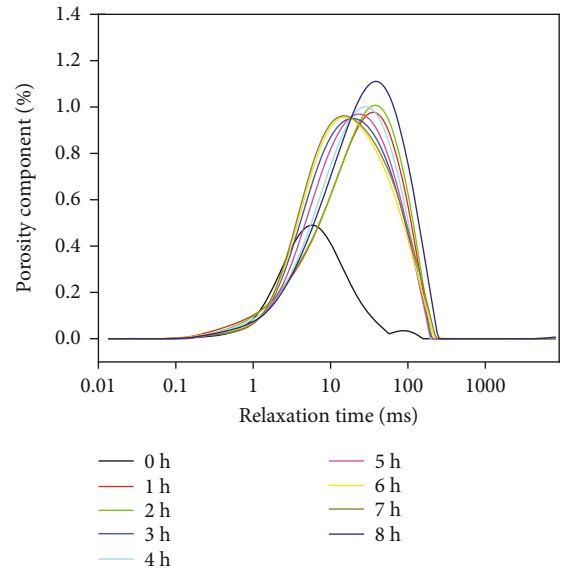

Figure 5: T_2 curves of A1 sample at different leaching times.

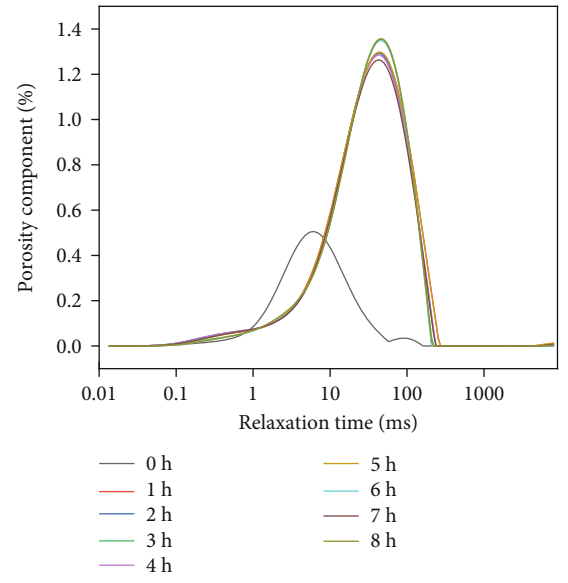

Figure 6: T_2 curves of A2 sample at different leaching times.

relaxation mechanism of NMR, there are three kinds of relaxation in the fluid of pores, namely, free relaxation, surface relaxation, and diffusion relaxation [21]. The transverse

Table 5: Permeability coefficient of samples in each stage of leaching process.

Leaching time/h	Leaching solution	Permeability coefficient K (10^{-5}m/s)			Leaching solution	Permeability coefficient K (10^{-5}m/s)		
		A1	B1	C1		A2	B2	C2
1	Magnesium sulfate solution	1.105	1.425	0.988	Deionized water	0.995	1.258	0.877
2		1.189	1.521	1.025		1.096	1.304	0.893
3		1.347	1.675	1.189		1.154	1.437	1.092
4		1.641	1.984	1.504		1.232	1.492	1.114
5		1.842	2.248	1.649		1.398	1.551	1.158
6		1.856	2.256	1.702		1.406	1.612	1.224
7		1.874	2.267	1.741		1.423	1.618	1.197
8		1.885	2.274	1.759		1.407	1.613	1.166

relaxation time T_2 can be expressed by the following formula:

$$\frac{1}{T_2} = \frac{1}{T_{2B}} + \frac{1}{T_{2\text{surface}}} + \frac{1}{T_{2E}}, \tag{3}$$

where T_{2B} is the free relaxation time of the fluid, ms; since the value of T_{2B} is much greater than T_2, when the magnetic field is uniform and T_{2E} is small enough, formula (3) can be simplified as

$$\frac{1}{T_2} = \frac{1}{T_{2\text{surface}}}. \tag{4}$$

Average T_2 (SDR) model is expressed as

$$K = aT_{2g}{}^{2\varnothing^4}, \tag{5}$$

$$a = F_s \cdot \rho, \tag{6}$$

where $\varnothing$ is the effective porosity of NMR; T_{2g} is the geometric mean of T_2 distribution; a is the parameter related to stratum type; F_s is the pore shape factor and usually takes 3; ρ is the surface relaxation rate of soil samples.

In the leaching process, the samples are in an inorganic hydro chemical environment, and the ions are mainly RE^{3+}, Mg^{2+}, H^+, etc. There are no hydrocarbons in the solution [22]. Therefore, the SDR model can be used to calculate the permeability coefficient of rare earth ore. Xu et al. [23] calculated the surface relaxation rate of rare earth by random walk algorithm, and the surface relaxation rate was 1.36. The obtained data have a good correlation with the permeability measured by indoor simulated leaching. According to the collected T_2 spectrum curves, as shown in Figures 5 and 6, the permeability coefficients of the soil column at each time are calculated and listed in Table 5.

According to the results detected by nuclear magnetic resonance instrument, the porosity of each sample at different times under the action of two leaching fluids over time is summarized. It is shown in Figures 7 and 8 that the fitting curves describe the variation characteristics of permeability coefficient during the leaching process in the two kinds of leaching solutions. In the process of $MgSO_4$ solution leaching, the permeability of samples increases greatly in 6 h. After 6 h, the permeability changes little and tends to stability. In this process, magnesium ions interact with rare earth ions in solution. In 5 h of $MgSO_4$ leaching, the permeability coefficients of A1, B1, and C1 climb gently. 5 h later, the permeability coefficient of each sample has no obvious change. During the deionized water leaching, a small number of microparticles in the ore body migrate, and the permeability coefficient of the sample increases rapidly in 3 h; after 3 h, the microparticles block in the pores in the ore body move to the bottom of the sample with the movement of deionized water, and the permeability coefficient of the sample remains almost unchanged.

3.2. Calculation of Pore Fractal Dimension. With the NMR reconstruction imaging technology, the pore image of ore leaching at each time is inverted and reconstructed [24]. Variation law of the pore microstructure at the leaching moment is analysed by inversion images of the middle longitudinal section of the column [25]. The representative images of 5 stages in the leaching process of group A, Figure 9, are compared with the images of the same stages of deionized water leaching, Figure 10. The whole leaching stage is mainly divided into five stages: water saturation of the sample, initial reaction, effective leaching, residual reaction, and end of reaction.

As shown in Figure 9, the leaching process is completed under the coupling action of seepage field and chemical field. Due to the effect of exchange reaction erosion, the particle shape changes from time to time, and the height of the sample will decrease, with the microparticles in the upper layer migrate downward with the leaching solution and fill the large pore diameter in the lower layer, resulting in the dynamic change of pore micromorphology. The pore radius also changes all the time. In the early stage of leaching, the sample changes from unsaturated state to saturated state, where the liquid buoyancy plays a leading role, and the number of micropores and small holes decreases rapidly. In the effective leaching stage, ion exchange reaction erosion plays a leading role, which changes the particle structure of the sample, decomposes some particles with larger particle size into smaller particles, and increases the proportion of pores below the middle pore, while decreases the proportion of pores above the large pore. As the reaction approaches to

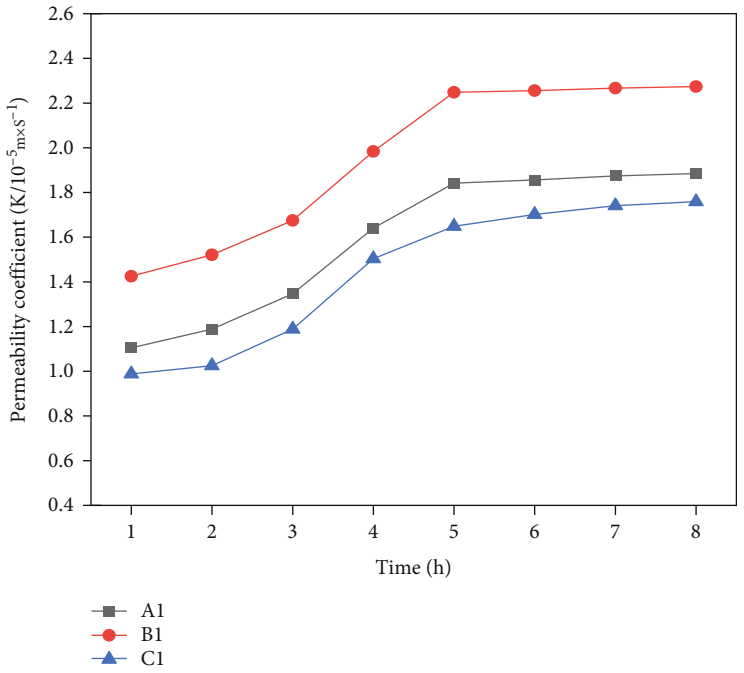

Figure 7: Permeability coefficient of $MgSO_4$ leaching sample.

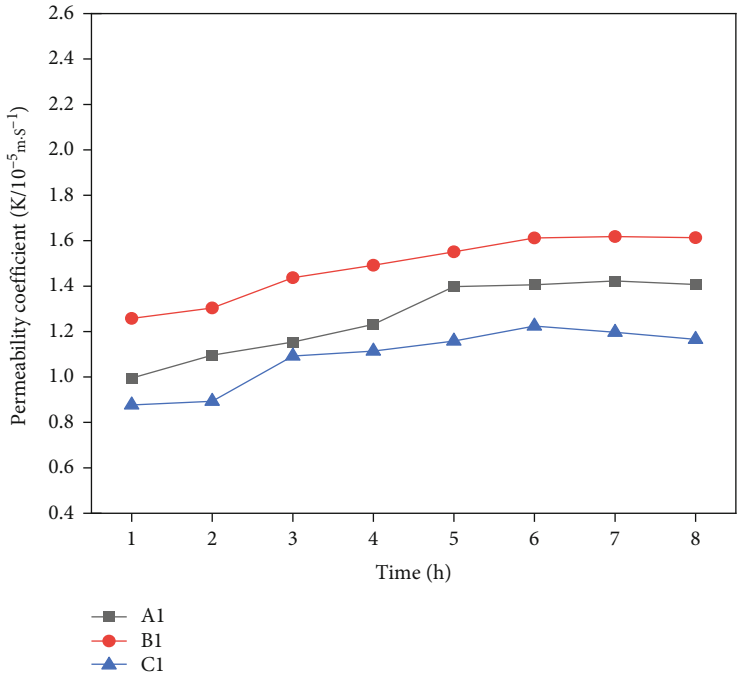

Figure 8: Permeability coefficient of deionized water leaching sample.

the end, the seepage of fluid plays a leading role. Under the action of a certain head pressure, a stable seepage channel is formed in the sample, and the distribution of pore sizes in the sample tends to be stable.

In the process of ion exchange, the positive trivalent rare earth ions are replaced by positive divalent magnesium ions into the solution. According to the principle of charge balance solution, the content of anions in the solution should also increase accordingly, resulting in the dissolution of anions in minerals into the solution, so that the solution can reach the charge balance state again. Due to the anions from the ore particles, the charge balance between the two surfaces is changed. As a result, a large number of uncharged microparticles are deposited on the surface of the ore body

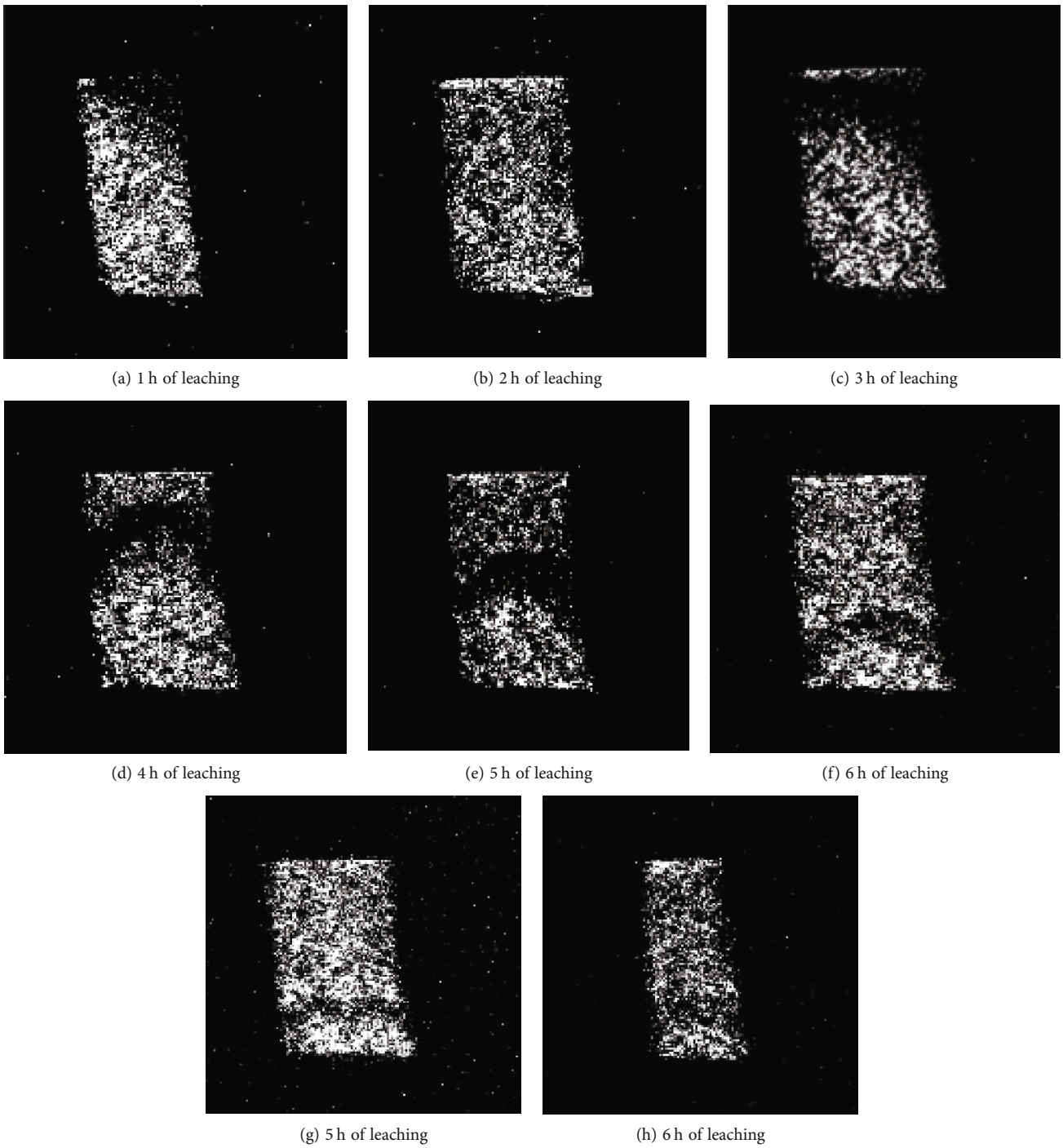

(a) 1 h of leaching (b) 2 h of leaching (c) 3 h of leaching

(d) 4 h of leaching (e) 5 h of leaching (f) 6 h of leaching

(g) 5 h of leaching (h) 6 h of leaching

Figure 9: Vertical axis profile of MgSO4 leaching inversion.

by Coulomb force, filling the pores with large aperture. With the completion of ion exchange reaction, most of the rare earth cations with positive trivalent have been separated from ore, and the thickness of the electric double layer of clay colloidal particles in the colloid will increases again, which will make the repulsion force of the electric double layer become the dominant force again, resulting in the release of the particles adsorbed around the macropores, and the macropores return to their original state, showing a fine pore structure. This shows that the ion exchange process in the leaching process of rare earth ore body will lead to the change of particle morphology and the deposition and release of fine particles in the ore body, resulting in the evolution of dynamic pore structure. At the same time, rare earth ions migrate downward through seepage, resulting in a significant increase in the positive charge content at the bottom of the sample, while the clay containing rare earth usually has a negative charge. Under the action of electric

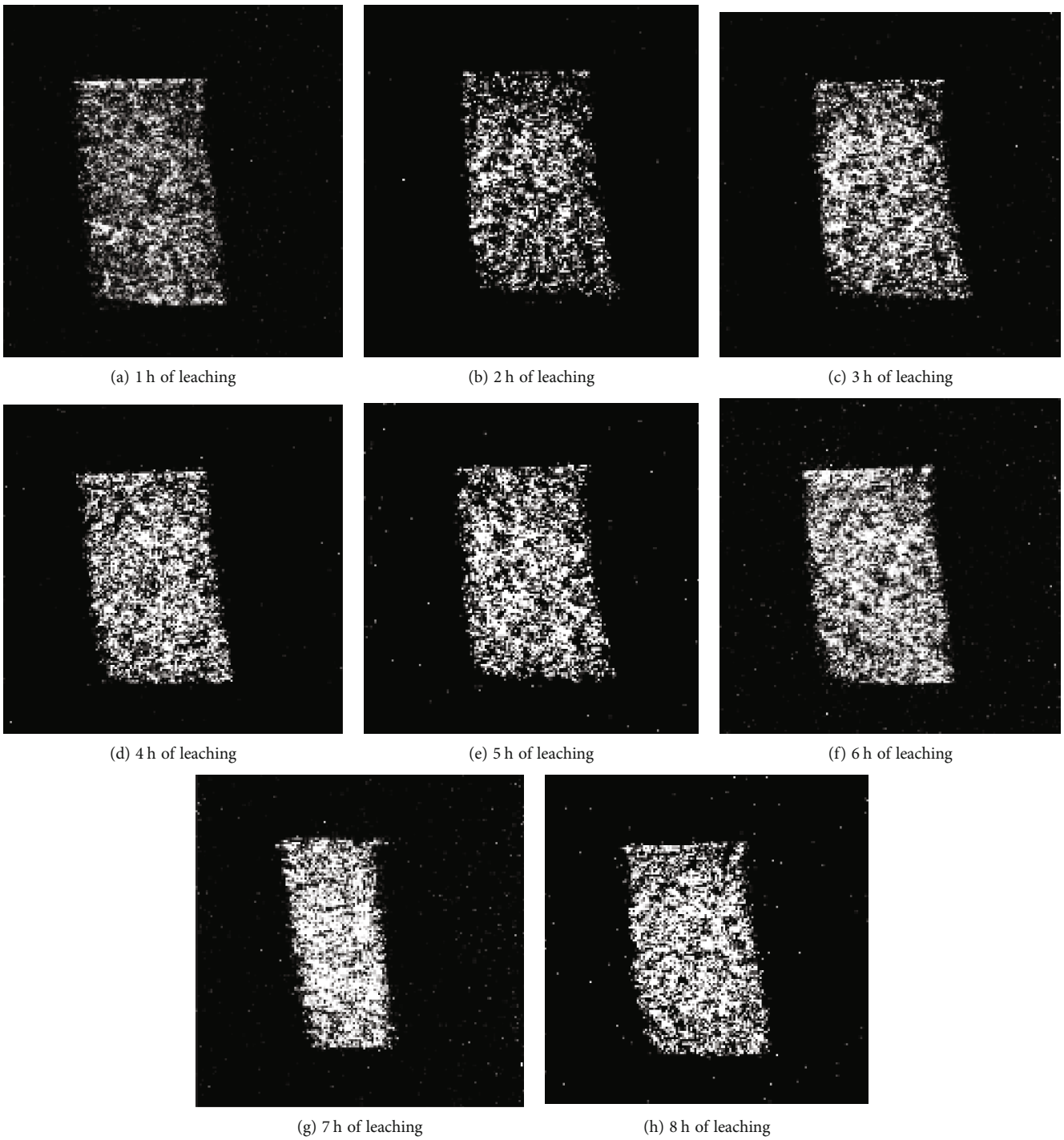

(a) 1 h of leaching (b) 2 h of leaching (c) 3 h of leaching

(d) 4 h of leaching (e) 5 h of leaching (f) 6 h of leaching

(g) 7 h of leaching (h) 8 h of leaching

Figure 10: Vertical axis profile of deionized water leaching inversion.

field force, these clays converge to the bottom of the sample, block the pores at the bottom of the sample, and change the pore structure.

The pore size distribution of soil is described by fractal theory, the microstructure characteristics of particle size can quantitatively describe the pore structure characteristics at each time in the leaching process, and the relationship between pore structure and seepage rule is revealed, to explore the influence of fractal dimension of soil pore on seepage characteristics of soil [26–28].

Pore fractal dimension D_f is a significant parameter to present the microscale change of soil pores [29], which is usually described by the distribution characteristics of pore accumulation number less than the specific pore, as shown in formula (2). In the logarithmic coordinate system, the corresponding relationship between different

Table 6: Fractal dimension of pores in each stage of the sample during ore leaching.

Leaching time/h	Leaching solution	A1		B1		C1		Leaching solution	A2		B2		C2	
		Fractal dimension	Growth rate/%	Fractal dimension	Growth rate/%	Fractal dimension	Growth rate/%		Fractal dimension	Growth rate/%	Fractal dimension	Growth rate/%	Fractal dimension	Growth rate/%
1	Magnesium sulfate solution	1.526	——	1.617	——	1.332	——	Deionized water	1.421	——	1.578	——	1.227	——
2		1.589	4.128	1.742	7.730	1.421	6.682		1.489	4.785	1.624	2.915	1.315	7.172
3		1.678	5.601	1.886	8.266	1.562	9.923		1.524	2.351	1.651	1.663	1.367	3.954
4		1.782	6.198	1.924	2.015	1.689	8.131		1.572	3.150	1.684	1.999	1.414	3.438
5		1.854	4.040	1.943	0.988	1.741	3.079		1.617	2.863	1.702	1.069	1.459	3.182
6		1.924	3.776	1.956	0.669	1.778	2.125		1.648	1.917	1.714	0.705	1.482	1.576
7		1.941	0.884	1.967	0.562	1.794	0.900		1.657	0.546	1.725	0.642	1.491	0.607
8		1.943	0.103	1.971	0.407	1.756	——		1.661	0.241	1.733	0.464	1.502	0.738

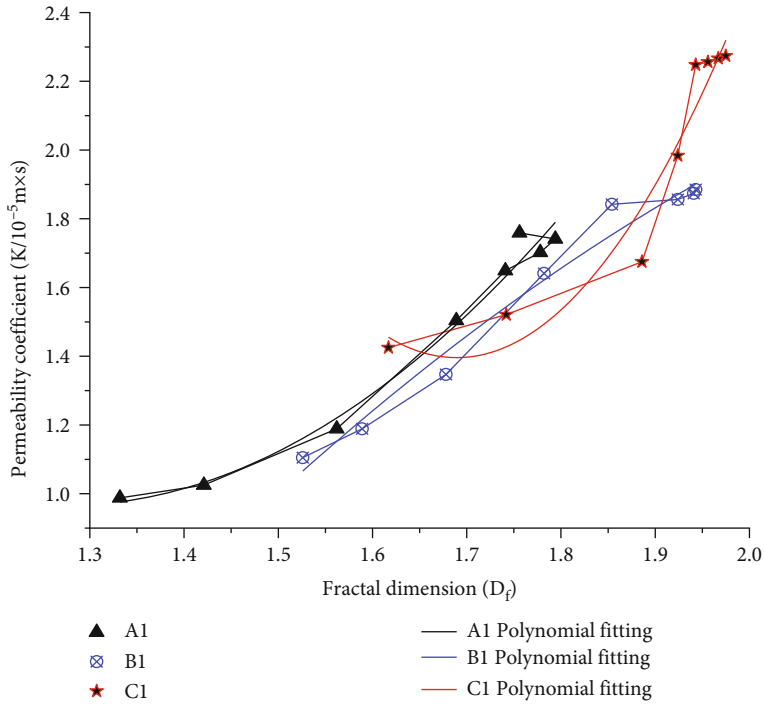

FIGURE 11: Relationship between fractal dimension and permeability coefficient of $MgSO_4$ leaching pores A1: $K = -1.05251 * D_f^2 + 5.65291 * D_f - 5.10929$. B1: $K = 11.31327 * D_f^2 - 38.22234 * D_f + 33.68001$. C1: $K = 3.01795 * D_f^2 - 7.6732 * D_f + 5.84253$.

pore sizes and their corresponding pore numbers was fitted [30].

MATLAB software was used to automatically remove miscellaneous points [31], divided and identified particles and pores, and calculated the fractal dimension of pores in the process of leaching, and the results are given by Table 6. It is clear that the fractal dimension of sample pores increases in the first 6 hours; from this moment onwards, it tends to enter into the comparatively stable period. In $MgSO_4$ solution, the growth rate of fractal dimension keeps at a large value in the effective leaching stage (2 h ~6 h), and the change trend is positively correlated. In deionized water, the fractal dimension increases, while the change trend of fractal dimension growth rate is negatively correlated within 2 h ~6 h. During the leaching process of $MgSO_4$ solution, Mg^{2+} and RE^{3+} in the solution react, which changes the grain structure of ore soil, resulting in the difference of fractal dimension between $MgSO_4$ solution and deionized water.

3.3. Relationship between Pore Structure and Permeability Coefficient. The characteristic parameters of meso structure of soil particles were described by fractal theory, to quantitatively analyse the variation of pore structure during leaching and calculate the permeability coefficient in each leaching stage according to the SDR model [32, 33]. The relationship between the permeability coefficient and fractal dimension was indicated, and the fitting curve was obtained, as shown in Figure 11. In the process of the two solutions of leaching, the permeability coefficient of samples is positively correlated with the fractal dimension of the pores. However, in $MgSO_4$ solution, the internal pore structure changed rapidly resulting from the coupling effect of seepage and ion exchange reaction, leading to the fluid flowing more easily in the pores. The polynomial function is used to fit the relationship between K and D_f. The fitting result shows that in the 95% confidence interval, R^2 is larger than 0.9143.

4. Conclusion

Based on SDR model and classification theory, the permeability coefficient and fractal dimension at different leaching time were calculated. And the evolution of the relationship between pore structure variation and seepage characteristics of ore-soil particles was established. The main conclusions are as follows:

(1) In the leaching process of deionized water, the permeability coefficient rises slightly due to the migration of ore-soil particles, but the growth rate is small; in the leaching process of $MgSO_4$, the permeability coefficient changes significantly, indicating that the change of permeability coefficient is closely related to the internal ion exchange reaction

(2) In the leaching process of deionized water, the fractal dimension increases, while the change trend of fractal dimension growth rate is negatively correlated with time in 2 h ~6 h. In the leaching process of $MgSO_4$, the growth rate of fractal dimension keeps at a large value in the effective leaching stage (2 h ~6 h), and the change trend is positively correlated with time

(3) The relationship between permeability coefficient and fractal dimension shows strong correlation, so

the mathematical relationship between permeability coefficient and fractal dimension can be fitted by polynomial function, and a method for estimating permeability coefficient based on fractal dimension of soil sample is obtained

Data Availability

The data that support the findings of this study are available from the corresponding author (VS) upon reasonable request.

Conflicts of Interest

The authors declare that there are no conflicts of interest regarding the publication of this paper.

Acknowledgments

This research was supported by the National Natural Science Foundation of China (51964014) and the Education Department of Jiangxi Province (GJJ209414).

References

[1] X. W. Zhou, D. X. Wen, and X. P. Luo, "The status quo and development trend of the extraction technology of ion-absorbed rare earth in southern China," *Nonferrous Metals Science and Engineering*, vol. 3, no. 6, pp. 81–85, 2012.

[2] B. Fan, L.-s. Zhao, Z.-y. Feng et al., "Leaching behaviors of calcium and magnesium in ion-adsorption rare earth tailings with magnesium sulfate," *Transactions of Nonferrous Metals Society of China*, vol. 31, no. 1, pp. 288–296, 2021.

[3] H. Zhengyan, Z. Zhang, R.'a. Chi et al., "Leaching hydrodynamics of weathered elution-deposited rare earth ore with ammonium salts solution," *Journal of Rare Earths*, vol. 35, no. 8, pp. 824–830, 2017.

[4] W. Que, Y. Tan, Y. Zeng, and S. Wang, *Geochemical Kinetics and Mass Transport of In Situ Uranium Leaching*, Atomic Energy Press, Beijing, 2004.

[5] S. H. Yin, Y. Qi, F. F. Xie, X. Chen, L. M. Wang, and Y. J. Shao, "Porosity characteristic of leaching weathered crust elution-deposited rare earth before and after leaching," *Chinese Journal of Nonferrous Metals*, vol. 28, no. 10, pp. 2112–2119, 2018.

[6] F. Shang-xin, C. Jun-rui, X. Zeng-guang, Q. Yuan, and C. Xi, "Mesostructural change of soil-rock mixtures based on NMR technology," *Rock and Soil Mechanics*, vol. 39, no. 8, pp. 2886–2894, 2018.

[7] J. G. Dong, H. B. Lv, and G. Q. Chen, "Pore-water form determined by using NMR method and its influence on soil permeability," *Transactions of the Chinese Society of Agricultural Engineering*, vol. 36, no. 6, pp. 74–80, 2020.

[8] D. H. Yang, C. F. Wei, R. T. Yan, Q. Tang, and L. Liu, "Experimental study on effects of fine particle migration and fabric change on permeability of clay," *Chinese Journal of Geotechnical Engineering*, vol. 41, no. 11, pp. 2009–2017, 2019.

[9] M. Altunbay, R. Martain, and M. Robinson, "Capillary pressure data from NMR logs and its implications on field economics," in *SPE Annual Technical Conference and Exhibition*, pp. 2–5, New Orleans, 2001.

[10] R. Ausbrooks, N. F. Hurley, and A. May, "Pore-size distribution in vuggy carbonates from core images, NMR and capillary pressure," in *SPE Annual Technical Conference and Exhibition*, pp. 3–5, Houston, 1999.

[11] Y. Nakashima and T. Kikuchi, "Estimation of the apertures of water-saturated fractures by nuclear magnetic resonance well logging," *Geophysical Prospecting*, vol. 55, no. 2, pp. 235–254, 2007.

[12] C. Liu, A. X. Wu, S. H. Yin, and X. Chen, "Nonlinear chaotic characteristic in leaching process and prediction of leaching cycle period," *Journal of Central South University*, vol. 23, no. 11, pp. 2935–2940, 2016.

[13] R. D. Peng, H. P. Xie, and Y. Ju, "Computation method of fractal dimension for 2-D digital image," *Journal of China University of Mining and Technology*, vol. 33, no. 1, pp. 19–24, 2004.

[14] R. D. Peng, Y. C. Yang, Y. Ju, L. T. Mao, and Y. M. Yang, "Computation of fractal dimension of rock pores based on gray CT images," *Chinese Science Bulletin*, vol. 56, no. 31, pp. 3346–3357, 2011.

[15] Y. R. Li and R. Q. Huang, "Relationship between joint roughness coefficient and fractal dimension of rock fracture surfaces," *International Journal of Rock Mechanics and Mining Sciences*, vol. 75, pp. 15–22, 2015.

[16] T. Hamm and I. Steinwart, "Adaptive learning rates for support vector machines working on data with low intrinsic dimension," *Annals of Statistics*, vol. 49, no. 6, pp. 3153–3180, 2021.

[17] K. Zhang, Y. L. Chen, W. H. Fan, X. Liu, H. Luan, and J. Xie, "Influence of intermittent artificial crack density on shear fracturing and fractal behavior of rock bridges: experimental and numerical studies," *Rock Mechanics and Rock Engineering*, vol. 53, no. 2, pp. 553–568, 2020.

[18] Y. B. Yao, J. Liu, D. M. Liu, J. Chen, and Z. Pan, "A new application of NMR in characterization of multiphase methane and adsorption capacity of shale," *International Journal of Coal Geology*, vol. 201, pp. 76–85, 2019.

[19] Y. Li, Y. H. Fu, and J. L. Chen, "Analysis on the changes of permeability of rare earth and its causes under different concentrations ore," *Mining Research and Development*, vol. 38, no. 12, pp. 117–120, 2018.

[20] R. H. Xie, L. Z. Xiao, and S. Q. Fu, "Temperature effect of nmr surface relaxation in water saturated rocks," *Journal of China University of Petroleum*, vol. 32, no. 2, pp. 45–52, 2008.

[21] W. D. Lu, L. Z. Xiao, W. Li, and D. Xiao, "Effects of diffusion due to internal gradients on NMR response in rocks," *Progress in Geophysics*, vol. 22, no. 2, pp. 556–561, 2007.

[22] M. Yang, J. C. Bi, and G. Z. Hu, "Influence of extreme temperature on the pore and fracture development of high- rank coal," *Advances in Civil Engineering*, vol. 2018, Article ID 4529751, 8 pages, 2018.

[23] W. Xu, Y. Z. Rao, D. Wang, L. Shi, and Y. Li, "Effect of pore radius distribution on infiltration of ion-absorbed rare earth ore," *Journal of Jiangxi University of Science and Technology*, vol. 41, no. 1, pp. 57–63, 2020.

[24] W. Chen and H. X. Du, "Pore analysis of high strength and high-performance concrete at high temperature based on CT test," *Concrete*, vol. 2018, no. 6, pp. 6–8, 2018.

[25] X. X. Cao, M. M. Feng, and K. H. Yuan, "Dynamic mechanical properties and damage mechanism of freeze-thaw sandstone under acid corrosion," *Geofluids*, vol. 2021, Article ID 7335284, 15 pages, 2021.

[26] Q. Y. Ma and Z. M. Cao, "Experimental study on fractal characteristics and energy dissipation of stabilized soil based on SHPB test," *Journal of Materials in Civil Engineering*, vol. 31, no. 11, pp. 1943–1959, 2019.

[27] R. Herfkens, L. Crooks, P. Davis et al., "Application of nuclear magnetic resonance (NMR) of hydrogen to the study of pathologic anatomy of the rat," *Investigative Radiology*, vol. 15, no. 5, p. 433, 1980.

[28] H. M. Zhang, G. S. Yang, and Y. Liang, "Experimental study on damage deterioration and tensile characteristics of rock under freeze-thaw environment," *Advanced Materials Research*, vol. 518-523, pp. 1749–1752, 2012.

[29] Y. F. Deng, X. B. Yue, S. Y. Liu, Y. Chen, and D. Zhang, "Hydraulic conductivity of cement-stabilized marine clay with metakaolin and its correlation with pore size distribution," *Engineering Geology*, vol. 193, pp. 146–152, 2015.

[30] X. Fukun, M. Xin, L. Lianchong et al., "Thermos-solid-gas coupling dynamic model and numerical simulation of coal containing gas," *Geofluids*, vol. 2020, Article ID 8837425, 9 pages, 2020.

[31] A. Gusso and L. Mello, "Fractal dimension of basin boundaries calculated using the basin entropy," *Chaos, Solitons & Fractals*, vol. 153, no. 2, pp. 111532–111540, 2021.

[32] Z. Minghua, Z. L. D. Jie, and Y. Pingbao, "Fractal theory-based study of the permeability of fly ash," *Journal of Hunan University (Natural Sciences)*, vol. 42, no. 1, pp. 75–80, 2015.

[33] J. Yang, J. J. Chen, Z. X. Yang, and H. L. Zheng, "A study of pore structure, pore fractal feature and permeability of unconsolidated sand," *Hydrogeology & Engineering Geology*, vol. 35, no. 3, pp. 93–98, 2008.

Hindawi
Geofluids
Volume 2022, Article ID 3222825, 11 pages
https://doi.org/10.1155/2022/3222825

Research Article

Experimental Simulation Study of Mine Water Acidification under the Action of Pyrite

Qingna Shui,[1] **Jiajia Liao**,[1] **Qi Wang**,[2] **Jiexiang Li**,[1,3,4] **Daping Xia**,[3,4,5] **Zicai Wang**,[1] **and Xinyi Wang**[1,3,4]

[1]*Institute of Resources & Environment, Henan Polytechnic University, Jiaozuo 454000, China*
[2]*College of Geosciences and Engineering, North China University of Water Resources and Electric Power, Zhengzhou 450045, China*
[3]*Collaborative Innovation Center of Coalbed Methane and Shale Gas for Central Plains Economic Region, Jiaozuo 454100, China*
[4]*Collaborative Innovation Center of Coal Work Safety and Clean High Efficiency Utilization, Jiaozuo 454100, China*
[5]*School of Energy, Henan Polytechnic University, Jiaozuo 454100, China*

Correspondence should be addressed to Xinyi Wang; wangxy@hpu.edu.cn

Received 27 December 2021; Accepted 23 April 2022; Published 16 May 2022

Academic Editor: Mingwei Chen

The discharge of acidic water has become an environmental issue of great concern worldwide. In order to investigate the characteristics and mechanism of acidic water induced by pyrite in sulfur-rich mines, indoor static precipitation and dynamic leaching simulation experiments were carried out under the conditions of pyrite content, rock particle size, media combination, and ambient temperature. At the same time, this paper used the gray correlation method to quantitatively analyze the influencing factors. The results showed that the degree of groundwater acidification was negatively correlated with the rock particle size and temperature and positively correlated with the pyrite content. The quantitative analysis of the effect of each factor on acid mine drainage pH was pyrite content > temperature > rock size. When considering different media conditions, the combined effect of the three media on reducing the acidification degree of mine water was limestone > gangue > coal. In addition, dynamic leaching and static soaking have different effects on the acidification of the mine water, with the latter acidifying more rapidly. It is also concluded that although pyrite enrichment was the main controlling factor affecting the acidification of mine water in nature, complexation of trivalent iron ions adsorbed in the formation was more likely to be the main causal mechanism for the rapid acidification of mine water in coal mining areas.

1. Introduction

Pyrite, which is the most common metal sulfide mineral on earth, occurs in huge volumes in sedimentary strata [1]. During the coal mining process, disturbances in the originally stable fields of groundwater flow, ground temperature, and hydrochemistry facilitate acid mine drainage (pH <5.5) in the coalfield area. This drainage leads to deterioration of the surface water quality in the mining area and affects the regional ecological environment and the mining of high-quality coal. Previous studies on pyrite and acid drainage mainly focused on the genetic characteristics of pyrite [2–5], the genetic mechanism of acid mine drainage [6, 7], the treatment of acid mine drainage [8–11], and the temporal effect of mine water on aquatic environments [12–15]. However, the main controlling factors of the formation process of acid mine drainage and its influence threshold remain unclear. Thus, it is difficult to effectively prevent acidification of mine water in sulfur-rich mines.

Numerous studies have been conducted on the acidic components of pyrite and the law of heavy metal leaching under normal temperature conditions. For example, Zhao et al. [16] solved the problem of water source identification in Xinzhi coal mine through free drainage column leaching experiments and revealed the water–rock interaction mechanism of the four main aquifers present in the mine. Jiang et al. [1] explored the surface oxidation law of pyrite under the coupling of multiple factors and established a model for predicting the oxidation rate of pyrite

under the coupling of multiple factors in a natural environment. Deng et al. [3] found that the leaching activity of sedimentary pyrite under an acid culture medium system is higher than that of medium-temperature hydrothermal pyrite. They also determined that the mineralogical origin of pyrite does not change its electrochemical dissolution mechanism. Tabelin et al. [17] performed batch leaching experiments and developed a thermodynamic/kinetic model to determine that hematite inhibits the oxidation of pyrite, whereas alumina enhances the overall oxidation and dissolution of pyrite. Hong et al. [18] simulated dynamic leaching and static soaking of leachates with various pH values into soil and concluded that the pH value of the leachate, leaching time, and occurrence form of fluorine in soil has a significant impact on fluorine leaching. Ran et al. [19] established an automatic temperature control spray system. Through dynamic leaching experiments on coal gangue at various temperatures, they found that the evolution of acid pollution caused by coal gangue self-heating oxidation was caused by alkaline components, nitrogen-containing substances, and oxidation. The acidic components produced were jointly determined. Li et al. [20] identified the optimal conditions for mineralization of quartz diabase, commonly known as maifanite or medical stone, by changing the pH value, ionic strength, and flow rate of the leaching solution as well as the size of the leached particles. Kuşlu et al. [21] studied the optimal leaching conditions for the dissolution of pyrite in chlorine-saturated water and identified the effective degrees of experimental variables, from high to low, as rock particle size, reaction temperature, solid–liquid ratio, and leaching time. Under the optimal leaching conditions, the dissolution rate of iron in pyrite was found to be 98.4%.

The above laboratory experiments focus on the study of the leaching law of chemical components in pyrite water. However, the main controlling factors and their influence thresholds in the formation of acidic mine water under multifactor coupling conditions remain unclear. Xinggong coalfield is located in the hilly area of the northern foothills of Mount Songshan in the middle reaches of the Yellow River Basin. With an area of about 488 km^2, this coalfield crosses the counties and cities of Zhengzhou, including Xingyang, Mixian, Gongyi, and Xinzheng and contains flaky, scattered, lenticular, nodular, and clumpy pyrite. The monitoring results showed that the pH value of the mine water in a mine in the Xinggong coalfield area was 5.11 in the wet season. According to the definition of acid mine water with pH value less than 5.5, acidification of the mine water appeared in the wet season. To explore the characteristics and mechanism of pyrite-induced acid water, this study conducts indoor experimental simulations under a combination of multiple factors such as pyrite content, medium composition, environmental temperature, and rock particle size based on samples obtained from Xinggong coalfield. The controlling factors as well as their degree of influence and thresholds are examined to provide technical support for the prevention and treatment of mine water acidification.

2. Sample Collection and Experiment

2.1. Sample Collection and Processing. The rock samples used in this study were taken from a mine in Xinggong coalfield. Pyrite samples were obtained about 200 m below the coal mine, and coal gangue rock and limestone were obtained from the surface. The samples were placed in snakeskin bags and were transported to the laboratory, where they were packaged in zipper-type plastic bags to prevent oxidation. After entering the laboratory, the rock samples were removed, and those with abundant pyrite were separated. All samples were crushed using a jaw crusher and selectively sorted using 5-mesh (4-mm aperture), 10-mesh (2 mm), and 20-mesh (0.825 mm) sieves for crushing. After sieving, rock particles of the same size were placed on respective waterproof polyvinyl chloride (PVC) tape segments for uniform mixing. The mixed rock samples were packaged in 20×25 − cm bags that were then sealed for later use.

2.2. The Experimental Setup

2.2.1. Experimental Factors and Condition Control. In the experimental design, the results of existing research and the actual hydrogeological conditions of the mine were considered. Factors such as the pyrite content, rock particle size, temperature, and occurrence medium were preliminarily set as the potential main controlling factors of pyrite oxidation. Then, this paper examined the influence of pyrite oxidation on acid mine water under the actions of these factors.

The coal seam mined was the Yi-$_1$ coal seam, the roof of which is composed of limestone containing pyrite. Coal gangue is the waste rock produced in the coal mining process; therefore, limestone, coal gangue, and coal were selected as media for the experiment. A related study showed that rock particle size affects the migration release of contaminants in water [22], so three different particle sizes of 2-4 mm, 2-0.825 mm, and<0.825 mm were selected. According to the literature, most of the ions were precipitated during the early stage of soaking [23]; hence, this paper used 20 days as the period of static soaking. In the dynamic water experiment, the leaching cycle was shorter than that of the static water experiment, and the release of elements was representative because the groundwater flow was slow [24]. However, the leaching process of elements mainly occurs at the early stage of leaching [25, 26], so the dynamic experimental period was set to 17 d. The average annual development temperature of tailings in the Gongyi mine area was 16°C to 20°C; and because it was mine water, at a depth of 200 m underground, the temperature above the surface was chosen for the experiment, so the static temperature was set at 25°C and 35°C as the study interval. In order to better explore the influence of temperature on the acid mine water produced by the oxidation of pyrite; therefore, 55°C was used as an auxiliary factor in the dynamic leaching experiment.

Regarding the solid–liquid ratio, the literature indicates that a smaller solid–liquid ratio involved in the reaction is related to higher concentrations of pollutants released by the dissolution of coal gangue per unit mass. Thus, a low

solid–liquid ratio is conducive to the dissolution and release of pollutants in coal gangue [27]. Because the liquid–solid ratio was 1 : 10 (L/kg) in previous static immersion experiments, the same value was adopted in the present study.

2.2.2. Experimental Methods and Procedures

(1) Static Immersion Experiment. A 5200-mL beaker was soaked in distilled water for 24 h. Afterward, the beaker was removed, allowed to dry naturally, and then rinsed with deionized water three or four times. Then, 500 g of the rock sample weighed using an analytical balance was added to the beaker along with 5000 mL of distilled water, and the mixture was stirred using a glass stirring rod. After the sample was fully soaked, a 25×25 – cm glass lid beaker was placed on top of the beaker to protect the contents from outside debris.

A thermostat was employed for the static water immersion experiment. In the early stage of the soaking process, the sampling interval was relatively short, at about one day during the first week of the experiment. To determine the water chemistry, 100 mL of the soaking liquid was filtered using a vacuum pump with a 0.45-μm filter membrane. The same volume of distilled water was added to the beaker to maintain the original solid–liquid ratio during the experiment.

(2) Dynamic Leaching Experiment. A schematic diagram of the experimental device is shown in Figure 1. The device included two customized plexiglass columns each with an inner diameter of 70 mm and a length of 500 mm. A plexiglass cover containing a hole at the upper end was attached, through which a rubber hose ran that was connected to an inlet tank composed of polyethylene. A valve and a peristaltic pump were connected to the rubber hose to control the leaching speed and volume. At the bottom of the device, the rubber hose ran through another opening and was connected to an eluent collector.

The upper and lower ends of the plexiglass tube were lined with a quartz sand layer 3 cm in thickness. Pyrite samples of different particle sizes, temperature, and percentage were selected for the dynamic leaching experiments. The total leaching height was 50 cm. The samples were loaded into the plexiglass column in several batches, whereby the sample was added until reaching the 5-cm mark on the column and was then pounded lightly using a wooden pestle to maintain uniform force and a flat and uniform surface. Then, quartz sand was added to reach an additional 3 cm. The sandstone and tailings samples were separated by a segment of nylon mesh to prevent the fine-particle ore from leaking and causing uneven water flow distribution [28]. Finally, the plexiglass cylinder was sealed by applying the plexiglass cover including the rubber hose. The flow rate was set to 100 mL h^{-1} to simulate the flow of water into the ground. After the leaching experiment using rock samples, samples of the leaching water were collected daily for a fixed period of time, and the samples were tested after filtration.

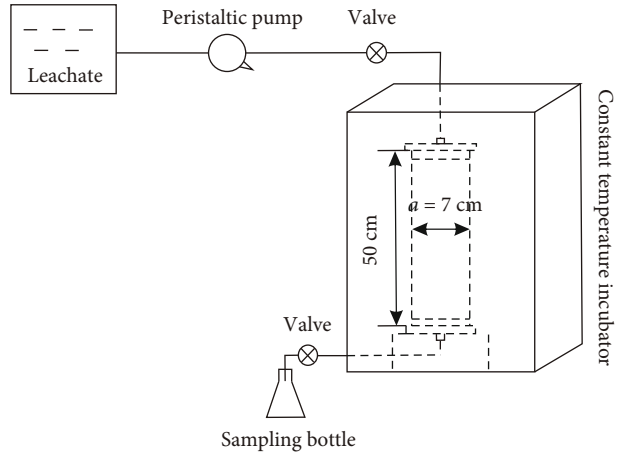

Figure 1: Diagram of dynamic leaching apparatus.

The design parameters of the dynamic leaching experiment are shown in Table 1.

2.3. Analytical Method. In order to semiquantitatively analyze the mineral chemical composition of the rock, the DF-4 electromagnetic ore crusher was used to crush the rock, and the mineral chemical composition was measured by the D8 ADVANCE X-ray diffractometer. Moreover, in addition, the chemical composition was analyzed using a QUANTX Energy-Dispersive X-ray fluorescence spectrometer, and a DHP-350 incubator was used for indoor simulation.

In order to determine the pH value of water samples, the collected water samples were filtered with 0.45-μm polyester fiber membrane immediately after collection, and then the pH value of each water sample was determined by PHB-3 pen pH meter.

3. Theoretical Basis

3.1. Composition Analysis of Rock Samples. Quantitative analysis of the core samples was performed on the basis of X-ray powder diffraction (XRD), the results of which are shown in Table 2. The pyrite samples were composed of for 66% pyrite and 34% kaolinite. Among the limestone samples, calcite and dolomite accounted for 94% and 6%, respectively, and the coal gangue samples contained pyrite, anorthite, and quartz. The inclusion of quartz in the coal gangue could be attributed to accuracy error of the current whole-rock XRD quantitative analysis method, which is not accurate for minerals of low content [18]. The results of XRD analysis showed that the mineral content differed substantially among the rock samples. Therefore, related experiments were performed to further clarify the results.

In the rock samples, the main elements were sulfur and iron followed by silicon and aluminum. The contents of other metal elements were low. The chemical composition analysis revealed that sulfur and iron together accounted for about 40% of the entire element content (Tables 3 and 4).

Table 1: Design of the dynamic leaching experiment including experimental conditions of 2–4-mm particle size and 50% pyrite content as examples.

Medium composition	Filling order	Fill height	Leaching water sample	Leaching speed
Limestone + pyrite	Quartz sand	3 cm	Distilled water	100 ml/h
	Limestone	22 cm		
	Pyrite	22 cm		
Coal gangue + pyrite	Quartz sand	3 cm		
	Quartz sand	3 cm		
	Coal gangue	22 cm		
	Pyrite	22 cm		
Coal + pyrite	Quartz sand	3 cm		
	Quartz sand	3 cm		
	Coal	22 cm		
	Pyrite	22 cm		
	Quartz sand	3 cm		

Table 2: Mineral compositions of the rock samples.

	Pyrite	Kaolinite	Dolomite	Calcite	Quartz	Anorthite
Pyrite	66	34				
Limestone			6	94		
Coal gangue	40				30	30

Table 3: Contents of main compounds in the pyrite rock samples (m/m%).

Compound	SO_3	SiO_2	Al_2O_3	Fe_2O_3	TiO_2	K_2O
Content	53.07	13.16	7.93	23.927	0.5566	0.5346
CaO	V_2O_5	ZrO_2	Cr_2O_3	SrO	NiO	Nb_2O_5
0.2001	0.0168	0.0114	0.001	0.0029	0.004	0.0017

Table 4: Contents of main elements in the pyrite rock samples (m/m%).

Compound	S	Si	Al	Fe	Ti	K
Content	21.51	6.156	4.16	16.63	0.332	0.429
Ca	V	Zr	Cr	Sr	Ni	Nb
0.083	0.0304	0.0254	0.0122	0.0074	0.0046	0.0036

3.2. Acid Produced through Pyrite Oxidation. Existing studies show that the main acid component of pyrite is S^{2-}state sulfur and that the neutralizing acid component is mainly carbonate. The neutralizing acid component that inhibits the discharge of acidic water is effective carbonate, and the acid production component that continues after the start of acid discharge is effective S^{2-}state sulfur [29]. Under anhydrous conditions, the surface of pyrite reacts directly with air as

$$FeS_2\,(s) + 11O_2(g) \longrightarrow 2Fe_2O_3(s) + 8SO_2\,(g), \quad (1)$$

$$2SO_2(g) + O_2(g) \longrightarrow 2SO_3\,(g), \quad (2)$$

$$4FeS_2(s) + 3O_2 \longrightarrow 2Fe_2O_3(s) + 8S\,(s). \quad (3)$$

Pyrite is oxidized directly to produce acid in the presence of water as

$$2FeS_2 + 7O_2 + 2H_2O \longrightarrow 2Fe^{2+} + 4H^+ + 4SO^{2-}_4, \quad (4)$$

$$4Fe^{2+} + O_2 + 4H^+ \longrightarrow 4Fe^{3+} + 2H_2O, \quad (5)$$

$$FeS_2 + 14Fe^{3+} + 8H_2O \longrightarrow 15Fe^{2+} + 2SO^{2-}_4 + 16H^+. \quad (6)$$

The total reaction is given as

$$FeS_2 + 15/4O_2 + 7/2H_2O = Fe(OH)_3 + 2SO^{2-}_4 + 4H^+. \quad (7)$$

The acid potential of coal gangue stacked for three to five months is two to three times higher than that of fresh coal gangue, which has the potential to produce strong acid [30]. Correlation analysis showed that the maximum acid-producing potential of coal gangue is not significantly correlated with the pyrite content, whereas the neutralization potential is significantly correlated with calcite. In the limestone samples, calcite and dolomite accounted for 94% and 6%, respectively. The main mineral components are the neutralizing acid components of carbonates such as $CaCO_3$ and $CaMg\,(CO_3)_2$. Therefore, adding limestone samples can cause the following reaction under an acidic environment:

$$CaCO_3 + 2H^+ = Ca^{2+} + H_2O + CO_2, \quad (8)$$

$$CaMg(CO_3)_2 + 4H^+ = Ca^{2+} + 2H_2O + 2CO_2 + Mg^{2+}. \quad (9)$$

The calcium carbonate in limestone reacts with the acidic water, which raises the pH of the water and inhibits its acidification.

4. Results and Discussion

4.1. Static Soaking Experiment

4.1.1. Effect of Pyrite Content on pH Value. To study the changes in the pH value of the liquid phase with changes in the pyrite content, a static immersion experiment was conducted at 25°C using limestone as the medium with pyrite percentages of 25%, 50%, 75%, and 100%. As shown in Figure 2, higher percentages of pyrite in the reaction sample related to stronger acidity in the water sample and a lower pH value. For samples with the same particle size and the same pyrite percentage, as the immersion time increased, the pH of the water sample also increased. When the pyrite content was 100%, the pH of the water sample reached its minimum, between 3.2 and 4.1. When the pyrite content was 75% to 100%, the pH of the water sample rises rapidly, changing from weak acid to neutral and weak acid to weak alkaline. The pH of the water sample with particle sizes of 2-4 mm rises from weak acid to neutral, and the pH of the water sample with a particle size of 0.825-2 mm and < 0.825 mm rises from weak acid to weak alkaline. When the pyrite content was between 50% and 75%, the change in pH was relatively smooth and decreased with the increase of pyrite content, which was negatively correlated. This result might be related to the limestone medium. It is inferred that the limestone will produce alkaline water during the soaking process, which neutralizes the acidic water produced by the hydrolysis of iron ions during the soaking process of the pyrite in the water sample and increases the pH value of the water.

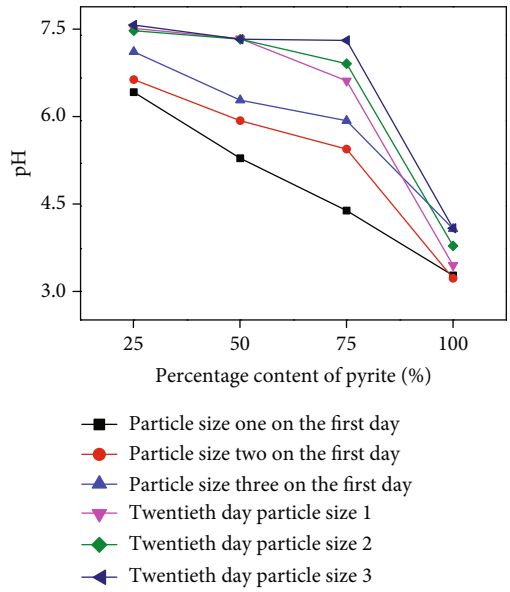

Figure 2: Static experiment results showing pH change corresponding to various pyrite contents.

4.1.2. Influence of Rock Sample Particle Size on pH Value. To ensure that the rock sample was in full contact with the distilled water to realize the rapid acidification of the mine water under the action of pyrite, the rock samples were broken into smaller sizes [31]. A static immersion experiment was conducted on rock samples of three particle sizes, and particle size analysis was conducted orthogonally with that of other experimental factors. The relationship between the particle size at different percentages and the pH value of the immersion water sample at 35°C is shown in Figure 3.

Figures 3(a) and 3(b) show pH changes occurring on day 1 and day 20 of the experiment, respectively. Figure 3(a)shows that a decrease in the particle size at the beginning of the experiment resulted in an increasing trend in the pH value. On the first day, the differences between particle sizes 0.825mm–2mm and < 0.825mm were 0.12, 1.6, 1.01, and 0.7. The differences on day 20 were −0.31, −0.07, −0.18, and−0.1. At the beginning of the experiment, a correlation was noted between such that as the particle size decreased, the pH value increased. This could be explained by the relationship in which a smaller particle size has a larger specific surface area and stronger water–rock interaction strength. In the particle size range, the pH difference on the first day of the experiment was larger, indicating that the particle size had a greater impact on the pH value at the beginning of the experiment. Twenty days after the experiment, the pH difference between the particle sizes was small, and the particle size has little effect on the pH value at that time. Negative values were obtained for particle sizes of 0.825 mm–2 mm and < 0.825 mm, which means that the pH value of the reaction group with small particle sizes was smaller than that of the large particle sizes. The soluble matter reacted completely, and the large and small particle sizes reacted more slowly. Therefore, in the later stage of the experiment, the soluble matter of the large particle sizes was released to a greater extent than that of the small particle sizes, which created a negative difference.

4.1.3. Influence of Temperature on pH Value. The reaction temperature was set to 25°C and 35°C; the medium was limestone; the pyrite content was set to 50%; and the pH value of the static soaking solution changed with the soaking time.

As shown in Figure 4, the pH value under different conditions increased with an increase in temperature. The pH at 35°C was greater than that at 25°C; therefore, the pH value was positively correlated with temperature. The absolute values of pH differences under the same conditions and different temperatures were 0.25, 0.2, 0.48, 0.16, 0.24, and 0.42, respectively. Therefore, it can be concluded that although temperature has a certain influence on the acidification of distilled water, the influence degree is not obvious. On day 20, the pH values of the three particle sizes were 7.44, 7.44, and 7.43, respectively. The reason may be that the added limestone had a significant effect on raising the pH of the

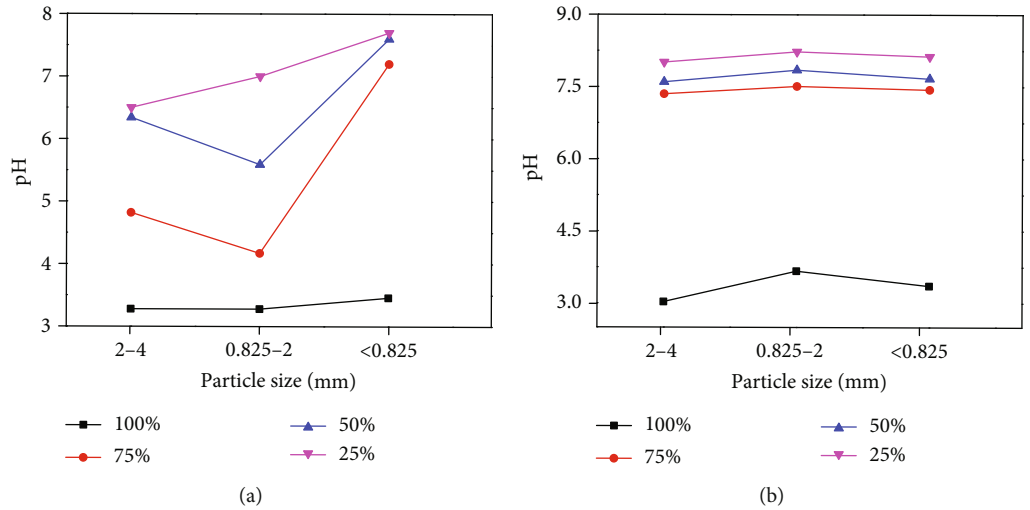

Figure 3: Results of static immersion experiment performed at 35°C showing pH change relative to particle size: (a) day 1; (b) day 20.

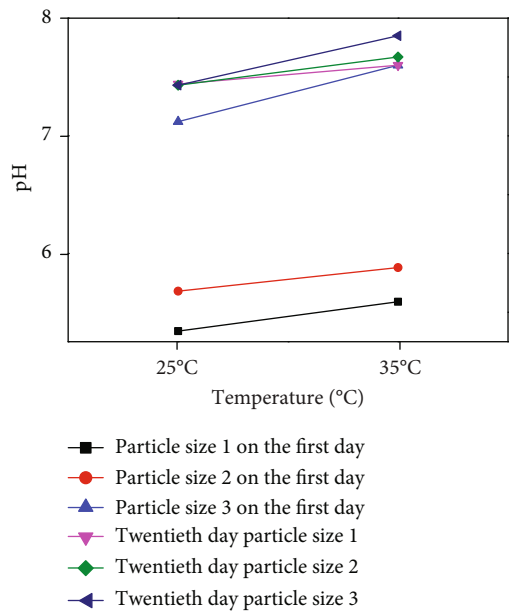

Figure 4: Influence of different temperatures on pH value.

acidic mine water, while the particle size had little effect on the pH value.

4.1.4. Influence of Medium on pH Value. In coal mines, the lithology differs among coal seams and affects the acidification of mine water to varying degrees. Figure 5 shows the pH values of coal, coal gangue, limestone, and coal gangue + limestone, all with 50% pyrite, against time.

The figure shows that as the immersion time increased, the pH values of the coal and the limestone soaking solutions first increased and then gradually stabilized, whereas those of the coal gangue and the coal gangue + limestone experimental groups increased with time, showing a trend of increasing, then decreasing, and increasing again before gradually stabilizing. The pH value of the coal experiment group was between 2.5 and 4.2, and the water samples showed strong acidity. Compared with the pH values of the other three groups of experiments (between 6 and 7.5), these values are significantly lower than those of the experimental groups including coal gangue, limestone, and coal gangue + limestone. In particular, the coal, coal gangue, limestone, and coal gangue + limestone had a significant influence on the acidic water produced by 50% pyrite under different media. The coal gangue and limestone had the same effect, which effectively reduced the production of acidic water. The combined effect of the four substrates was limestone > coal gangue + limestone > coal gangue > coal.

4.2. Dynamic Leaching Experiment

4.2.1. Influence of Pyrite Content on pH Value. To simulate the influence of different pyrite contents in the dissolution process of groundwater, a dynamic leaching experiment was conducted under the condition of 25°C, and the pH value changed with time.

As shown in Figure 6, the pH change trend for different pyrite contents under the same leaching conditions was consistent with that shown in the static immersion test. In particular, a larger pyrite percentage was related to stronger acidity in the water sample, with lower pH values showing greater degrees of influence. In the long-term leaching and soaking experiments using 100% pyrite, the water samples were always acidic. It is inferred that the acid production rate of pyrite is greater than the neutralization rate of its alkaline components. The other three groups of experiments showed neutral to weakly alkaline pH after the experiments ended. In addition, the pH values of water samples with varying pyrite contents showed an upward trend over time. Specifically, the pH increase was rapid at the early stages and slower at the later stages before finally stabilizing.

4.2.2. Influence of Rock Sample Particle Size on pH Value. Figure 7 shows that with the same particle size, the pH value

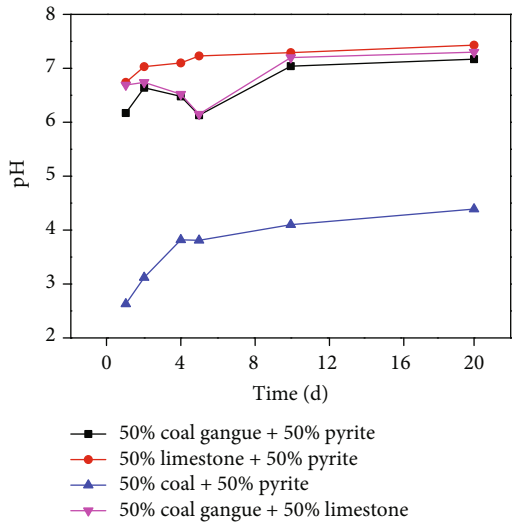

Figure 5: Changes in pH value with time under different media conditions.

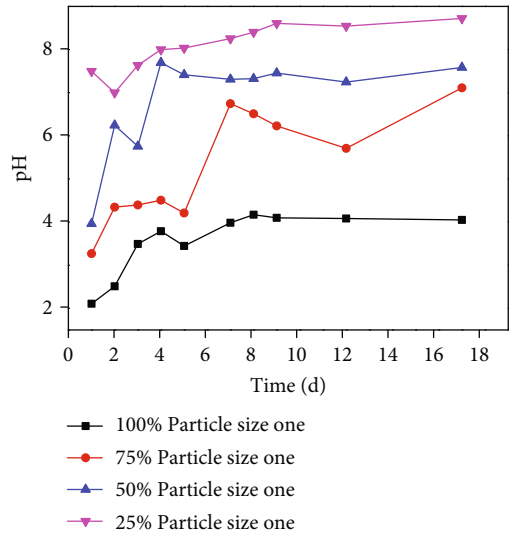

Figure 6: Changes in pH under varying contents of pyrite in a dynamic experiment.

of the leaching solution first increased and then decreased with an increase in the leaching time. During the middle of the leaching, the pH value reached its maximum value. At the beginning of the experiment, the pH value increased as the particle size decreased. The reason for this is inferred to be that the smaller the particle size, the larger the specific surface area, and the content of water-soluble acidic components is less than the sum of alkaline components and the mineral neutralization of rock samples, so the pH value increases. In addition, the low degree of weathering within the large particle size, the slow release of elements, and precipitates such as calcium sulfate and iron produced by pyrite and calcite adhere to the calcite surface, hindering the continuation of the reaction, thereby increasing the pH value. As the leaching experiment continued, the substances in the sample continued to participate in the reaction of oxidation acid production, and the content of the water-soluble acidic components was greater than that of alkaline components. This gradually increased the acidity of the leaching solution and decreased the pH value. In general, the experimental groups of the three particle sizes showed that even in the process of leaching, the difference in particle size within the experimental group had a certain impact on the pH value of the leaching solution. However, the influence of the pyrite content on the pH value of the liquid phase was not obvious.

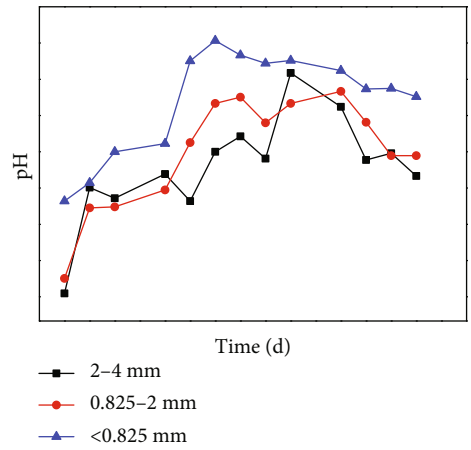

Figure 7: Dynamic experiment of pH values under different particle sizes.

4.2.3. Influence of Temperature on pH Value. The separate reaction temperatures were set as 25°C, 35°C, and 55°C, with pyrite and limestone each accounting for 50%. The changes in pH value of the leachate with soaking time are shown in Figure 8. On the first day of the leaching experiment, the mean pH of the leachate was 4.11, which is acidic. However, the value increased with the progress of the experiment and tended to stabilize about eight days later to neutral or nearly neutral values. However, an increase in the experimental temperature led the pH of the leachate to increase more rapidly. When the reaction was complete, the pH value of the leachate tended to be neutral. This was because pyrite and limestone account for 50%, respectively, and $CaO + H_2SO_4 = CaSO_4\downarrow + H_2O$ neutralization reaction will occur, so as to increase the pH value and inhibit the acidification degree of water and make its pH gradually tend to neutral.

4.2.4. Influence of Medium on pH Value. To study the influence of different media on the acid produced by pyrite, the pH values of the leaching liquid over time were noted after mixing different media with 50% pyrite at 25°C, as shown in Figure 9. With an increase in time, the change trends of the pH values of the different media were essentially the same, all showing increases followed by decreases and then gradually stabilization. This trend is obviously different from the static soaking law. In the middle of leaching, the pH value of the leaching solution reached its maximum. Similar to the static soaking result, the coal gangue and limestone slowed the acidification of the mine water, which effectively

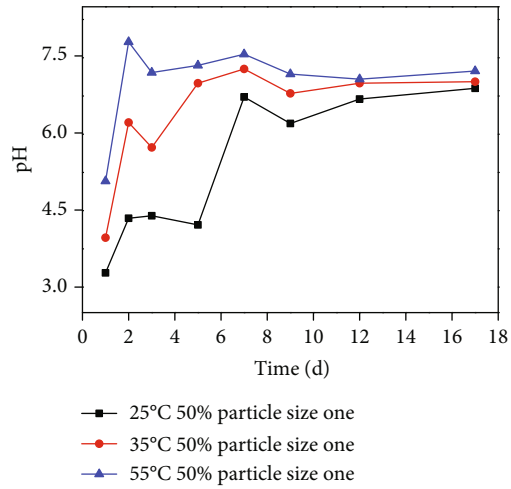

Figure 8: Influence of different temperatures on pH value.

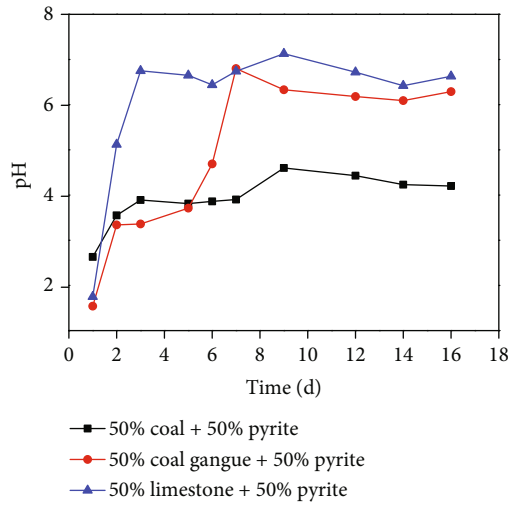

Figure 9: Changes in pH value with time under different media conditions.

reduced the production of acidic water. The combined effect of the three substrates was limestone > gangue > coal.

4.3. Correlation Analysis between pH of Pyrite Acidification and Influencing Factors. Based on the grey system theory [32], pH value of pyrite acidification was taken as a reference sequence, and all influencing factors were taken as a comparison sequence. The normalization method was adopted to conduct dimensionless processing of the original data to eliminate the errors brought by different data levels and increase the comparability of each index. The correlation coefficient between the comparison sequence and the reference sequence was calculated. Because the composition of the rock samples was the key factor in determining and inhibiting the production of acid water by pyrite, which could not be quantified, so it was not involved in the gray correlation analysis. The resulting correlations of pyrite content, rock size, and temperature were obtained and ranked. The results were shown in Table 5.

Table 5: Correlation degree of each index.

Index	Static soaking		Dynamic leaching	
	Correlation degree	Ranking	Correlation degree	Ranking
Pyrite content	0.74	1	0.65	1
Rock particle size.	0.52	3	0.59	3
Temperature	0.58	2	0.60	2

From the above table, it can be seen that the relationship between the pH dependence of each factor in the soaking and drenching experiments was pyrite content > temperature > particle size. The results showed that the pyrite content was the main controlling factor for mine water acidification compared with other factors. It is consistent with the experimental findings.

According to previous research progress [33], in the static leaching experiment, the correlation coefficient between pyrite content and pH was 0.74, which was a strong correlation, and the correlation coefficients between rock particle size and temperature and pH were 0.52 and 0.58, respectively, which were moderate correlations; in the dynamic leaching experiment, the correlations between all three factors on pH were moderate correlations.

5. Discussion and Analysis

The results of the static immersion and dynamic leaching experiments indicate that in the sulfur-rich sedimentary strata, the lithology, background temperature, percentage of pyrite, or characteristics of pore development can cause acidification of groundwater with varying degrees of influence. Generally, the content of pyrite was the most important factor influencing the acidification of mine water. The degree of acidification of acid mine water was determined mainly by the initial percentage of pyrite in the formation and occurred more rapidly in pyrite-rich areas of coalfields. That is, water with greater acidity was easily produced. Although the temperature of the formation had a strong role in the rapidly acidification of mine water, no significant temperature difference was noted in the overlying sedimentary strata at the same level in nongeothermal anomaly areas of the coalfield and the mining area. Therefore, in areas with little temperature change, temperature is not a main factor in the acidification of mine water. The effect of pore size on the acidification of mine water was relatively low; therefore, it is not necessary to consider pore development in the water-conducting stratum when formulating actual engineering measures. In addition, when pyrite coexists with coal gangue and limestone, it has a significant buffering effect on the acidity of the mine water.

Although the pyrite content of the coal gangue samples accounted for 40%, however, studies have found that the correlation between the pyrite content and the maximum acid production potential of the coal gangue was not significant. In addition, the acid production potential of the coal gangue stacked for 3~5 months was 2~3 times higher than the fresh coal gangue, but its acid production potential was

also not high, and most of the pH value was about 6.5 after stabilization [34]. Mineral analysis of coal gangue did not detect the relevant minerals that can neutralize acid mine water, but coal gangue often exists containing Ca, Mg, K, Na, and other carbonate compounds; these carbonates were easy to neutralization reaction in water, thereby buffering the degree of acidification in the mine water. Li et al. [35] discussed the effect of dispersive alkaline matrix system composed of limestone and wood chips on the treatment of acid mine water in closed coal mine, and the research results showed that the dispersive alkaline matrix method was effective in raising the pH of acid mine water. And the calcite content in the limestone samples reaches 94%, and its components were mainly $CaCO_3$, $CaMg(CO_3)_2$, etc., which will certainly affect the acidification process of the mine water. The experimental results of adding coal showed that the addition of coal had little effect on acid water or might aggravate the acidification of mine water. The reason may be that after the coal was mined and stockpiled to the surface, the physical and chemical conditions of the coal changed, and those sulfides formed in the reduction environment encountered surface water or were exposed to air and began to decompose while generating large amounts of acidic wastewater.

During the dynamic leaching experiment, the trend of the pH value of the leaching liquid in each experimental group was essentially the same. All showed the characteristics of rapid decline in the pH, reaching the minimum value at the first sampling and increasing with time. Specifically, the pH value gradually increased and finally stabilized. If it is assumed that the continuous oxidation of pyrite during the experiment caused the pH value to decrease, before the pyrite is completely oxidized, the pH value of the leachate will increase. The oxidation of pyrite was continuously reduced or remained essentially unchanged. Therefore, on the basis of the immersion and leaching experiment results, it is inferred that the pyrite was oxidized, and the iron formed after oxidation was quickly leached into the water, which enabled the complexation reaction and the subsequent rapid acidification of the distilled water. As the experiment progressed, the iron adsorbed onto the surface of the pyrite decreased, which caused the acidification degree of the distilled water to gradually decrease. The complexation reaction equation is

$$Fe^{3+} + 3H_2O = Fe(OH)_3 + 3H^+. \quad (10)$$

The acidification process of coal mine water is not caused by the process of pyrite oxidation; rather, it occurs through the process of iron conversion to the $Fe(OH)_3$ complex after the pyrite oxidation. Therefore, to prevent the formation of acidic mine water, the geological and hydrogeological conditions of the site can be combined to delineate the enrichment area of pyrite, and corresponding engineering measures can be formulated to prevent the formation of complexes to reduce the amount of acidic water produced.

6. Conclusions

(1) In the immersion and leaching experiments, the pH value of distilled water changed with the rock particle size, medium, pyrite content, and temperature. Among them, the pyrite content was the most important factor affecting the acidification of mine water. In the experimental groups with different particle sizes, the pH value of the distilled water increased with a decrease in particle size. In the experimental groups with different pyrite content, a greater pyrite content related to greater acidity of the water. When using different media, the additions of limestone and the coal gangue reduced the acidification degree of the leaching and the soaking water samples. In the different temperature experimental group, higher temperatures related to higher pH values in the distilled water. The gray correlation method was used to quantitatively analyze the correlation degree of various factors to pH: pyrite content > temperature > rock particle size

(2) The acidification process of the mine water in the coalfield area is based on the conversion process of iron to $Fe(OH)_3$ complexes after the oxidation of pyrite. Therefore, this factor can be combined with the geological and hydrogeological conditions of the site to delimit the enrichment area of the pyrite when formulating corresponding engineering measures to prevent the formation of such complexes. In addition, compared with open and flowing water bodies, a closed environment with added limestone can effectively reduce the production of acid mine water

Data Availability

All data included in this study are available by contacting the first author.

Conflicts of Interest

The authors declare that they have no conflicts of interest.

Acknowledgments

This work was supported by the National Natural Science Foundation of China (41802186, 41972254, and 42102297), Innovative Science and Technology Talents Team Construction Project of Henan Province (CXTD2016053), and Special Funds for Higher Education Basic Scientific Research Funds of Henan Province (NSFRF200103).

References

[1] W. Jiang, T. U. Zhihong, Z. Shu et al., "A brief overview on the mechanism and kinetic influencing factors of the pyrite surface oxidation," *Metal Mine*, vol. 50, no. 3, pp. 88–102, 2021.

[2] H. X. Qiu, G. S. Zhang, H. J. Wen, R. Peng, Q. K. Meng, and S. L. Li, "Mineralogical characteristics and genesis of pyrrhotite

in the Baicao V-Ti magnetite deposit in the Huili area of the Panzhihua-Xichang rift," *Acta Mineralogica Sinica*, vol. 41, no. 3, pp. 245–257, 2021.

[3] S. Deng, W. H. Gu, and G. S. He, "Difference in leaching behavior and electrochemical properties of pyrite with different genetic mineralogy in acidic medium," *Mining and Metallurgical Engineering*, vol. 41, no. 1, pp. 85–89, 2021.

[4] F. D. Zhao, F. Huang, S. Gao, B. Y. Zhang, and L. Meng, "A study on the characteristics and genesis of pyrite in the Zhaishang gold deposit, Gansu Province, NW China," *Acta Mineralogica Sinica*, vol. 39, no. 6, pp. 637–648, 2019.

[5] K. N. Li, M. Wang, Y. A. Qi, W. T. Yang, and C. C. Zhong, "Genesis and ecological significance of berry-shaped pyrite in Thalassinoides bacae of the Zhangxia Formation of the Miaoling series of the Cambrian in Western Henan," *Chinese Journal of Paleontology*, vol. 58, no. 4, pp. 445–455, 2019.

[6] M. Bomberg, J. Mäkinen, M. Salo, and P. Kinnunen, "High diversity in iron cycling microbial communities in acidic, iron-rich water of the Pyhäsalmi Mine, Finland," *Geofluids*, vol. 2019, Article ID 7401304, 18 pages, 2019.

[7] B. Liu and J. She, "Analysis of the causes of acidification of Tangshan abandoned mine water body and treatment plan," *Environmental Science and Technology*, vol. 34, no. S1, article 217, 2011.

[8] D. Gu, T. Li, J. Li et al., "Current status and prospects of coal mine water treatment technology in China," *Coal Science and Technology*, vol. 49, no. 1, pp. 11–18, 2021.

[9] W. Shao, Y. Song, and C. H. Wang, "Research on treatment of acid mine drainage by artificial wetland," *Environmental Engineering*, vol. 29, no. 5, pp. 45–47, 2011.

[10] Y. J. Sun, G. Chen, Z. M. Xu et al., "Research progress of water environment, treatment and utilization in coal mining areas of China," *Journal of China Coal Society*, vol. 45, no. 1, pp. 304–316, 2020.

[11] L. Y. Zeng, C. Z. Yang, S. Li, and J. Y. Gong, "Treatment of PNP wastewater by pyrite photo-electric-Fenton," *Environmental Science and Technology*, vol. 42, no. 9, pp. 142–146, 2019.

[12] C. J. Booth, "Strata-movement concepts and the hydrogeological impact of underground coal mining," *Groundwater*, vol. 24, no. 4, pp. 507–515, 1986.

[13] M. Kalin, A. Fyson, and W. N. Wheeler, "The chemistry of conventional and alternative treatment systems for the neutralization of acid mine drainage," *The Science of the Total Environment*, vol. 366, no. 2-3, pp. 395–408, 2006.

[14] P. L. Younger, "Mine water pollution in Scotland: nature, extent and preventative strategies," *Science of the Total Environment*, vol. 265, no. 1-3, pp. 309–326, 2001.

[15] A. K. Singh, M. K. Mahato, B. Neogi, B. K. Tewary, and A. Sinha, "Environmental geochemistry and quality assessment of mine water of Jharia coalfield, India," *Environmental Earth Sciences*, vol. 65, no. 1, pp. 49–65, 2012.

[16] F. H. Zhao, Y. Guo, H. F. Sun, and M. H. Zhu, "Free drainage column leaching experiment and mechanism of water-rock interaction in main aquifers of Xinzhi coal mine," *Journal of China Coal Society*, vol. 44, no. 4, pp. 1207–1215, 2019.

[17] C. B. Tabelin, S. Veerawattananun, M. Ito, N. Hiroyoshi, and T. Igarashi, "Pyrite oxidation in the presence of hematite and alumina: I. Batch leaching experiments and kinetic modeling calculations," *Science of the Total Environment*, vol. 580, pp. 687–698, 2017.

[18] X. P. Hong, Y. Zhang, H. D. Liang, Y. Li, and S. Lv, "Experimental study on fluorine in acidic water dynamic leaching and static soaking of soil," *Earth and Environment*, vol. 43, no. 3, pp. 356–362, 2015.

[19] Z. Ran, W. L. Liu, Y. T. Pan, W. C. Liu, Z. R. Gao, and Y. X. Zhao, "Influence of temperature on dynamic leaching characteristics of coal gangue," *Journal of China Coal Society*, vol. 44, no. 4, pp. 1239–1246, 2019.

[20] X. Y. Li, H. Peng, S. Xiong, S. X. Gong, and S. Y. Li, "Experimental study on dissolving performances of Maifan stone under different leaching conditions," *Environmental Science and Technology*, vol. 44, no. 1, pp. 13–23, 2021.

[21] S. Kuşlu, T. Çalban, and S. Çolak, "Evaluation of leaching conditions for dissolution of pyrite in chlorine-saturated water," *Chemical Engineering Communications*, vol. 198, no. 4, pp. 504–515, 2010.

[22] J. Z. Di, S. H. Bao, Y. Yang et al., "Study on the influence of particle size on the dissolution and release law of pollutants from coal gangue," *Coal Science and Technology*, vol. 48, no. 4, pp. 178–184, 2020.

[23] X. D. Wang, X. Sun, Q. S. Liu, H. B. Wei, Z. K. Wang, and H. W. Pan, "Research progress on the dissolution and release of pollutants in mineral products," *Rock and Mineral Testing*, vol. 32, no. 1, pp. 15–21, 2013.

[24] B. He, Y. Zhang, and X. D. Li, "Experimental study on the dissolution of main polluting components of coal gangue," *Bulletin of Silicate*, vol. 33, no. 9, pp. 2217–2222, 2014.

[25] D. F. Pflughoeft-Hassett, D. J. Hassett, K. E. Eylands, G. F. Weber, and C. E. Martin, "An assessment of residues from duct injection demonstration sites," *Air & Waste*, vol. 44, no. 10, pp. 1214–1218, 1994.

[26] D. S. Wu, B. S. Zheng, X. D. Kang et al., "Study on the leaching behavior of coal gangue and its environmental impact——taking Huainan Panxie mining area as an example," *Earth and Environment*, no. 1, pp. 55–59, 2004.

[27] J. P. Xia, X. J. Ren, Z. S. Zhang, J. Tao, and R. Yang, "Experimental study on acid leaching and dissolution of high-speed iron and low-aluminum coal gangue," *Chemical Engineering*, vol. 41, no. 3, pp. 59–62, 2013.

[28] X. Y. Wang, J. Yang, and H. X. Guo, "Research on soil heavy metal pollution caused by coal gangue stacking in mining area," *Journal of China Coal Society*, no. 6, pp. 808–812, 2006.

[29] J. W. Li, X. Li, H. M. Wu, Y. H. Chen, and S. Basra, "Consumption of acid and neutralizing acid components of pyrite and the determination of effective components," *Environmental Chemistry*, vol. 30, no. 4, pp. 869–873, 2011.

[30] Y. Q. Sun, Q. Yang, L. Duan, and X. D. Wang, "Analysis on the acid production potential of Hancheng coal gangue," *Coal Conversion*, vol. 41, no. 1, pp. 72–79, 2018.

[31] P. Liu and F. Yan, "The harm of coal gangue to the environment and its comprehensive treatment," *China Mining Industry*, no. 8, pp. 49–51, 2008.

[32] J. L. Deng, "Introduction to Grey system theory," *The Journal of Grey System*, vol. 1, no. 1, pp. 1–24, 1989.

[33] J. C. Zhuang, Z. Y. Xu, and F. Huang, "Grey correlation analysis of foreign trade and industrial scale growth – a case study of Guangxi," *Southeast Asia*, no. 11, pp. 70–73, 2008.

[34] B. Liang, Q. Dong, and L. G. Jiang, "Experimental study on static prediction of acid potential of coal gangue," *Nonmetallic Ore*, vol. 39, no. 1, pp. 31–33, 2016.

[35] L. Xiangxiang, C. Hua, Z. Liugen et al., "Distribution characteristics and environmental significance of nitrogen and phosphorus in coal mining subsidence water in Huainan," *Journal of China University of Science and Technology*, vol. 44, no. 11, pp. 926–932, 2014.

Hindawi
Geofluids
Volume 2022, Article ID 5187800, 12 pages
https://doi.org/10.1155/2022/5187800

Research Article

Experimental Study on Capillary Water Migration Characteristics of Tailings with Different Particle Sizes

Di Liu,[1,2] **Caiwu Lu**,[1,2] **Minjie Lian**,[1,2,3] **Qinghua Gu**,[1,2] **and Ying Jing**[2,4]

[1]*School of Resource Engineering, Xi'an University of Architecture and Technology, Xi'an 710055, China*
[2]*Xi'an Key Laboratory for Intelligent Industrial Perception, Calculation and Decision, Xi'an 710055, China*
[3]*Sinosteel Mining Co. Ltd., Beijing 100080, China*
[4]*School of Management, Xi'an University of Architecture and Technology, Xi'an 710055, China*

Correspondence should be addressed to Ying Jing; johanlibeite@163.com

Received 7 December 2021; Accepted 8 April 2022; Published 11 May 2022

Academic Editor: Gangwei Fan

Capillarity influences the long-term stability of the dam greatly and affects the sustainable development of tailings dam. The online monitoring capillary water rise test system was independently developed by SM3001B temperature and humidity sensor, SU9101B RS485 converter, SV3010 data acquisition system, and other equipment to carry out the whole process test of water absorption and water release of tailings with different particle sizes. The results show that the capillary rising trend of tailings with different particle sizes is basically consistent, the relationship between the rising height and the diameter are negatively correlated, and the logarithm function can better fit the height of capillary rising over time well enough. The water content of tailing capillary zone decreases with the height, and the smaller the size of tailings, the greater the change of water content. The water release process of tailings is an unsaturated permeability process, which largely depends on the saturation before water release. The larger the particle size of tailings is, the smaller the water content after water release. Based on the above results, the relationship between capillary diameter and tailings particle size was discussed, and the relationship formula between water content change and particle size was deduced. The research results systematically show the water migration law under the tailing capillaries. It is suggested that the unsaturated tailings water content index should be added in the monitoring of the saturated surface of tailings dam.

1. Introduction

The discharge of tailings in our country is very large. The accumulated tailings not only occupy land resources but also cause environmental pollution. The resource utilization of tailings has become a major concern. Tailing pond is a special hydraulic structure produced by the combination of two technologies of "tailing utilization" and "tailing storage" [1]. Its hydraulic phenomena are complex and changeable (see Figure 1), and it has the characteristics of service and construction at the same time. A large number of studies have shown that the most important factor affecting the stability of a dam is water [2–4]. Rainfall, tailing discharging, surface runoff, seepage [5], evaporation, etc. will all affect the water content of the dam. Generally, the water content of the dam body is in a dynamic equilibrium state. Once the equilibrium is broken, there will be safety hazards.

The relationship between gravity water and the stability of tailings dams is the research object of most existing tailings dam stability research methods and models, such as the mechanical properties of tailings [6, 7], liquefaction of the dam body [8], and seepage safety hazards [9–11], the mechanism and mode of dam failure caused by floodplain [12], and the mechanism of dam instability caused by rainfall [13], while the influence of stagnant water in the unsat-

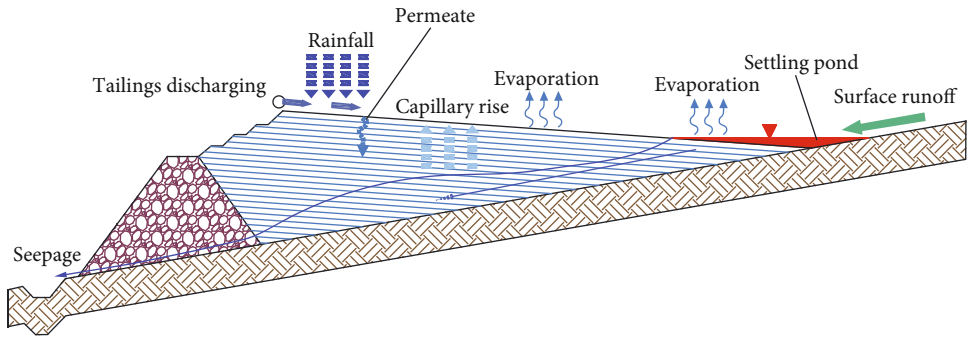

Figure 1: Complex hydraulic phenomena in tailing dam.

urated zone in the tailings dam on its stability is often ignored [14], until María et al. [15] first proposed in 2009 that the capillary action of water may greatly reduce the safety reserve of tailings dams. Prior to this, the research on capillary action at home and abroad was mainly carried out around the prevention of roadbed diseases. The research objects included the comprehensive test method of capillary water rise [16] and the rising law of capillary water in other media, such as sandy soil [17], clay [18, 19], and loess [20]. And the study of the effect of capillary water on the stability of tailings dams is rarely reported.

With the capillary water rising to the slope of the dam, after the water evaporates, the salt in it remains and crystallizes, which is the result of capillary action. Capillary ascent is a slow and continuous process that is often overlooked, which results in a large amount of capillary water in the pores between the tailing particles. Yin et al. [21] studied the characteristics of pore water migration and its mechanism of action on the mesostructure of tailings. They proposed that the calculated height of the infiltration line can be determined by the height of the capillary water above it and analyzed the dam stability accordingly. Liu et al. [22] studied the maximum rising height of tailings capillary water. Zhang et al. [23] systematically studied the impact of the difference in particle gradation on the rising process of capillary water and the physical and mechanical properties of the dam material in the capillary water belt. The results showed that the moisture content of the tailings in the capillary water belt and the physical and mechanical indexes such as severity, cohesion, and internal friction angle change with the change of capillary water height. Zhang et al. [24] studied the rise of capillary water in a tailing dam by temperature and air pressure through indoor experiments. However, none of the above studies dealt with the change of water content of the dam body caused by capillary absorption and release of water.

Tailings are a mixture of sand-powder-clay particles [25]. After the deposition and consolidation of tailings particles with different gradations, microscopically similar capillary channels are formed. In addition, due to the existence of matrix suction, external conditions for the formation of capillary action in the tailings dam are provided. The effect of capillary action on the dam is essentially the weakening of the strength of the dam after the water migration caused by the nonequilibrium matrix potential and the capillary effect [26], which essentially affects the water content of the dam. In particular, the rise of the water level of the infiltration surface shortens the path of capillary action and speeds up the replenishment of the upper water by capillary action. The increase in water content will reduce the strength of the tailings and bring harm to its stability. Therefore, full attention should be paid to the design, monitoring, and subsequent maintenance of tailing dams.

At present, research on the change of water content of tailing dams under the influence of capillary action has just started. Based on the basic theories of capillary absorption and water release, using the self-developed capillary water absorption and release experiment device, the capillary water absorption and release experiments of tailings with different particle sizes were carried out to explore the migration characteristics of capillary water in tailings.

2. Materials and Methods

2.1. Tailings Samples. Tailings used in the test was taken from a copper mine tailing pond in Shaanxi province. The particle size ranged from 0.5 to 250 μm, mainly concentrated in 100 to 200 μm. To avoid the influence of impurity content, first wash the sample thoroughly, then air, grind, and dry it. Finally, the dried tailings are screened and graded to obtain tail fine sand, tail silty sand, and tail silty soil for test; the specification followed for determination of the grain size distribution of tailing soil is "Safety technical regulations for the tailing pond (AQ 2006-2005)." The cumulative particle distribution curve of tailings of tail fine sand, tail silty sand, and tail silty soil is shown in Figure 2. The particle grading index and main physical properties index are shown in Table 1.

2.2. Experimental Device. The test device is a self-developed on-line capillary-rising monitoring testing system (OM-CRT). Figure 3 shows the five main parts of the device, including capillary water absorption test device, online water content monitoring system, data acquisition system, water supply, and drainage system.

The main body of the testing system is composed of 3 transparent polymethyl methacrylate columns including specimen loading structure and the supporting structure. The size of specimen loading structure is designed to avoid

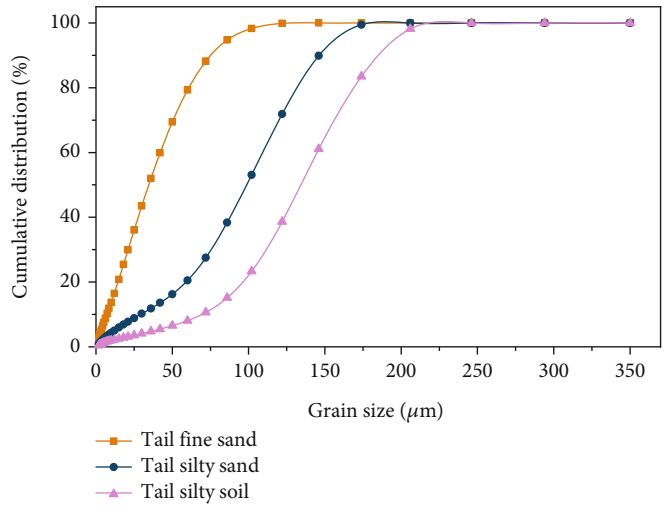

Figure 2: The cumulative particle distribution curve of tailings.

Table 1: Particle composition parameters tailings and main physical property indexes of tailings.

Particle group	Particle size range (μm)	Effective grain size d_{10} (μm)	Median grain size d_{50} (μm)	Constrained grain size d_{60} (μm)	Uniformity coefficient C_u	Initial moisture content w (%)
Tail fine sand	125~180	69.12	134.19	155.12	2.24	2.51
Tail silty sand	75~125	29.20	98.63	114.26	3.91	2.92
Tail silty soil	5 ~ 75	7.13	34.6	42.56	5.96	3.31

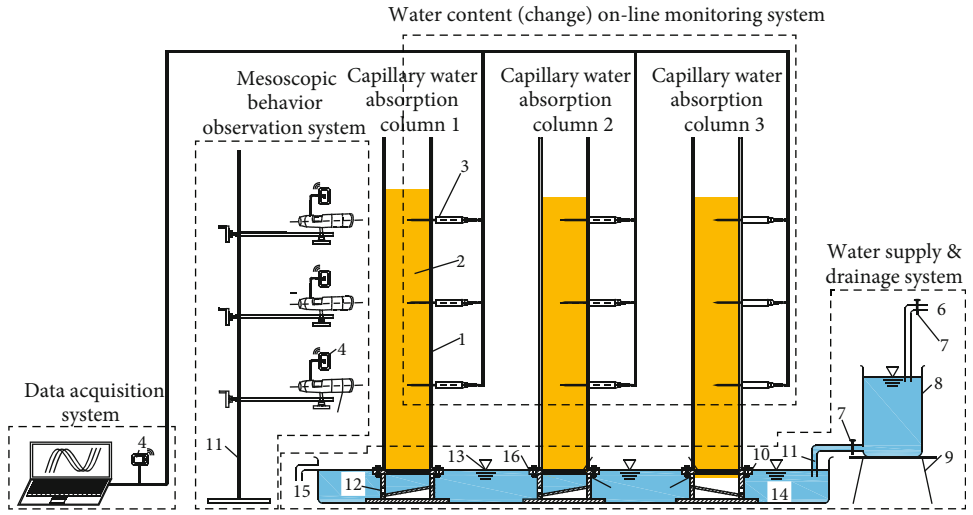

Figure 3: The schematic diagram of OM-CRT system. 1—tube wall; 2—tailings; 3—water sensor; 4—cloud module; 5—distortionless microscope; 6—water source; 7—valve; 8—water storage tank; 9—trestle; 10—porous disk; 11—constant speed water supply pipe; 12—scupper and outlet pipe; 13—constant water lever; 14—water-in; 15—water-out; 16—geotextile.

the influence of the polymethyl methacrylate columns radian on the observation effect and meet the requirements of specimen size [18] that the inner diameter is 110 mm, the height is1200 mm, and the wall thickness is 5 mm. The supporting structure is 100 mm high, and its inner diameter and thickness of the wall are consistent with the specimen loading structure. A water inlet is provided at a height of 50 mm on the side. The two are separated by a porous disk with a rubber gasket at the middle interval for sealing. The disk is 10 mm thick and filled with small holes with a diameter of 3 mm to ensure that the water can contact the tailings. Geotextile with a diameter of 110 mm covers the disk to prevent the leakage of tailings particles. The polymethyl methacrylate columns are engraved with scales, of which the zero point is cap height of the porous disc and minimum is 1 mm, with one on

Table 2: Main technical indexes of SM3001B.

Sensor type	Probe length (mm)	Probe diameter (mm)	Moisture measuring range (%)	Temperature range (°C)	Response time (s)	Moisture accuracy (%)	Temperature measurement accuracy (°C)	Voltage (V)
SM 3001B	75	3	0~100	-30~60	<1	3%	0.5	0~10

Figure 4: Preparation process of tailing sample.

each side of symmetry to provide reference for recording the wetting front and the saturation front.

The online moisture content monitoring system is mainly consist of 9 SM3001B temperature and humidity sensors, a SU9101B RS485 converter, a SV3010 data acquisition system, and a computer. The key technical indexes of SM3001B temperature and humidity sensor can be seen in Table 2.

The data and image acquisition system mainly consists of computer and SV3010 data acquisition system. SV3010 data acquisition software has a main interface include measurement points list, running screen, real-time curve, historical curve, and data report. The main interface can be switched to the list of measurement points and the data report which could show the historical data in interface.

The water source is the water pipe in the laboratory, from which it is then distributed to the water tank through the siphon principle. The water tank is equipped with a drainage pipe to ensure the liquid level in the tank is constant.

2.3. Experimental Program. According to the composition of tailings' particle size, this test is divided into three groups including tail fine sand, tail silty sand, and tail silty soil. The specific steps are shown in Figure 4.

(1) Prepare and load specimens: the plexiglass columns are numbered 1#, 2#, and 3#. In order to prevent the formation of water migration channels between the loaded tailings and the inner wall of the column, a thin layer of petroleum jelly should be evenly coated on the inner wall. According to the test plan, put the prepared tailing sand, tailing silt, and tailing silt into columns 1#, 2#, and 3#, respectively (the

sensors placed on column 1# are M4, M5, M6, and the installation heights are 200 mm, 400 mm, 600 mm; the sensors placed on the 2# column are M1, M2, and M3, and the installation heights are 200 mm, 400 mm, and 600 mm; the sensors placed on the 3# column are M7, M8, and M9, and the installation heights are 200 mm, 400 mm, and 600 mm). Perform stratified sample loading and seismic compaction every 5 cm to ensure uniform sample loading, and maintain a certain dry density by the scale and filling mass calculations. Keep the loaded tailings specimen standing for 48 h for the test.

(2) Adjust and install equipment: install the online moisture-content sensor in the prepared hole reserved for the plexiglass column, seal it with glass glue, and check to make sure the sensor circuit is in good working condition. Adjust the online water-content monitoring equipment (M1–M9) to ensure effective data output and storage.

(3) Capillary-water absorption test: turn on the water-supply device to supply water to the tank according to the siphon principle. At the same time, turn on the drainage device to ensure that the water tank level (i.e., the height of the infiltration line) always remains at the bottom of the specimen.

(4) Record data: capillary water began to rise in the three columns which was consistent for observing and recording. The elevation of the wet front was regularly recorded, and digital imaging was carried out until the water column stopped rising and the ambient temperature was kept constant during the test. The water content distribution of the cylinder in the process of capillary water absorption is monitored by the water sensor, and the corresponding data are collected. When the data of each monitoring equipment is stable, the test is completed.

(5) Capillary-water release test (as shown in Figure 5): after the capillarity water absorption test is completed, drain the water from the tank and start the water release test in the natural state. The water collection system keeps recording the monitoring data of M1~M9 sensor during the whole test.

3. Results and Discussion

The movement characteristics of capillary water mainly include the height and water content distribution of capillary. The analysis and research on the capillary rise characteristics of different particle size tailings are as follows.

3.1. The Influence of Particle Size on the Capillary Height of Tailings. The force generated by water from wet tailings makes the water have an energy, which is converted into an equal amount of gravitational potential energy by work and exhibits a certain volume of capillary height [27]. By regularly measuring the rising height of the capillary wetting front in 1#, 2#, and 3# columns, the variation law of the capillary height with time could be obtained.

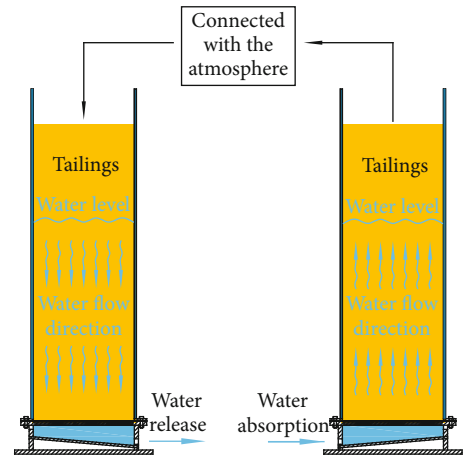

Figure 5: The schematic diagram of water absorption and release of tailings.

Figures 6(a)–6(c) show that the capillary height in the column of tail fine sand, tail silty sand, and tail silty soil is basically consistent over time, which can be divided into three stages: the early stage of rapid rise, the middle stage of slow rise, and the late stage of stability. The capillary height increases with time and stops until the rising height of capillary water reaches a stable value. Figure 6 also shows the capillary height is obviously affected by the particle size of tailings. The smaller the particle size is, the higher the capillary height is. Data of the first 11000 minutes of the capillary water with different particle size tailings are fitted, and the results are shown in Table 3.

The relationship between the rise height of capillary water with different particle sizes and time both satisfies the logarithmic function: $y = a\text{-b} * \ln(x + c)$ and the regression is significant. The fitting equation is

$$H = a\text{-b} * \ln(t + c), \tag{1}$$

where H is the height of capillary water rising, t is the corresponding time, and a, b, and c are the constant.

According to Table 3, the variation rules of constants a, b, and c in the fitting equation of capillary water rise with the particle size of tailings were obtained as shown in Figure 7. As can be seen in Figure 7, the value of constants a, b, and c gradually increased with the increase of the average particle size of the tailings. With the increase of the particle size of tailings, the value of the constant c generally decreases. According to the change rule of the rise height of capillary water over time as shown in Figures 6 and 7, the tailings corresponding to the fitting equation with a large coefficient c value can reach a large rise height of capillary water within a short time after the beginning of the test.

Figure 8 shows the time taken for the capillary water to rise to the height of 10 cm, 20 cm, 30 cm, and 40 cm in the column of tail fine sand is less than the tail silty sand and tail silty soil. However, when it rises to 50 cm, the rising rate of

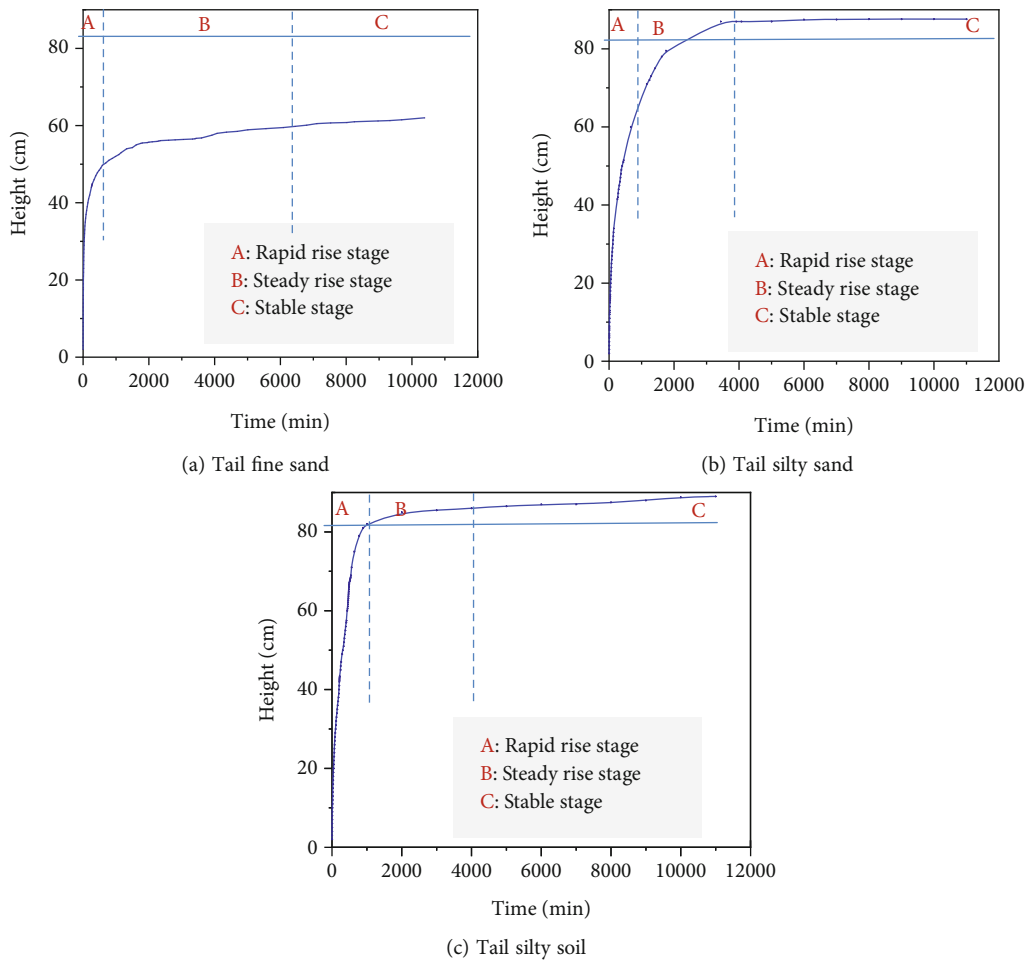

(a) Tail fine sand

(b) Tail silty sand

(c) Tail silty soil

Figure 6: The relationship between capillary height and absorption time.

Table 3: Capillary water height fitting equations for tailings with different particle size.

Grain group	The average particle size (μm)	Coefficient			Fitting equation	Regression coefficient
		a	b	c		
Tail fine sand	152.5	6.59	-6.35	0.18	$y = 6.59 + 6.35 * \ln(x + 0.18)$	0.9924
Tail silty sand	100	-21.05	-12.1	0.5	$y = -21.05 + 12.10 * \ln(x + 0.5)$	0.9352
Tail silty soil	40	-138.98	-31.85	96.93	$y = -138.98 + 31.85 * \ln(x + 96.93)$	0.9924

capillary water decreased obviously. Meanwhile, the rising rate of capillary water in the column of tail silty sand and tail silty soil exceeded that of tail fine sand. The time it takes to reach 60 cm high in tail fine sand column is 2734 minutes less than that in the tail silty sand, but 233 minutes more than it takes in the tail silty soil. It has taken only 2.3 minutes for the capillary water in the tail fine sand column to rise to 10 cm high, followed by 11.5 min in the tail silty sand, and 10 min in the tail silty soil. It can be seen in the early stage of rainstorm, the capillary action of tailings shows up within a short time, and the infiltration surface of tailings dam will rise rapidly to a certain height, which should be considered in the engineering practice.

3.2. The Influence of Particle Size on Moisture Content of Capillary Zone

3.2.1. Capillary Water Absorption Test Results. The relationship between moisture content in different sections of tail fine sand, tail silty sand, and tailing silty soil columns and time are shown in Figures 9(a)–9(c), respectively.

As can be seen from Figure 9(c), the moisture content of the capillary water in the tail silty soil changed most significantly. The reason is that the particle size is small and the matrix potential is large. According to Kelvin's equation of equation (8) [28], when capillary water is absorbed at the beginning, capillary water migrates from bottom to top due

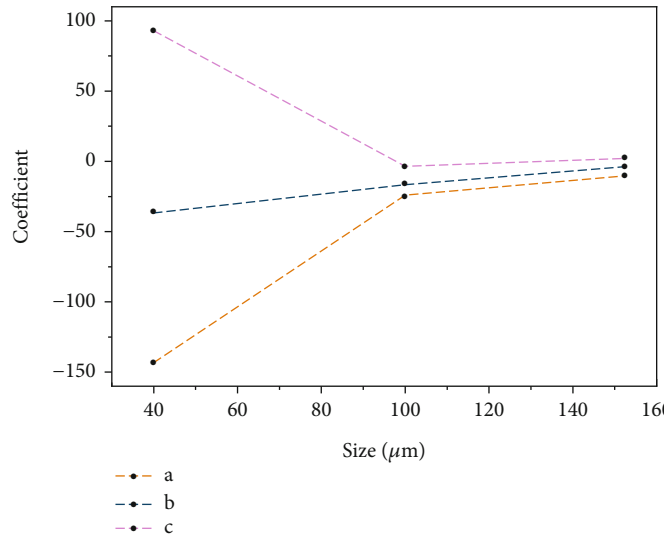

Figure 7: Relations between coefficients a, b, c and particle size.

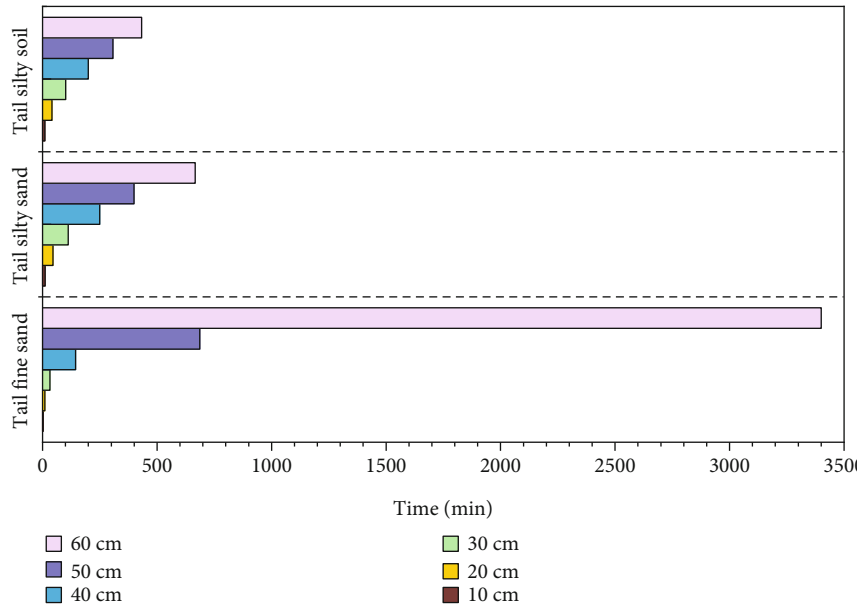

Figure 8: Comparison of capillary water height.

to the action of the matrix potential. When pore gas pressure equals pore water pressure, capillary water in tailings samples will no longer migrate.

$$(u_a\text{-}u_w) = \frac{2T_s}{R_s}, \tag{2}$$

where u_a, u_w is the pore gas pressure and pore water pressure of tailings, T_s is the surface tension on both sides of the surface, and R_s is the radius of curvature.

The relationship between the instantaneous water content and time in different sections of the three columns is similar to that of the water-soil characteristic curve, which presents "*S*." The moisture content of tail fine sand ranged from 2.51% to 20.6%, with an average value of 11.55% and a variation value of 18.09%. The moisture content of tail silty sand is 2.92%~21.05%, with an average value of 11.985% and a variation value of 18.13%. The moisture content of tail silty soil is 3.31%~23.77%, with an average value of 13.54% and a variation value of 20.46%. The sensors of M1, M4, and M7 are closest to the bottom of the cylinder, and the water content changes most significantly. The moisture content at the bottom of the tail silty soil is 23.77% at most and saturated.

Figure 10 shows the moisture content of the tailings capillary zone in the three columns decreased with the height of capillary water. The relationship between the height of capillary water and the moisture content is inverse "*S*." The smaller the particle size is, the smaller the difference of moisture content in each section after the rise of capillary water would be, indicating that the smaller the particle size of

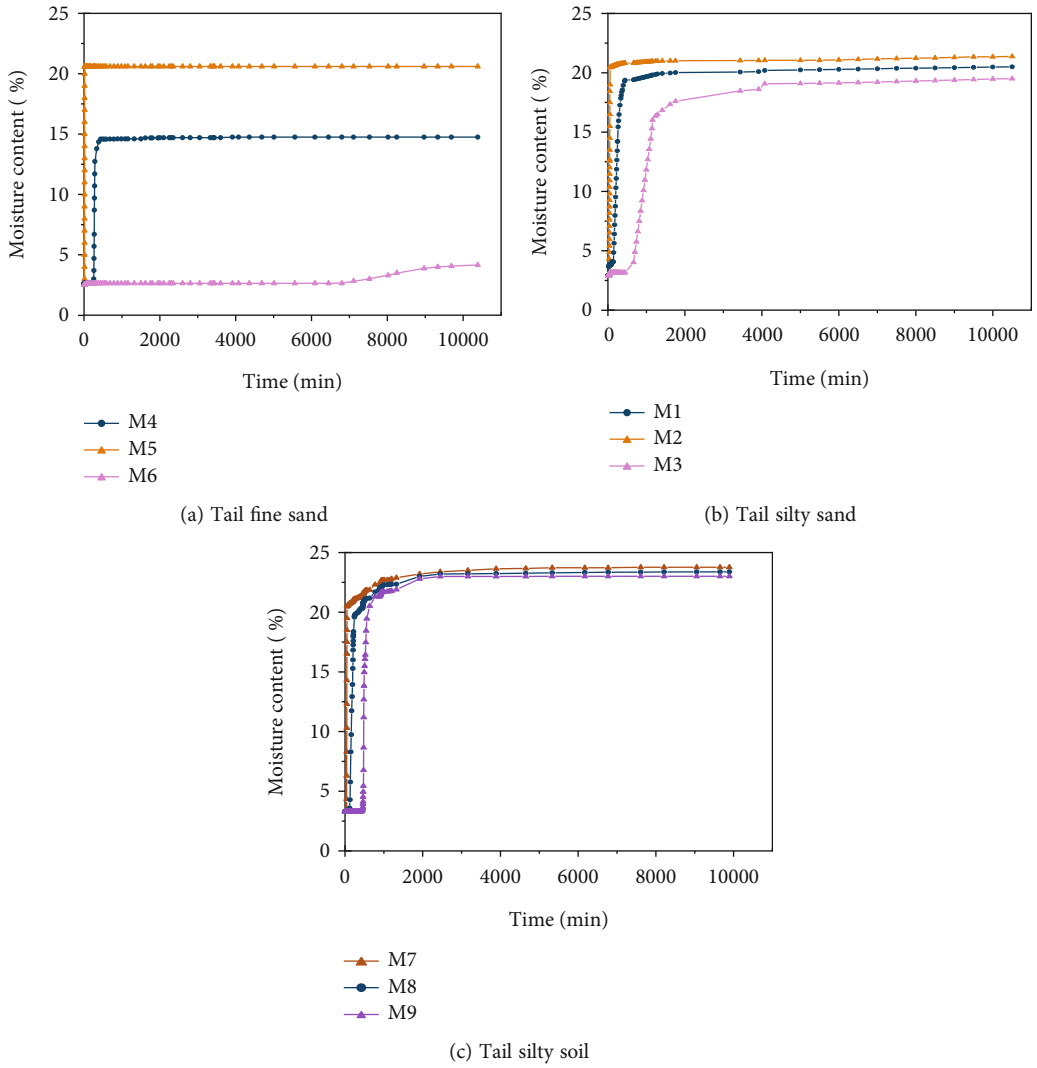

Figure 9: The relationship between moisture content and time at different sections.

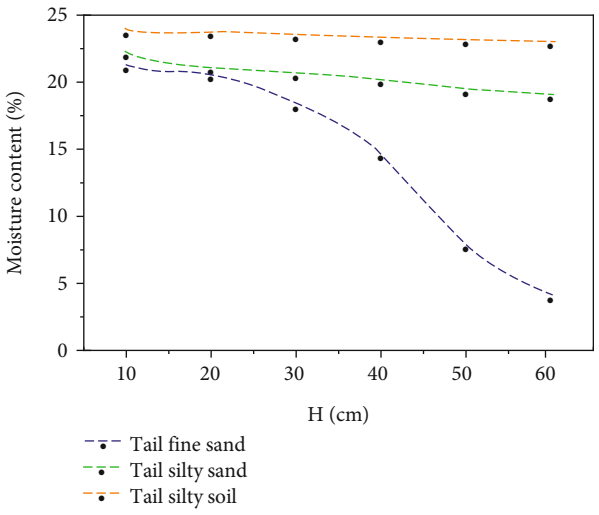

Figure 10: Relationship between moisture content and capillary height.

tailings is, the stronger the capillary water absorption capacity would be.

3.2.2. Capillary Water Release Test Results. Water release is the release by gravity of the water from the tailings that are saturated due to capillitia from the upper part of the dam as the position of the infiltration line drops. Figure 11 shows the changes of the water content in each section during the water release.

Capillary water release is an equal inverse process of capillary water absorption. However, due to hysteresis effect caused by the complex pore structure of tailings, the relationship between water content and matric suction in water absorption and water release process is not equivalent, which is also the fundamental reason why the water absorption and water release processes of tailings must be studied separately.

In the process of releasing water from tailings, the rate of releasing water affects the degree of saturation of tailings, and the degree of saturation also restricts the rate of releasing water. At the beginning of water release, tailings have a

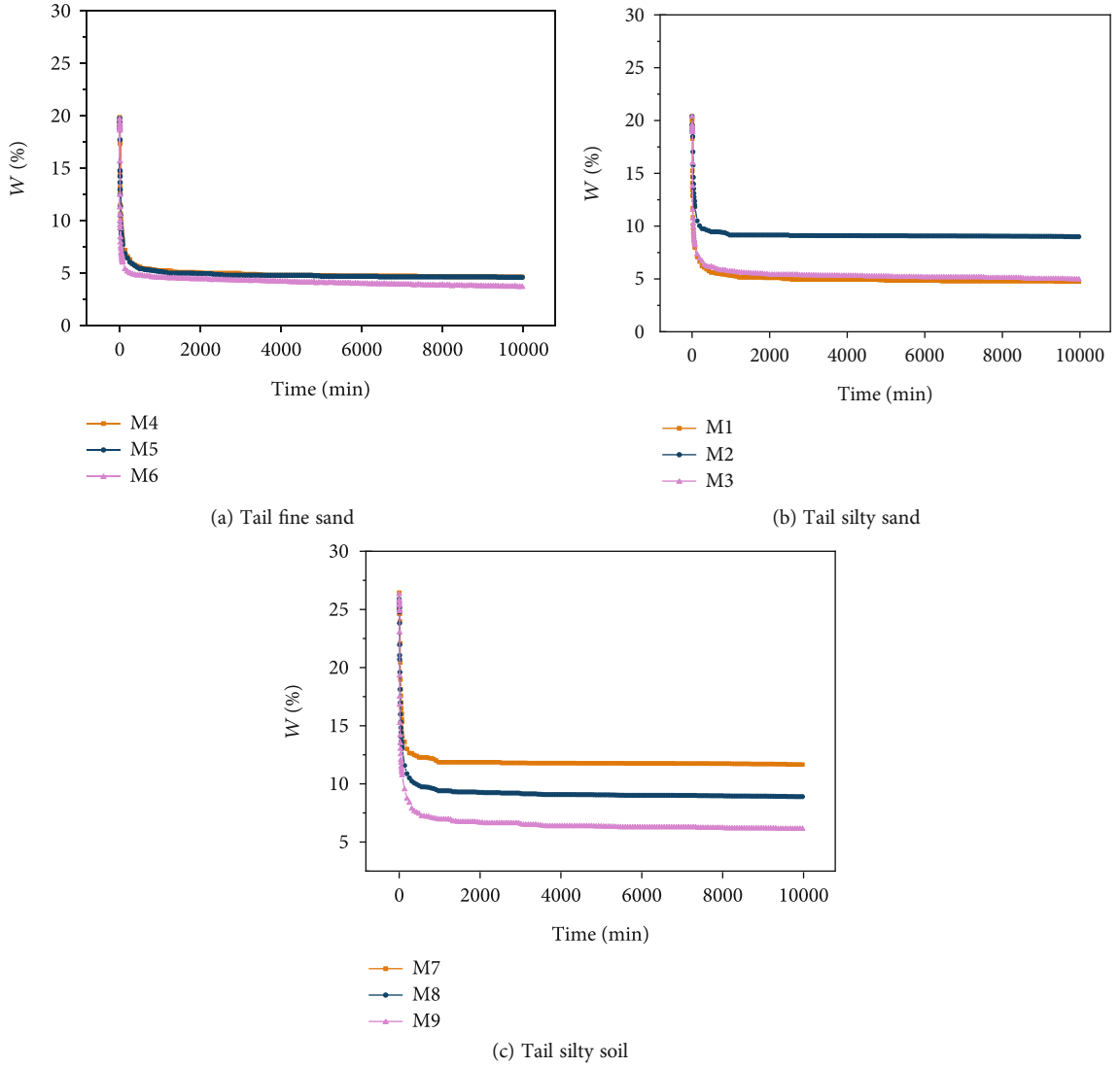

Figure 11: The moisture content change diagram of different sections in the water release process.

high degree of saturation, and free water flows down under its own gravity. Take the water release process of tailings as an example. After 400 min of continuous water release, a large amount of capillarity water and gravity water in macropores begin to release, breaking the original capillarity equilibrium state. Matric suction continues to increase. When the tailings saturation reaches the capillary critical saturation, the capillary water flowing in the pores begins to release. The release water volume increases with the time, and the tailings saturation gradually decreases.

After 1800 min of continuous water release, most of the capillary water has been released, and the rate of water release becomes slower. The reason is that the amount of water between the particles is very small, and a completely connected bending liquid level cannot be formed. When the pressure of the air on the tailings is less than the suction of the tailings on the thin film water, the saturation of the tailings has become very low, and the release of water has become very small. The permeability coefficient is mainly dependent on the state of water in the macropores. If the intake flow of macropores is interrupted, the permeability coefficient will be reduced. Meanwhile, the water in the small pores may be isolated, so the seepage cannot be carried out. Water in large pores, due to low suction, tends to be released when saturation is low, while water in small pores is the opposite. When the suction value of the tailings particles on the thin film water is less than the air pressure value, the thin film water on the surface of the tailings gradually breaks away from the suction force and is connected with each other to form a flow channel, which is released until the final water release is no longer changed. At this time, the saturation of the tailings has reached the critical saturation of the thin film and will no longer continue to reduce to a stable state.

In conclusion, the water release process is actually an unsaturated seepage process, which mainly depends on the saturation. When the water level drops, the pore channels are of different sizes, the smaller the channels, the greater the flow resistance, the smaller the hydraulic gradient, and the lower the flow rate, which also indicates that the smaller the

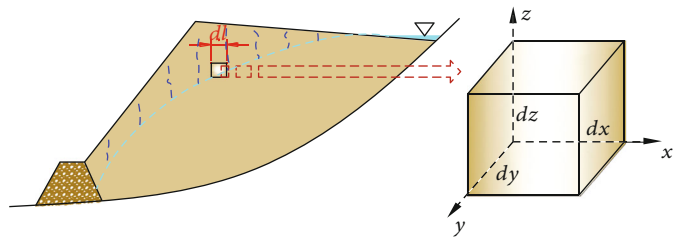

Figure 12: Tailing element model.

particle size is, the stronger the water-holding performance is. In other words, the moisture content after water release of powder tailings (as shown in Figure 11(c)) is greater than that of sand tailings (as shown in Figures 11(a) and 11(b)).

3.3. The Influence Mechanism of Particle Size on the Rise of Capillary Water in Tailings

3.3.1. Derivation of the Formula for Moisture Content Change under Capillary Action. The formula of water content per unit volume of tailings under capillary water absorption is preliminarily derived by using a microelement model (Figure 12) without considering other seepage effects. The initial volumetric water content is w_i, the water content after time t is w_t, and the change of water content in tailings after capillary action time t is

$$dQ_w = (w_t - w_i)dxdydz. \tag{3}$$

Q is moisture content. Considering the influence of capillary water pressure, the vertical capillary water velocity can be calculated as

$$q(z) = -\frac{k}{\mu}\left(\frac{ds}{dz} + \rho_w g \sin\phi\right), \tag{4}$$

where k is the permeability coefficient of unsaturated tailings, μ is the viscosity coefficient of the solution, ρ_w is the solution density, g is gravity acceleration, ϕ is the angle between capillary and horizontal direction, and s is the suction.

The buried depth of the infiltration line is h (the distance between the infiltration line and the dam slope), the maximum height of the capillary water rising is h_c, and then the integral of formula (4) is

$$\mu\int_h^{h_c}\frac{q}{k}dz = -[s + \rho_w g(h_c - h)\sin\phi]. \tag{5}$$

According to the law of conservation of mass, the velocity of capillary water can also be expressed as

$$q_t = \frac{dz}{dt}\frac{dA(h_c)}{dA(z)} = \frac{dz}{dt}. \tag{6}$$

Substituting formula (6) into formula (5),

$$\frac{\mu}{k(z)}(h_c - h)\frac{dz}{dt} = -[s + \rho_w g(h_c - h)\sin\phi]. \tag{7}$$

Assume $k(z)$ is constant, $\phi = 90°$; after interval integration formula (7) in $[h_c, z]$, the relationship between the time t and the corresponding capillary rise height $z(h < z < h_c)$ can be written as

$$t = \frac{\mu(h_c - h)(h_c - z)}{[P + \rho_w g(h_c - h)]k}, \tag{8}$$

where t is the time required for capillary water to reach height z.

$$Q_{w1} = \iiint(w_t - w_i)dxdydz = w_t - w_i = \Delta\omega, \tag{9}$$

where w_t is the moisture content in tailings after time t and w_i is the initial moisture content.

According to equations (4) and (8), the capillarity moisture content per unit volume after time t is

$$Q_{w2} = qt \times 1 = -\frac{(h_c - h)(h_c - z)}{s + \rho_w g(h_c - h)}\left[\frac{ds}{dz} + \rho_w g\right]. \tag{10}$$

From $Q_{w1} = Q_{w2}$, the change in moisture content $\Delta\omega$ can be calculated as

$$\Delta w = -\frac{(h_c - h)(h_c - z)}{s + \rho_w g(h_c - h)}\left[\frac{ds}{dz} + \rho_w g\right], \tag{11}$$

$$\text{or} w_t = -\frac{(h_c - h)(h_c - z)}{H + h_c - h}\left[\frac{dH}{dz} + 1\right] + w_i, \tag{12}$$

where q is the vertical capillary velocity, H is the suction head elevation, h is the distance between subgrade surface and groundwater level, h_c is the maximum rising height of capillary, P is the suction in unsaturated soil, ρ_w is the capillary water density, g is the acceleration of gravity, and s is the suction force.

The change of tailing moisture content caused by capillarity is related to the maximum rise height h_c of capillary water and the elevation of capillary suction head. Both h_c and H are directly related to the particle size of tailings (capillary diameter d in tailings) and the properties

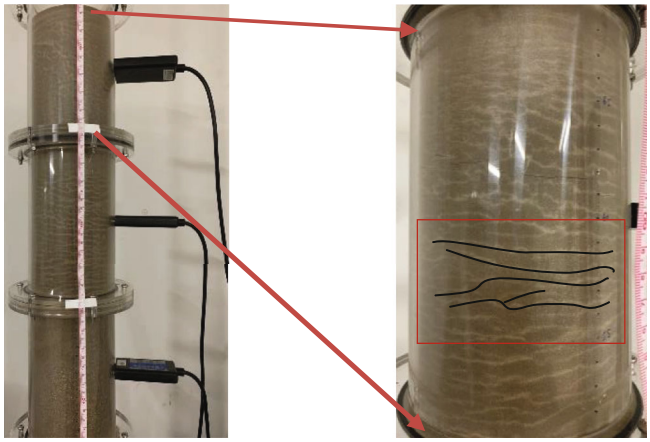

Figure 13: Discontinuous capillary band.

of tailings. Therefore, moisture content is a function of particle size of tailings.

3.3.2. Formation of Discontinuous Capillary Bands. The capillary water in the tailings is in a dynamic flow equilibrium state, and the capillary water is affected by the comprehensive action of capillary force, inertia force, viscous resistance, and its own gravity. In the early stage of capillary water rising, the surface tension is much greater than the gravity of the rising water column, so the rising speed is faster. However, as the capillary water column increases, its gravity gradually increases and approaches the surface tension, resulting in a gradual slowing of the rising velocity. Through the analysis of the ascent, in the initial stage of capillary water rising, the capillary water is less watery; the parameters related to the amount of liquid, such as viscous resistance and gravity of capillary water, are also relatively small; at this time, the capillary pressure and inertia force play a dominant role, which is enough to balance the gravity of the capillary water. Therefore, the early uplift force is very large. In addition, discontinuous capillary bands appeared on the upper part of the soil column, presenting a corrugated bedding structure (as see in Figure 13). This is due to the insufficient water supply caused by the rapid rise of capillary water in the initial stage of the rising. At this time, the tailings near the saturation line are close to the saturation state, and the larger water content produces a larger capillary uplift resistance, which reduces the capillary uplift force significantly, so the rise velocity decreases significantly. As the rising height of capillary water increases, the viscous resistance and gravity have balanced a large part of the capillary lifting force, and the content of capillary water in the tailing sand becomes very small, and the subtracting effect also becomes weak. Therefore, the late rising speed is slow and persistent. Synthetically analyzing the whole process of capillary rise, the dynamic of capillary rise showed an obvious decreasing trend.

4. Conclusions

The whole process of capillary water rising test was carried out for tailings with three particle sizes by using OM-CRT system. The conclusions are as follows:

(1) The rising trend of capillary water in tailings with different particle sizes is basically consistent. The process of the capillary water rising is obvious in three stages, which shows the characteristics of rising rapidly first, then slowly and stably lately. The height and rate of capillary rise are negatively correlated with the particle size of tailings. Logarithm function can fit the relationship between time and the height of capillary water rising in tailings and time very well: $H = a\text{-}b * \ln(t + c)$

(2) The inner moisture content of the tailings dam is always changing. The change of moisture content is a function of the particle size of tailings. The moisture content of the capillary zone of tailings with different particle size decreases with the increase of height and presents an "S" shape. The instantaneous moisture content of different sections showed an inverse "S" shape with the change of time. The smaller the particle size is, the smaller the moisture content difference of each section after the rise of capillary water is

(3) The process of releasing water with decreasing saturation of tailings is an unsaturated seepage process in the form of natural drainage. When the particle size of tailings is larger, the flow resistance of slurry water is smaller, and the moisture content after water release is smaller. In other words, the water content of sand tailings is greater than that of powder tailings

(4) A physical model for determining the capillary diameter from the inter-particle pore approximation is constructed by this paper. From the limit point of close packing and loose packing, the relationship between capillary diameter and particle size is derived, the relationship between tailing particle size and capillary water rise height is determined as well. The maximum rise height of capillary water and the change value of water content can be determined according to the particle size, which overcomes the difficulty in measuring them

Data Availability

No data were used to support this study.

Conflicts of Interest

The authors declare that there is no conflict of interest regarding the publication of this paper.

Acknowledgments

This work was financially supported by the National Natural Science Foundation of China (Nos. 51774228 and 51904220).

References

[1] C. Qi and A. Fourie, "Cemented paste backfill for mineral tailings management: review and future perspectives," *Minerals Engineering*, vol. 144, article 106025, 2019.

[2] C. C. Qi, "Big data management in the mining industry," *International Journal of Minerals, Metallurgy and Materials*, vol. 27, no. 2, pp. 131–139, 2020.

[3] D. Liu, M. J. Lian, C. W. Lu, and W. Zhang, "Effect of the lenticles on moisture migration in capillary zone of tailings dam," *International Journal of Minerals, Metallurgy and Materials*, vol. 27, no. 8, pp. 1036–1045, 2020.

[4] M. Fattah, H. Omran, and M. Hassan, "Flow and stability of alwand earth dam during rapid drawdown of water in reservoir," *Acta Montanistica Slovaca*, vol. 22, pp. 43–57, 2017.

[5] C. Yang, Y. Wang, L. Wang, J. Huang, Q. Li, and L. Wu, "The slotted tube overlay geotextile in tailing pond radial seepage test model and analysis of the permeation characteristics," *Geofluids*, vol. 2021, 11 pages, 2021.

[6] X. Chen, X. Shi, J. Zhou, X. Du, Q. Chen, and X. Qiu, "Effect of overflow tailings properties on cemented paste backfill," *Journal of Environmental Management*, vol. 235, pp. 133–144, 2019.

[7] Y. Zhao, A. Soltani, A. Taheri, M. Karakus, and A. Deng, "Application of slag–cement and fly ash for strength development in cemented paste backfills," *Minerals*, vol. 9, pp. 1–19, 2019.

[8] T. S. Nemer, "The Bisri dam project: a dam on the seismogenic Roum fault, Lebanon," *Engineering Geology*, vol. 261, article 105270, 2019.

[9] Y. Wang, J. Chai, J. Cao, Y. Qin, and X. Zhang, "Effects of seepage on a three-layered slope and its stability analysis under rainfall conditions," *Natural Hazards*, vol. 102, no. 3, pp. 1269–1278, 2020.

[10] C. Zhang, J. Chai, J. Cao, Z. Xu, Y. Qin, and Z. Lv, "Numerical simulation of seepage and stability of tailings dams: a case study in Lixi, China," *Water*, vol. 12, no. 3, p. 742, 2020.

[11] D. Zhou, Z. Zhang, J. Li, and X. Wang, "Seepage-stress coupled modeling for rainfall induced loess landslide," *Theoretical & Applied Mechanics Letters*, vol. 9, no. 1, pp. 7–13, 2019.

[12] H. Hu and X. Zhang, "Failure mode analysis of cemented sand and gravel material dam," *Science of Advanced Materials*, vol. 10, no. 9, pp. 1286–1295, 2018.

[13] X. Y. Kong and G. J. Wang, "Experiment research on the reinforced triaxial compression of tailings material and infiltration rainfall of tailings dam," *Journal of Computational and Theoretical Nanoscience*, vol. 13, no. 9, pp. 6419–6423, 2016.

[14] M. Fattah, M. Ahmed, and N. Ali, "Effect of hydraulic conductivity of unsaturated soil on the earth dam performance," *Matec Web of Conferences*, vol. 162, article 01008, 2018.

[15] M. T. Zandarín, L. A. Oldecop, R. Rodríguez, and F. Zabala, "The role of capillary water in the stability of tailing dams," *Engineering Geology*, vol. 105, no. 1-2, pp. 108–118, 2009.

[16] A. Zhou, R. Huang, and D. Sheng, "Capillary water retention curve and shear strength of unsaturated soils," *Canadian Geotechnical Journal*, vol. 53, no. 6, pp. 974–987, 2016.

[17] "Soil biogeochemistry of the capillary fringe in laboratory mesocosms with contrasting soil textures," *Soil Science Society of America Journal*, vol. 84, no. 3, pp. 1011–1021, 2020.

[18] J. H. Zhang, F. Li, L. Zeng, J. L. Zheng, Y. Q. Zhang, and Y. Q. Zhang, "Effect of cushion and cover on moisture distribution in clay embankments in southern China," *Journal of Central South University*, vol. 27, no. 7, pp. 1893–1906, 2020.

[19] M. Fattah and A. Al-Lami, "Behavior and characteristics of compacted expansive unsaturated bentonite-sand mixture," *Journal of Rock Mechanics and Geotechnical Engineering*, vol. 8, no. 5, pp. 629–639, 2016.

[20] L. T. Zhan, G. Y. Li, W. G. Jiao, J. W. Lan, Y. M. Chen, and W. Shi, "Performance of a compacted loess/gravel cover as a capillary barrier and landfill gas emissions controller in Northwest China," *The Science of the Total Environment*, vol. 718, pp. 137195–137195, 2020.

[21] G. Yin, Q. Zhang, Z. Wei, W. Wang, and W. Geng, "Experimental study of migration characteristics of pore water and its effect meso-structure of tailings," *Chinese Journal of Rock Mechanics & Engineering*, vol. 31, pp. 71–79, 2012.

[22] X. Z. Liu, Z. J. Zhang, L. I. Ya-Jun, and W. X. Pan, "Study on a method of determining the coefficient C of capillary in tailings sand of a certain tailings dam," *Journal of University of South China(Science and Technology)*, vol. 27, pp. 23–26, 2013.

[23] Z. J. Zhang, Y. J. Li, X. Z. Liu, W. X. Pan, and Y. Liu, "Rising law of capillary water in tailings dam of metal mine," *Chinese Journal of Nonferrous Metals*, vol. 24, pp. 1345–1351, 2014.

[24] Q. C. Zhang, Y. K. Tian, Z. J. Zhang, Y. J. Li, and Y. Liu, "Influence of temperature and air pressure on rising law of capillary water in tailings dam of metal mine," *Chinese Journal of Nonferrous Metals*, vol. 27, pp. 1016–1022, 2017.

[25] S. Tian, X. Dai, G. Wang, Y. Lu, and J. Chen, "Formation and evolution characteristics of dam breach and tailings flow from dam failure: an experimental study," *Natural Hazards*, vol. 107, no. 2, pp. 1621–1638, 2021.

[26] T. Streck and T. Weber, "Analytical expressions for noncapillary soil water retention based on popular capillary retention models," *Vadose Zone Journal*, vol. 19, no. 1, article e20042, 2020.

[27] S. F. Nia and K. Jessen, "Theoretical analysis of capillary rise in porous media," *Transport in Porous Media*, vol. 110, pp. 141–155, 2015.

[28] J. Liu, S. J. Xiao, J. Zhang, Y. Y. Zhang, and Y. Y. Tian, "Discussion on derivation of kelvin equation," *University Chemistry*, vol. 31, no. 3, pp. 68–72, 2016.

Hindawi
Geofluids
Volume 2022, Article ID 7382233, 19 pages
https://doi.org/10.1155/2022/7382233

Research Article

Applied Research of Water Jet Technology in Preventing Rock Burst Occurred in Roadways

Zeng-qiang Yang,[1,2,3] **Cang-yan Xiao**,[1] **Chang-hao Li**,[4] **and Chang-le Ren**[1]

[1]*School of Transportation Engineering, Jiangsu Vocational Institute of Architectural Technology, Xuzhou, Jiangsu 221116, China*
[2]*Xuzhou Coal Mining Group Corp., Ltd., Xuzhou 221111, Jiangsu, China*
[3]*China University of Mining & Technology, State Key Laboratory of Coal Resources and Mine Safety, Xuzhou, Jiangsu 221116, China*
[4]*Yuwu Mining Co.Ltd., Lu'an Group, Changzhi 046103, China*

Correspondence should be addressed to Cang-yan Xiao; 10859@jsjzi.edu.cn

Received 28 November 2021; Accepted 24 March 2022; Published 4 May 2022

Academic Editor: Gangwei Fan

Taking mining area 2502 in the Huayan mine field which was affected by strong geological tectonic stress as an engineering background, the water jet technology is studied through in-site survey, laboratory test, theoretical analysis, numerical simulation, and field industrial test. The research results are as follows: the burst tendency of No. 5 coal seam can be reduced to a certain extent after softening with water, and then the water jet technology is used to prevent rock burst of roadways; the typical characteristics of rock-burst accidents mainly cause heaving floor and serious deformation of two sides. The occurrence mechanism of rock burst in roadway ribs has two different forms, and they are static load dominant type and dynamic load dominant type. The abutment stress concentration value is higher than a certain concentration static load, it will affect the coal and rock medium in the floor, and the coal and rock medium in the floor will be transformed into a plastic state and then occur rock burst; the water jet technology for roadway ribs can effectively prevent rock burst of roadway ribs and floor based on the dynamic and static loads superposition theory and Terzaghi theory. Based on the results of numerical simulation, the specific parameters of water jet technology for roadway ribs in 250204 tailgate are as follows: the diameter and length of initial borehole are 110 mm and 20.0 m, the diameter and length of water jet section are 500 mm and 15.0 m, and the spacing between adjacent water jet boreholes is 3.0 m; the monitoring result of signal intensity by EMR indicates that the decreasing amplitude of signal intensity of EMR is about 60.2% on the side of coal-pillar rib, and the decreasing amplitude of signal intensity of EMR is about 68.6% on the side of solid-coal rib; the convergences monitoring result indicates that the convergence ratio of roadway height is about 3.2%, and the convergence ratio of roadway width is about 2.3% in the pressure relief roadway part; the water jet technology is not only helpful to the prevention of rock burst for the roadway ribs but also can play a good prevention of rock burst for roadway floor. The research results provide a theoretical foundation and a new guidance for preventing rock burst in roadway ribs and floor with similar engineering geological conditions.

1. Introduction

During the underground mining and driving activities, the surrounding rock around mining or driving space is easy to cause rock burst under the superposition disturbance of high concentrated static load and strong dynamic load [1–4]. Therefore, it is necessary to take pressure relief and prevention measures for the coal and rock mass around the mining or driving space.

In recent years, due to the popularization of fully mechanized mining hydraulic support and the improvement of mining face support strength, most of the underground

damage caused by rock burst occurs in the roadways. Statistics show that 75% of rock burst accidents occurs in two parallel roadways of the mining face. Therefore, the research on rock burst prevention of roadways under strong mine pressure condition is one of the main contents. There have been a lot of pressure relief measures for coal mass, such as pressure relief measures for large diameter drilling, pressure relief measures of coal seam water injection, and pressure relief measures for deep hole blasting [5, 6]. These conventional measures can relieve the pressure of coal and rock mass to a certain extent and then play a preventive effect of rock burst. In recent years, the water jet technology has also been applied to the coal mine rock burst prevention work. Because the burst tendency of coal and rock mass can be reduced in saturated water state (softening state), the water jet technology is used to relieve high pressure of surrounding rock and then prevent rock burst. The water jet technology has been used in underground mines for many years, and this technology has no spark, no dust, and no wear characteristics compared to traditional mechanical operation [7, 8].

Many scholars have studied the application of water jet technology in underground mining field. Shen et al. [9] analyzed the pressure relief mechanism of coal seam after special drill slots were formed in coal mass and showed that the special drill slots in coal mass could significantly improve permeability of coal seam and pressure relief degree and then effectively prevented coal and gas outburst. Shen [10] studied the coal mass breaking mechanism and indicated that the coal mass breaking includes three processes: crack generation, water wedge action, and surface scouring. The Fluent software is used to analyze the water jet force, water jet target distance, and punching radius, and the simulated results were applied to the prevention of gas outburst. Dou et al. [11, 12] studied the punching method of water jet technology in preventing rock burst and the specific construction parameters by Flac2D software, and the feasibility of this technology in preventing rock burst was verified by field industrial test. Yang et al. [13] studied the occurrence mechanism of rock burst in surrounding rock of roadways and indicated that using water jet to punch an initial borehole could form a water jet section (weak structure zone) inside the roadway ribs. This weak structure zone can transfer and release the high concentrated static load accumulated inside the roadway ribs and then prevent rock burst in roadway ribs.

It can be seen that many scholars have applied the water jet technology in the field of preventing rock burst; however, there is little research on whether this technology can satisfy the pressure relief effect in the area affected by strong geological structure. This paper takes mining area 2502 in the Huayan mine field which was affected by strong geological tectonic stress as an engineering background, and the application of water jet technology in roadway ribs is studied. The purpose is to verify the prevention of rock burst and pressure relief effect of water jet technology for roadway ribs and floor and then provide a theoretical foundation and a new guidance for preventing rock burst in roadway ribs and floor with similar engineering geological conditions.

2. General Situation of Geology

2.1. Mining and Engineering Geological Conditions. Huayan mine field, which is almost entirely located in the north of Huating County, Gansu Province, was affected by strong geological tectonic stress. Under the influence of this stress, the activities in this region have reached a climax, and the structural form of the fault fold belt on the western margin has been basically shaped after the Yanshan movement. As a result, the horizontal stress is much greater than the vertical stress in this mine field. A syncline axis and an anticline axis pass through the whole Huayan mine field under the influence of large folding structure. The main mining No. 5 coal seam is also affected by the large folding structure during its mining period. The geological structure plan of Huayan mine field is shown in Figure 1.

The Huayan mine field was officially divided into Huating, Yanbei, Shanzhai, and Chenjiagou coal mines for independent mining with the approval of the Ministry of land and resources in 2006. According to the geological exploration data of Huayan mine field, the relative position and mine field size of the whole Huayan mine field are shown in Figure 2. The main mining coal seam of Huating, Yanbei, Shanzhai, and Chenjiagou coal mines is the No. 5 coal seam, which is nearly horizontal. The strike angle of this coal seam is about 330°~345°, inclined to the west. The dip angle of this coal seam is about 0°~15°, and the mean thickness of this coal seam is 40.6 m. The No. 5 coal seam is an extra thick coal seam. The coal quality belongs to long flame coal with ultralow ash, ultralow sulfur, low-medium phosphorus, high volatile matter, medium and high calorific value, high chemical activity, and low melting point. It is easy to sort and excellent. All coal mines are equipped with domestic advanced fully mechanized top coal caving high-yield and high-efficiency equipment for layered fully mechanized top coal caving mining.

Among these coal mines in Huayan mine field, Yanbei coal mine is located in the middle of the Huayan mine field. It is adjacent to Shanzhai coal mine in the north, Huating coal mine in the south, Chenjiagou coal mine in the west, and local small coal mines in the east. At present, the main mining area in Yanbei coal mine is mining area 2502, which is about in the +860 m~+1171 m level elevation, and its corresponding ground level elevation is about in the +1557 m~+1580 m. The folding structure is developed in this mining area, with anticline axis in the east and syncline axis in the west. All the mining and driving faces are currently being mined or have been mined out cross a syncline structure, which lead to rock-burst accidents, and strong underground pressure appears continuously. There are no faults and other geological structures in this mining area. The thickness of No. 5 coal seam in mining area 2502 is 18.2 m~54.5 m, with a mean thickness of 31.0 m. The layered fully mechanized top coal caving mining technology is adopted in panels of mining area 2502. At present, the first layer (upper layer) is being mined, with a thickness of 9.5 m~15.4 m and a mean thickness of 12.0 m. The mining height of panels in mining area 2502 is 3.0 m, with a top coal caving height of 9.0 m, and the ratio between mining and caving is about 1 : 3. The

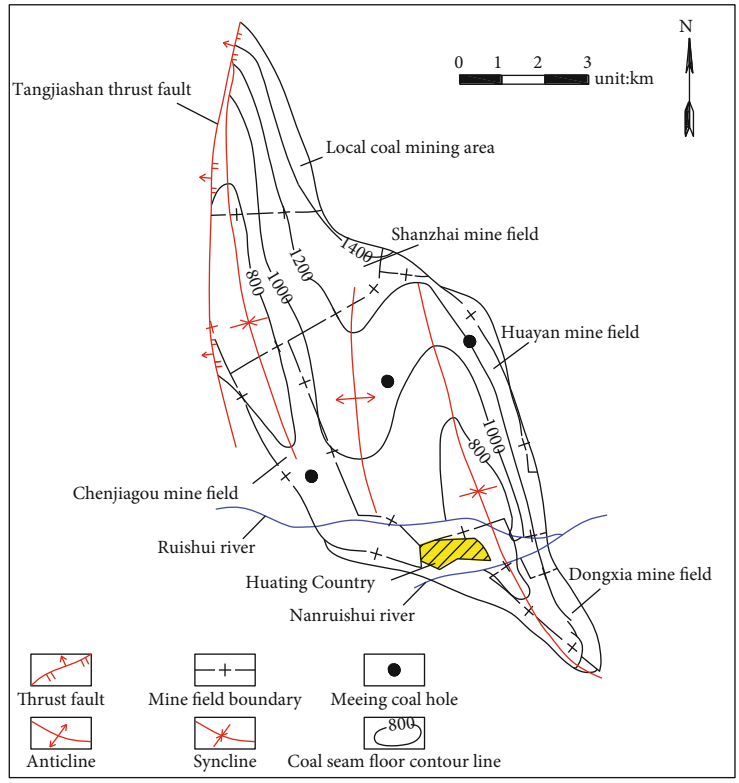

Figure 1: Geological structure plan of Huayan mine field.

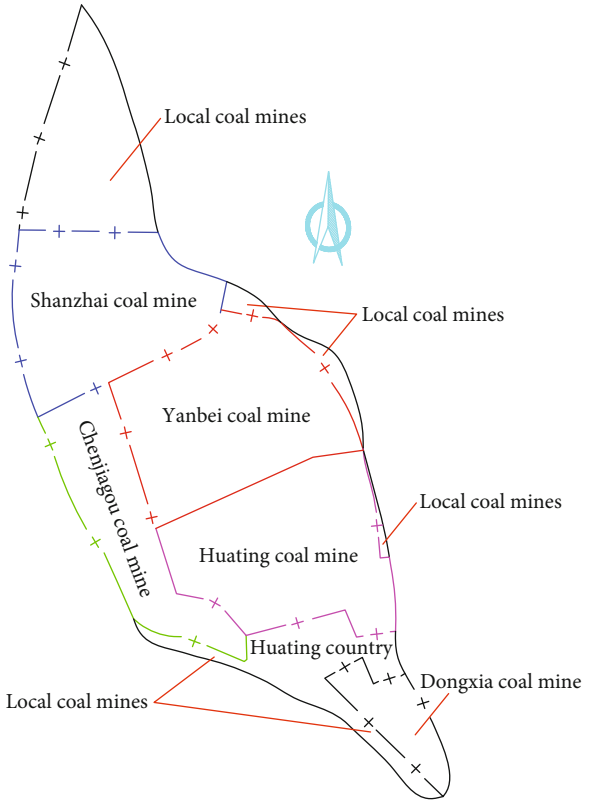

Figure 2: The relative position and mine field size of the whole Huayan mine field.

first panel in the mining area 2502 is the panel 250205, and it has been mined out currently. The panel 250206 that can be seen as a succeeding panel of the panel 250205 is now being mined, and it is the second panel in the mining area 2502. The panel 250204 that can be seen as a succeeding of the panel 250206 is now being driven, and it is the third panel in the mining area 2502. The plan of mining and driving engineering in the mining area 2502 is shown in Figure 3.

2.2. Burst Tendency Test Result of No. 5 Coal Seam

2.2.1. The Burst Tendency Test Indexes. According to China's national standard (GB/T 25217.2-2010) of coal burst tendency classification and index determination method [14, 15], coal samples that are taken from the No. 5 coal seam in the mining area 2502 and then the standard specimens (the specific size of each cylinder:50 mm × 100 mm) were processed, and the mechanical properties are tested in a laboratory with corresponding qualifications. The coal-burst tendency judgment standard is shown in Table 1.

INLINE FX

According to Table 1, when the burst tendency test indexes of D_T, W_{ET}, $K_{E,}$ and R_C are contradictory, the number of test standard specimens should be increased, and their classification can be carried out by fuzzy comprehensive evaluation method or probability statistics method.

2.2.2. The Test Methods. The coal burst tendency in natural state and saturated water state (softening state) should be measured, respectively, that is, one loading test and cyclic

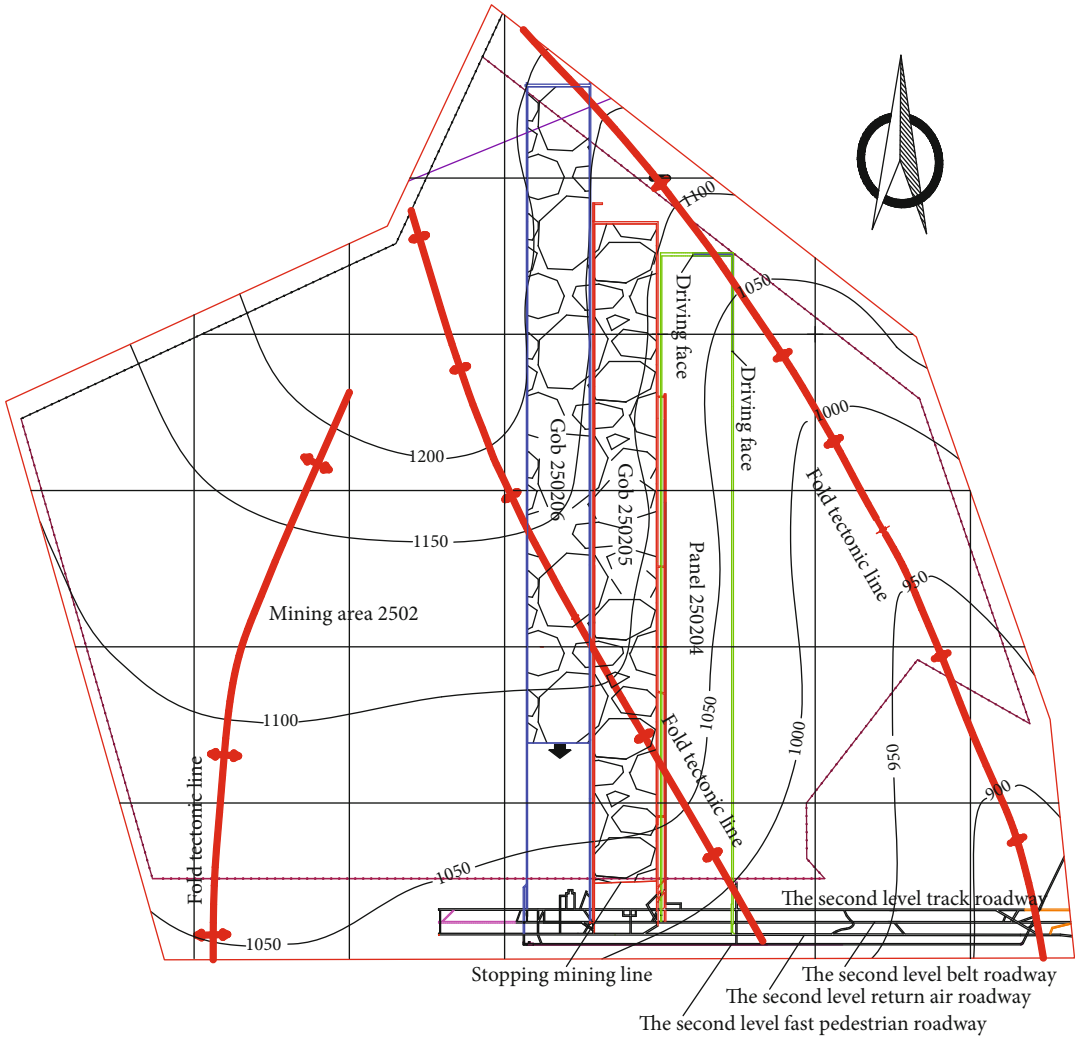

Figure 3: The plan of mining and driving engineering in mining area 2502.

Table 1: The coal-burst tendency judgment standard.

Name		Burst tendency test indexes			
		D_T/ms	W_{ET}	K_E	R_C/MPa
Computing model		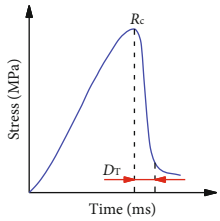	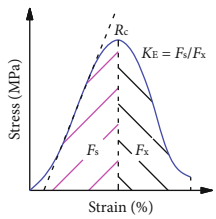	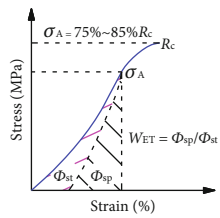	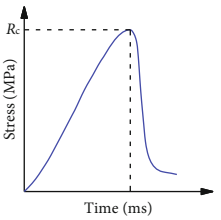
Burst tendency judgment standard	No burst tendency	$D_T > 500$	$W_{ET} < 2.0$	$K_E < 1.5$	$R_C < 7.0$
	Weak burst tendency	$50 < D_T \leq 500$	$5.0 > W_{ET} \geq 2.0$	$5.0 > K_E \geq 1.5$	$7.0 \leq R_C < 14.0$
	Strong burst tendency	$D_T < 50$	$W_{ET} \geq 5.0$	$K_E \geq 5.0$	$R_C \geq 14.0$

Note: D_T is the dynamic failure time; W_{ET} is the elastic energy index; K_E is the burst energy index; R_C is the uniaxial compressive strength.

loading test should be conducted for 6 times, respectively, so a total of 12 coal standard specimens need to be processed. 14 coal standard specimens are processed in this test, two of which are for standby. The coal samples are taken from different locations in the mining area 2502, and then, they are processed into coal standard specimens with cylindrical

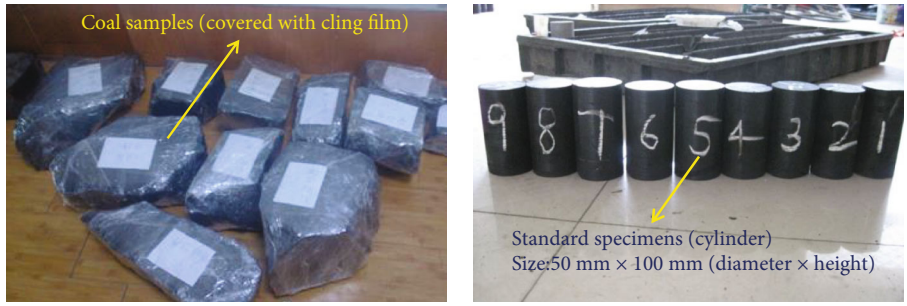

(a) (b)

Figure 4: The picture of coal samples before and after processing. (a) Before processing. (b) After processing.

size of 50 mm × 100 mm (diameter × height). The picture of coal samples before and after processing is shown in Figure 4.

In this test, the coal burst tendency in natural state and saturated water state (softening state) needs to be measured, respectively. Therefore, 7 coal standard specimens are completely immersed in clean water for more than 48 hours in advance (fully ensure that coal standard specimens are saturated with water), and the other 7 coal standard specimens are wrapped in sealed bags and stored in dry state. The experimental loading device adopts SANS material testing machine produced by Shenzhen xinsansi material testing Co., Ltd., which is high-precision and can control the loading speed, and is used to measure the coal standard specimen loading and the whole process curve of stress strain. This experimental machine can set the loading mode manually, and the loading process is directly controlled by the computer. The experimental machine (SANS material testing machine) is shown in Figure 5.

In order to get burst tendency test indexes of D_T, W_{ET}, K_E, and R_C, the corresponding test methods are as follows [16]:

(a) Dynamic failure time (D_T): measuring the load borne by the coal standard specimens with the load sensor until these specimens are damaged. The measured signals are transmitted to the computer data acquisition and processing system through the dynamic resistance strain gauge. According to the measured data, the system directly draws the corresponding dynamic failure time curve, enlarges the key part of the maximum failure load in this curve, and accurately gives the dynamic failure time (D_T) value

(b) Elastic energy index (W_{ET}): the cyclic loading method is adopted to load the coal standard specimens to about 75%~85% of the load limit, then unload to a small load, and then continue to load until these specimens are completely damaged. The load borne by these specimens is measured by the load sensor, and the axial deformation of these specimens is measured by the displacement sensor. The measured signals are recorded and stored by the computer data acquisition system, and after data processing, the calculation diagram of elastic energy index is drawn to calculate the elastic energy index (W_{ET}) value

(c) Burst energy index (K_E): under uniaxial compression, the coal standard specimens are directly loaded at one time until they are completely destroyed. The load borne by these specimens is measured by the load sensor, and the axial deformation of these specimens is measured by the displacement sensor. The measured signals are recorded and stored by the computer data acquisition system, and the calculation diagram of burst energy index is drawn after data processing to calculate the burst energy index (K_E) value

(d) Uniaxial compressive strength (R_C): the uniaxial compressive strength of coal standard specimens is directly recorded by the signal recorder during the loading process of the press, and the uniaxial compressive strength (R_C) value is calculated according to the maximum pressure and the parameters of the corresponding coal standard specimen

2.2.3. The Test Results. The dynamic failure time (D_T) parameters of coal standard specimens in natural state and saturated water state (softening state) obtained by the test are shown in Table 2.

The elastic energy index (W_{ET}) parameters of coal standard specimens in natural state and saturated water state (softening state) obtained by the test are shown in Table 3.

The burst energy index (K_E) parameters of coal standard specimens in natural state and saturated water state (softening state) obtained by the test are shown in Table 4.

The uniaxial compressive strength (R_C) parameters of coal standard specimens in natural state and saturated water state (softening state) obtained by the test are shown in Table 5.

Combined with Tables 2, 3, 4, and 5, the burst tendency test result of the No. 5 coal seam is determined, as shown in Table 6.

It can be seen from Table 6 that the No. 5 coal seam has a strong burst tendency in natural state, and it has a weak burst tendency in saturated water state (softening state). This shows that the burst tendency of the No. 5 coal seam can be reduced to a certain extent after softening with water.

2.3. Typical Characteristics of Rock-Burst Accidents. According to the monitoring records of rock-burst accidents of

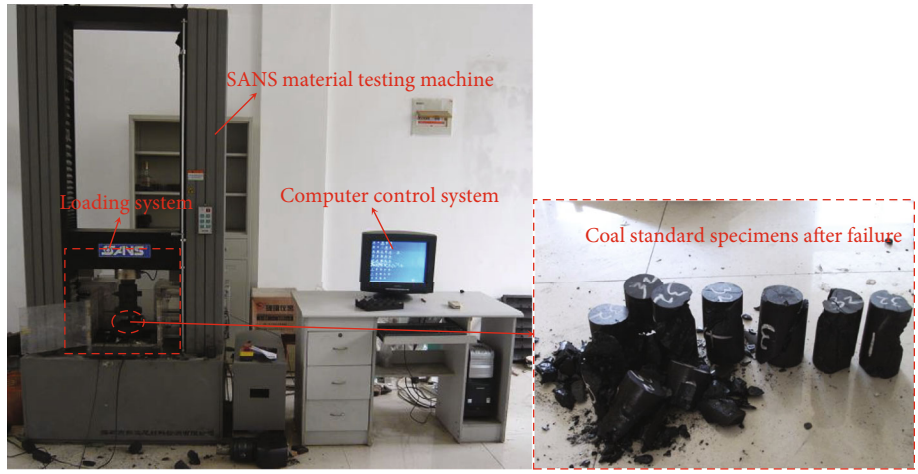

Figure 5: The SANS material testing machine.

Table 2: The parameters of dynamic failure time (D_T) under different states.

State	Number	Height/mm	Diameter/mm	Cross s section area/mm^2	Dynamic failure time/ms	Mean dynamic failure time/ms
Natural state	NS1	100	50	1962.5	141	206
	NS2	101	50	1962.5	250	
	NS3	100	50	1962.5	203	
Saturated water state	SWS1	99	50	1962.5	425	473
	SWS2	99	50	1962.5	568	
	SWS3	100	50	1962.5	427	

Table 3: The parameters of elastic energy index (W_{ET}) under different states.

State	Number	Height/mm	Diameter/mm	Cross s section area/mm^2	Elastic energy index	Mean elastic energy index
Natural state	NS4	102	50	1962.5	10.4	9.4
	NS5	100	50	1962.5	8.7	
	NS6	96	50	1962.5	9.0	
Saturated water state	SWS4	97	50	1962.5	3.2	3.7
	SWS5	99	50	1962.5	4.5	
	SWS6	99	50	1962.5	3.4	

Table 4: The parameters of burst energy index (K_E) under different states.

State	Number	Height/mm	Diameter/mm	Cross s section area/mm^2	Burst energy index	Mean burst energy index
Natural state	NS7	100	50	1962.5	4.7	5.4
	NS8	100	50	1962.5	5.1	
	NS9	96	50	1962.5	6.3	
Saturated water state	SWS7	102	50	1962.5	2.5	2.1
	SWS8	101	50	1962.5	1.4	
	SWS9	98	50	1962.5	2.5	

panels 250205 and 250206 in the mining area 2502 during their mining periods, the typical characteristics of mine pressure behaviors can be counted as shown in Table 7.

According to Table 7, it can be seen from these monitoring records of panels 250205 and 250206 (1#~7# monitoring records belong to the panel 250205 and 8#~16# monitoring

Table 5: The parameters of uniaxial compressive strength (R_C) under different states.

State	Number	Height/mm	Diameter/mm	Cross s section area/mm^2	Uniaxial compressive strength/MPa	Mean uniaxial compressive strength/MPa
Natural state	NS10	101	50	1962.5	16.8	15.4
	NS11	103	50	1962.5	13.5	
	NS12	100	50	1962.5	15.8	
Saturated water state	SWS10	96	50	1962.5	11.5	9.8
	SWS11	101	50	1962.5	8.5	
	SWS12	99	50	1962.5	9.5	

Table 6: The burst tendency test result of the No. 5 coal seam.

State	Dynamic failure time/ms	Elastic energy index	Burst energy index	Uniaxial compressive strength/MPa	Burst tendency
Natural state	206 (weak)	9.4 (strong)	5.4 (strong)	15.4 (strong)	Strong burst tendency
Saturated water state	473 (weak)	3.7 (weak)	2.1 (weak)	9.8 (weak)	Weak burst tendency

records belong to the panel 250206) that almost all of the typical rock-burst accidents occurred during their mining periods were located in syncline geological structure influence area. These typical mine pressure behaviors mainly caused heaving floor and serious deformation of two sides. The typical surrounding rock failure forms of roadways on site are shown in Figure 6.

According to Figure 6, it can be seen that the typical mine pressure behavior of ribs is extrusion deformation, which means that there are high stresses concentrated in both ribs of the roadway. The high stress concentration is caused by the superposition of mining stress and self-weight stress caused by buried depth. It also can be seen that the typical mine pressure behavior of floors is heaving floor, and the deformation degree of heaving floor is different, severe in some places, mild in others. When the deformation degree of heaving floor is serious, the section shrinkage of roadway is large, and the roadway cannot meet normal production operation, and even cause equipment damage and casualties. Therefore, it is necessary to take effective methods to relieve the pressure of roadway surrounding rock. In particular, pressure relief is carried out for floor and two ribs of roadway.

3. Occurrence and Prevention Mechanisms of Rock Burst

3.1. Occurrence Mechanism of Rock Burst in Roadways

3.1.1. The Occurrence Mechanism in Roadway Ribs. Based on the superposition mechanism of dynamic and static loads, the occurrence mechanism of rock burst in roadway ribs has two different forms, and they are static load dominant type and dynamic load dominant type, respectively [17, 18]. The occurrence mechanism schematic diagram of rock burst in roadway ribs is shown in Figure 7.

According to Figure 7(a), it can be seen that the static load dominant type of rock burst is caused by high concentration static load (σ_j), and the concentration static load is enough to induce rock burst. Then, a rock-burst accident is induced by instantaneous instability and failure of a certain range of coal mass in shallow part of the roadway ribs; according to Figure 7(b), it can be seen that the dynamic load dominant type of rock burst is caused by strong dynamic load disturbance (σ_d), and the concentration static load is not enough to induce rock burst. Then, a rock-burst accident is induced by instantaneous instability and failure of a certain range of coal mass in shallow part of the roadway ribs. No matter what kind of rock burst, the occurrence positions are all a certain range of coal mass in shallow part of the roadway ribs. Therefore, it is necessary to take targeted measures to relieve pressure and prevent rock burst.

3.1.2. The Occurrence Mechanism in Roadway Floor. When a roadway is located in syncline geological structure influence area, the horizontal tectonic stress (σ_x) is at a high level, and a certain range of coal mass in shallow part of the roadway floor is in a state of plastic deformation due to extrusion of higher horizontal tectonic stress. Based on the Thessarky theory [19], it can be known that when the vertical stress caused by a certain range of coal mass in shallow part of the roadway ribs exceeds a certain value instantly, it will cause a certain range of coal mass in shallow part of the roadway floor to be unstable and destroyed instantly and then induce a rock-burst accident. The occurrence mechanism schematic diagram of rock burst in roadway floor is shown in Figure 8.

3.2. Prevention Mechanism of Rock Burst in Roadways

3.2.1. The Prevention Mechanism in Roadway Ribs. According to the above analysis of coal standard specimens in natural state and saturated water state (softening state), it can be

Table 7: The monitoring records of typical rock-burst accidents.

Location	Number	Time	Location	Range of influence/m	Specific characteristics
Panel 250206 in syncline geological structure influence area	1	2013-04-02	250206 headgate	28	The section of roadway was inverted trapezoid at the most serious position. The lower width and height of this section changed from 4.8 m to 4.3 m and 4.0 m to 3.5 m, respectively.
	2	2013-04-13	250206 tailgate	198	At 774-853 m, the lower left corner of the roadway was seriously inflated, the track is inclined and displaced, the roof of the upper right corner is seriously sunk, and the height of roadway was only 2.9 m in the most severe position.
	3	2013-04-22	250206 headgate	240	The heaving floor of roadway was serious, the mean value of heaving floor was 0.3 m, and the most serious value of heaving floor was 0.62 m.
	4	2013-04-29	250206 headgate	45	The mean value of heaving floor was 0.48 m, and the most serious value of heaving floor was 0.94 m. the left rib (mining direction) of roadway was seriously deformed, with a mean deformation of 0.38 m, and the most serious deformation of left rib was 0.69 m.
	5	2013-05-11	250206 tailgate	216	This time is mainly heaving floor of roadway, with a mean value of 0.4 m, the most serious value of 0.96 m, and slight influence in roadway roof and two ribs.
	6	2013-05-18	250206 headgate	121	The mean value of heaving floor was 0.6 m, and the most serious value of 1.82 m; the right rib (mining direction) of roadway changed from 4.5 m to 2.9 m.
	7	2013-05-24	250206 headgate	200	The mean value of heaving floor was 0.93 m, and the most serious value is 1.63 m; the whole track of the roadway in the severe section was lifted as a whole.
Panel 250205 in syncline geological structure influence area	8	2015-01-02	250205 tailgate	60	In the severely deformed section, the roadway was seriously deformed and damaged, the roof and floor were connected, and the two ribs moved close greatly.
	9	2015-01-07	250205 tailgate	54	At 936-990 m, the value of heaving floor was 0.4-0.8 m, and the belt rack was lifted and tilted outwards.
	10	2015-02-07	250205 tailgate	150	At 1600-1750 m, the value of heaving floor was 0.3-1.1 m, the roof subsidence is small, and the track is lifted and tilted outward.
	11	2015-02-12	250205 headgate	60	The roof sunk by 0.3 m, the value of heaving floor was 0.3-0.5 m, the track was lifted, and the transfer train was overturned.
	12	2015-02-18	250205 tailgate	20	The two ribs of roadway moved close to 0.3-0.5 m, and the roof and floor changed a little.
	13	2015-02-28	250205 tailgate	70	The floor bulged by 0.3-0.5 m, and the two ribs moved closer by 0.1-0.3 m.
	14	2015-03-08	250205 tailgate	15	The periodic weighting of the panel 250205 caused the heaving floor of roadway in advance of the mining face.
	15	2015-04-19	250205 tailgate	8	The floor bulged by 0.2-0.3 m, and the two ribs (mining direction) of roadway were seriously deformed, with a mean deformation of 0.28 m in left rib and 0.22 m in right rib.
	16	2015-05-10	250205 tailgate	11	The value of heaving floor was serious, with a mean value of 1.9 m, the most serious value is 2.4 m.

concluded that the water can effectively soften a certain range of coal mass in shallow part of the roadway ribs, and then the burst tendency test indexes of coal seam are reduced. Under the circumstances, the certain range of coal mass in shallow part of the roadway ribs is not easy instantaneous instability and failure, and then a rock-burst accident is not easy to occur in roadway ribs. Therefore, the water jet technology is used to prevent rock burst of roadway ribs. The prevention mechanism schematic diagram of rock burst in roadway ribs is shown in Figure 9.

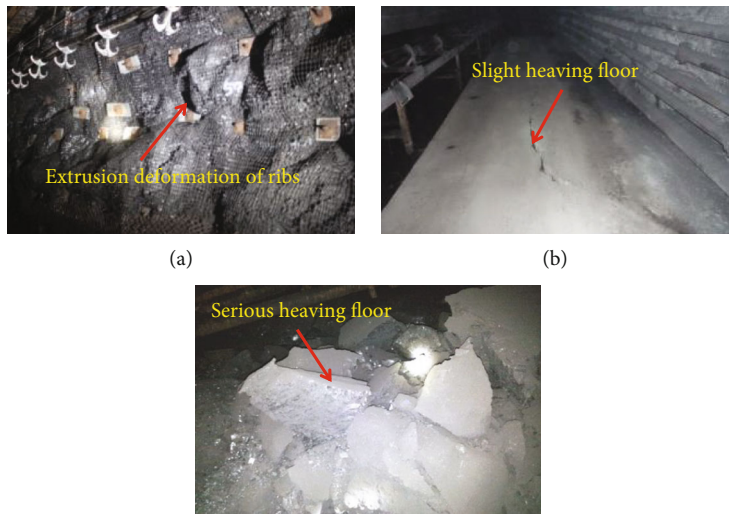

(a) (b) (c)

Figure 6: The typical surrounding rock failure forms of roadways on site. (a) Extrusion deformation of ribs. (b) Slight heaving floor. (c) Serious heaving floor.

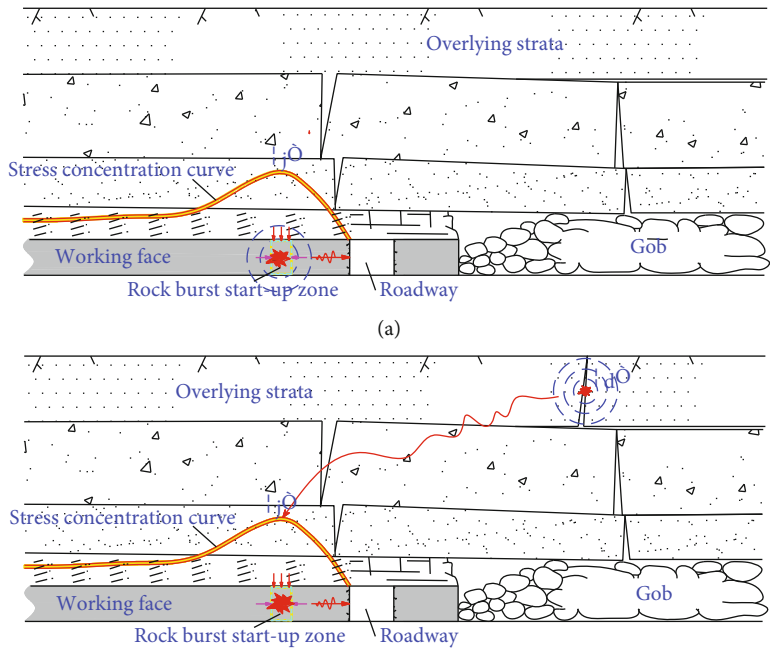

Figure 7: The occurrence mechanism schematic diagram of rock burst in roadway ribs. (a) Static load dominant type. (b) Dynamic load dominant type.

According to Figure 9, the prevention mechanism of rock burst by water jet technology can be obtained by comparing this pressure relief measure before and after using on the roadway ribs. From the perspective of elastic strain energy, before using the pressure relief measure of water jet technology, when the elastic strain energy (E_a) accumulated in rock burst start-up zone (I) is greater than the critical value of induced rock burst, a certain range of coal mass in rock burst start-up zone (I) is unstable and destroyed instantly, then the rock burst start-up zone (I) becomes activated. However, after using the pressure relief measure of water jet technology, when the elastic strain energy (E_c) accumulated in rock burst start-up zone (II) is greater than the critical value of induced rock burst, a certain range of coal mass in rock burst start-up zone (II) is unstable and destroyed instantly, then the rock burst start-up zone (II) becomes activated. But the rock burst start-up zone (II) is in the depth part of the roadway rib and there is a water jet zone (weak structure zone) in the path of its energy propagation and release. The water jet zone (weak structure

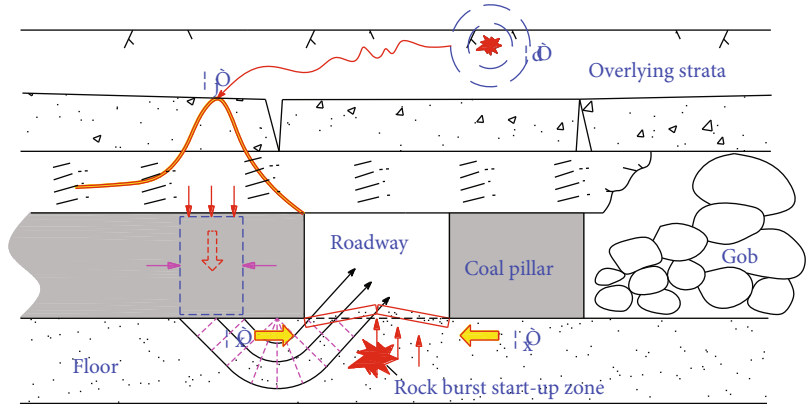

Figure 8: The occurrence mechanism schematic diagram of rock burst in roadway floor.

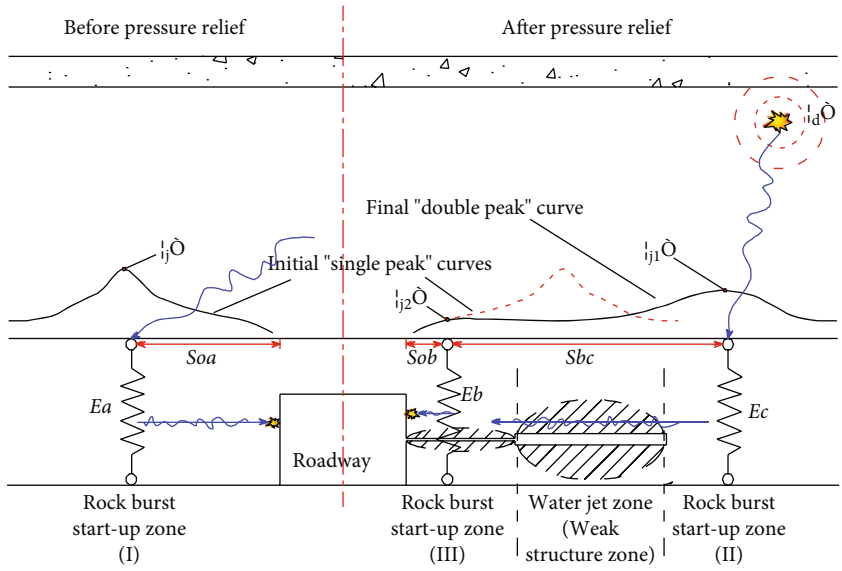

Figure 9: The prevention mechanism schematic diagram of rock burst in roadway ribs.

zone) can effectively absorb and scatter the elastic strain energy (E_c) in its propagation process, and the residual elastic strain energy (E_b) accumulated in rock burst start-up zone (III) is at a low level. At the moment, the rock burst start-up zone (III) is not easy to activate and the roadway rib is not prone to rock burst occurrence.

From the perspective of abutment stress, it can be seen that the existence of water jet zone (weak structure zone) makes the initial "single peak" curve change to a final "double peak" curve, and the initial single peak high concentration static load (σ_j) changes to a final double peak concentration static loads (σ_{j1} and σ_{j2}), and these concentration static loads satisfy the following conditions: $\sigma_j > \sigma_{j1} > \sigma_{j2}$. The distance relation between these concentration static loads and the roadway rib satisfies the following conditions: $S_{bc} > S_{oa} > S_{oc}$. It can be seen that after taking water jet technology, the high concentration static load (σ_j) is transferred to the depth part of the roadway rib, and the stress concentration degree is reduced as peak concentration static load (σ_{j2}). This means that static load dominant type of rock burst will not occur.

In addition, after using the pressure relief measure of water jet technology, there will be a lot of water left in the water jet zone (weak structure zone), and it will play an auxiliary role in softening the coal mass in shallow part of the roadway rib. This will further reduce the possibility of the occurrence of rock burst in roadway rib.

3.2.2. The Prevention Mechanism in Roadway Floor. It is assumed that when the abutment stress concentration value is higher than concentration static load (σ_v), it will affect the coal and rock medium in the floor, and the coal and rock medium in the floor will be transformed into a plastic state. Based on the Terzaghi theory, the prevention mechanism schematic diagram of rock burst in roadway floor is shown in Figure 10.

According to Figure 10, from the perspective of abutment stress, before using the pressure relief measure of water jet technology, the width range of abutment stress concentration value higher than concentration static load (σ_v) can be defined as a; after using the pressure relief measure of water jet technology, there is a certain range of pressure

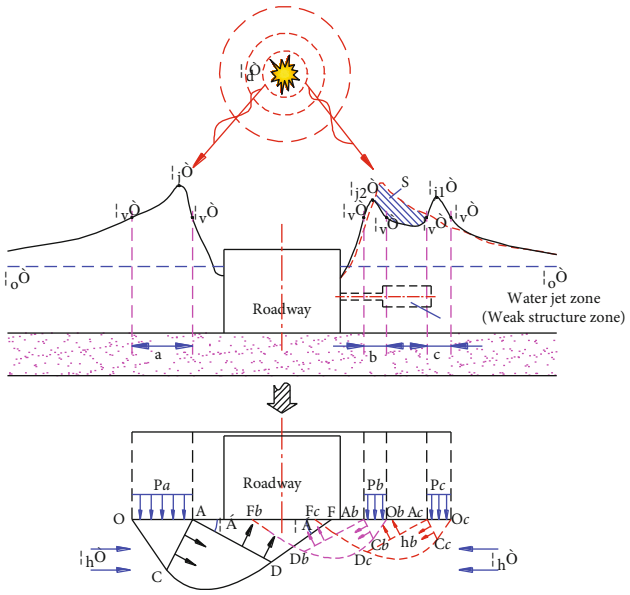

Figure 10: The prevention mechanism schematic diagram of rock burst in roadway floor.

relief zone that does not meet the abutment stress concentration value higher than concentration static load (σ_v), so the width range of abutment stress concentration value higher than concentration static load (σ_v) is discontinuous and it can be defined as b and c. According to the research results of relevant literature, the width ranges of abutment stress concentration value higher than concentration static load (σ_v) satisfy the following conditions: $a > b + c$. Therefore, the superposition area of plastic state zones (S_{AbObCb} and S_{AcOcCc}) is less than the area of plastic state zones (S_{AOC}). After using the pressure relief measure of water jet technology, the area of plastic zone in floor is smaller and its degree of heaving floor caused by instantaneous sliding instability will be reduced. It can be seen that after the pressure relief measure of water jet technology is taken for the roadway ribs, the prevention effect of rock burst in floor can be achieved at the same time.

4. Mechanism Analysis of Water Jet Technology

4.1. Introduction of Water Jet Technology. The construction process of water jet technology for roadway rib is as follows:

(a) Firstly, it is necessary to drill an initial borehole on the roadway rib with an ordinary drill bit, and the borehole diameter (d) should meet the requirements of subsequent water jet punching. If this is not done, the nozzles can easily be blocked by pulverized coal during subsequent operations. Therefore, based on the selected model of water jet drill bit (model ZJN94/3), the initial borehole diameter should be greater than 94 mm, and then an ordinary drill bit with diameter of 110 mm is adopted

(b) Secondly, when the length of an initial borehole (L) reaches its design length, the ordinary drill bit is backlogged and replaced with a water drill bit (model ZJN94/3). The water drill bit (model ZJN94/3 cannot be used directly for drilling to prevent the nozzles from being blocked by pulverized coal. Then, according to the initial design, the water jet drill bit is used to punch the initial borehole, and then a length of punching section (l_2) is formed, namely, water jet section. In order to prevent safety accidents caused by borehole return water with slag, the residual length of this initial borehole (l_1) can be seen as a protected zone without punching by water jet drill bit. The diameter of water jet section (D) is determined by the water jet parameters

(c) Thirdly, the water supply is provided by pumping, and the water pressure is regulated by BOTK-01 series water pressure regulating systems. The drill stems are hollow, and they are connected in turn to provide water supply path. When the adjusted water supply reaches the position of water jet drill bit through this path, finally water supply is sprayed out by three nozzles on the water jet drill bit, and the three nozzles are 120° to each other

(d) Finally, the three water jets punch the initial borehole wall by rapidly rotating with the water jet drill bit and continuously moving axially with the drill stems (hollow), and then, a water jet section is formed. This water jet section can play a good pressure relief effect for the roadway ribs and floor

The schematic diagram of water jet technology for roadway rib is shown in Figure 11.

4.2. Punching Mechanism of Water Jets. When the water supply is sprayed out of the nozzles, it will change into water jets and punch the initial borehole wall. The number of water jets is determined by the number of nozzles on the water jet drill bit. Based on the water drill bit (model ZJN94/3), it can be known that there are three water jets punching the initial borehole wall. The punch capacity of water jets can be adjusted by changing nozzles with different diameters (d_0). The schematic diagram of water jets punching initial borehole wall is shown in Figure 12.

When the pressure and quantity of flow parameters of water supply are determined, the theoretical quantity of flow of these nozzles is also determined accordingly. The theoretical quantity of flow can be calculated by the following formula [20]:

$$q_t = 2.1 \cdot (d_e)^2 \sqrt{p}, \quad (1)$$

where q_t is the theoretical quantity of flow of these nozzles; d_e is the equivalent diameter of these nozzles; and p is the pressure of water jet at the nozzle exit.

The practical quantity of flow of these nozzles is depended by the geometric shape, inner surface roughness, and internal flow state of these nozzles, which is mainly determined by the field test. According to the statistical

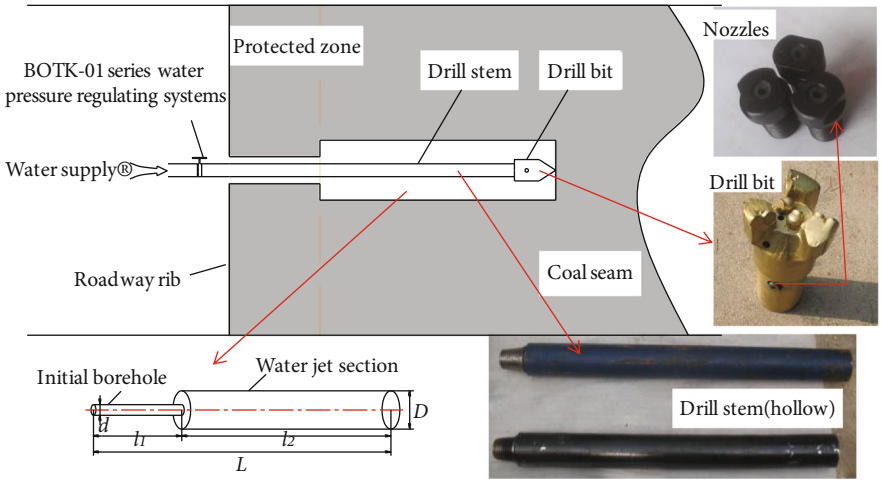

Figure 11: The schematic diagram of water jet technology for roadway rib.

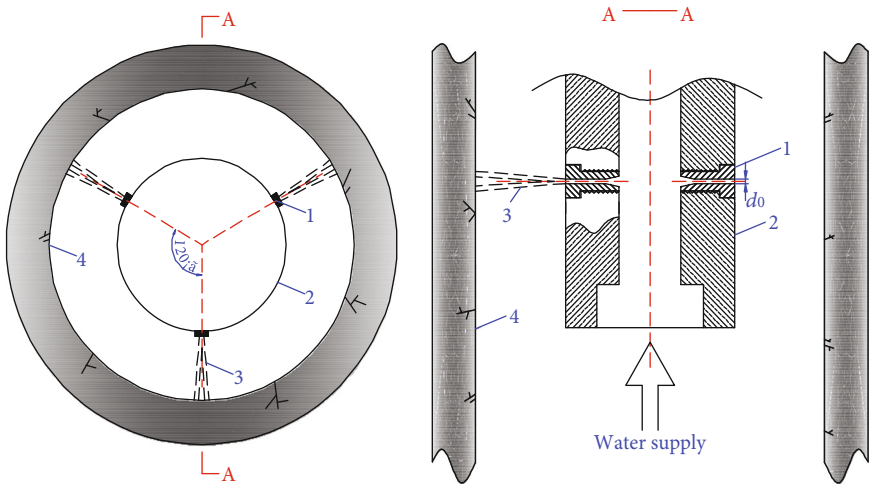

Figure 12: The schematic diagram of water jets punching initial borehole wall. (a) The plan view. (b) A-A cross-section view. Note: 1 is the nozzle; 2 is the water jet drill bit; 3 is the water jet; and 4 is the initial borehole wall.

results of relevant literatures [21], the flow coefficients under different models of nozzles are shown in Table 8.

Therefore, the practical quantity of flow of these nozzles can be calculated by the following formula:

$$q = \mu \cdot q_t, \tag{2}$$

where q is the practical quantity of flow of these nozzles, calculated in terms of flow per minute; μ is the flow coefficient.

For multiple nozzles, they should be converted into equivalent diameter of nozzles for calculation. The equivalent diameter can be expressed as the following formula:

$$d_e = \sqrt{(d_0)^2 + (d_1)^2 + (d_2)^2 + \cdots + (d_n)^2}, \tag{3}$$

where d_e is the equivalent diameter of nozzles; n is the number of nozzles.

Table 8: The flow coefficients under different models of nozzles.

Models of nozzles	Flow coefficient
Thin-wall orifice	0.62
Extension stub	0.82
Internal extension stub	0.71
Conical convergence model (contraction angle 13°-14°)	0.95
Conical expansion model (5°-7°)	0.45
Streamline model	0.98

Since the practical quantity of water flow is better monitored in practice and the model of nozzles can also be determined in advance, according to Equations (1) and (2), its expression can be known as the following formula:

$$p = 0.227 \frac{q^2}{\mu^2 \cdot (d_e)^2}. \quad (4)$$

During the water jets punching, the dynamic pressure of water jets acting on the initial borehole wall causes the internal stress in the coal mass of initial borehole wall. When the maximum shear stress of this internal stress exceeds the ultimate compressive strength of the coal mass, the coal mass is damaged. Therefore, in order to destroy the coal mass of initial borehole wall and form a larger range of water jet section, it is necessary to make the pressure of water jet at the nozzle exit greater than the ultimate compressive strength of the coal mass.

According to Figure 11, the nozzle model can be seen as an extension stub and its flow coefficient (μ) is about 0.82. The diameter of this nozzle model for water jet drill bit (model ZJN94/3) is 1.6 mm, 2.0 mm, 2.5 mm, and 3.0 mm, respectively. Assuming that the adjustable range of practical quantity of flow for water supply is about 100 L/min~300 L/min, and then based on Equation (4), the change law of pressure of water jet at the nozzle exit can be obtained as shown in Figure 13.

According to Figure 13, it can be seen that the pressure of water jet at the nozzle exit increases exponentially with the increasing of practical quantity of flow for water supply under any nozzle diameter condition. Under the same practical quantity of flow for water supply condition, the smaller the nozzle diameter is, the greater the pressure of water jet at the nozzle exit is. According to Table 5, the mean uniaxial compressive strength of coal standard specimens from No. 5 coal seam in mining area 2502 has been known to be 15.4 MPa. Then, combining with Figure 13, it can be seen that when the diameter of this nozzle model for water jet drill bit (model ZJN94/3) is 1.6 mm, 2.0 mm, and 2.5 mm, there is a pressure of water jet at the nozzle exit that can provide higher strength than the mean uniaxial compressive strength of the No. 5 coal seam under certain practical quantity of flow for water supply. But when the diameter of this nozzle model for water jet drill bit (model ZJN94/3) is 3.0 mm, the practical quantity of flow for water supply is almost 300 L/min, and the corresponding pressure of water jet at the nozzle exit can be higher than 15.4 MPa. Therefore, this nozzle model with diameter of 3.0 mm is not considered. The larger the practical quantity of flow for water supply is, the stronger the slag carrying capacity of return water is. Therefore, this nozzle model with diameter of 2.0 mm is selected for field industrial test, and the practical quantity of flow for water supply should be higher than 236 L/min and less than 300 L/min.

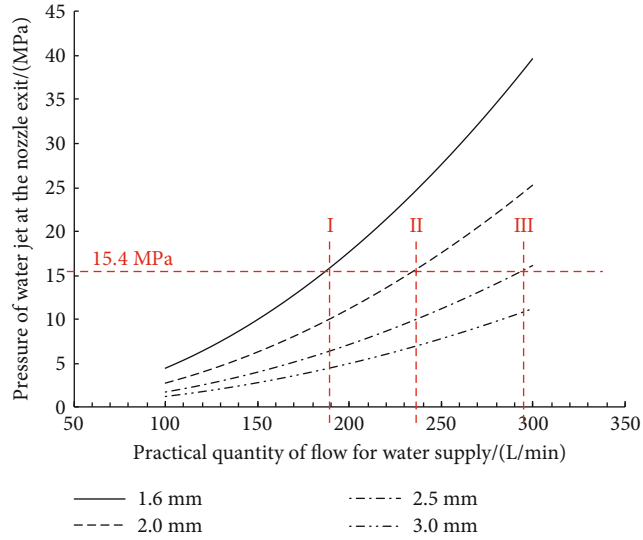

Figure 13: The change law of pressure of water jet at the nozzle exit.

5. Field Industrial Test

5.1. The Implementation Method

5.1.1. The Determination of Spacing and Diameter Parameters. The panel 250204 is now being driven, and it is the third panel in the mining area 2502. The field industrial test is carried out on the ribs of 250204 tailgate before its mining stage. The water jet pressure relief measure is applied to roadway part in syncline geological structure influence area. The mean buried depth of the panel 250204 is about 580 m. It is assumed that the corresponding diameters of water jet section (D) are taken as 200 mm, 300 mm, and 400 mm, respectively. Then, the spacing between adjacent water jet boreholes (L) can be determined by numerical simulation method, and the numerical simulation results of different spacing between adjacent water jet boreholes are shown in Figure 14.

It can be seen from Figure 14(a) that the vertical stress between adjacent water jet boreholes begins to overlap slightly on the condition of diameter 300 mm and further at the diameter of 400 mm. As the diameter of these adjacent water jet boreholes is further increased, the vertical stress between adjacent water jet boreholes begins to overlap adequately and the coal mass between adjacent water jet boreholes changes into plastic state at the diameter of 500 mm. The plastic state zone between each two adjacent water jet boreholes is connected to form a wide range of pressure relief structure zone, and this zone can effectively transfer and release the high concentrated static load in roadway rib.

It can be seen from Figure 14(b) that when the spacing between adjacent water jet boreholes (L) increases from 3.0 m to 5.0 m, the vertical stress between adjacent water jet boreholes cannot overlap adequately at diameters of 300 mm, 400 mm, and 500 mm. At this point, if the vertical stress between adjacent water jet boreholes can overlap sufficiently, it is necessary to further increase the diameter of these adjacent water jet boreholes. Considering that too large diameter of water jet boreholes requires more pressure of water jet at the nozzle exit and time for punching, and the stability of water jet boreholes is poor, it is not suitable to set too large spacing between adjacent water jet boreholes.

In summary, the relatively reasonable spacing between adjacent water jet boreholes is determined to be 3.0 m and the corresponding diameter of water jet section is determined to be 500 mm.

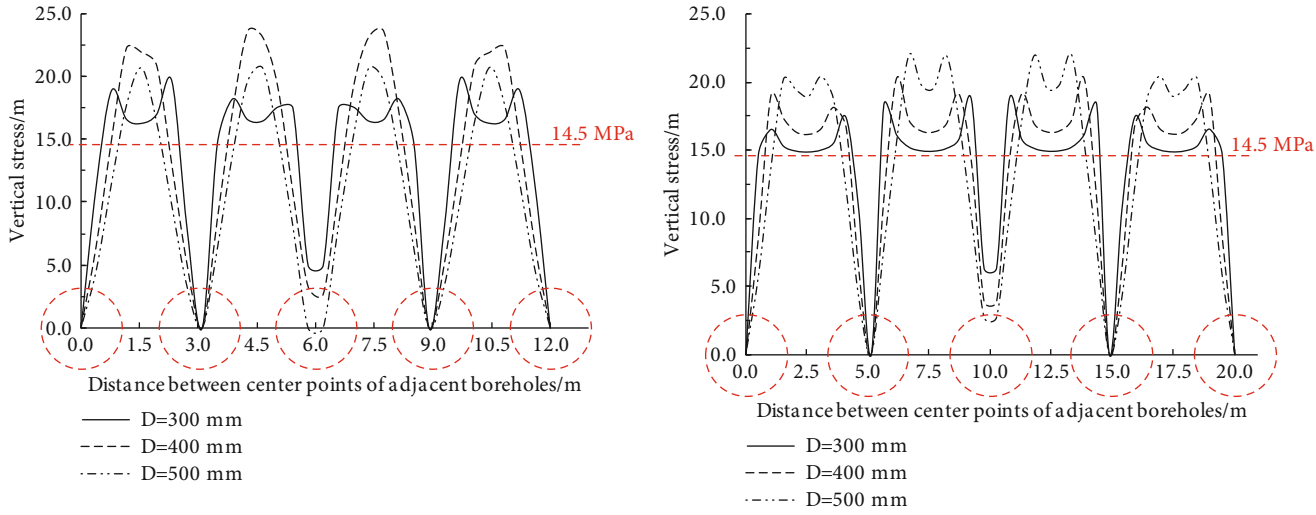

FIGURE 14: The numerical simulation results of different spacing between adjacent water jet boreholes. (a) When L is 3.0 m. (b) When L is 5.0 m.

5.1.2. The Determination of Length Parameter. The water jet borehole length (l_2) can be determined by numerical simulation results. Before pressure relief by using water jet technology for the roadway rib, the change law of abutment stress curve is shown in Figure 15(b). It can be seen that the abutment stress curve can be divided into three zones, and they are the reduced pressure zone (I), the increased pressure zone (II), and the stable pressure zone (III) from the outer roadway rib to the inner coal mass, respectively. High concentrated static load is easy to accumulate in the increased pressure zone (II) and then induces the coal mass instant instability and the occurrence of rock burst under the condition of static and dynamic loads superposition. Therefore, the water jets should be mainly used to punch the increased pressure zone (II) and the water jet borehole length (l_2) can be determined by numerical simulation method. According to the numerical simulation results in Figure 15(b), the width of increased pressure zone (II) is about 15.0 m, and then the corresponding water jet borehole length (l_2) can be taken as 15.0 m. The residual length of this initial borehole (l_1) can be determined to be 5.0 m.

With the increase of abutment stress in the coal mass, the microcracks in the coal mass will be further compacted, and the permeability of the coal mass will be further reduced. A steady flow method is also used to verify the position of stress peak, and its schematic diagram is shown in Figure 15(a). This method mainly forms a certain confined space in an initial borehole through two sealed capsules with certain water pressure (usually for 2.0~3.0 MPa), and the certain water pressure can be adjusted by pressure gage. The dimension of connecting rod between two sealed capsules is 1.0 m. When the certain confined space is formed in an initial borehole, use nitrogen gas cylinder to supply gas to this confined space and keep the flow stable by a flowmeter. According to this method, the position where the flow stability is minimum, that is, the position of peak stress, can be measured. As shown in Figure 15(b), the minimum steady flow position is about 10 m away from the roadway rib, which basically overlapped with the numerical simulation peak stress position, further verifying the accuracy of the simulation results.

After pressure relief by using water jet technology for the roadway rib, the change law of abutment stress curve is also shown in Figure 15(b). It can be seen that the stress in the increased pressure zone (II) has been transferred and released, and almost all the stress in this zone is less than 14.5 MPa at this time. It can be seen that water jets punching can play a good pressure relief effect in the coal mass of increased pressure zone (II), so as to effectively prevent the occurrence of rock burst.

5.1.3. The Specific Construction Scheme. According to the specific parameters of water jet boreholes determined above, the field engineering application is carried out on the two ribs of the 250204 tailgate, namely, the coal-pillar rib and the solid-coal rib. The length of the 250204 tailgate for field engineering application is about 60 m. Before using water jet technology, the initial boreholes with a diameter of 110 mm are adopted on both coal-pillar rib and solid-coal rib, and 21 initial boreholes with an interval of 3.0 m are constructed symmetrically on the coal-pillar rib and solid-coal rib. The orifice position of every initial borehole is about 1.2 m~1.5 m away from the floor, and the inclination of every initial borehole is about 3°~5°, which is conducive to the return water and slag carrying in the subsequent water jet construction; after using water jet technology, when the length of an initial borehole reaches 20.0 m, the ordinary drill bit is backlogged and replaced with a water drill bit (model ZJN94/3). Then, according to the above analysis, the water jet drill bit is used to punch the initial boreholes, and then water jet sections with a length of 15.0 m and a diameter of 500 mm is formed inside the roadway ribs. The specific construction scheme of water jet technology in the 250204 tailgate is shown in Figure 16.

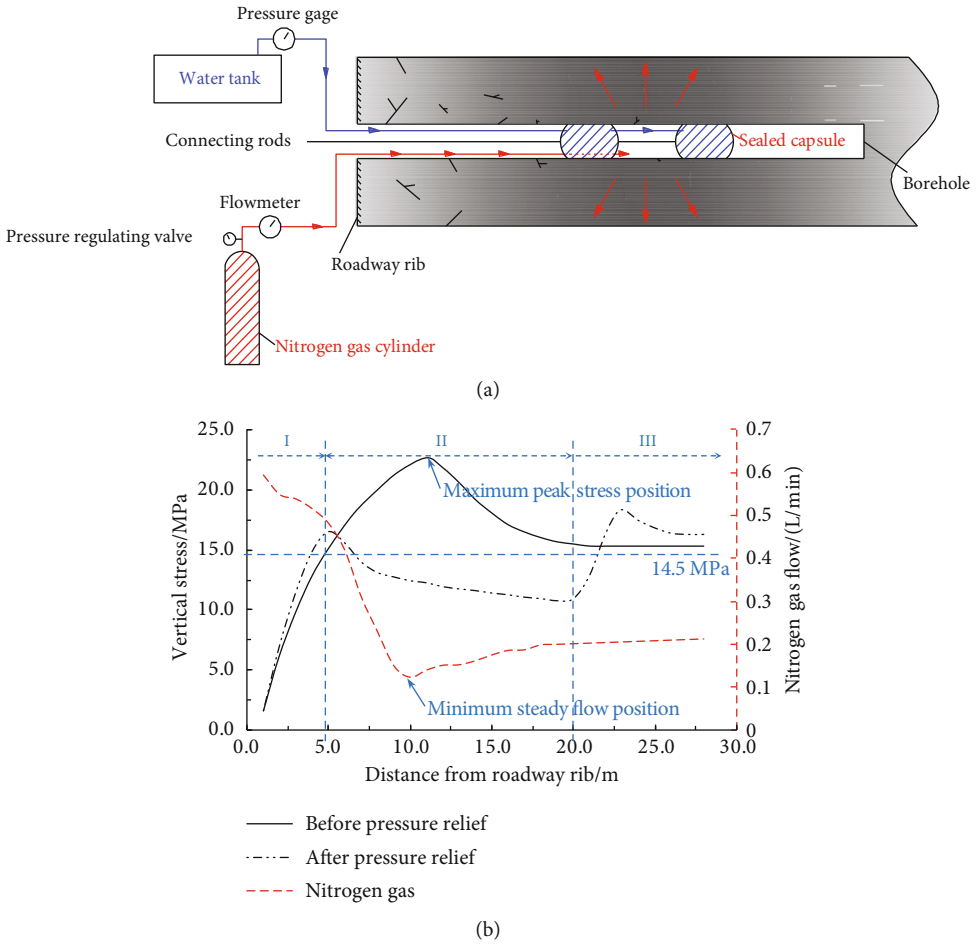

FIGURE 15: The numerical simulation results of water jet borehole length. (a) Schematic diagram of steady flow method. (b) Numerical simulation results. Note: I is the reduced pressure zone; II is the increased pressure zone; and III is the stable pressure zone.

5.2. The Field Monitoring Results

5.2.1. The EMR Monitoring Result. As the signal intensity of electromagnetic radiation (EMR) is positively correlated with the stress state of coal mass inside roadway ribs [22]; therefore, a KBD-5 Exib series of electromagnetic radiation monitor is used to monitor the change law of stress state for coal mass inside the roadway ribs. Before and after using water jet technology on the roadway ribs, a receiving antenna is used to monitor the roadway ribs by noncontact means, and the interval distance of adjacent monitoring points is about 2.0 m. The effective monitoring of maximum depth for this EMR is 22 m, and it can meet the requirements of field monitoring. The monitoring diagram of coal-pillar side is shown in Figure 17.

According to Figure 17, the monitoring result of signal intensity by EMR on solid-coal rib and coal-pillar rib is shown in Figure 18. It can be seen from Figure 18 that the overall signal intensity of EMR after using water jet technology is lower than that before using water jet technology. On the side of coal-pillar rib, the mean signal intensity of EMR before using water jet technology is about 44.2 mV, and the mean signal intensity of EMR after using water jet technology is about 17.6 mV. The decreasing amplitude of signal intensity of EMR is about 60.2%, as shown in Figure 18(a); on the side of solid-coal rib, the mean signal intensity of EMR before using water jet technology is about 49.7 mV, and the mean signal intensity of EMR after using water jet technology is about 15.6 mV. The decreasing amplitude of signal intensity of EMR is about 68.6%, as shown in Figure 18(b).

The above analysis shows that the water jet technology for roadway ribs can well relieve and transfer the high concentration stress accumulated in coal mass inside the roadway ribs and then makes the coal mass inside the roadway ribs in a good stress environment.

5.2.2. The Convergences Monitoring Result. After using water jet technology, a "cross-shaped" observation method is used to monitor the convergences of surrounding rock in the pressure relief roadway part [23]. The convergences of surrounding rock are monitored mainly through the pegs installed on the roadway surface, and the corresponding measurement tools are lines, telescoping rods, and trpes. The pegs can be divided into roof peg, rib pegs, and floor peg, and their arrangement is shown in Figure 19(a). According to Figure 19(a), it can be seen that the roof peg and floor peg are installed in the middle of the roof and floor, respectively, and the rib pegs are symmetrically

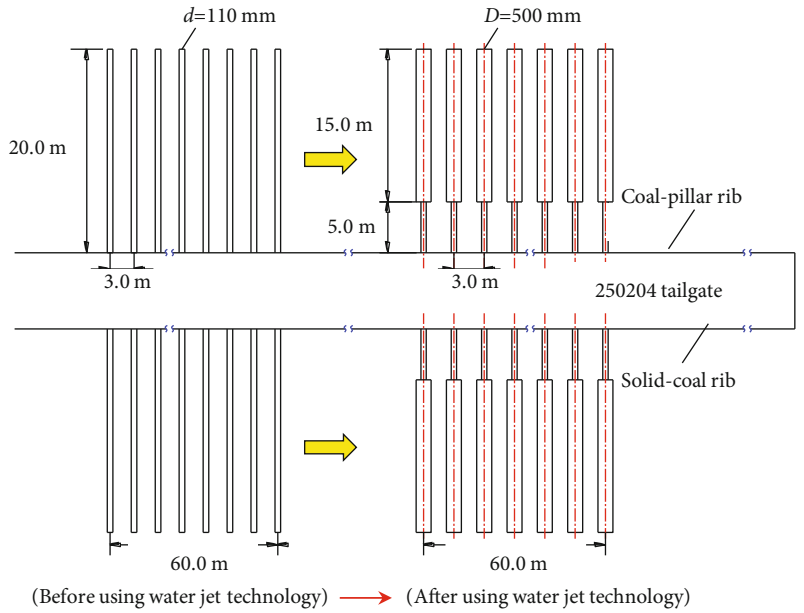

Figure 16: The specific construction scheme of water jet technology in the 250204 tailgate.

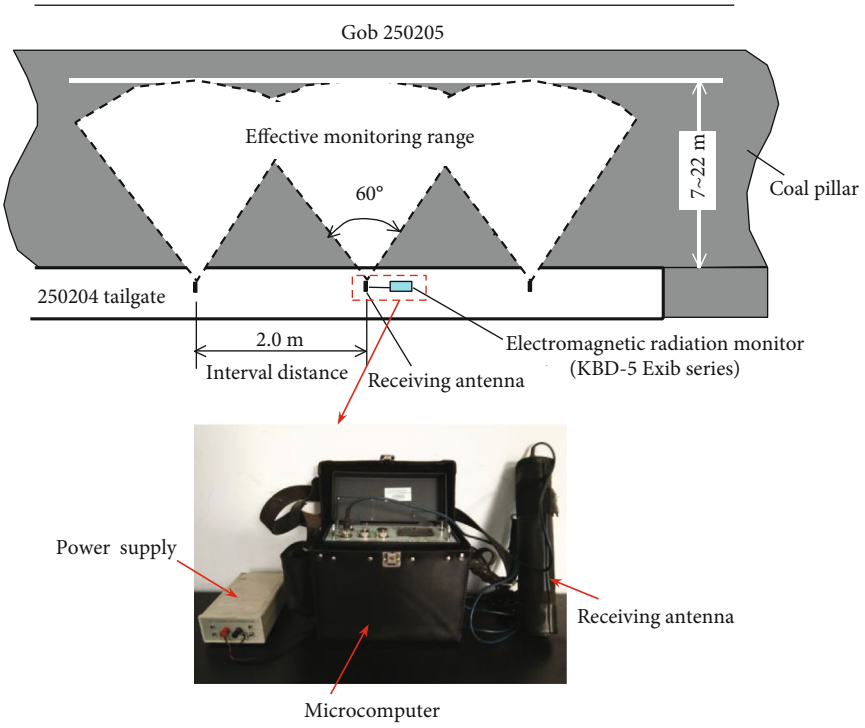

Figure 17: The monitoring diagram of coal-pillar side in the 250204 tailgate.

installed 2.0 m away from the floor. A total of 3 groups of measuring stations are arranged in the pressure relief roadway part with an interval distance of 15 m, and the mean convergences monitoring result are shown in Figure 19(b).

According to Figure 19(b), it can be seen that the mean convergence of roof to floor increases with the increase of observation time, and the maximum mean convergence of roof to floor is about 129 mm at 38 days; the mean convergence of solid-coal rib to coal-pillar rib also increases with the increase of observation time, and the maximum mean convergence of solid-coal rib to coal-pillar rib is about 109 mm at 38 days. The mean convergence rates of roof-to-floor and solid-coal rib to coal-pillar rib both begin to decrease at 20 days and then stabilize at 29 days.

As the width and height of 250204 tailgate are 4.8 m and 4.0 m, respectively, the convergence ratio of roadway height

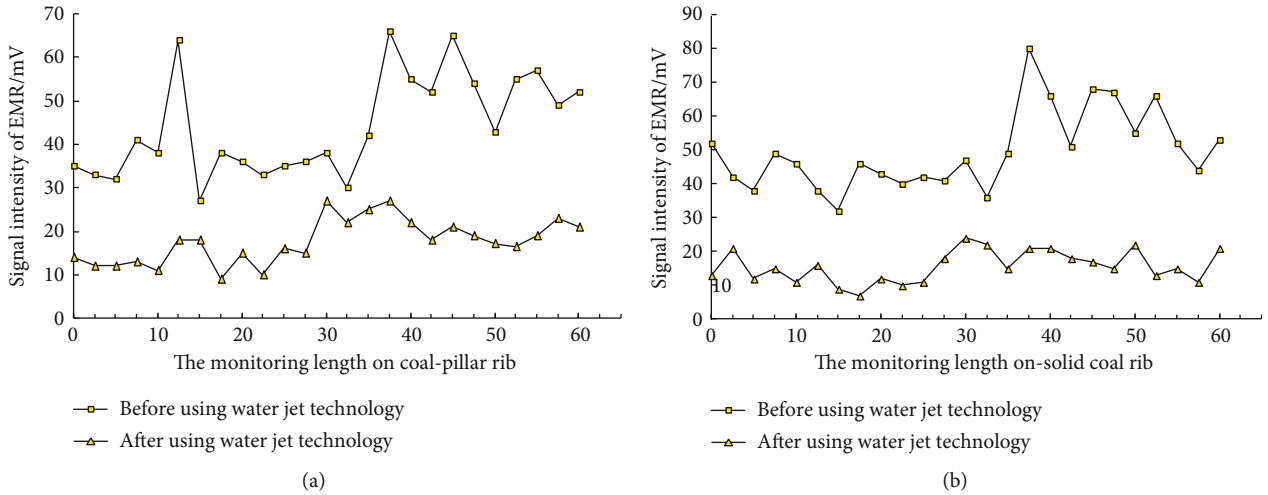

Figure 18: The monitoring result of signal intensity by EMR. (a) On solid-coal rib. (b) On coal-pillar rib.

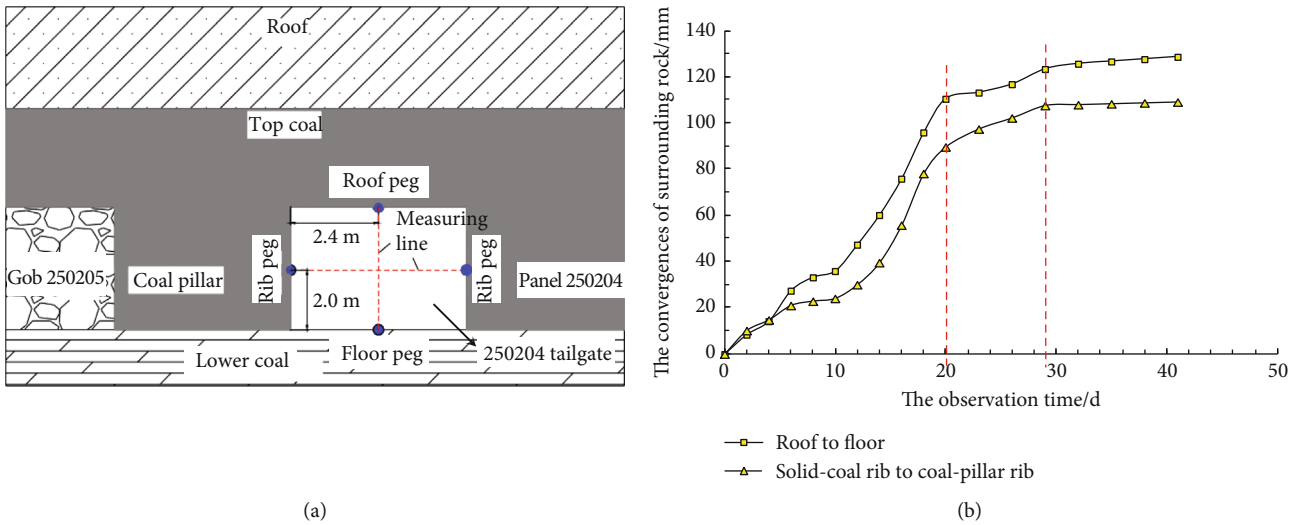

Figure 19: The "cross-shaped" observation method in the pressure relief roadway part. (a) Schematic diagram of "cross-shaped" observation method. (b) Mean convergences monitoring result.

is about 3.2% and the convergence ratio of roadway width is about 2.3%. Both the convergence ratios of roadway height and width are controlled within 5.0%, which means that the control effect of surrounding rock for the 250204 tailgate is good. It can be seen that the effective pressure relief for the ribs is also helpful for the pressure relief of the floor and thus improve the stress environment of coal and rock medium in the floor. Therefore, the water jet technology is not only helpful to the prevention of rock burst for the roadway ribs but also can play a good prevention of rock burst for roadway floor.

6. Conclusions

(1) Huayan mine field was affected by strong geological tectonic stress, and the horizontal stress is much greater than the vertical stress in this mine field. The mining and driving spaces are easily affected by this strong geological tectonic stress and then induce rock burst. Based on the burst tendency test result of No. 5 coal seam before and after saturated water state, the burst tendency of No. 5 coal seam can be reduced to a certain extent after softening with water

(2) According to the monitoring records of rock-burst accidents of panels 250205 and 250206 in the mining area 2502 during their mining periods, these typical mine pressure behaviors mainly caused heaving floor and serious deformation of two sides. Therefore, it is necessary to take effective methods to relieve the pressure of floor and two ribs of roadway

(3) Based on the superposition mechanism of dynamic and static loads, the occurrence mechanism of rock burst in roadway ribs has two different forms, and they are static load dominant type and dynamic load

dominant type, respectively. No matter what kind of rock burst, the occurrence positions are all a certain range of coal mass in shallow part of the roadway ribs. Therefore, it is necessary to take targeted measures to relieve pressure and prevent rock burst. Based on the Thessarky theory, it can be known that when the vertical stress caused by a certain range of coal mass in shallow part of the roadway ribs exceeds a certain value instantly, it will cause a certain range of coal mass in shallow part of the roadway floor to be unstable and destroyed instantly and then induce rock burst

(4) The water can effectively soften a certain range of coal mass in shallow part of the roadway ribs, and then, the burst tendency test indexes of coal seam are reduced. Therefore, the water jet technology is used to prevent rock burst of roadway ribs. After the pressure relief measure of water jet technology are taken for the roadway ribs, the prevention effect of rock burst in floor can be achieved at the same time

(5) The field industrial test is carried out on the ribs of the 250204 tailgate before its mining stage. The EMR monitoring result shows that the water jet technology for roadway ribs can well relieve and transfer the high concentration stress accumulated in coal mass inside the roadway ribs and then make the coal mass inside the roadway ribs in a good stress environment; the convergences monitoring result shows that the effective pressure relief for the ribs is also helpful for the pressure relief of the floor and thus improve the stress environment of coal and rock medium in the floor

Data Availability

All data used to support the findings of this study are included within the article, and there are no any restrictions on data access.

Conflicts of Interest

The authors declare no conflicts of interest.

Acknowledgments

The work is supported by the Key Project of National Natural Science Foundation of China (Nos. 51634001, 51574243, 51404269, and 51674253).

References

[1] L. M. Dou, J. He, A. Y. Cao, S. Y. Gong, and W. Cai, "Rock burst prevention methods based on theory of dynamic and static combined load induced in coal mine," *Journal of China Coal Society*, vol. 40, no. 7, pp. 298–310, 2015.

[2] L. M. Dou, J. Z. Bai, X. W. Li, and H. He, "Study on prevention and control technology of rockburst disaster based on theory of dynamic and static combined load," *Coal Science and Technology*, vol. 46, no. 10, pp. 1–8, 2018.

[3] Y. D. Jiang, Y. X. Zhao, H. W. Wang, and J. Zhu, "A review of mechanism and prevention technologies of coal bumps in China," *Journal of Rock Mechanics and Geotechnical Engineering*, vol. 9, no. 1, pp. 180–194, 2017.

[4] L. M. Dou, Y. D. Jiang, H. S. Liu, S. Y. Gong, W. Cai, and G. A. Zhu, "Monitoring and pre-warning of rockburst hazard with technology of stress field and wave field in underground coalmines," *Chinese Journal of Rock Mechanics and Engineering*, vol. 36, no. 4, pp. 803–811, 2017.

[5] Z. Q. Yang, *Occurrence Mechanism of Rock Burst and Its Prevention Methods under Complicated Geological Conditions*, China University of Mining and Technology, Beijing, China, 2018.

[6] Z. Q. Yang, C. Liu, Y. Dong, L. M. Dou, and J. K. Wu, "Study on properties of grouting materials and reinforcement effect in coal roadways influenced by dynamic pressure," *Geotechnical & Geological Engineering*, vol. 2019, no. 37, pp. 3329–3342, 2019.

[7] Z. Q. Yang, C. Liu, S. C. Tang, L. Dou, and J. Cao, "Rock burst mechanism analysis in an advanced segment of gob-side entry under different dip angles of the seam and prevention technology," *International Journal of Mining Science and Technology*, vol. 28, no. 6, pp. 891–899, 2018.

[8] Z. Q. Yang, L. M. Dou, C. Liu, M. Xu, Z. Lei, and Y. Yao, "Application of high-pressure water jet technology and the theory of rock burst control in roadway," *International Journal of Mining Science and Technology*, vol. 26, no. 5, pp. 929–935, 2016.

[9] C. M. Shen, B. Q. Lin, F. W. Meng, Q. Zhang, and C. Zhai, "Application of pressure relief and permeability increased by slotting a coal seam with a rotary type cutter working across rock layers," *International Journal of Mining Science and Technology*, vol. 22, no. 4, pp. 533–538, 2012.

[10] W. P. Shen, *Numerical Simulation of Jet for Hydraulic Flushing and Study of Coal Breaking Mechanism in Coal*, Henan Polytechnic University, Jiaozuo, China, 2011.

[11] L. M. Dou, C. P. Lu, Z. L. Mou, Q. Yu-hong, and Y. Jing-ming, "Intensity weakening theory for rockburst and its application," *Journal of China Coal Society*, vol. 30, no. 5, pp. 690–694, 2005.

[12] L. M. Dou, Z. Q. Yang, and X. M. Ding, "Application of high pressure water jet coal cutting in mine pressure bumping prevention and control," *Coal Science and Technology*, vol. 41, no. 6, 2013.

[13] Z. Q. Yang, C. Liu, F. S. Li, L. M. Dou, G. W. Li, and D. W. Wang, "The mechanism and application of high-pressure water jet technology to prevent compound dynamic disaster," *Arabian Journal of Geosciences*, vol. 14, no. 13, pp. 1–20, 2021.

[14] K. Gao, G. D. Qiao, Z. G. Liu, J. Liu, F. H. Zhu, and S. C. Zhang, "On classification conception of coal and gas outburst mechanism and its application," *Journal of Mining & Safety Engineering*, vol. 36, no. 5, pp. 1043–1051, 2019.

[15] C. P. Lu, L. M. Dou, and X. R. Wu, "Controlled weakening mechanism of dynamic catastrophe of coal and rock and its practice," *Journal of China University of Mining & Technology*, vol. 35, no. 3, pp. 301–305, 2006.

[16] A. W. Wang, Y. S. Pan, and B. Y. Zhao, "Study of energy absorption principle of anti-bump bolt-cable," *Journal of China University of Mining & Technology*, vol. 46, no. 4, pp. 739–747, 2017.

[17] G. A. Zhu, L. M. Dou, Z. L. Li, W. Cai, Y. Kong, and J. Li, "Mining-induced stress changes and rock burst control in a

variable-thickness coal seam," *Arabian Journal of Geosciences*, vol. 9, no. 5, pp. 365–376, 2016.

[18] W. Cai, L. M. Dou, G. Y. Si et al., "A new seismic-based strain energy methodology for coal burst forecasting in underground coal mines," *International Journal of Rock Mechanics and Mining Sciences*, vol. 123, no. 5, 2019.

[19] J. F. Pan, Y. Ning, Z. H. Qin, S. Wang, and Y. Xia, "Dredging technology of pressure with deep-hole interval blasting based on theory of rock burst start-up," *Chinese Journal of Rock Mechanics and Engineering*, vol. 31, no. 7, pp. 1414–1421, 2012.

[20] F. Huang, Y. Y. Lu, S. Q. Li, and F. J. Zhao, "Influence of velocity of high-pressure water jet on failure patterns of sandstone," *Chinese Journal of Rock Mechanics and Engineering*, vol. 35, no. 11, pp. 2259–2265, 2016.

[21] Z. Z. Zhang, J. L. Xin, J. J. Bai, X. Yu, W. Yu, and M. Deng, "Determination of cyclic filling length in gob-side entry retained with roadside filling and its application," *Shock and Vibration*, vol. 2021, 16 pages, 2021.

[22] Z. Z. Zhang, J. J. Bai, Y. Chen, and S. Yan, "An innovative approach for gob-side entry retaining in highly gassy fully-mechanized longwall top-coal caving," *International Journal of Rock Mechanics and Mining Sciences*, vol. 80, pp. 1–11, 2015.

[23] G. C. Zhang, L. J. Chen, Z. J. Wen et al., "Squeezing failure behavior of roof-coal masses in a gob-side entry driven under unstable overlying strata," *Energy Science & Engineering*, vol. 2020, pp. 1–14, 2020.

Hindawi
Geofluids
Volume 2022, Article ID 8991574, 12 pages
https://doi.org/10.1155/2022/8991574

Research Article

Roof Bolting Anchoring Performance Research on the Entry under the Gob of Close-Distance Coal Seam

Yongjie Yang[1], **Gang Huang**[1] **and Haiyu Ji**[2]

[1]*State Key Laboratory of Mining Disaster Prevention and Control Co-Founded by Shandong Province and the Ministry of Science and Technology, Shandong University of Science and Technology, Qingdao 266590, China*
[2]*Changsha Digital Mine Info Tech CO., LTD, Changsha 410000, China*

Correspondence should be addressed to Gang Huang; huanggang@sdust.edu.cn

Received 14 February 2022; Accepted 12 April 2022; Published 2 May 2022

Academic Editor: Mingwei Chen

Seam spacing plays a crucial role in selecting roof bolting of the close-distance coal seam. This work utilized three methods to determine the minimum roof bolting seam spacing of the lower coal seam (LCS) entry after the upper coal seam (UCS) mining. Based on the entry of the No.3-2 coal seam (LCS) in Chaili Coal Mine in China, theoretical analysis, pull-out bolt test, and numerical simulation were performed to calculate the maximum floor failure depth of the UCS and to determine the minimum seam spacing of the roof bolting. The maximum floor failure depth of the UCS determined through theoretical analysis and numerical simulation is 3.2 m and 3.3 m, respectively. In general, the anchorage length of rock bolting is less than 2.4 m, so the minimum seam spacing is 5.6 m or 5.7 m. To further determine the anchorage performance of the roof, the pull-out test was employed on the entry roof of the LCS. When the seam spacing is no less than 6 m, the test results show that the pull-out force of the bolt is more significant than 30kN; in addition, the numerical simulation results indicate that the roof-to-floor and rib-to-rib convergence are relatively small. Therefore, the LCS entry's minimum roof bolting seam spacing can be determined as 6 m. This study could be used to select and design roof bolting under similar close-distance coal seam conditions.

1. Introduction

The close-distance coal seam (CDCS) reserves are abundant in China [1]. Affected by mining and geological conditions, the mining method of the CDCS is primarily based on experience. Descending mining, which is widely used in the CDCS, first retreats the upper coal seam (UCS) and then develops the entry in the lower coal seam (LCS) until the overburden is stable. The entry in the LCS is mostly located under the gob or chain pillar. Due to the small seam spacing, the mining activity in the LCS will contribute to the destruction of the overburden time after time, which challenges the surrounding rock control of the entry. Therefore, seam spacing is a crucial factor in the entry's support design, especially under the gob in the LCS. Due to the UCS's mining, the LCS roof is badly damaged when the seam spacing is minimal, and the rock bolts anchor in the loose and broken surrounding rock, leading to poor roof anchoring performance. In addition, it is hard to obtain a good support effect with rock bolting. At this time, passive support such as steel arch support is supposed to be taken into account to ensure the surrounding rock stability of the LCS entry. Conversely, when the seam spacing is large, the roof of the LCS seam is relatively complete, and the rock bolt can be anchored in the stable surrounding rock. At this time, the rock bolting could reach well technical and economic effects.

The fracture and development law of the overburden of UCS in CDCS has received a great deal of research attention. Li et al. obtained the development characteristics of the overburden using the geological penetration radar [2, 3]. With a physical similarity simulation (PSS), Li et al. [4] determined the first and the periodic weighting interval of the main roof. Cui et al. [5, 6] used 3DEC to analyze the development law of the overlying strata's cracks in western China. Ning et al. [7] evaluated the height of fractured zones of the CDCS. Zhang et al. [8] researched the overburden's bearing structure and stability characteristics employing numerical simulation, PSS, and theoretical analyses.

Figure 1: The position of Chaili Coal Mine.

Several recent studies have focused on floor failure depth and stress distribution during UCS mining. Zhang et al. [9] built a floor failure mechanical model of the UCS. Sun et al. [10] proposed a mechanical model based on half-plane theory to obtain the evolution law of the floor. Tan et al. [11] utilized micro seismic techniques, numerical simulations, and borehole inspection to explore the distributions of strata failure. By using UDEC, Liu et al. [12] analyzed the stress distribution of LCS.

Recent studies have explored the LCS entry's optimal layout and surrounding rock stability control in CDCS. Wang et al. [13] suggested that the creep characteristics of surrounding rock are the most critical factor in selecting for the entry's layout of the LCS in deep mines. Wu et al. [14] built a mechanical model to research the stress distribution under chain pillars and adopted numerical simulation to select the optimal entry layout in ultra-close coal seams. Xu et al. [15] focused on the different excavation schemes in the CDCS mining and determined to leave a small coal pillar for excavation. Zhang et al. [16] established a layout of the entry using numerical simulation to minimize the risk of disasters. Zhang et al. [17] put forward the grouting reinforcement method of local fractured zones under a super thick hard roof in an ultra-close-distance coal seam. Zhang et al. [18] focused on surrounding rock stability control and technical parameter design for the gob-side entry retained under the gob.

In conclusion, a large body of literature has focused on the fracture and development law of the overburden of UCS, floor failure depth and stress distribution during UCS mining, and the optimal layout and the surrounding rock stability control of LCS entry in CDCS. As the decisive factor of surrounding rock stability control of the LCS entry, it is necessary to deepen the research on seam spacing further. Due to the complexity of mining and geological conditions, rock bolting or steel arch support is widely used in LCS entry. However, quantitative research on roof bolting technology and support parameters according to the seam spacing size has not yet been conducted. In this paper, taking the tailgate of the No.3-2 coal seam (LCS) in Chaili Coal Mine as an example, the performance of roof bolting is comprehensively studied by three methods. First, the theoretical analysis was used to calculate the maximum floor failure depth. Then, the pull-out test was carried out to determine the minimal seam spacing for roof bolting. With the thought that the distribution depth of yield zone of the floor can represent the maximum floor failure depth, the numerical model was established by FLAC3D. In addition, because the rock bolts are supposed to anchor in relatively intact rock mass, the bolts should not reach the edge of the yield zone in the numerical simulation while determining the minimal seam spacing. This study could be used to select and design roof bolting under similar CDCS conditions.

2. Mining and Geological Conditions

Chaili Coal Mine is located in Tengzhou City, Shandong Province, China, as shown in Figure 1. The current mining seam is the No.3 coal seam. No.3 coal seam is divided into No.3-1 coal seam and No.3-2 coal seam, and the thickness of these two coal seams is 4.8 m and 3.2 m, respectively. The seam spacing between No.3-1 coal seam and No.3-2 coal seam varies from 2 m to 9 m. Figure 2 shows the generalized stratigraphy column.

The panel layout for the No.3 coal seam is 150 m wide by 1766 m long, with a 5 m wide chain pillar between the panels. The tailgate in No.3-2 coal seam under the gob is developed with the dimension of 4 m long ×3.2 m wide,

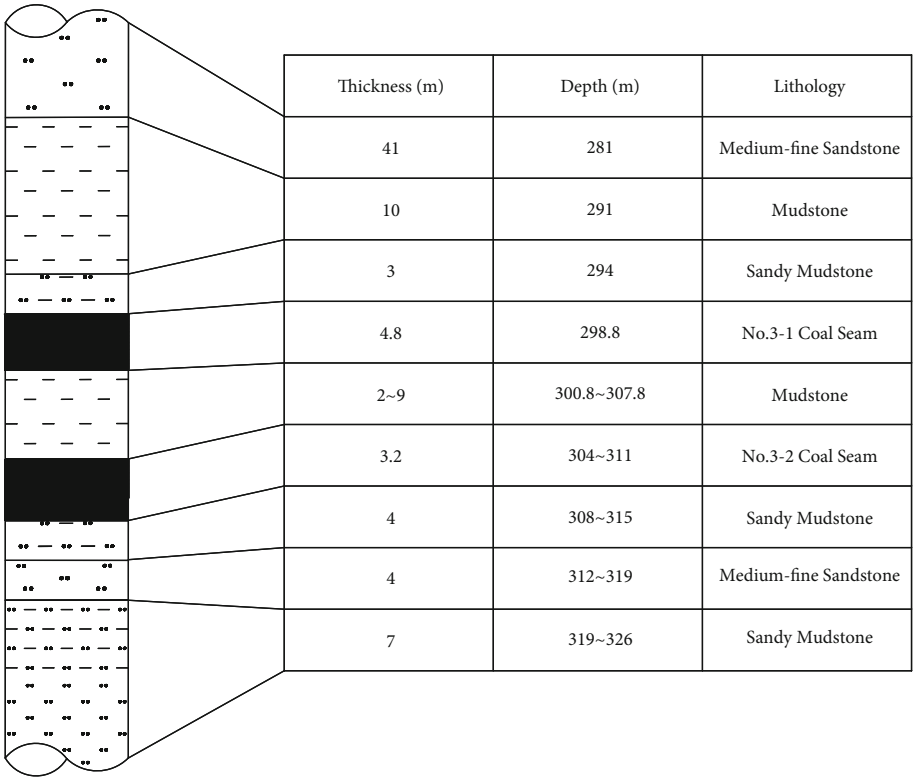

Thickness (m)	Depth (m)	Lithology
41	281	Medium-fine Sandstone
10	291	Mudstone
3	294	Sandy Mudstone
4.8	298.8	No.3-1 Coal Seam
2~9	300.8~307.8	Mudstone
3.2	304~311	No.3-2 Coal Seam
4	308~315	Sandy Mudstone
4	312~319	Medium-fine Sandstone
7	319~326	Sandy Mudstone

Figure 2: Generalized stratigraphy column.

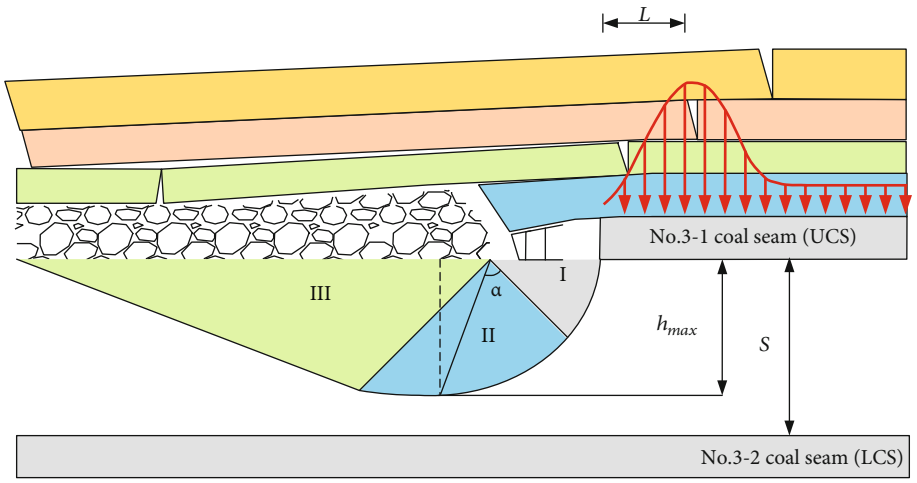

Figure 3: Schematic diagram of the failure depth of No.3-1 coal seam floor.

located directly below the tailgate of No.3-1 coal seam. Furthermore, the cross-section of the tailgate is supported by steel arches.

3. Calculation of the Floor Failure Depth of No.3-1 Coal Seam

According to Zhang [9], the floor failure mechanical model of No.3-1 coal seam (UCS) can be established as shown in Figure 3. Plastic deformation of the floor of the UCS is forming (Area I) when reaching the limit of elasticity. Up to the peak value, the plastic failure zones within the abutment pressure range are linked together, leading to the floor heave of the gob and the plastic deformation transferring from Area II to Area III, forming a continuous sliding surface. At this time, the maximum floor failure depth h_{max} is reached.

Where S is the seam spacing between No.3-1 coal seam and No.3-2 coal seam ranging from 2 m to 9 m.

h_{max} is the maximum floor failure depth of No.3-1 coal seam.

L is the distance between the peak front abutment pressure and the panel.

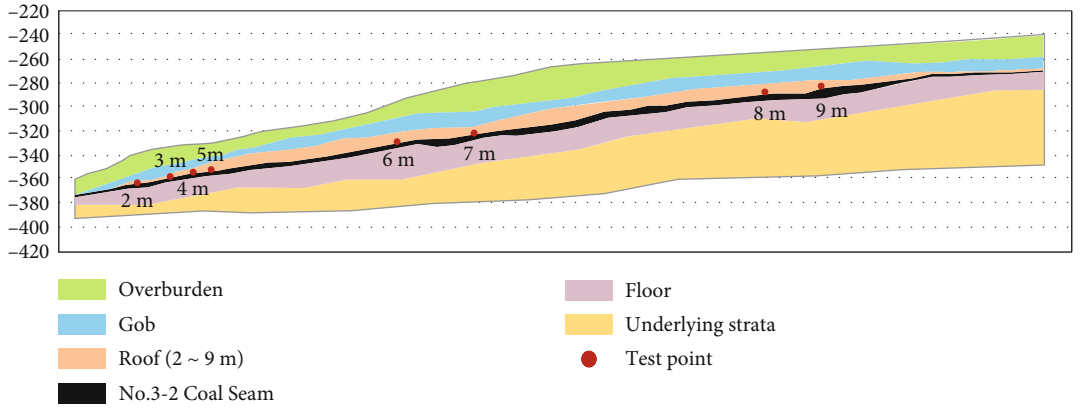

Figure 4: Arrangement of measuring points for bolt pull-out test.

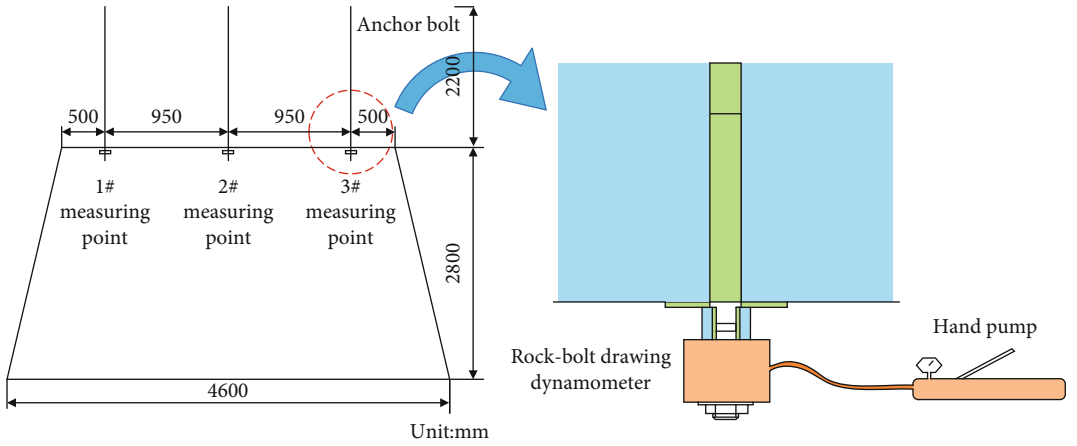

Figure 5: Installation position of test rock bolt of the entry.

Based on the research of Zhang [9] and Sun [19], the floor failure depth can be calculated by Equations (1)–(4):

$$h_{\max} = L \cdot e^{\alpha \tan \varphi_f} \cdot \sin \theta, \tag{1}$$

$$L = \frac{M}{2\zeta f} \ln \frac{K\gamma H + c \cdot \cot \varphi}{\zeta \cdot c \cdot \cot \varphi}, \tag{2}$$

$$\alpha = \varphi_f - \frac{\varphi}{2} + \frac{\pi}{4}, \tag{3}$$

$$\theta = \frac{\varphi_f}{2} + \frac{\pi}{4}, \tag{4}$$

where φ_f is the internal friction angle of the floor, 30°.

φ is the internal friction angle of the No.3-1 coal seam, 28°.

M is the height of the gob, 10.6 m.

K is the stress concentration coefficient, 1.4.

γ is the average bulk density of the overburden, 25 kN/m^3.

H is the average buried depth of the No.3-1 coal seam, 300 m.

c is the cohesion of the No.3-1 coal seam, 1.45 MPa.

f is the friction coefficient of the interface between the No.3-1 coal seam and the floor ($f = \tan \varphi$).

ζ is the triaxial stress coefficient, $\zeta = (1 + \sin \varphi)/(1 - \sin \varphi)$.

Therefore, the maximum floor failure depth of No.3-1 coal seam is as follows:

$$h_{\max} = 3.2\text{m}. \tag{5}$$

4. Roof Bolt Pull-Out Test of No.3-2 Coal Seam under the Gob of No.3-1 Coal Seam

To verify the anchorage performance of the roof of the LCS (No.3-2 coal seam) in the CDCS, the bolt pull-out test was carried out on the roof of No.3-2 coal seam to determine the minimum seam spacing of the roof bolting. If the pull-out force of the bolt is more significant than 30kN, it is considered that the roof is in good anchorage condition [20]. Otherwise, it is considered that the roof is not suitable for rock bolting.

4.1. Test Materials

(1) rock-bolt drawing dynamometer (measuring range is 200kN, and resolution is 1.0kN)

(2) jumbolter

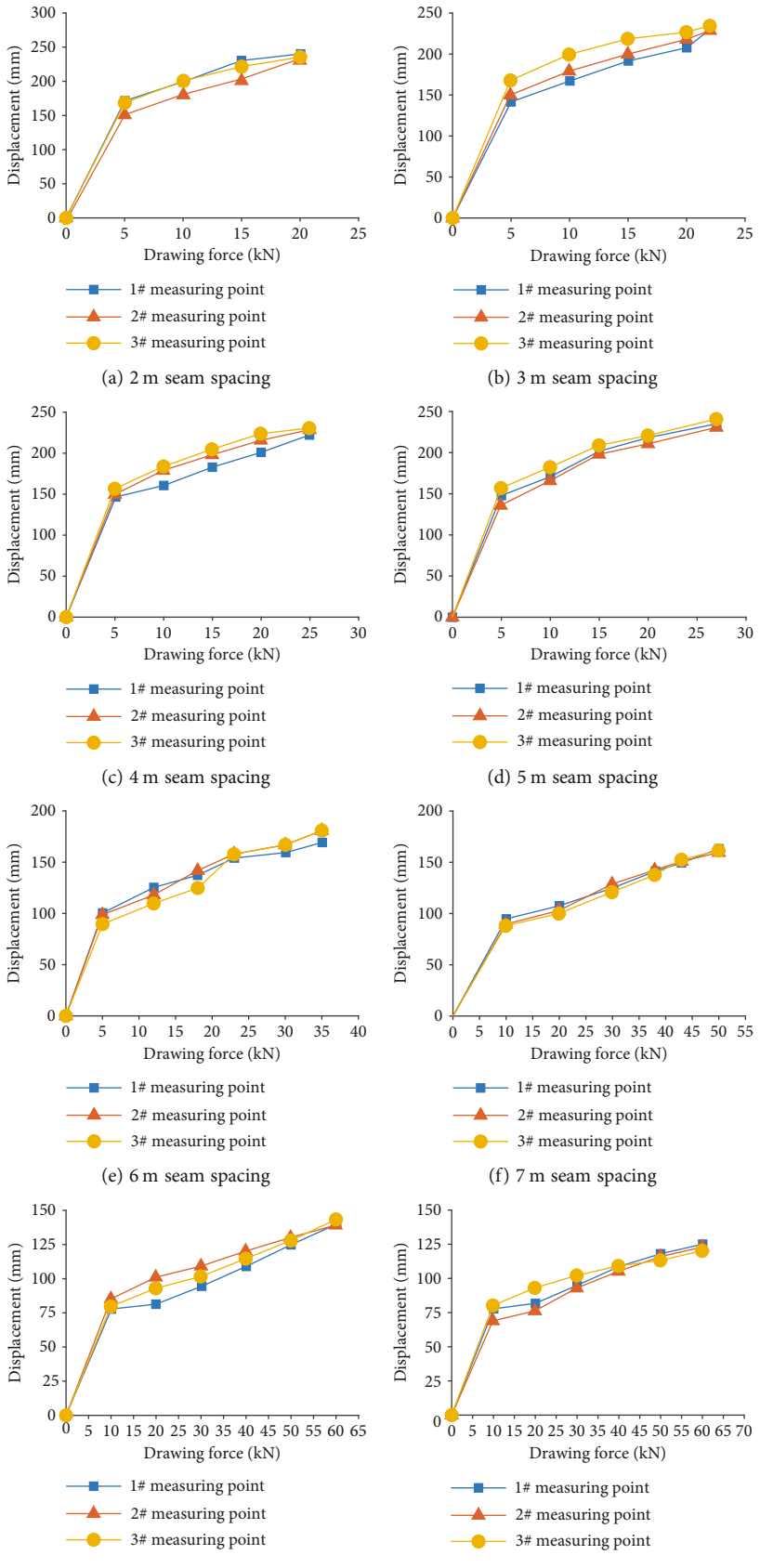

Figure 6: Drawing force-displacement curve of test rock bolt.

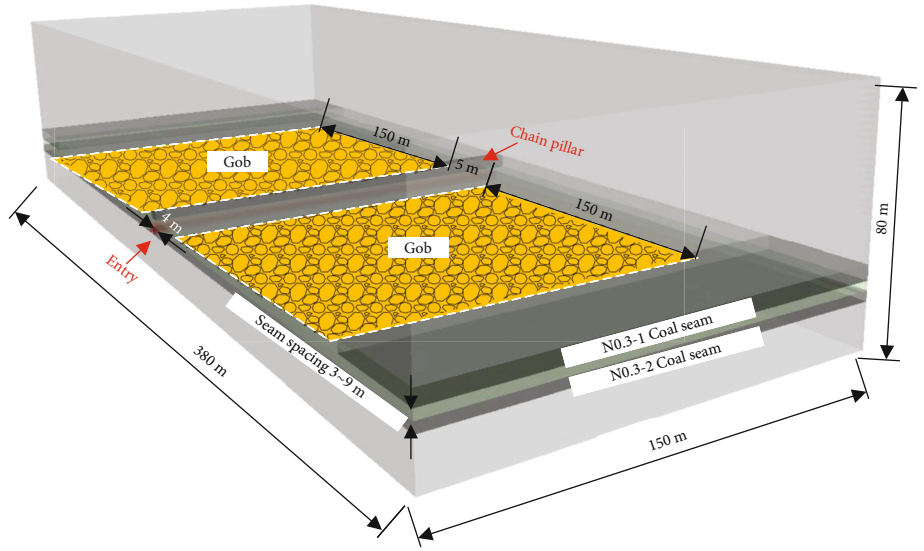

Figure 7: Configuration of the model performed using FLAC3D.

Table 1: Rock strata properties used in the numerical model.

No.	Lithology	Thickness (m)	D (kg/m^3)	K (MPa)	G (MPa)	T (MPa)	c (MPa)	f (deg)
1	Medium-fine sandstone	41	2535	4000	1500	3.00	3.50	35
2	Mudstone	10	2526	2500	1200	6.50	1.38	30
3	Sandy mudstone	3	2731	3340	3280	1.32	1.48	33
4	No.3-1 coal seam	4.8	1462	1500	1020	4.30	1.04	31
5	Mudstone	3-9	2526	2500	1200	6.50	1.38	30
6	No.3-2 mudstone	3.2	1462	1500	1020	4.30	1.04	31
7	Sandy mudstone	4	2738	1800	1100	2.00	2.50	28
8	Medium-fine sandstone	4	2731	6340	9280	4.23	3.48	33
9	Sandy mudstone	7	2731	3340	3280	1.32	1.48	33

Where D is the average density of the rock strata, kg/m^3. K is the bulk modulus of the rock strata, MPa. G is the shear modulus of the rock strata, MPa. T is the tensile strength of the rock strata, MPa. c is the cohesion of the rock strata, MPa. f is the friction angle of the rock strata, deg.

(3) rock bolt (Φ20mm × L2000mm), and resin cartridge (Φ18mm × L600mm)

4.2. Test Method. The test site is shown in Figure 4. Eight test points were arranged at a seam spacing of 2-9 m. The jumbolter was used for the roof bolt installation within two days of headgate excavation, and the bolt pull-out test was carried out within 4 hours.

As shown in Figure 5, three test rock bolts were installed on the entry roof at every test point, the side bolts were 500 mm away from the entry's rib, and the other was in the middle. During bolt installation, the bearing plate must be in close contact with the surface of the surrounding rock of the entry and the installation torque of tension nut was supposed to be relatively large (100~185 Nm) [20, 21]. Therefore, the installation torque of the tension nut was made 150 Nm. The drawing dynamometer should be coaxial with the bolt axis. Meanwhile, ensure that the bolt body does not contact the borehole wall. After installing the test bolt, apply bolt load slowly and continuously, and record bolt displacement every 5kN. Stop the pressure application and record the value of the hand pump until the test bolt fails.

4.3. Test Results and Analysis. Figure 6 indicates that with the increase of drawing force, the displacement of test bolts gradually increases under different seam spacing.

(1) As shown in Figure 6(a), when the initial drawing force reaches 5kN, the displacement of test bolts reaches 170 mm. With the increase of drawing force, the test displacement increases, and the displacement is 250 mm when the drawing force is 20kN. When the drawing force is 21kN (<30kN), all three test bolts fail, indicating that the roof bolt does not have anchor performance under the 2 m seam spacing

(2) Figures 6(b), 6(c), and 6(d) also present that when the drawing force is less than 30kN, all three bolts are pulled out at a seam spacing of 3-5 m

(3) At the 6 m seam spacing, what is striking in Figure 6(e) is that when the drawing force reaches

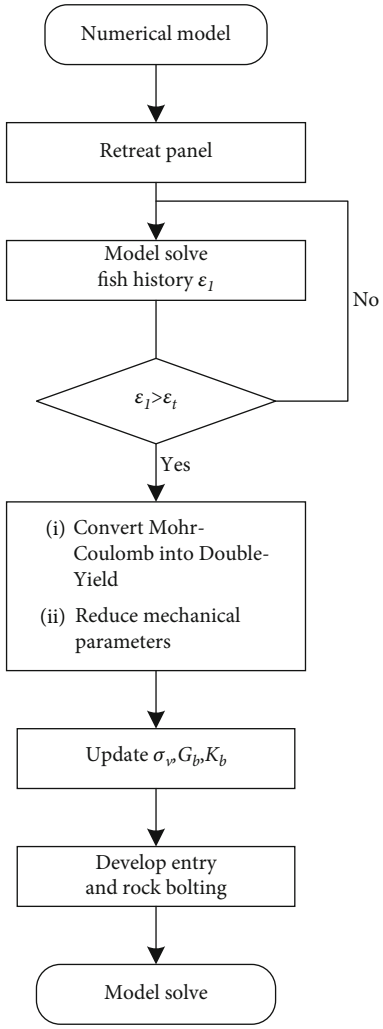

Figure 8: Numerical simulation process by FLAC3D.

30kN, the entire test bolts do not fail. Meanwhile, the displacement of the bolts is small

(4) Figures 6(f), 6(g), and 6(h) show the test results at a seam spacing of 7-9 m. When the drawing force reaches 30kN, the displacement is also small. The maximum drawing force that test bolts fail is 50kN, 60kN, and 65kN, respectively

Consequently, when the seam spacing between No.3-1 coal seam and No.3-2 coal seam is no less than 6 m, the drawing force of test bolts can reach 30kN, the roof of the entry in No.3-2 coal seam is in good anchoring condition.

5. Numerical Modeling

The floor failure depth of No.3-1 coal seam (UCS) and seam spacing significantly influence the coal entry support in the No.3-2 coal seam (LCS). According to the calculation results of the floor failure depth of No.3-1 coal seam in Section 3 and the test results in Section 4, determining the minimum seam spacing of the rock bolts may cause

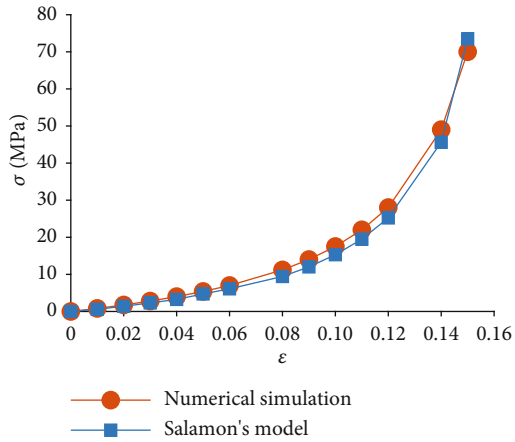

Figure 9: The stress-strain fitting curve.

safety problems. As an effective tool for studying rock mechanics behaviors in underground spaces [22, 23], this section further studies the floor failure depth of the No.3-1 coal seam after mining and the bolt anchoring performance under different seam spacing by numerical simulation.

5.1. Numerical Configuration. A numerical model (Figure 7) using FLAC3D software was established to explore the floor failure depth of No.3-2 coal seam (LCS) and the anchoring performance of roof bolting. The dimensions of the model were 380 m(length) ×150 m(width) ×80 m(height). The panel layout for No.3-1 coal seam (UCS) was 150 m wide by 150 m long with a 5 m wide chain pillar between the panels. The tailgate in No.3-2 coal seam under the gob was excavated with the dimension of 4 m long ×3.2 m wide, located directly below the tailgate of No.3-1 coal seam. A vertical load of 6 MPa was applied to the upper boundary to simulate an overburden pressure by assuming the overlying unit weight is 25kN/m^3. The final scaled rock mass properties are listed in Table 1.

5.2. Simulation Plans. Where σ_v is the vertical stress where the overlying strata apply on gangue.

G_b is the shear modulus of the gangue in the gob.

K_b is the bulk modulus of the gangue in the gob.

As shown in Figure 8, the numerical model was solved in this simulation using the following steps:

(1) the retreat of the two panels of No.3-1 coal seam (UCS) after initial balance, respectively

(2) the development of the entry of No.3-2 coal seam (LCS) with seven different seam spacing (3-9 m)

The caved materials are then compacted and consolidated after panel advances far enough in longwall mining [24, 25]. Consequently, the entry of the LCS in CDCS is supposed to develop until the gob is generally consolidated. The constitutive model applied in the caved zone is Double-Yield to simulate this actual situation. In

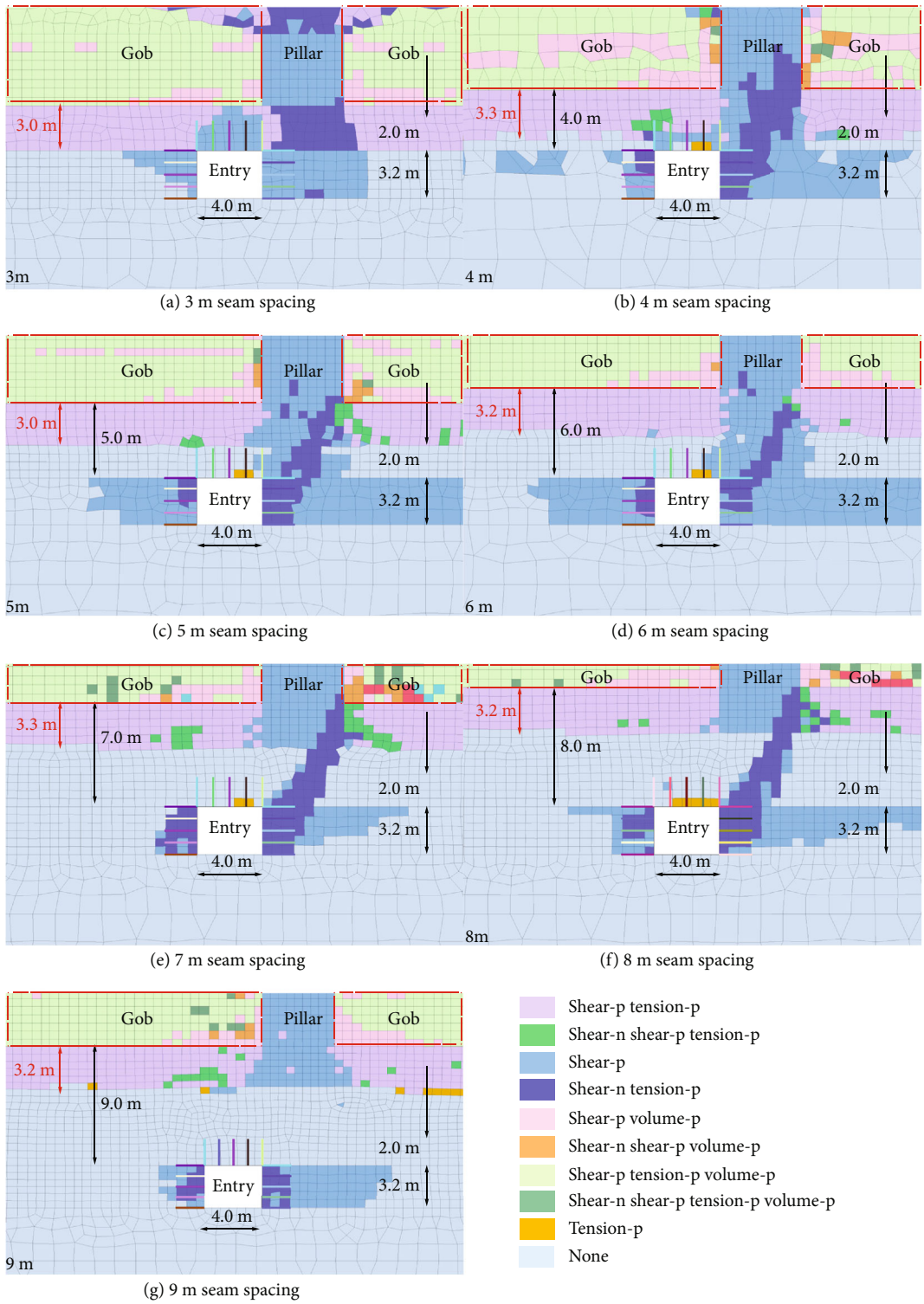

Figure 10: Yield zone distributions around entry for different seam spacing.

addition, the Saint Venant theory is used to determine the range of caved zone, which is given by

$$\varepsilon_1 > \varepsilon_t, \tag{6}$$

where ε_1 is the maximum principal strain.

ε_t is the critical value of tensile strain.

Precisely, the two panels retreated in the No.3-1 coal seam (UCS) after several timesteps. According to Equation (6), when $\varepsilon_1 > \varepsilon_t$, it is considered that the overburden of the UCS has collapsed. Therefore, customize the function in fish to determine the range of caved zone, and compare the results with those calculated by empirical formula, as shown in Figure 9. If the range of caved zone is consistent with the

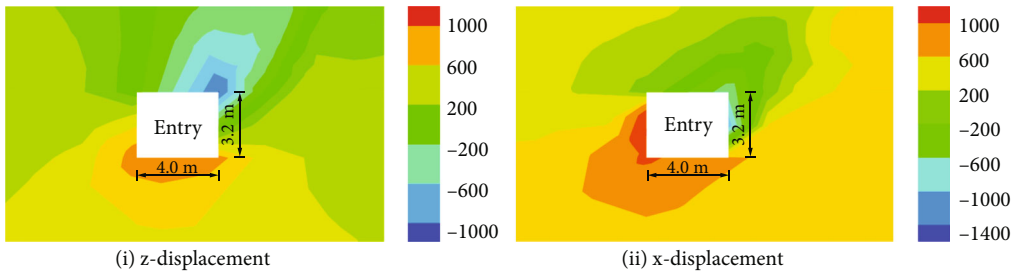

(i) z-displacement (ii) x-displacement

(a) 3 m seam spacing

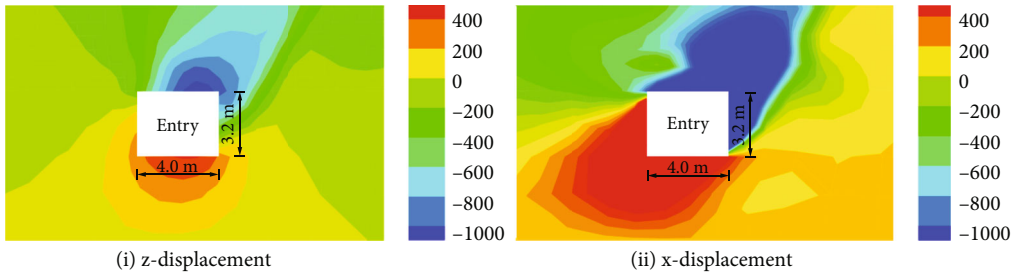

(i) z-displacement (ii) x-displacement

(b) 4 m seam spacing

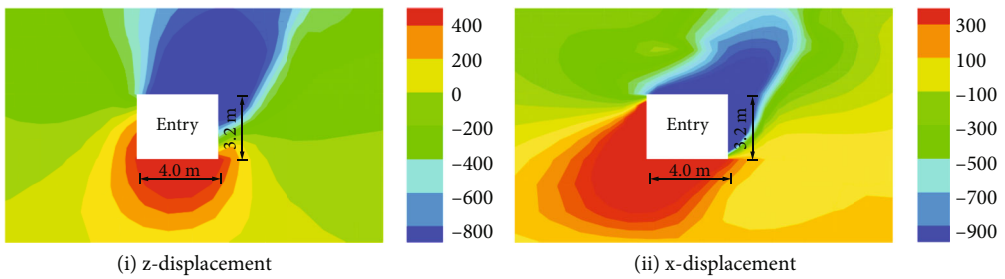

(i) z-displacement (ii) x-displacement

(c) 5 m seam spacing

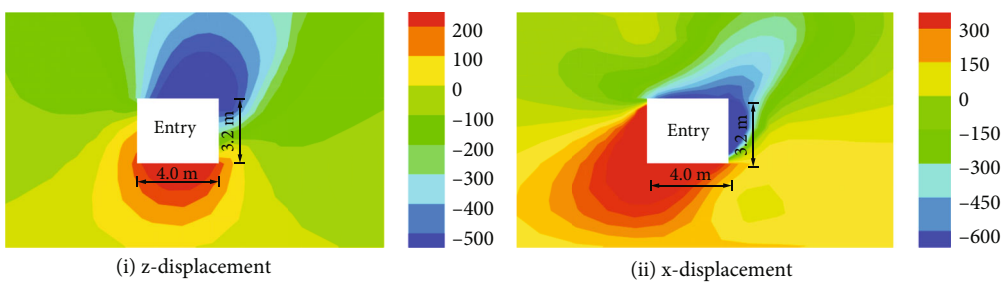

(i) z-displacement (ii) x-displacement

(d) 6 m seam spacing

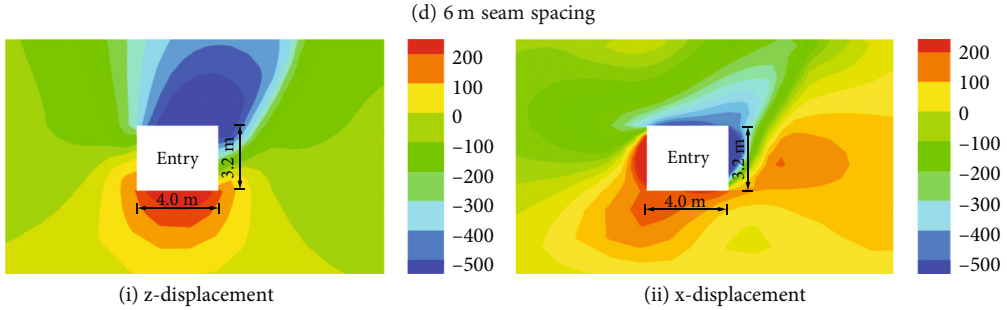

(i) z-displacement (ii) x-displacement

(e) 7 m seam spacing

Figure 11: Continued.

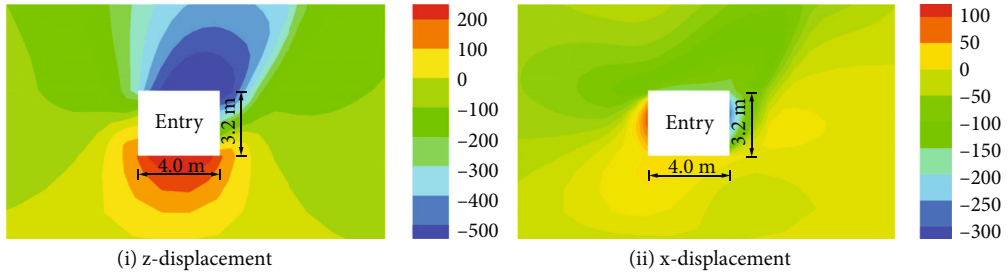

(i) z-displacement (ii) x-displacement

(f) 8 m seam spacing

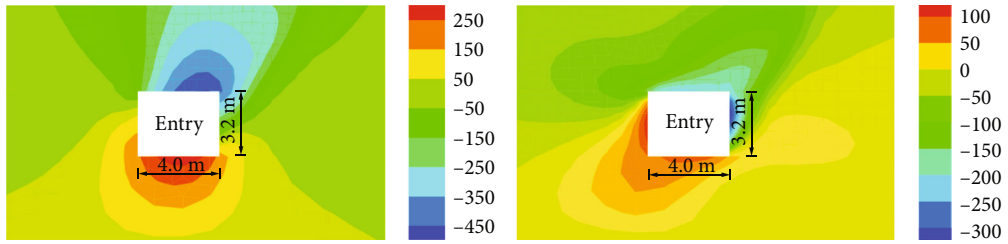

(i) z-displacement (ii) x-displacement

(g) 9 m seam spacing

Figure 11: Displacement distribution around entry for different seam spacing.

result of empirical formula [26], then convert the constitutive model of caved zone from Mohr-Coulomb to Double-Yield. At the same time, the mechanical parameters in the yield zone are reduced to simulate the fractured zone, the vertical stress σ_v, volume modulus K_b, and the shear modulus G_b of the gangue in the gob are updated at regular intervals until the balance is calculated. Based on the research of Bai et al. [27], the properties of double-yield constitutive model can be given by

$$K_b = \frac{4G_b}{3} = \frac{\sigma_v}{2\varepsilon}. \tag{7}$$

As shown in Equation (7), the volume modulus K_b, the shear modulus G_b and the vertical stress σ_v can be expressed as a function of the vertical strain ε. Consequently, after several intervals, such as 50 timesteps, the vertical strain of the gob material is recorded in numerical simulation, and then changes these properties according to Equation (7). Then, the LCS entry is developed once every 5 m and rock bolting until the end of the development.

5.3. Yield Zone Distribution around Entry for Different Seam Spacing. This part is set out to seek the proper seam spacing for roof bolting of the entry of No.3-2 coal seam (LCS). The floor failure depth is reflected by the yield zone of the floor of No.3-1 coal seam (UCS). According to suspension theory, rock bolts are supposed to anchor in relatively intact rock strata. Therefore, the end of the rock bolt had better anchor out of the yield zone. Figure 10 shows the yield zone distribution around entry for different seam spacing (3-9 m).

Figure 10 shows that with the increase of seam spacing, the floor failure depth (ranging from 3.0 to 3.3 m) of No.3-1 coal seam (UCS) has no noticeable change, but the yield zone around the entry, particularly the roof, gradually decreases.

(1) Figures 10(a), 10(b), and 10(c) show the yield zone distribution at a seam spacing of 3-5 m. It can thus be seen, the yield zone around entry is large, and the rock bolt cannot anchor in relatively intact rock strata

(2) At the 6 m seam spacing, what stands out in Figure 10(d) is that the end of the rock bolt exactly anchors out of the yield zone. Meanwhile, the distribution of yield zone around entry is small

(3) Figures 10(e), 10(f), and 10(g) also present the distribution of yield zone around entry is not large, and the rock bolt can anchor in the relatively intact rock strata

(4) Thus, when the seam spacing between No.3-1 coal seam and No.3-2 coal seam is no less than 6 m, the distribution of yield zone is not large, and the rock bolt can anchor in relatively intact rock strata

5.4. Deformation of Surrounding Rock of the Entry for Different Seam Spacing. It is one of the purposes of rock bolting to control the deformation of surrounding rock. Figure 11 shows the deformation of the surrounding rock of the entry for different seam spacing.

As shown in Figures 11 and 12, with the increase of seam spacing, the convergence of roof-to-floor and rib-to-rib gradually decreases. In addition, the convergence of the right rib is greater than the left rib.

(1) At 5 m seam spacing, the convergence of roof-to-floor and rib-to-rib is 801 mm and 1261 mm,

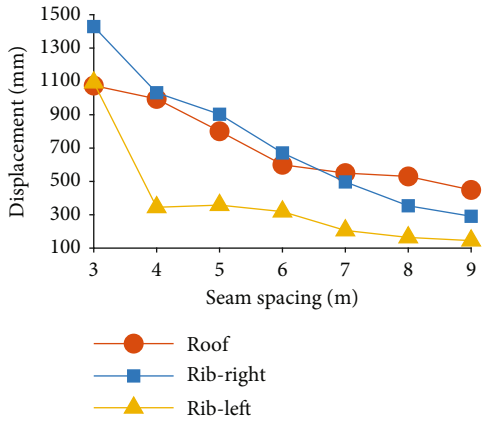

FIGURE 12: Simulation displacement of surrounding rock of the entry for different seam spacing.

respectively. The surrounding rock deformation of the entry is quite large, indicating that the rock bolting performance is terrible.

(2) When the seam spacing is no less than 6 m, the convergence of roof-to-floor and rib-to-rib is relatively small. At 6 m seam spacing, the convergence of roof-to-floor and rib-to-rib is 600 mm and 990 mm, respectively. At 9 m seam spacing, the convergence of roof-to-floor and rib-to-rib is 449 mm and 436 mm, respectively. Compared with the seam spacing of 3-5 m, the surrounding rock of the entry is well controlled.

Consequently, when the seam spacing is no less than 6 m, the rock deformation of the entry is relatively small, the yield zone around the entry is under control, and the rock bolting performance is relatively good.

6. Discussion

In Section 3, through theoretical analysis, it was found that the peak value of front abutment pressure is 2.5 m in front of the panel, and then the floor failure depth of the No.3-1 coal seam (UCS) was 3.2 m. Compared to the previous calculation results, the value of L is minor, mainly because the buried depth H of the No.3-1 coal seam (UCS) is small, and L is closely related to H (see Equation (2)).

The result of the pull-out test of roof bolting in Section 4 showed that the pull-out force of bolt can reach 30kN at the seam spacing of more than 6 m, suggesting that the rock bolts can be anchored in the relatively intact rock strata, which was consistent with the suspension theory.

Section 5 determined that the maximum failure depth of the No.3-1 coal seam (UCS) is 3.0-3.3 m by numerical simulation, which was consistent with the theoretical analysis results in Section 3. Furthermore, the simulation results showed that the rock bolting performance is good when the seam spacing exceeds 6 m, which coincided with the pull-out test in Section 4.

What is noteworthy is that this work was based on Chaili Coal Mine. Due to different mining and geological conditions, the applicability of presented theoretical analysis, pull-out test, and numerical simulation methods on other coal mines should be further studied.

7. Conclusions

(1) The maximum floor failure depth calculated by the theoretical analysis was 3.2 m. Generally, the anchorage length of the rock bolt is less than 2.4 m. Thus, the roof bolting seam spacing is at least 5.6 m.

(2) The pull-out bolt test was carried out on the lower coal seam's entry roof. The results show that when the seam spacing is no less than 6 m, the drawing force is more significant than 30kN. Therefore, the minimum seam spacing of roof bolting is taken as 6 m.

(3) Numerical simulation was set out to seek the floor failure depth and the performance of roof bolting. Simulation results show that the floor failure depth of the upper coal seam is 3.0-3.3 m. Compared with 3-5 m seam spacing, when the seam spacing is no less than 6 m, the yield zone of the lower coal seam's roof is relatively not large. The surrounding rock deformation of the entry significantly decreases, indicating that the performance of roof bolting is good.

In conclusion, through theoretical analysis, pull-out bolt test, and numerical simulation, this paper determines the minimum seam spacing of roof bolting is 6 m, where the entry under the gob of the close-distance coal seam. This study quantitatively studies the influence of seam spacing on selecting support methods, providing a reference for roof bolting design of coal entry under similar conditions.

Data Availability

The data used to support the findings of this study are available from the corresponding author upon request.

Conflicts of Interest

The authors declare that they have no conflicts of interest.

Acknowledgments

This research was funded by the National Natural Science Foundation of China (Grant nos. 51574156 and 52074166).

References

[1] S. Jie, L. Zhen-hua, H. Cun-han, C. Zheng-zheng, X. You-lin, and C. Zu-guo, "Catastrophe mechanism of stress-fissure coupling field in mining close distance seams in Southwest China," *Geofluids*, vol. 2021, 9 pages, 2021.

[2] Y. Li, Y. Ren, S. Peng, H. Cheng, N. Wang, and J. Luo, "Measurement of overburden failure zones in close-multiple coal

seams mining," *International Journal of Mining Science and Technology*, vol. 31, no. 1, pp. 43–50, 2021.

[3] Y. Li, J. Wang, Y. Chen, Z. Wang, and J. Wang, "Overlying strata movement with ground penetrating radar detection in close-multiple coal seams mining," *International Journal of Distributed Sensor Networks*, vol. 15, no. 8, 2019.

[4] X. Li, W. He, and Z. Xu, "Study on law of overlying strata breakage and migration in downward mining of extremely close coal seams by physical similarity simulation," *Advances in Civil Engineering*, vol. 2020, 11 pages, 2020.

[5] F. Cui, C. Jia, X. Lai, Y. Yang, and S. Dong, "Study on the law of fracture evolution under repeated mining of close-distance coal seams," *Energies*, vol. 13, no. 22, p. 6064, 2020.

[6] F. Cui, C. Jia, and X. Lai, "Study on deformation and energy release characteristics of overlying strata under different mining sequence in close coal seam group based on similar material simulation," *Energies*, vol. 12, no. 23, p. 4485, 2019.

[7] J. Ning, J. Wang, Y. Tan, and Q. Xu, "Mechanical mechanism of overlying strata breaking and development of fractured zone during close-distance coal seam group mining," *International Journal of Mining Science and Technology*, vol. 30, no. 2, pp. 207–215, 2020.

[8] J. Zhang and B. Wang, "Study on the bearing structure and stability of overlying strata: an interval gob in shallow buried coal mining of Northwest China," *Arabian Journal of Geosciences*, vol. 14, no. 4, 2021.

[9] W. Zhang, D. Zhang, D. Qi, W. Hu, Z. He, and W. Zhang, "Floor failure depth of upper coal seam during close coal seams mining and its novel detection method," *Energy Exploration & Exploitation*, vol. 36, no. 5, pp. 1265–1278, 2018.

[10] Z. Sun, Y. Wu, Z. Lu, Y. Feng, X. Chu, and K. Yi, "Stability analysis and derived control measures for rock surrounding a roadway in a lower coal seam under concentrated stress of a coal pillar," *Shock and Vibration*, vol. 2020, 12 pages, 2020.

[11] Y. Tan, T. Zhao, and Y. Xiao, "In situ investigations of failure zone of floor strata in mining close distance coal seams," *International Journal of Rock Mechanics and Mining Sciences*, vol. 47, no. 5, pp. 865–870, 2010.

[12] X. Liu, X. Li, and W. Pan, "Analysis on the floor stress distribution and roadway position in the close distance coal seams," *Arabian Journal of Geosciences*, vol. 9, no. 2, 2016.

[13] X. Wang, J. Wang, X. Chen, and Z. Chen, "A roadway in close distance to coal seam in deep mine: location selection and supporting practice based on creep characteristics of surrounding rocks," *Archives of Mining Sciences*, vol. 66, no. 3, pp. 407–419, 2021.

[14] G. Wu, X. Fang, H. Bai, M. Liang, and X. Hu, "Optimization of roadway layout in ultra-close coal seams: a case study," *PLoS One*, vol. 13, no. 11, article e0207447, 2018.

[15] X. Gao, S. Zhang, Y. Zi, and S. K. Pathan, "Study on optimum layout of roadway in close coal seam," *Arabian Journal of Geosciences*, vol. 13, no. 15, 2020.

[16] Y. Zhang, J. Yang, J. Zhang et al., "Modeling the spatial and temporal evolution of stress during multiworking face mining in close distance coal seams," *Advances in Civil Engineering*, vol. 2021, Article ID 5624972, 11 pages, 2021.

[17] W. Zhang, J. Guo, K. Xie et al., "Comprehensive technical support for safe mining in ultra-close coal seams: a case study," *Energy Exploration & Exploitation*, vol. 39, no. 4, pp. 1195–1214, 2021.

[18] Z. Zhang, M. Deng, J. Bai, S. Yan, and X. Yu, "Stability control of gob-side entry retained under the gob with close distance coal seams," *International Journal of Mining Science and Technology*, vol. 31, no. 2, pp. 321–332, 2021.

[19] W. Sun, Z. Qin, Q. Li, G. Chen, and T. Li, "Study on optimization of roadway position in pre-mining upper layered concave–convex coal body," *Geotechnical and Geological Engineering*, vol. 37, no. 5, pp. 3739–3748, 2019.

[20] Z M G o S Energy, *Technical Specifications for Rock Bolting in Coal Mine Roadways in Zibo Mining Group*, China Coal Industry Publishing House, Beijing, 2013.

[21] Technical specifications for rock bolting in coal mine roadways, GB/T 35056-2018. (2018).

[22] Z. Guangchao, Z. Chuanwei, C. Miao et al., "Ground response of entries driven adjacent to a retreating longwall panel," *International Journal of Rock Mechanics and Mining Sciences*, vol. 138, p. 104630, 2021.

[23] G. Zhang, Z. Wen, S. Liang et al., "Ground response of a gob-side entry in a longwall panel extracting 17 m-thick coal seam: a case study," *Rock Mechanics and Rock Engineering*, vol. 53, no. 2, p. 497, 2020.

[24] G. Zhang, F. He, H. Jia, and Y. H. Lai, "Analysis of gateroad stability in relation to yield pillar size: a case study," *Rock Mechanics and Rock Engineering*, vol. 50, no. 5, pp. 1263–1278, 2017.

[25] G. Zhang, Y. Li, X. Meng et al., "Distribution law of in situ stress and its engineering application in rock burst control in Juye mining area," *Energies*, vol. 15, no. 4, p. 1267, 2022.

[26] G. Zhu, B. Liu, L. Dou, Y. P. Wu, and Z. W. Ding, "Numerical simulation for whole process of longwall mining on the basis of goaf compaction effect," *Journal of China University of Mining and Technology*, vol. 48, no. 4, pp. 775–783, 2019.

[27] Q. Bai, S. Tu, Y. Yuan, and F. T. Wang, "Back analysis of mining induced responses on the basis of goaf compaction theory," *Journal of China University of Mining and Technology*, vol. 42, no. 3, p. 355, 2013.

Hindawi
Geofluids
Volume 2022, Article ID 1608734, 13 pages
https://doi.org/10.1155/2022/1608734

Research Article

A New Evaluation Method for Water Blocking Performance of Coal Seam Floor: Model Construction, Case Application, and Water-Preserved Strategy

Baobin Gao,[1,2,3,4] Chuangnan Ren,[1,2] and Shaopeng Song[1,2]

[1]*State Collaborative Innovation Center of Coal Work Safety and Clean-Efficiency Utilization, Jiaozuo, Henan 454000, China*
[2]*State Key Laboratory Cultivation Base for Gas Geology and Gas Control, Henan Polytechnic University, Jiaozuo, 454000 Henan, China*
[3]*Key Laboratory of Resources, Environment and Disaster Monitoring of Shanxi Province, Taiyuan, 030000 Shanxi, China*
[4]*Henan Key Laboratory of Underground Engineering and Disaster Prevention (Henan Polytechnic University), Jiaozuo, 454000 Henan, China*

Correspondence should be addressed to Chuangnan Ren; chuangnanrcn@163.com

Received 21 December 2021; Revised 3 March 2022; Accepted 15 April 2022; Published 2 May 2022

Academic Editor: Gangwei Fan

In order to scientifically guide the water-preserved mining of the coal seam floor and make up for the shortcomings in the conventional evaluation of water blocking performance of the coal seam floor, according to the system resilience theory, the difference between the vulnerability and resilience of the coal seam floor is analyzed, and three elements and nine indicators for evaluating water resistance toughness of the coal seam floor are determined. In the evaluation process, first of all, the maximum difference normalization method is used to conduct a dimensionless analysis of quantifiable indicators to determine the importance of the corresponding indicators, and the AHP software yaahp10.1 is used to determine the weight vector of each indicator. Secondly, the single-factor membership degree is determined according to the single-factor resilience grade classification criterion and membership function and finally combined with the weight vector for fuzzy synthesis calculation and comprehensive evaluation. The model is applied to a specific project. Research has shown that in the water hazard threat area of No. 10 coal seam floor in Jiegou Coal Mine, Anhui Province, the performance of system vulnerability elements is weak, the performance of system recoverability elements is better, and the performance of system adaptability elements is extremely poor. From the perspective of the whole life cycle, determining the treatment target area, optimizing the rock formation modification and repairing materials, and enhancing the water resources carrying capacity can improve the water resistance toughness of the coal seam floor. Related conclusions verify the effectiveness of the evaluation model. Furthermore, an optimized strategy for coal seam floor water retention mining is proposed: the technology system of water-preserved mining for coal seam floor contains 3 stages and 3 detections, which provides a scientific basis for the in situ protection of high-pressure limestone water from coal seam floor.

1. Introduction

With the needs of national economic development, since 1999, the coal industry has developed rapidly, and a series of environmental problems caused by coal development have emerged [1]. Under the background of the new era, the situation of water resources and water environmental protection is urgent, and the protection of water resources in the mining of coal resources has attracted much attention, especially in areas where limestone water is an important water source for local industrial, agricultural, and domestic water and mine limestone water resources. The in situ protection has become an important part of water-preserved mining and has been included in the green mining system [2, 3]. In 2003, Academicians Qian et al. proposed water-preserving mining technology for coal mines [4].

Subsequently, the water-preserving coal mining team represented by Fan et al. proposed "a reasonable selection of development areas and appropriate coal mining methods" in 2005 to realize coal mining. Research ideas for water resources protection in the process. In recent years, relevant scholars have conducted a lot of theoretical innovation and technical application research on coal seam roof and floor water-preserved mining. In terms of coal seam floor water-preserved mining, Fan et al.'s team [5] from the Key Laboratory of Exploration and Comprehensive Utilization of Mineral Resources, Xi'an, China, Dong et al.'s team from Xi'an Research Institute of China Coal Technology Engineering Group [6, 7], and Zhang et al.'s team from China University of Mining and Technology [8, 9] have used drilling and grouting techniques to carry out engineering practices in China's central and western coal fields and initially achieved effective results.

As a key indicator of coal seam floor, water blocking performance is one of the main research points in the field of floor water hazard prevention and water-preserved mining on confined water. Over the years, domestic and foreign scholars have paid more attention to the vulnerability of the floor system in the research on the water blocking performance of coal seam floor [10–12]. Vulnerability refers to the possibility of damage to the system's subsystems and components under external pressure. Resilience was originally a concept in physics, representing the ability of a material to absorb energy during plastic deformation and fracture. In the 1970s, ecologist Holling firstly used resilience to describe the persistence of natural systems and the ability to absorb various changes and disturbances; Bi et al. believe that the definition of resilience should focus on three capabilities: the system's ability to reduce the probability of being affected by adverse events, the ability to absorb disturbances after an adverse event occurs, and the ability to quickly rebuild system performance [13]. At present, in the field of urban system disaster prevention and mitigation engineering, it is generally believed that resilience and reliability, vulnerability, and adaptability are all important concepts of security risk management. From the perspective of the full life cycle of the system, vulnerability is an important stage in the evolution of system performance; resilience can be understood as corresponding to the entire process of system performance evolution. The research from vulnerability to system resilience reflects the cognitive transformation process of the concept of disaster prevention and mitigation from rigid resisting confrontation emphasizing resistance to flexible resolution emphasizing adaptation [14, 15], which can help decision-makers formulate more scientific and reasonable water-preserved mining plans for coal seam floor. In the past, most of the evaluation of the water blocking performance of the coal seam floor focused on the evaluation of the risk of water inrush from the floor [16–18]. As a staged safety assessment, the water inrush risk assessment provides a scientific basis for further floor water damage management. However, it should be noted that the water blocking performance of the coal seam floor will change with the intervention of safety technology and the impact of the ecological environment. Traditional floor water blocking performance evaluation is limited by the staged thinking in the evaluation index system and does not fully consider the impact of water-preserved mining technology. At the same time, it ignores the relevant factors related to the ecological environment of the mining area [19]. In addition, in terms of evaluation methods, expert scoring methods are usually used to obtain weights and membership degrees. For quantifiable index factors, dimensionless processing is rarely used to obtain weights. With the continuous development of the theory and technology of water-preserving mining on confined water, this type of evaluation model is obviously unable to meet the needs of evaluation.

In view of this, based on the system toughness theory and from the perspective of the whole life cycle, a water resistance toughness evaluation model applicable to the water retention mining of coal seam floor is provided. Further, the model is applied to specific engineering cases. As a whole life cycle evaluation model, the model is not limited to a certain stage of system development and was aimed at providing a whole life cycle evaluation and optimization basis for in situ protection of highly pressurized tuff water in coal seam floor to achieve the protection of water resources and water environment in coal mines.

2. Evaluation Model Construction

2.1. Selection of Evaluation Indicators

2.1.1. The Water Resistance Toughness of Coal Seam Floor. Regarding the relationship between vulnerability and resilience, both are considered to be the intrinsic properties of the system and are easily affected by the external environment. The difference is that vulnerability focuses on the risk of damage to the system under the influence of disturbances when a disaster occurs, involving the partial phases of the system's life cycle, while resilience emphasizes the system's ability to withstand disasters and the ability to recover from disasters, corresponding to the entire life cycle of the system [20]. Vulnerability analysis is an essential part of maintaining system stability, preventing system damage, and improving system resilience. It is reflected in the risk analysis and control before disturbance events. Resilience analysis focuses on the whole process of system performance recovery and readaptation when the disturbance event occurs afterwards. According to the evolution law of system resilience under disturbance, the water resistance toughness of coal seam floor should include four stages: stabilization, destruction, recovery, and adaptation [21]. Based on the above point of view, from the perspective of the life cycle of the system, the resilience evolution curve of the coal seam floor under disturbance is shown in Figure 1.

According to Figure 1, when the system's resilience drops to a minimum, the system's performance changes from vulnerability to resilience. Generally, it takes a long time to realize self-recovery and readaptation with the help of system ontology elements, so technical intervention needs to be considered. Moreover, the final system performance improvement or degradation depends on the degree of compatibility of the system with the external environment. In

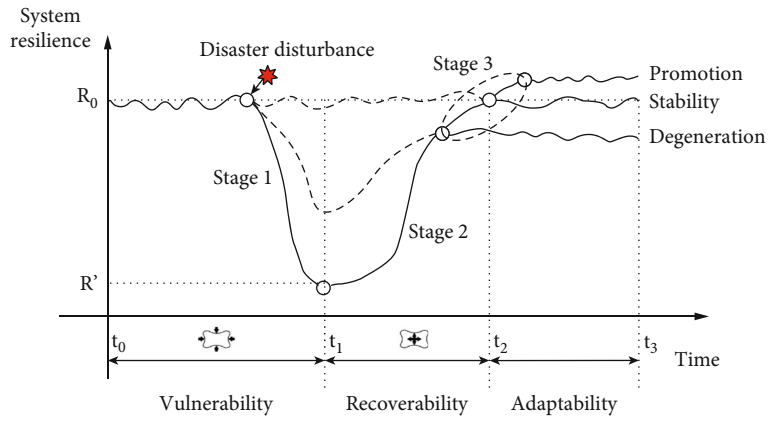

Figure 1: The resilience evolution curve of coal seam floor under disturbance.

summary, it can be initially obtained that the key elements that affect the performance of the system should include three elements: system vulnerability, system recoverability, and system adaptability. This is similar to the viewpoints of the four important elements of man-machine-environment-management in safety system engineering. The difference is that safety system engineering focuses on phased risk management and control, and system resilience theory is based on the sustainable development of the whole life cycle. The water resistance toughness of the coal seam floor is a key indicator for water-preserved mining on confined water, and it needs to be considered from the perspective of the system's full life cycle.

(1) Stage 1 ($t_0 - t_1$) corresponds to system vulnerability, where the scientific level involves engineering geological features and the technical level should focus on the identification of target areas for treatment. At this stage, the system can still operate normally, but the risk already exists. If the risk can be effectively controlled in the early stage and not allowed to continue to evolve into an accident potential, the system can remain stable. In theory, it exists, but it is usually unrealistic in specific projects, and there is no absolute safe state. When the risk further evolves into an accident potential, the system has developed to stage 1. The factors affecting the development of stage 1 are related to the mining engineering geology, including the original geological factors and the influence of mining on geological factors, collectively referred to as system vulnerability elements

(2) Stage 2 ($t_1 - t_2$) corresponds to systematic restorability, and the scientific level involves the mechanism of coal seam floor restoration, and the technical level should focus on the modification of rock seam restoration. This stage occurs after stage 1, where the accident potential has caused some accident damage, but the system still maintains some robustness. In turn, the system performance starts to recover under the condition of self-repair or external technical intervention. Self-repair is rare, so the factors affecting the development of stage 2 are related to the coal seam floor water damage management technology, involving drilling, grouting, and other key technical parameters, collectively referred to as system recoverability elements

(3) Stage 3 ($t_2 - t_3$) corresponds to system adaptability, the scientific level involves the water carrying capacity of the coal mine, and the technical level should focus on the evaluation of the effect of water preservation mining. This stage is influenced by the resilience and ecological compatibility of the system and may result in three types of outcomes: promotion, stability, or degeneration, which to some extent reflects the adaptability of the system. Factors affecting stage 3 include surface ecological governance and water resources carrying capacity, which are collectively referred to as system adaptability elements

2.1.2. Establishment of Evaluation Index System. In summary, according to the analysis of the water resistance toughness of the coal seam floor, the criterion layer of the evaluation index for the water resistance toughness of the floor is determined: system vulnerability elements *A*, system recoverability elements *B*, and system adaptability elements *C*. Among them, system vulnerability elements are consistent with the vulnerability evaluation indicators. The difference is that the resilience evaluation considers its compression resistance and self-recoverability, and the vulnerability considers the possibility of damage. System recoverability elements involve the modification and repair of the floor rock. At present, the commonly used technical method is grouting reinforcement, so technical indicators related to drilling, grouting, and detection need to be considered. System adaptability elements involve the surface and mine water environmental carrying capacity. If the surface ecology of the mining area is poor and the groundwater is seriously polluted, it will indirectly affect the water resistance toughness of the coal seam floor. The evaluation index system is detailed in Table 1.

Table 1: Evaluation index system of water resistance toughness of coal seam floor.

Target layer	Criterion layer	Indicator layer
Water resistance toughness of coal seam floor X	System vulnerability elements A	Coal seam mining impact $A1$
		Performance of the water-resisting strata $A2$
		Water inrush intensity of aquifer $A3$
		Influence of geological structure $A4$
	System recoverability elements B	Drilling technology $B1$
		Reinforcement technology $B2$
		Detection technology $B3$
	System adaptability elements C	Surface ecological governance $C1$
		Water resources carrying capacity $C2$

Coal seam mining impact $A1$ can be further refined into influencing factors such as coal seam mining depth, coal seam inclination, coal seam mining height and thickness, working surface size, coal seam mining intensity, and overburden rock load. Performance of the water-resisting strata $A2$ can be further refined into influencing factors such as waterproof rock layer thickness, lithology and strata combination, location of the water-retaining rock formation, the inclination angle of the water-resistant rock formation, and development height of conduction zone. Water inrush intensity of aquifer $A3$ can be further refined into influencing factors such as water pressure of aquifer, water richness of aquifer, and permeability of aquifer. Influence of geological structure $A4$ can be further refined into influencing factors such as fault development degree, location of folds, karst collapse column situation, and ancient weathering crust situation. Drilling technology $B1$ can be further refined into influencing factors such as selection of drilling method, drilling layout plan, and drilling construction technology. Reinforcement technology $B2$ can be further refined into influencing factors such as selection of grouting method, grouting materials and pulping process, and determination of grouting parameters. Detection technology $B3$ can be further refined into influencing factors such as geological exploration before drilling, detection of grouting effect, and advance detection before mining. Surface ecological governance $C1$ can be further refined into influencing factors such as vegetation coverage rate, mining subsidence degree, and surface water status. Water resources carrying capacity $C2$ can be further refined into influencing factors such as mine water replenishment status, pollution degree of mine water, and utilization rate of mine water.

2.2. Construction of Evaluation Model

2.2.1. Evaluation Methods

(1) Maximum Difference Normalization Method. Since the different dimensions of each influencing factor will affect the final result, the data needs to be normalized. The normalization formula is shown in formulas (1) and (2).

For the index factors that can improve the performance of the system, the larger the quantified value, the positive correlation formula is selected to normalize, such as the waterproof rock layer thickness d.

$$X_i = \frac{x_i - \min(x_i)}{\max(x_i) - \min(x_i)}. \quad (1)$$

For the index factors that reduce the performance of the system, the smaller the quantified value, the negative correlation formula is selected to normalize, such as the water pressure of aquifer p.

$$X_i = \frac{\max(x_i) - x_i}{\max(x_i) - \min(x_i)}. \quad (2)$$

In the formulas, $\max(x_i)$ is the maximum value of a certain index factor; $\min(x_i)$ is the minimum value of a certain index factor x_i; X_i is the value after removing the dimensions. For the quantifiable indicators that can be tested in the field, similar model tests, or numerical simulations, the indicators are dimensionless by means of polarization, and their importance is ranked according to the slope of the fitted curve [22].

(2) AHP. Combining the above dimensionless analysis, construct a judgment matrix according to the 1-9 scale judgment table in the analytic hierarchy process, perform calculations, and determine the weight vector W of each indicator. In order to evaluate the consistency of the calculation results of the total ranking of levels, it is necessary to calculate the consistency index (CI), the random consistency index (RI), and the consistency ratio (CR) for consistency testing. If $CR < 0.1$, the judgment matrix is considered to have satisfactory consistency. Among them, the calculation method of each index is as follows:

$$CI = \sum_{j=1}^{m} W_{aj} CI_j,$$

$$\mathrm{RI} = \sum_{j=1}^{m} W_{aj}\mathrm{RI}_j,$$

$$\mathrm{CR} = \frac{\mathrm{CI}}{\mathrm{RI}}. \tag{3}$$

In the formulas, W_{aj} represents the total ranking weight of the element A_j in the a level; CI is the total ranking consistency index of the level; CI_j is the consistency index of the judgment matrix of the next level corresponding to A_j; RI is the random total ranking of the level Consistency index; RI_j is the random consistency index of the judgment matrix in the next level corresponding to A_j; CR is the random consistency ratio of the total ranking of the level. In this paper, AHP auxiliary software yaahp10.1 is used to construct the judgment matrix, check the consistency, and process the calculation results.

(3) Fuzzy Comprehensive Evaluation Method. Firstly, determine the factor set U and the judgment set V of the judgment object.

$$\begin{aligned} U &= (u_1, u_2, \cdots, u_n), \\ V &= (v_1, v_2, \cdots, v_m). \end{aligned} \tag{4}$$

Secondly, construct the fuzzy relationship matrix. Each factor u_i in the evaluation factor set U belongs to the membership degree r_{ij} of each level v_j, and then, the membership degree of the factor u_i relative to each level in the evaluation set is

$$R_i = (r_{i1}, r_{i2}, \cdots, r_{im}). \tag{5}$$

Then, the membership degree set R of all influencing factors in the factor set U is obtained, which is called the fuzzy relationship matrix.

$$R = (r_{ij}) \begin{bmatrix} r_{11} & \cdots & r_{1n} \\ r_{21} & \cdots & r_{2m} \\ \cdots & \cdots & \cdots \\ r_{m1} & \cdots & r_{mn} \end{bmatrix} (i = 1, 2, \cdots, m/j = 1, 2, \cdots, n). \tag{6}$$

2.2.2. Model Architecture. Based on the above evaluation method selection, the key links of the evaluation model structure are determined as follows: (1) analysis and determination of index weights, (2) single-factor toughness ranking and affiliation determination, and (3) fuzzy comprehensive evaluation. The specific evaluation model architecture is shown in Figure 2.

Through single-factor toughness grade division, membership function, and Delphi method, the membership degree of the evaluation index is comprehensively determined, and then combined with the determined weight vector W, the fuzzy synthesis calculation is carried out according to the following formula. According to the principle of maximum membership degree, the final evaluation result is obtained.

$$Z = W \times R = (W_1, W_2, \cdots, W_n) \times (R_1, R_2, \cdots, R_n), \tag{7}$$

3. Case Application

3.1. Engineering Application of the Model. The No. 10 coal seam in the lower mining area of East-10, Jiegou Coal Mine, Anhui Province, China, was affected by the hidden water hazard of the floor high-pressure limestone during mining. In 2019, the mine adopted multibranch horizontal well grouting for advanced regional grouting reinforcement treatment. It is planned to evaluate the effect of water-retaining mining through the water resistance toughness evaluation model of coal seam floor and at the same time provide an evaluation basis for further improving the water environment of the mining area and realizing the in situ protection of coal seam floor high-pressure limestone water.

3.1.1. Analysis and Determination of the Weight of Each Index. Select indicators that can be processed quantitatively: coal seam mining impact $A1$, performance of the water-resisting strata $A2$, water inrush intensity of aquifer $A3$, and influence of geological structure $A4$, and analyze the degree of influence. Among them, coal seam mining impact $A1$ selects the coal seam dip angle: α as the characterization parameter; performance of the water-resisting strata $A2$ selects the waterproof rock layer thickness: d as the characterization parameter; water inrush intensity of aquifer $A3$ selects water richness: p as the characterization parameter; influence of geological structure $A4$ selects the distribution density of faults: ρ as the characterizing parameter. The maximum water pressure Ps that the coal seam floor can withstand is used as the toughness parameter. The impact of α, d, p, and ρ on it is shown in Figure 3.

Specific parameters of the No. 10 coal seam of Jiegou Coal Mine are selected, physically modelled, and numerically simulated for analysis. For the indicators $A1$, $A2$, $A3$ and $A4$, which can be quantified, the dimensionless analysis was carried out using the extreme difference standardisation method. The range of values for α is 0-50°, d is 0-20 m, p is 0-5 L/s•m, and ρ is 0-1. The fitted curve of the maximum water pressure that the coal seam floor can withstand under the influence of different factors is plotted. Based on the rate of change of the slope of the fitted curve, a preliminary judgement can be made on the order of importance of each indicator: A4 > A2 > A3 > A1. According to Figure 3, the maximum water pressure Ps that the coal seam floor can withstand increases with increasing collapse overburden load q and water barrier thickness d and decreases with

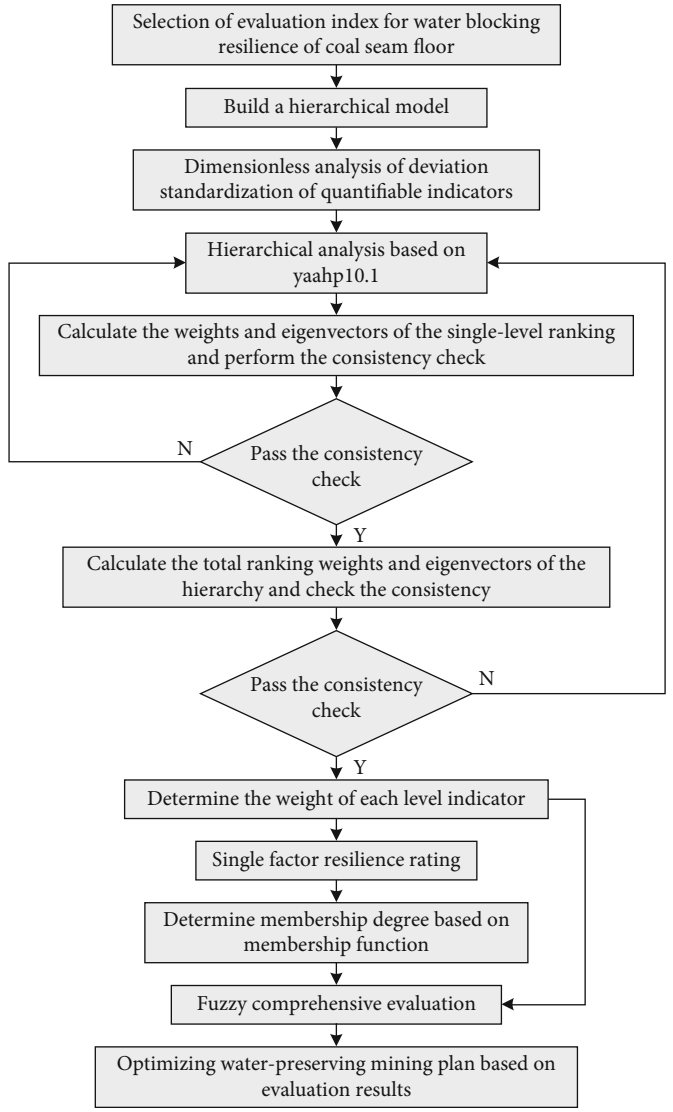

Figure 2: Framework of evaluation model for water resistance toughness of coal seam floor.

increasing aquifer water richness p and fault distribution density ρ. Among them, the related factors of geological structure and water-resisting layer have the most obvious influence on the water-resisting performance of the coal seam floor.

Usually, in evaluation models, weights usually need to have a certain degree of generalisability. For indicators that can be quantified and analyzed, the ranking of the weights needs to be combined with more similar projects and experience for weighting if there are deviations from experience. The above data is taken from the specific case of Jiegou Coal Mine and is consistent with experience. Drilling technology $B1$, reinforcement engineering $B2$, detection technology $B3$, surface ecological management $C1$, and water resources carrying capacity $C2$, which cannot be quantified, can be combined with similar projects. Before carrying out the level analysis, build the bottom water resistance toughness hierarchical structure model, as shown in Figure 4.

The weight is determined using AHP software yaahp10.1 for hierarchical structure model division, judgment matrix construction, and calculation result processing. The judgment matrixes are as follows:

$$X = \begin{bmatrix} 1 & 3 & 2 \\ 1/3 & 1 & 1/2 \\ 1/2 & 2 & 1 \end{bmatrix},$$

$$A = \begin{bmatrix} 1 & 1/4 & 1/3 & 1/5 \\ 4 & 1 & 3 & 1/3 \\ 5 & 3 & 1 & 1/4 \\ 3 & 1/3 & 1/4 & 1 \end{bmatrix},$$

$$B = \begin{bmatrix} 1 & 1/3 & 1/5 \\ 3 & 1 & 1/2 \\ 5 & 2 & 1 \end{bmatrix},$$

$$C = \begin{bmatrix} 1 & 1/2 \\ 2 & 1 \end{bmatrix}. \quad (8)$$

The consistency of the judgment matrix is 0.0089, 0.0688, 0.0036, and 0.000, respectively, satisfying the consistency requirement. The calculated weight vector is as follows:

$$\begin{aligned} W_1 &= [0.071, 0.268, 0.141, 0.520], \\ W_2 &= [0.110, 0.309, 0.581], \\ W_3 &= [0.333, 0.667], \\ W &= [0.539, 0.164, 0.297]. \end{aligned} \quad (9)$$

3.1.2. Single-Factor Toughness Ranking and Affiliation Determination. The determination of the affiliation degree is the core part in the fuzzy comprehensive evaluation. Based on the specific engineering practice, the affiliation degree determination in the evaluation of similar projects is analyzed, and the toughness level of each index factor is divided, as shown in Table 2.

The index factors of the water resistance toughness of the floor can be broadly divided into two categories, namely, qualitative factors and quantitative factors. For example, coal seam mining impact $U11$, performance of the water-resisting strata $U12$, water inrush intensity of aquifer $U13$, and influence of geological structure $U14$ are quantifiable index factors, which can be determined by the membership function according to the quantified value. Establish the following membership function:

$$f_1(u) = \begin{cases} 1, & u < a_1, \\ \dfrac{a_2 - u}{a_2 - a_1}, & a_1 \le u < a_2, \\ 0, & a_2 \le u < a_3, \\ 0, & u \ge a_3, \end{cases} \quad (10)$$

$$f_2(u) = \begin{cases} 0, & u < a_{1,} \\ \dfrac{u - a_1}{a_2 - a_1}, & a_1 \le u < a_{2,} \\ 0, & a_2 \le u < a_{3,} \\ 0, & u \ge a_3, \end{cases} \quad (11)$$

$$f_3(u) = \begin{cases} 0, & u < a_1, \\ 0, & a_1 \le u < a_{2,} \\ \dfrac{a_3 - u}{a_3 - a_2}, & a_2 \le u < a_3, \\ 0, & u \ge a_3, \end{cases} \quad (12)$$

$$f_4(u) = \begin{cases} 0, & u < a_1, \\ 0, & a_1 \le u < a_2, \\ \dfrac{u - a_2}{a_3 - a_2}, & a_2 \le u < a_3, \\ 1, & u \ge a_3. \end{cases} \quad (13)$$

As coal seam mining impact $U11$, water inrush intensity of aquifer $U13$, and influence of geological structure $U14$ increase, the resilience is negatively correlated with a decreasing trend. Select (13) to determine the degree of membership of the "extremely good resilience" grade, and select (10) to determine the degree of membership of the "extremely poor resilience" grade. With the enhancement of performance of the water-resisting strata $U12$, the resilience shows a positive correlation enhancement trend. Select (10) to determine the degree of membership of the "extremely poor resilience" grade, and select (13) to determine the "extremely good resilience" grade. The degrees of membership, such as drilling technology $U21$, reinforcement technology $U22$, detection technology $U23$, surface ecological governance $U31$, and water resources carrying capacity $U32$, are factors that cannot be accurately quantified. The membership of these factors can be based on actual engineering and similar projects. It is determined in combination with the Delphi method. According to the specific conditions of Jiegou Coal Mine, the membership degree of each index factor of the water resistance toughness of the coal seam floor in the treatment area and the membership degree matrix of the criterion layer are further obtained as follows:

$$\begin{aligned} R_1 &= \begin{bmatrix} R_{11} \\ R_{12} \\ R_{13} \\ R_{14} \end{bmatrix} = \begin{bmatrix} 0.05,0.20,0.50,0.25 \\ 0.10,0.45,0.30,0.15 \\ 0.20,0.65,0.10,0.05 \\ 0.20,0.50,0.25,0.05 \end{bmatrix}, \\ R_2 &= \begin{bmatrix} R_{21} \\ R_{22} \\ R_{23} \end{bmatrix} = \begin{bmatrix} 0.05,0.20,0.50,0.25 \\ 0.05,0.15,0.60,0.20 \\ 0.20,0.45,0.25,0.10 \end{bmatrix}, \\ R_2 &= \begin{bmatrix} R_{21} \\ R_{22} \end{bmatrix} = \begin{bmatrix} 0.60,0.25,0.10,0.05 \\ 0.65,0.20,0.15,0.00 \end{bmatrix}. \end{aligned} \quad (14)$$

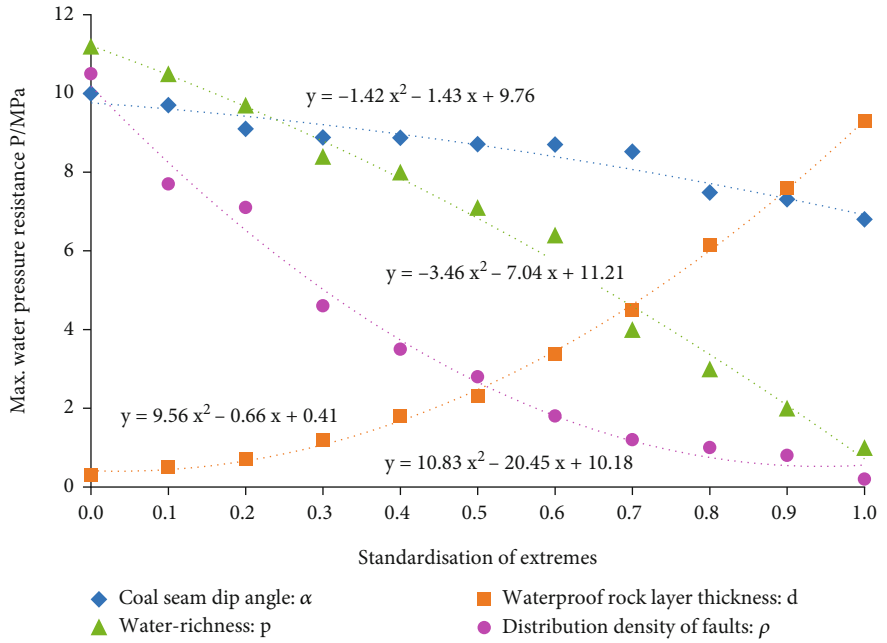

Figure 3: The relationship curve between the maximum water pressure P and system vulnerability elements of coal seam floor.

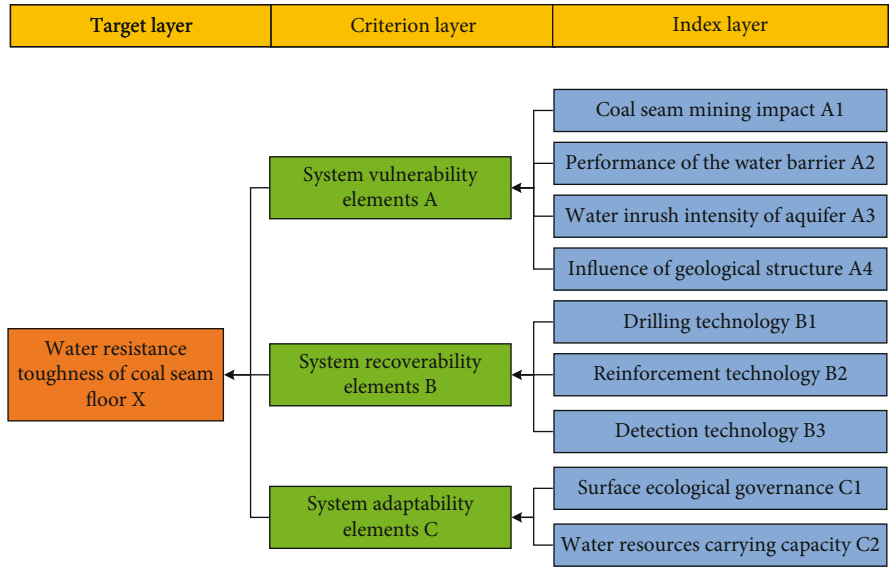

Figure 4: Hierarchical structure model of water resistance toughness of coal seam floor.

3.1.3. Fuzzy Comprehensive Evaluation. Fuzzy comprehensive evaluation is a compound operation of the weight and the judgment matrix of each influencing factor. The first-level fuzzy evaluation results are as follows:

$$\begin{aligned} Z_1 &= W_1 \times R_1 = [0.163, \mathbf{0.486}, 0.260, 0.091], \\ Z_2 &= W_2 \times R_2 = [0.137, 0.330, \mathbf{0.386}, 0.147], \\ Z_2 &= W_3 \times R_3 = [\mathbf{0.633}, 0.217, 0.133, 0.017]. \end{aligned} \tag{15}$$

After finishing Z_1, Z_2, and Z_3, the matrix R is obtained, and the second-level fuzzy evaluation operation is performed. The results are as follows:

$$Z = W \times R = [0.298, \mathbf{0.381}, 0.243, 0.078], \tag{16}$$

where Z represents the comprehensive evaluation result, and Z_1, Z_2, and Z_3 represent the criterion-level evaluation result.

Table 2: Single-factor toughness rating.

Index factor		Toughness evaluation level criteria			
		Very bad	Worse	Better	Excellent
$U1$	U11	$\alpha \geq 45^{\circ}$	$25^{\circ} < \alpha < 45^{\circ}$	$8^{\circ} < \alpha < 25^{\circ}$	$\alpha \leq 8^{\circ}$
	U12	$d \leq 0$	$0 < d < 10$ m	10 m $< d <$ 20 m	$d \geq 20$ m
	U13	$p > 5$ L/s•m	3 L/s•m $< p <$ 5 L/s•m	1 L/s•m $< p <$ 3 L/s•m	$p < 1$ L/s•m
	U14	$\rho > 0.8$	$0.5 < \rho < 0.8$	$0.2 < \rho < 0.5$	$\rho < 0.2$
$U2$	U21	Serious damage to the key rock formation	Poor matching of construction technology	Good match of construction technology	Less damage to the key rock formation
	U22	Widespread pollution	Local pollution	No obvious pollution	Green and ecofriendly
	U23	Basic geophysical prospecting	Multi-mode combined detection	Whole process detection	Real-time dynamic detection
$U3$	U31	Poor governance	General governance	Ecological restoration is in progress	Green ecology
	U32	High pollution index	Average pollution index	Limited water carrying capacity	High water carrying capacity

3.2. Result Analysis. According to the principle of maximum degree of membership, the water resistance toughness level of the floor of the No. 10 coal seam treatment area in Jiegou Coal Mine is judged. From the perspective of the life cycle of the system, according to Z, the water resistance toughness of the floor system of the No. 10 coal seam is weak. The detailed analysis is as follows:

(1) According to Z_1, the performance of system vulnerability elements is weak. This reflects that after advanced regional grouting and reinforcement treatment, as the coal seam is further mined, there are still dangerous areas with greater water inrush risk. Under the combined action of faults, karst collapse columns, and high-pressure limestone water, the self-repairing ability of the key water-resisting strata of the coal seam floor is poor. Therefore, it is necessary to continuously repair and strengthen the regional aquifer on the basis of advanced detection and carry out decompression or transformation of the aquifer. From the perspective of accuracy and efficiency, the determination of the governance target area should be focused on

(2) According to Z_2, it can be concluded that system recoverability elements are with better resilience, because the treatment area has previously adopted multibranch horizontal well grouting for advanced treatment. However, the traditional drilling and grouting method will inevitably cause damage to the original rock formation. Rock formation damage caused by multibranch drilling is irreversible, and it is difficult to achieve in situ water retention. At the same time, the selected grouting material (mainly cement) cannot achieve resilience repair well. Therefore, it is urgent to optimize and upgrade the in situ water-preserved technology. The impact of grouting materials on the groundwater environment should be determined, and the hardening and water-resisting and durability properties of the materials under the influence of groundwater should be explored. The properties of various materials need to be mastered, and then, low-cost, harmless, high-performance pressure-bearing floor rock water channel blocking green materials and floor rock self-repairing materials can be developed

(3) According to Z_3, system adaptability elements have extremely poor resilience. Generally, water-preserved mining in mining areas mainly focuses on subsequent safe production, and less attention is paid to the effect of groundwater resources protection. Combining the specific conditions of the Jiegou Coal Mine, and according to the corresponding monitoring data in five dimensions of water volume, water quality, water area, hydrodynamic force, and water and heat capacity, it can be obtained that the groundwater carrying capacity of Jiegou Coal Mine is poor, which indirectly affects the water blocking performance of the coal seam floor. From the side, it reflects the relevance of the improvement of the water resistance toughness of the coal seam floor and the ecological environment. Therefore, when carrying out water-preserving mining on confined water, attention should be paid to the improvement of the ecological environment of the mining area after the implementation of water-preserving mining technology, so as to achieve the coordination between safe mining and ecological environmental protection

4. Discussions

4.1. Strategies for Improving the Water Resistance Toughness of Coal Seam Floor. In summary, relying on the whole life cycle perspective, the whole process evolution of water-resisting toughness can effectively guide the implementation

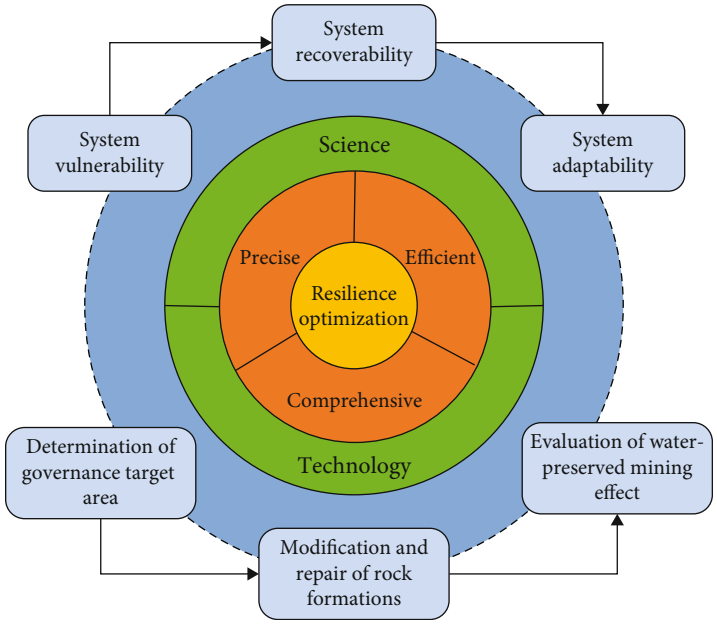

Figure 5: Optimization strategy for water resistance toughness of coal seam floor.

of the whole stage of water conservation mining project. The process of coal seam floor from mining damage characteristics to toughness recovery and then to water bearing capacity enhancement contains the whole process of toughness evolution. It also corresponds to 3 stages of the project: determination of governance target area, modification and repair of rock formations, and evaluation of water-preserved mining effect. Based on the above analysis, the optimization strategy for water resistance toughness of coal seam floor is obtained, as shown in Figure 5.

The core of the idea of optimizing the water resistance toughness of coal seam floor is "precise, efficient, and comprehensive": "precision" refers to making the determination of the floor treatment target area more precise; "efficient" refers to the provision of technical routes for modification and repair of rock formations to improve construction efficiency; "comprehensive" means to make up for the lack of attention to the effect of water resources protection in the evaluation of the effect of water-preserved mining.

4.2. New Technology System of Water-Preserved Mining for Coal Seam Floor. Based on the above analysis, the technology system of water-preserved mining for coal seam floor is constructed, and the specific technology system framework is shown in Figure 6. The system is based on 3 stages: "determination of governance target area, modification and repair of rock formations, and evaluation of water-preserved effects". The 3 stages are all based on detection technology, forming 3 detections including "advanced detection, detection while drilling, and detection before mining" to ensure safe construction and mining.

(1) The first stage is the determination of governance target area, including two links: vertical horizon determination and lateral target determination

According to the calculation formula of the broken ring depth of the floor, the development depth of the broken zone under the influence of mining is estimated, and the ideal depth of the grouting target area is preliminarily determined according to the principle that the modified aquifer should avoid the broken zone as much as possible. Further, combined with the mine hydrogeological data, analyze the lithology and rock formation combination, divide the aquifer and aquifer, and determine the final optimal grouting layer.

Calculation of the maximum failure depth of the floor rock mass at the edge of the stope:

$$h_1 = \frac{1.57\gamma^2 H^2 L_x}{4R_c^2}. \tag{17}$$

Calculation of the maximum failure depth of the bottom rock mass of the longwall working face:

$$h_2 = \frac{(n+1)H}{2\pi}\left(\frac{2\sqrt{K}}{K-1} - \arccos\frac{K-1}{K+1}\right) - \left(\frac{R_c}{\gamma(K-1)}\right), \tag{18}$$

where γ is the bulk density of the rock mass, N/m^3; H is the mining depth, m; L_x is the slope length of the working face, m; R_c is the uniaxial compressive strength of the rock mass, MPa; n is the maximum stress concentration factor, usually taken 1.5~5; φ_0 is the friction angle in the rock body, °; and $K = (1 + \sin\varphi_0)/(1 - \sin\varphi_0)$.

The horizontal target position is determined on the basis that the vertical horizon has been determined, using geological detection methods such as multifrequency continuous electrical method, GIS spatial analysis tools, and borehole television method. The relevant parameters are accurately

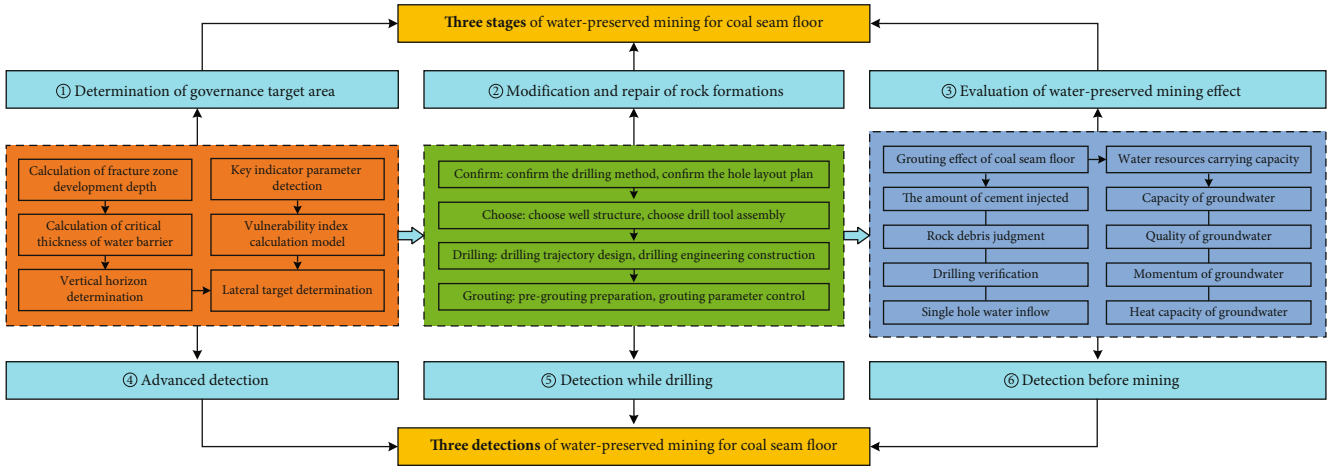

Figure 6: Framework of in situ water-preserved technology system for coal seam floor.

detected. The spatial analysis function of ArcGIS is used for interpolation analysis to generate a normalized thematic map of key index parameters. With the help of the position coordinates of the thematic map, the single-factor influence value function $f_i(x, y)$ is given. Fuzzy analytic hierarchy process (FAHP) is used to calculate the AHP weight of each factor, and the entropy weight method (EW) is used to calculate the entropy weight of each factor. Calculate the composite weight according to formula (19), and according to formula (20) of vulnerability index, integrate three factors of aquifer, confined aquifer, and geological structure, and evaluate the weak interval of water-resisting as a lateral grouting target.

$$W_i = \frac{w_i x_i}{\sum_{i=1}^{n} w_i x_i}, \tag{19}$$

$$VI = \sum_{i=1}^{n} W_i \cdot f_i(x, y). \tag{20}$$

In the formulas, w_i is the single-factor level analysis weight; x_i is the single-factor entropy weight; n is the number of factors; and (x, y) is the geographic coordinates.

(2) The second stage is the modification and repair of the rock formation, including the four steps of determination, selection, drilling, and grouting

At present, most of the grouting schemes only consider the reconstruction of the aquifer but do not fully consider the repair of the original aquifer, so that the two can form a joint water blocking body with stronger continuity and integrity. Rock grouting modification repair is a commonly used method and means to change the hydrogeological conditions of rock mass. According to the first stage, the treatment target area, that is, the construction location, can be preliminarily determined. Before the project is carried out, it is necessary to fully consider the ground construction conditions, the buried depth of the coal seam, and the water pressure of the coal seam floor, comprehensively determine the drilling method (surface or underground), and then determine the hole layout plan and drilling sequence. According to the drilling method, select the wellbore structure and drilling tool combination. Taking the multibranch horizontal drilling technology as an example, the drilling usually adopts a three-split and two-stage cased wellbore structure. After that, the design and construction of drilling engineering and grouting engineering are carried out.

(3) The third stage is the evaluation of water retention effect, including the evaluation of rock grouting effect and the evaluation of water resources carrying capacity restoration

According to the provisions of the relevant standards, in the area where the ground area treatment is implemented, the geophysical method should be used to test the effect before the excavation. If there is no abnormality, the excavation can be carried out normally; if any abnormality is found, drilling is used to verify and control the standards. Before mining, geophysical exploration and drilling methods should be used to verify the effect to ensure that no large water inrush points occur in the grouting diffusion area of branch holes. The grouting effect of the coal seam floor can be verified by four indicators: the amount of injected mud and water, judgment of cuttings, drilling verification, and single-hole gushing volume.

From the perspective of mine groundwater ecological protection, taking the restoration of water resources carrying capacity as the breakthrough point, and based on the results of the topographic, geomorphological, and hydrogeological exploration of the coal field, the key indicators for the evaluation of the water protection effect of the floor limestone are proposed, including water quantity, water quality, hydrodynamics and water quality, and heat capacity. By grasping the key indicators of mine water resources ecological protection and the corresponding thresholds, the groundwater conditions of the floor can be objectively and clearly reflected in a quantitative form. At the same time, it can solve the problem of insufficient attention to the mine

ecological environment in the evaluation of water conservation and mining effects.

5. Conclusions

(1) Based on the theory of system resilience, an evaluation index system for water resistance toughness of coal seam floor was established, which specifically included three types of evaluation elements: system vulnerability elements A, system recoverability elements B, and system adaptability elements C, in detail, including 9 evaluation indicators: coal seam mining impact $A1$, performance of the water-resisting strata $A2$, water inrush intensity of aquifer $A3$, influence of geological structure $A4$, drilling technology $B1$, reinforcement technology $B2$, detection technology $B3$, surface ecological governance $C1$, and water resources carrying capacity $C2$

(2) The range standardization-AHP-fuzzy comprehensive evaluation method is adopted to construct an evaluation model with index weight analysis and determination, resilience grade division and membership determination, and fuzzy comprehensive evaluation as the main links. The integration of the maximum difference normalization method and the membership function overcomes the deficiencies of experts' scoring to a certain extent and solves the problem of determining the weight of multiple indicators in a semiquantitative manner

(3) The evaluation model is applied to the specific engineering practice. According to the evaluation results Z_1, Z_2, Z_3, and Z, it can be seen that improving the water resistance toughness of coal seam floor requires determining the treatment target area, optimizing the modification and repair of rock formations materials, and improving the water resources carrying capacity. To a certain extent, this verifies the validity of the evaluation index and the practical value of the evaluation model. It should be noted that the evaluation index system is not yet complete, and further adjustments and optimizations should be made to the actual project

(4) According to the view of the whole life cycle, the whole process evolution of water resistance toughness can effectively guide the implementation of the whole stage of engineering technology. The in situ water retention technology system of coal seam floor is proposed, with 3 stages as the main body and 3 detections as the backing. 3 stages involve "determination of governance target area, modification and repair of rock formations, and evaluation of water-preserved mining effect"; 3 detections involve " advanced detection, detection while drilling, and detection before mining". The purpose is to provide strategies and measures for water protection in mining, to form an effective technical solution for in situ water protection of coal seam floor

Data Availability

The data used to support the findings of this study are available from the corresponding author upon request.

Conflicts of Interest

We declare that we do not have any commercial or associative interest representing a conflict of interest in connection with the paper submitted.

Acknowledgments

This study was supported by the NSFC-Shanxi Coal-Based Low-Carbon Joint Fund Key Project (Grant No. U1810203), Key R&D and Promotion Projects in Henan Province (Grant No. 212102310013), and Open Fund Grant Project of Key Laboratory of Resource Environment and Disaster Monitoring in Shanxi Province (2019-06). We would like to express our gratitude to engineers from Anhui Jiegou Mining Industry Co., Ltd. and Henan Yuzhong Geological Prospecting Engineering Co., Ltd. for their help in the field tests. We thank the Key Laboratory of Resource Environment and Disaster Monitoring in Shanxi Province and the State Key Laboratory Cultivation Base for Gas Geology and Gas Control.

References

[1] L. M. Fan and X. D. Ma, *Theory and Practice of Water-Preserving Coal Mining*, Science Press Publishing, 2019.

[2] S. P. Peng and Y. L. Bi, "Strategic consideration and core technology about environmental ecological restoration in coal mine areas in the Yellow River basin of China," *Journal of China Coal Society*, vol. 45, no. 4, pp. 1211–1221, 2020.

[3] D. Z. Gu, J. F. Li, Z. G. Cao et al., "Technology and engineering development strategy of water protection and utilization of coal mine in China," *Journal of China Coal Society*, vol. 46, no. 10, pp. 3079–3089, 2021.

[4] M. G. Qian, J. L. Xu, and X. X. Miu, "Coal mine green mining technology," *Journal of China University of Mining & Technology*, vol. 32, no. 4, pp. 343–348, 2003.

[5] L. Fan, X. Ma, Z. Jiang, K. Sun, and R. J. Ji, "Review and thirty years prospect of research on water-preserved coal mining," *Coal Science and Technology*, vol. 47, no. 7, pp. 1–30, 2019.

[6] S. N. Dong, X. M. Guo, Q. S. Liu et al., "Model and selection criterion of zonal preact grouting to prevent mine water disasters of coal floor limestone aquifer in North China type coalfield," *Coal Geology & Exploration*, vol. 48, no. 4, pp. 1–10, 2020.

[7] S. N. Dong, Z. X. Liu, S. T. Zheng et al., "Technology and application of large curtain grouting water conser-vation mining based on macroscopic and mesoscopic characteristics of rock mass," *Journal of China Coal Society*, vol. 45, no. 3, pp. 1137–1149, 2020.

[8] D. S. Zhang, G. W. Fan, S. Z. Zhang, L. Q. Ma, and X. F. Wang, "Equivalent water-resisting overburden thickness for water-conservative mining: conception, method and application," *Journal of China Coal Society*, vol. 47, no. 1, pp. 128–136, 2022.

[9] M. B. Chi, "Evaluation of water resources carrying cpacity and decision-making of scientific coal mining scale in northwest

mining area of China: a case study in Yining mining area," *China University of Mining and Technology*, 2019.

[10] Z. M. Xu, S. S. Liu, J. F. Li et al., "Research on hydrogeological structure division of coal seam floor and quantitative evaluation method of water barrier capacity," *Coal Science and Technology*, vol. 50, no. 2, pp. 187–194, 2022.

[11] S. Q. Liu, Q. Wu, Z. Li, Y. F. Zeng, Q. D. Yuan, and Y. L. Yu, "Evaluation and application of vulnerability of water inrush and variable weight in mining area with multi-coal floor and single aquifer," *Journal of China University of Mining & Technology*, vol. 50, no. 3, pp. 587–597, 2021.

[12] S. Q. Liu, Q. Wu, Y. F. Zeng, H. J. Gong, and Z. Li, "The improved AHP vulnerable index method based on GIS," *Earth Science*, vol. 42, no. 4, pp. 625–633, 2017.

[13] W. Bi, Y. C. Tang, T. T. Mao, X. H. Sun, and Q. M. Li, "Review on resilience management of urban infrastructure system," *China Safety Science Journal*, vol. 31, no. 6, pp. 14–28, 2021.

[14] Y. Wang, J. H. Huang, S. S. Fu, X. We, and B. Wu, "A shift in paradigm for system safety: comparative study of risk and resilience," *China Safety Science Journal*, vol. 28, no. 1, pp. 62–68, 2018.

[15] H. Lang, W. U. Chao, Y. Mian, and W. Bing, "Application of resilience theory in field of safety science," *China Safety Science Journal*, vol. 27, no. 3, pp. 1–6, 2017.

[16] L. L. Zhao, G. F. Wen, and L. S. Shao, "GSPCA-LSSVM model for evaluating risk of coal floor groundwater bursting," *China Safety Science Journal*, vol. 28, no. 2, pp. 128–133, 2018.

[17] J. Sun, L. G. Wang, and H. F. Lu, "The analysis of the water-inrush dangerous areas in the inclined coal seam floor based on the theory of water-resisting key strata," *Journal of Mining & Safety Engineering*, vol. 34, no. 4, pp. 655–662, 2017.

[18] B. B. Gao, J. J. Chang, and Z. G. Wang, "Optimized FCE model for evaluating floor water burst hazard and its application," *China Safety Science Journal*, vol. 26, no. 7, pp. 96–101, 2016.

[19] J. Q. Wang, M. Y. Lu, Q. X. Wang, X. G. Li, and W. R. Zhai, "Study on ecological environment assessment of water-preserved mining based on entropy weight method and cloud model," *Coal Science and Technology*, vol. 48, no. 7, pp. 158–162, 2020.

[20] E. Aguinaga, I. Henriques, C. Scheel, and A. Scheel, "Building resilience: a self-sustainable community approach to the triple bottom line," *Journal of Cleaner Production*, vol. 173, pp. 186–196, 2018.

[21] Z. Z. Li, D. F. Fu, J. X. Wang, K. Min, and J. Zhang, "Urban resilience assessment model for waterlogging disasters and its application," *Journal of Tsinghua University (Science and Technology)*, vol. 62, no. 2, pp. 266–276, 2021.

[22] X. Wang, *Shallow Goaf Site under Cyclic Dynamic Loading Research on Deformation Mechanism and Evaluation System of High-Speed Railway Subgrade*, Henan Polytechnic University, 2020.

Hindawi
Geofluids
Volume 2022, Article ID 3964502, 15 pages
https://doi.org/10.1155/2022/3964502

Research Article

Design and Optimization of a Triangular Shear Piezoelectric Acceleration Sensor for Microseismic Monitoring

Yannan Shi[1,2] **Shuaishuai Jiang**[1] **Yang Liu**[3] **Yiying Wang**[1] **and Penglei Qi**[1]

[1]*School of Mechanical and Equipment Engineering, Hebei University of Engineering, Handan 056038, China*
[2]*Handan Key Laboratory of Intelligent Vehicle, Handan 056038, China*
[3]*School of Mechanical Electronic & Information Engineering, China University of Mining and Technology (Beijing), Beijing 100083, China*

Correspondence should be addressed to Yang Liu; liuyangebox@126.com

Received 10 December 2021; Revised 23 March 2022; Accepted 28 March 2022; Published 25 April 2022

Academic Editor: Gangwei Fan

Aiming at the characteristics of low sensitivity and narrow frequency range of existing microseismic monitoring sensors for mine water hazard prevention and control, a piezoelectric acceleration sensor for microseismic monitoring based on a kind of triangular shear structure is proposed. Firstly, the structure of the triangular shear piezoelectric acceleration sensor is designed, and its dynamic model is built. The structural and material parameters related to natural frequency and sensitivity are analyzed. Then, the selection of piezoelectric ceramic materials is discussed. The parametric design of the designed sensor is carried out, and its finite element structural model is built by ANSYS. The modal analysis, resonance response analysis, and piezoelectric analysis of the designed sensor are carried out. The simulation results indicate that the working frequency and sensitivity of the designed sensor meet the requirements of microseismic monitoring. Response surface optimization is adopted to analyze the influence of sensor element design variables on the sensitivity and resonant frequency of the designed sensor. The reoptimized design of the reference sensor improves the resonant frequency of the designed sensor by 9.46% and the charge sensitivity by 18.96%. Finally, the designed sensor is calibrated, and the microseismic signal detection experiment is carried out. The results indicate that the resonant frequency of the designed sensor is 6150 Hz, the working frequency is 0.1-2050 Hz, and the charge sensitivity is 1600 pC/g. The sensor can detect microseismic signals with a wide frequency range and high sensitivity.

1. Introduction

In recent years, mine water inrush dynamic disasters caused by mining activities have occurred frequently, which has become one of the main disasters that continue to threaten coal mine safety production. The possibility of water inrush dynamic disasters in mines will further aggravate with the increase of mining depth [1]. It damages mining equipment and facilities, affects safe production, and threatens the lives of miners. Microseismic monitoring technology has been widely used as an effective means to deal with the above disaster [2]. This technology uses sensors to sense the microseismic signals generated by rock fracture during the formation of coal mine water inrush channel, locate the microseismic time, explain the focal mechanism, and realize the real-time, continuous, and full space prediction of mine water inrush events [3]. As an important part of the microseismic monitoring system, the performance of the sensor is essential to the prediction accuracy of mine water inrush events. Therefore, it is an urgent problem to develop a sensor with a wide working frequency and high sensitivity to improve the comprehensiveness and accuracy of microseismic signal acquisition.

The interferometric optical fiber geophone has high sensitivity and wide dynamic range, which is suitable for detecting microseismic signals. In 2004, Tsinghua University developed a three-component mandrel optical fiber accelerometer, which can be used for downhole petroleum exploration [4]. The working frequency band is 3~800 Hz, and the on-axial acceleration sensitivity is 39 dB re rad/g. Optical fiber microseismic detection technology is widely used in petroleum geophysical exploration, but in the fields with poor production conditions

such as coal mines, the performance of the sensor needs to be further improved. The sensitivity of the piezoelectric accelerometer developed in [5] is 19 V/g, and the dynamic range is 80 dB. The piezoelectric six-axis acceleration sensor developed in [6] uses a single inertial mass, which can measure the six-axis acceleration and is linearly coupled in all directions. The axial sensitivity can reach 0.695 V/g, and the natural frequency can reach 25 kHz. A biaxial differential piezoelectric accelerometer with bimorph and independent mass structure is studied [7]. The resonant frequency of the accelerometer optimized by the finite element method is about 7.4 kHz, and the sensitivity of the two axes is 1556 pC/g and 1363 pC/g, respectively. The natural frequency of the piezoelectric MEMS accelerometer designed in [8] is about 29.8 kHz, and the maximum sensitivity is about 0.2 mV/g, which needs further improvement. Although the MEMS sensor studied in [9] can monitor microseismic signals, its frequency range is small and cannot monitor microseismic signals more comprehensively.

The performance of the piezoelectric accelerometer in bending mode is studied in [10], and the sensitivity is associated with the system parameters by using a set of approximate formulas. The cantilever beam structure of bimorph is adopted, and the sensitivity can reach at least 500 pC/g. A piezoelectric thick film acceleration sensor with large bandwidth and temperature compensation is reported in [11]. Its natural frequency is 40 kHz, and its sensitivity is 6 mV/ms^{-2}. A circular piezoelectric accelerometer is developed by using PZT thick film material with a large piezoelectric coupling coefficient in [12, 13]. Its sensitivity can reach 7.6 pC/g, the resonance frequency is about 3.7 kHz, and the structure is more robust. A shear-mode high-temperature piezoelectric acceleration sensor is studied by using YCOB Crystal in [14], which can withstand the high-temperature environment of 1250°C, and the sensitivity value is 8.7 ± 1.6 pC/g. Compared with the PZT accelerometer with a similar structure, the piezoelectric accelerometer adopts BNKBT lead-free ceramic ring as a sensing element, which has good performance and wide frequency response [15]. The platformed unimorph accelerometer adopts a curved plate with a castellated surface to form a sensing structure, which will increase the stress in the piezoelectric crystal and produce higher charge output. The accelerometer has the characteristic that the noise is inversely proportional to the charge output at the low frequency [16]. A sensor using Li-doped ZnO film with a double piezoelectric layer structure is proposed in [17]. This sensor can obtain the maximum output at the resonance frequency. Moreover, the output sensitivity can be improved with the above structure.

The MOEMS accelerometer designed in [18] uses a micromechanical sensing structure and a grating interferometer to exhibit low cross-axis sensitivity. Under the optimum design conditions, the sensitivity of the accelerometer is 2485 V/g, and the resonance frequency is 34.5 Hz. MEMS accelerometers can be designed using various types of piezoelectric materials. By studying the bulk phase and thin-film form of piezoelectric materials, high-performance MEMS accelerometers can be configured using microprecision machining or hybrid integration methods [19, 20]. The piezoelectric geophone with a multilayer spiral corrugated cantilever beam has a low natural frequency due to the long structure of the cantilever beam, and the corrugated structure improves its sensitivity [21, 22].

In addition, numerical simulation can be used to visualize several specifics that cannot be obtained in experiments. Therefore, appropriate analysis models can be used to explain the function of design variables and the relationship between variables and performance [23]. Although the above methods are of strategic significance in the research and development of sensors, when microseismic monitoring is applied in coal mines, the frequency range of sensors needs to reach 1500 Hz and have enough sensitivity.

Based on the above literature collection and analysis, a piezoelectric acceleration sensor for microseismic monitoring based on a kind of triangular shear structure is designed. The structure is improved based on the basic triangular shear structure to improve the sensitivity of the designed sensor. The dynamic model is analyzed, and the material of the sensor is selected. Then, the parametric design of the piezoelectric acceleration sensor is carried out. The finite element model of the designed sensor is built by ANSYS, and its structural rationality, resonant frequency, and sensitivity are analyzed. The sensitivity and resonant frequency are optimized by the response surface optimization method. Finally, the prototype of the designed sensor is developed, and its design scheme, theoretical calculation, and simulation analysis are verified by experiments.

2. Scheme Design and Working Principle

2.1. Structure Design. The structure of the piezoelectric acceleration sensor mainly includes the compression type, shear type, and bending type. Among them, the compression acceleration sensor has the merits of high mechanical strength and resonance frequency. The bending type has low mechanical strength and resonance frequency, but high sensitivity. The shear structure has the characteristics of small volume, high mechanical strength, high resonance frequency, resistance to substrate deformation, and temperature impact and can measure low-frequency signals [24]. Microseism is a small vibration caused by rock fracture or fluid disturbance. To detect microseismic signals more accurately and comprehensively, it is necessary to ensure that the sensor has a high resonance frequency and sufficient sensitivity. Therefore, the triangular shear structure is selected in the design of the sensor. Figure 1 shows the structure of the triangular shear piezoelectric acceleration sensor, which consists of the piezoelectric element, base, shell, conductive sheet, insulating sheet, seismic mass, and fastener. Moreover, in order to intuitively obtain the information of different components of the sensor, the 3D view inside the shell is shown in Figure 2. The piezoelectric elements are distributed on the three planes of the regular triangular prism of the base. The piezoelectric elements, the conductive sheet, and the seismic mass are fixedly connected to the base through the radial force generated by the extrusion of the insulating sheet by the fastener. Compared with other types of piezoelectric acceleration sensors, separating the piezoelectric

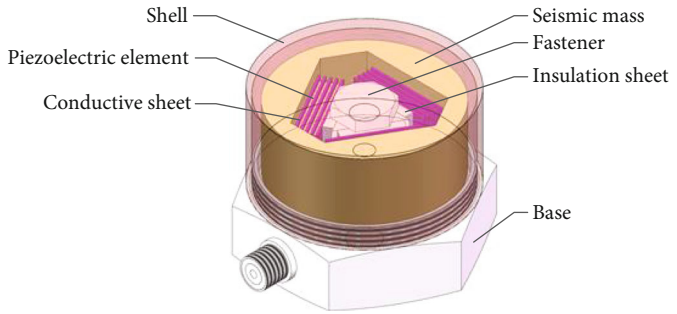

Figure 1: Structure of the triangular shear piezoelectric acceleration sensor.

element from the base can reduce the effects of thermal transient and base bending [14].

The active component of the sensor in Figure 2 is the piezoelectric element. When the sensor receives a microseismic signal, the shear force is equal to the product of the acceleration received by the seismic mass and the mass acting on each piezoelectric element. The piezoelectric element generates an electric charge proportional to the shear force. There are four independent piezoelectric elements on each side, and the connection form is electrical parallel output. The triangular shear structure has three sides, and each side is also the electrical parallel output. The output voltage is the voltage of a single piezoelectric element, and the amount of charge is the sum of all piezoelectric elements.

2.2. Working Principle. The working principle of the piezoelectric acceleration sensor is to convert the acceleration signal to be measured into an electrical signal based on the positive piezoelectric effect of the piezoelectric crystal. The dynamic model of the sensor can be equivalent to a single degree of freedom system, including mass (m)-spring (k)-damping (c) [25, 26], as shown in Figure 3. The sensor base is connected to the vibrating surface. When the sensor senses the acceleration signal, the piezoelectric element deforms under the action of the inertia force of the mass, causing the change of charge and realizing the conversion from the acceleration signal to the electrical signal.

In Figure 3, the mass of the seismic mass in the shell of the sensor is m. The piezoelectric material and friction resistance in the sensor are expressed by spring and damper, respectively, and the stiffness coefficient and damping coefficient are k and c, respectively. When an external vibration signal is sensed by the sensor, a displacement response $x_i(t)$ will be generated on the vibrating surface. Under the action of inertia, the vibration displacement of the seismic mass is $x_m(t)$, and its displacement $x_o(t)$ relative to the base can be expressed as

$$x_o(t) = x_m(t) - x_i(t). \tag{1}$$

Under the action of the spring and damper, the motion equation of the seismic mass can be expressed as

$$m\frac{d^2x_m(t)}{dt^2} = -kx_o(t) - c\frac{dx_o(t)}{dt}. \tag{2}$$

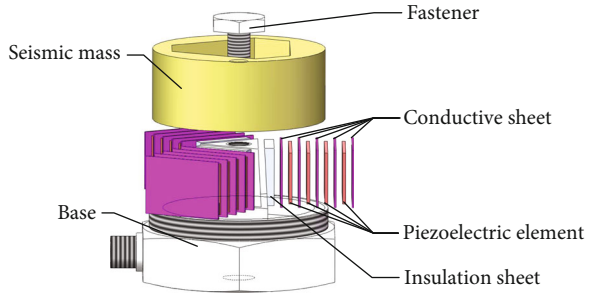

Figure 2: 3D view inside the shell of the sensor.

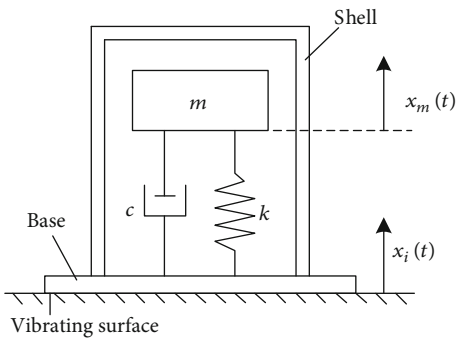

Figure 3: Dynamic model of the piezoelectric acceleration sensor.

Substituting equation (1) in equation (2), the differential equation of the system can be obtained as

$$m\frac{d^2x_o(t)}{dt^2} + c\frac{dx_o(t)}{dt} + kx_o(t) = -m\frac{d^2x_i(t)}{dt^2} = -ma, \tag{3}$$

where a is the measured acceleration.

The Fourier transform of equation (3) is obtained as

$$\frac{x_0(j\omega)}{a} = -\frac{(1/\omega_n)^2}{1-(\omega/\omega_n)^2 + 2\zeta(\omega/\omega_n)j}, \tag{4}$$

where ω_n and ζ can be evaluated as the following:

$$\omega_n = \sqrt{\frac{k}{m}}, \tag{5}$$

Table 1: The specific nonpiezoelectric materials and their properties of the designed sensor.

Component	Material	Young's modulus (N/m^2)	Density (kg/m^3)	Poisson's ratio
Seismic mass	Tungsten alloy	34×10^{10}	17500	0.27
Base	Stainless steel	20×10^{10}	7860	0.3
Conductive sheet	Brass	10.4×10^{10}	8600	0.37
Insulation sheet	Alumina ceramic	30×10^{10}	3600	0.24
Shrink ring	Aluminium alloy	9×10^{10}	2700	0.32

Table 2: The electrical and mechanical properties of the piezoelectric material.

Material	Density (kg/m^3)	Piezoelectric constant (pC/N)			Poisson's ratio	Modulus of elasticity (GPa)					
		d_{31}	d_{33}	d_{15}		C_{11}^E	C_{12}^E	C_{13}^E	C_{33}^E	C_{44}^E	C_{66}^E
PZT-5H	7800	-274	593	741	0.33	126	79.5	84.1	117	23	23.5

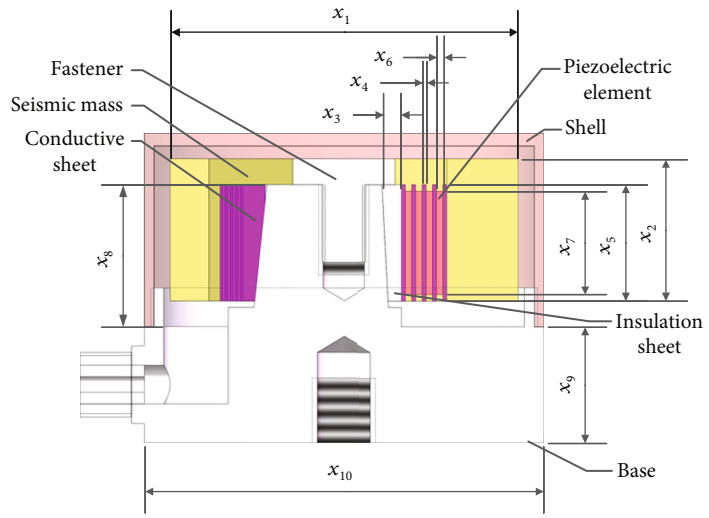

Figure 4: Ten design variables of numerical analysis.

$$\xi = \frac{c}{2\sqrt{km}}, \tag{6}$$

where ω_n and ζ are the natural frequency and damping ratio of the sensor, respectively.

From equation (4), it can be concluded that the natural frequency is one of the important parameters affecting the dynamic characteristics of the sensor, which is determined by the equivalent mass and stiffness constant. The resonant frequency of the sensor can be given by

$$f_n = \frac{1}{2\pi}\sqrt{\frac{k}{m}}. \tag{7}$$

Therefore, the following relationship can be obtained from equation (4):

$$\left|\frac{x_0}{a}\right| = \frac{1}{\omega_n^2\sqrt{\left[1-(\omega/\omega_n)^2\right]^2 + (2\zeta\omega/\omega_n)^2}}. \tag{8}$$

In a specific frequency range, the inertial force exerted by the seismic mass on the piezoelectric element is alternating stress exerted, and the seismic mass approximately obeys Newton's second law:

$$F = ma, \tag{9}$$

where F is the inertial force.

Table 3: Ten design variables and their size ranges.

Design variable	Description	Reference size (mm)	Size range (mm)
x_1	Seismic mass diameter	27	26–28
x_2	Seismic mass height	11	10–12
x_3	Insulation sheet thickness	1.5	1.4–1.6
x_4	Conductive sheet thickness	0.3	0.25–0.35
x_5	Conductive sheet height	9	8–9
x_6	Piezoelement thickness	0.5	0.4–0.6
x_7	Piezoelement height	8	7–8
x_8	Base triangular prism height	11	10–12
x_9	Base thickness	9	7–9
x_{10}	Base inscribed circle outer diameter	31	30–32

Under the fixed premise, the amount of charge Q generated on the piezoelectric element is directly proportional to the force F:

$$Q = d_{ij}F = d_{ij}ma = d_{ij}kx_o(t), \tag{10}$$

where d_{ij} is the piezoelectric constant of the piezoelectric element.

Combining equations (8) and (10), the charge sensitivity of the sensor is obtained by

$$S_Q = \left|\frac{Q}{a}\right| = \frac{d_{ij}k}{\omega_n^2\sqrt{\left[1-(\omega/\omega_n)^2\right]^2 + (2\zeta\omega/\omega_n)^2}}, \tag{11}$$

where S_Q is the charge sensitivity.

Therefore, the sensitivity of the sensor is inversely proportional to the natural frequency and directly proportional to the piezoelectric coefficient. The designed sensor will compromise between high resonant frequency and high sensitivity [27]. When designing the sensor, the sensitivity can be improved by selecting materials with a high piezoelectric coefficient or reducing the natural frequency.

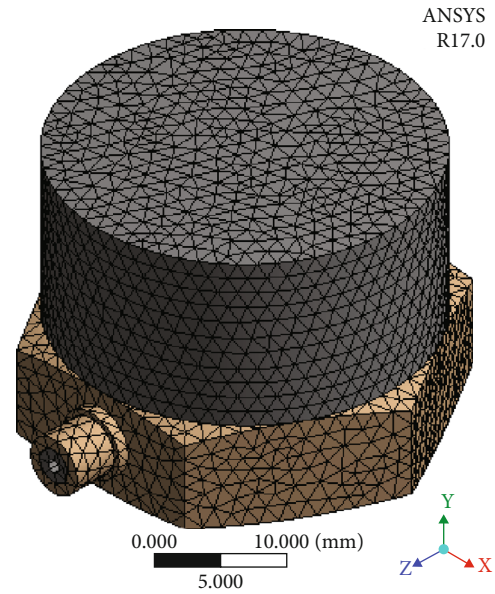

Figure 5: Finite element model of the designed sensor.

2.3. Material Selection. The designed sensor in this paper adopts a triangular shear structure, and the piezoelectric constant of the piezoelectric effect is mainly d_{15}. Commonly used piezoelectric materials mainly include SiO_2, $BaTiO_3$, PZT, and PVDF. Through the comparison of material properties, it is concluded that PZT-5H has a greater piezoelectric constant than other types of piezoelectric materials. In addition, the material has high dielectric properties and electromechanical coupling coefficient, which makes it have high sensitivity and fast response. More importantly, the temperature and time stability of the electromechanical parameters are strong. Because PZT-5H has better piezoelectric performance, the piezoelectric element of the sensor designed in this paper adopts PZT-5H.

According to the relevant data, the material selection of each sensor component is determined. The specific nonpiezoelectric materials and their properties are shown in Table 1. The electrical and mechanical properties of the piezoelectric material are shown in Table 2.

2.4. Parameterization Design. Design of Experiments (DOE) [28] has been used for effective simulation experiments. Using DOE test points, the resonant frequency and voltage are numerically calculated through modal analysis and piezoelectric analysis. The numerical modeling method approximately uses DOE test points to solve the relationship between design variables and performance.

Taking the YD-62 piezoelectric acceleration sensor as a reference sensor, the geometric standard of the internal components of the sensor is deduced. Ten design variables determined by the reference sensor are shown in Figure 4, and their size ranges are shown in Table 3.

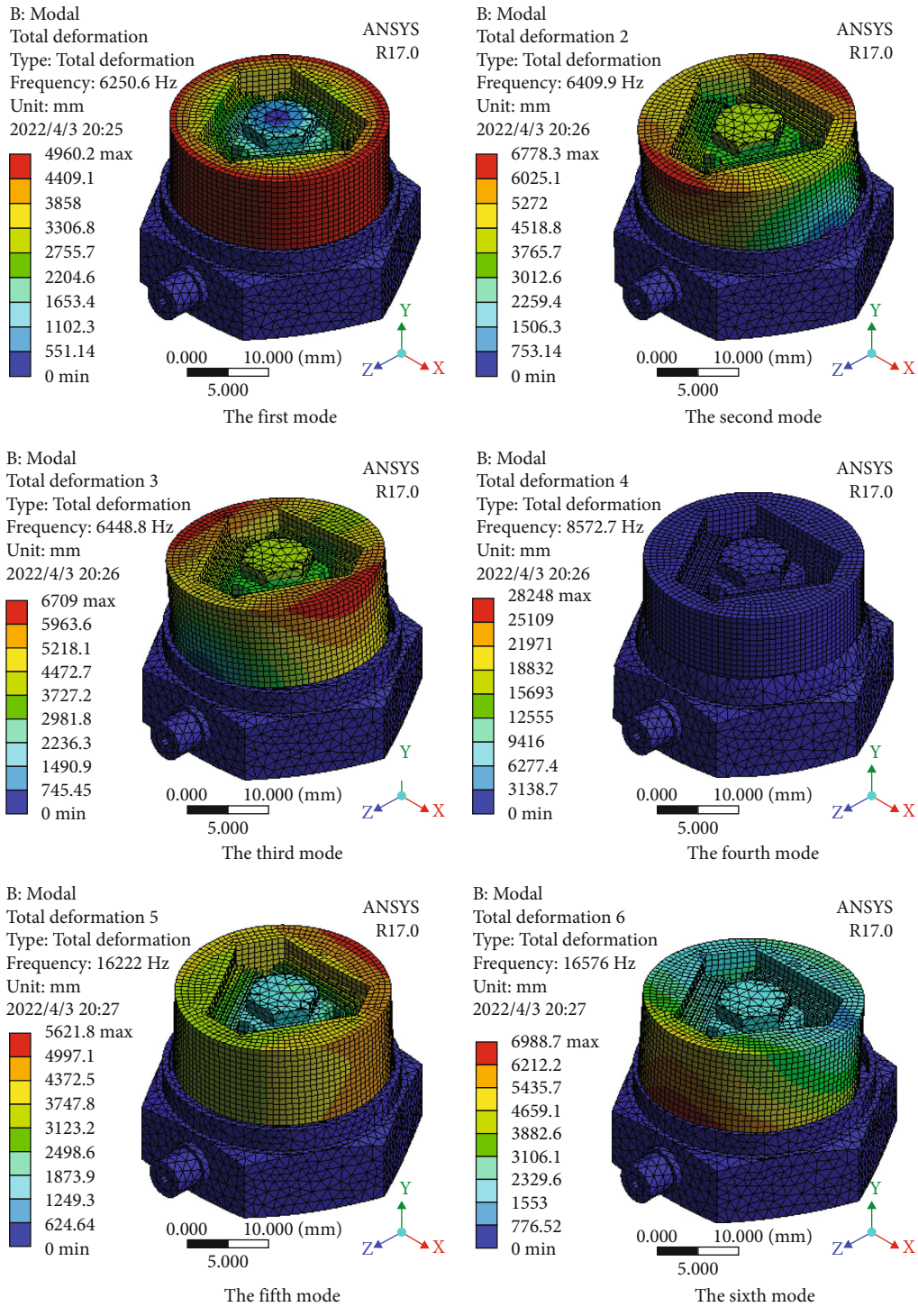

Figure 6: The first to sixth vibration modes.

3. Finite Element Analysis

According to the geometric and material parameters of the piezoelectric acceleration sensor, the structural model of the designed sensor is built by SOLIDWORKS, and the contact constraints are set in the assembly. Then, the above structural model is imported into ANSYS to build the finite element model of the designed sensor. At the same time, the original contact constraint is automatically transformed into bonded constraint. Then, the material parameters such as piezoelectric matrix, stiffness matrix, and dielectric constant are input. When meshing, the piezoelectric material part of the sensor is selected as SOLID226 element, and the metal material part is selected as SOLID186 element. The base and shell are meshed by tetrahedral elements, and other elements are hexahedral elements. The polarization direction of

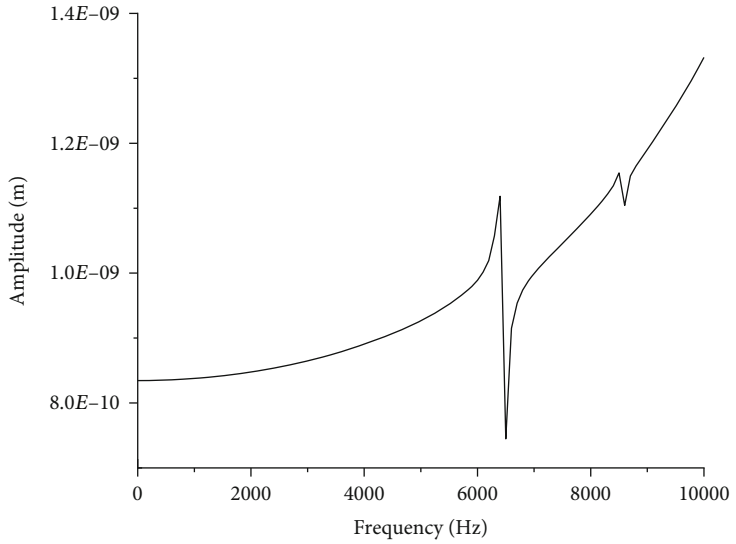

Figure 7: Sensor resonance frequency response.

each piezoelectric element is set by defining the local coordinate system, and then, the corresponding electrode surface is added. The fixed displacement constraint is added to the bottom surface of the sensor, and the acceleration load is applied to the whole model [29]. Figure 5 shows the meshing result of the sensor finite element model. The total number of elements and nodes is 42990 and 127838, respectively. Through modal analysis, harmonic response analysis, and piezoelectric analysis, the sensitivity and resonance frequency of the sensor can be calculated.

3.1. Modal Analysis. An important characteristic of the piezoelectric acceleration sensor is the response to different resonance frequencies, which can be studied by modal analysis. The upper cut-off frequency of the sensor depends on the resonance frequency of the amplitude-frequency curve. Dynamic characteristics mainly study the resonance frequency of the structure under dynamic load, which is an important parameter in structural design. The resonance frequency can be determined by modal analysis of the designed sensor using ANSYS [30]. Figure 6 shows the vibration modes of the designed sensor from 1st to 6th.

It can be concluded from the simulation results that the vibration frequencies from the first to the sixth mode are 6250.6 Hz, 6409.9 Hz, 6448.8 Hz, 8572.7 Hz, 16222 Hz, and 16576 Hz, respectively. There is a certain gap between the first and second modes of the sensor. The second mode is very close to the third mode, and they gradually increase rapidly from the third mode. The first mode is the rotational movement of the parts in contact with the triangular prism around the Y-axis. The main position of the second and third deformation modes is the bottom area of the triangular prism of the base, but the direction of bending deformation is orthogonal. The main position of the fourth mode deformation is the upper surface of the shell, and the fifth and sixth mode deformations are mainly caused by the deformation and sliding of piezoelectric elements and conductive

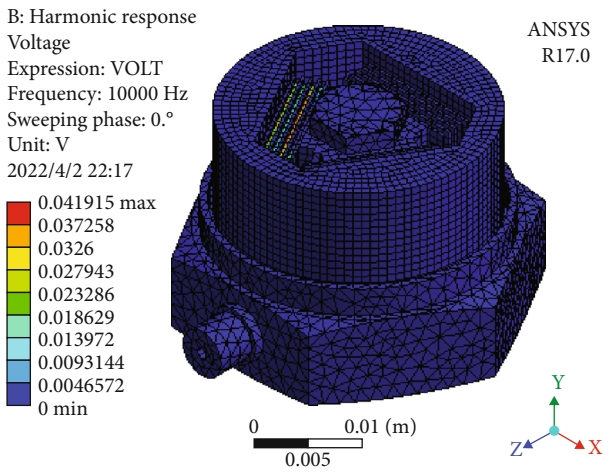

Figure 8: Voltage distribution diagram of the designed sensor.

sheets caused by the seismic mass. From the above analysis, the resonant frequency of the sensor is 6250.6 Hz. According to the amplitude-frequency characteristics of the sensor, 1/3 of the resonant frequency is taken as the upper frequency to reduce the amplitude error.

3.2. Harmonic Vibration Response Analysis. The target vibration direction of the sensor is the Y-axis direction. In this paper, the steady-state forced vibration of the sensor is solved by the harmonic response analysis method, and the inertial acceleration load of the microseismic signal is added to the bottom of the base. According to the resonance frequency obtained from modal analysis, the frequency range is tentatively determined as 0-10 kHz. One hundred frequency bands are defined within 0-10 kHz; that is, every 100 Hz is a frequency band [31].

In the equivalent system of the piezoelectric acceleration sensor, the damping coefficient is usually between 0.002 and 0.25. When the damping is air, the damping coefficient is

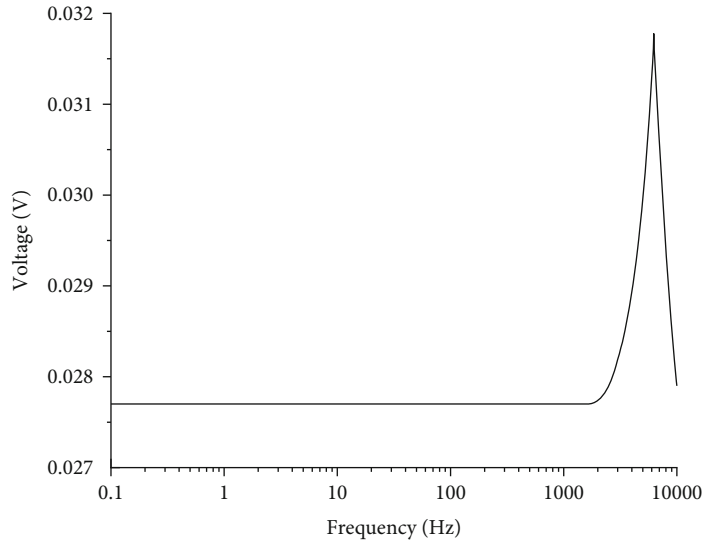

Figure 9: Voltage frequency diagram of the piezoelectric element.

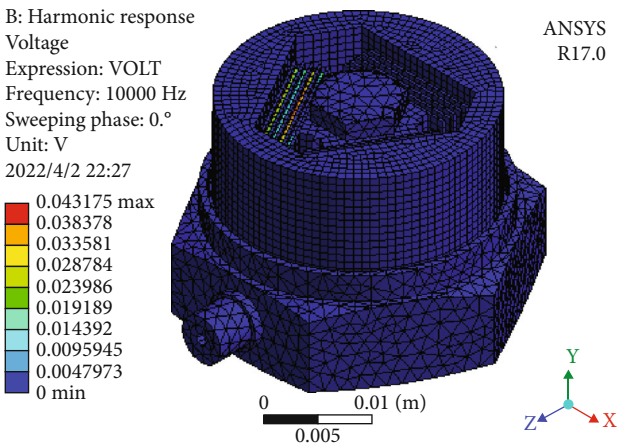

Figure 10: Voltage distribution diagram for case 1.

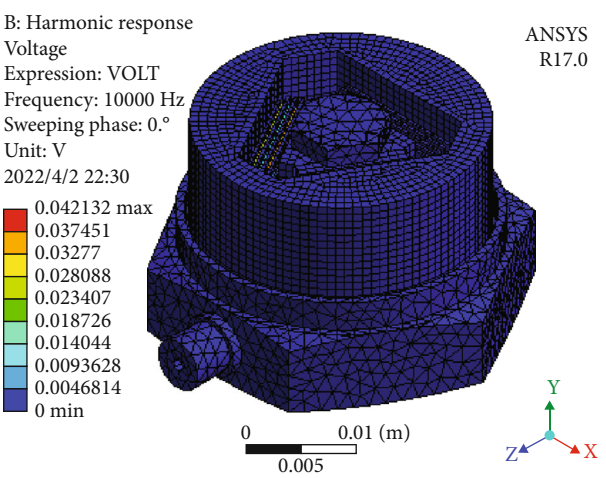

Figure 12: Voltage distribution for case 3.

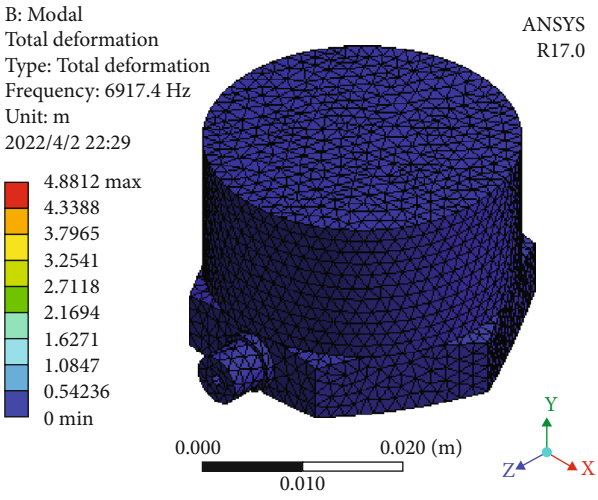

Figure 11: Modal analysis result for case 2.

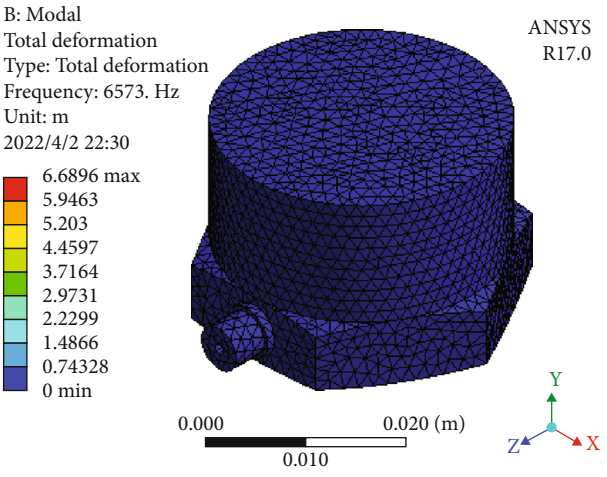

Figure 13: Modal analysis result for case 3.

Table 4: Values of optimized design variables and the results of cases 1, 2, and 3.

Case	x_1 (mm)	x_2 (mm)	x_3 (mm)	x_4 (mm)	x_5 (mm)	x_6 (mm)	x_7 (mm)	x_8 (mm)	x_9 (mm)	x_{10} (mm)	R.F. (Hz)	C.S. (pC/g)
1	27	12	1.4	0.285	8	0.4	7	11	7	30.6	6250	1945
2	26	11.96	1.5	0.3	8	0.4	7	11	7	30	6841.9	1635
3	27	11.17	1.4	0.28	8	0.4	7	10.5	7.8	31	6471.6	1817
Reference	27	11	1.5	0.3	9	0.5	8	11	9	31	6250.6	1635

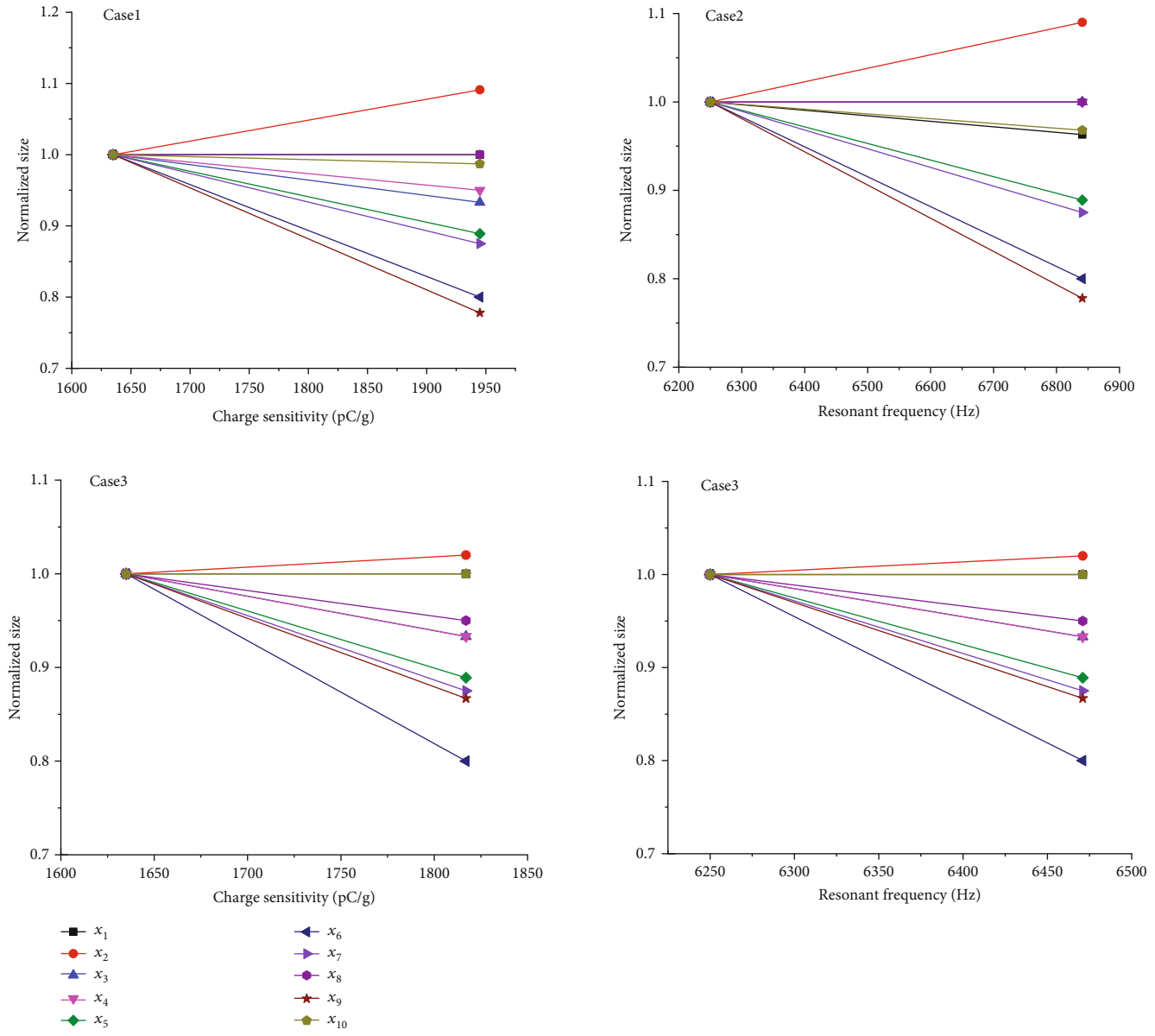

Figure 14: In all cases, the change in the normalized size of each design variable is relative to the reference design.

0.01. Therefore, in the above analysis, the value of the damping coefficient in the equivalent system remains constant ($c = 0.01$) [10]. Under the action of the simulated microseismic acceleration signal, the sensor produces resonant motion. After solving and processing, the harmonic response result of the sensor structure is obtained as shown in Figure 7.

According to the modal analysis results, the resonant frequency of the sensor is 6250.6 Hz. Therefore, the resonance frequency response curve should theoretically reach the peak amplitude at 6250.6 Hz. It can be seen from Figure 7 that the average amplitude of the first half is 8.4×10^{-10} m; the maximum amplitude is 1.1×10^{-9} m, appearing near 6250 Hz. Therefore, the maximum amplitude appears at the resonance

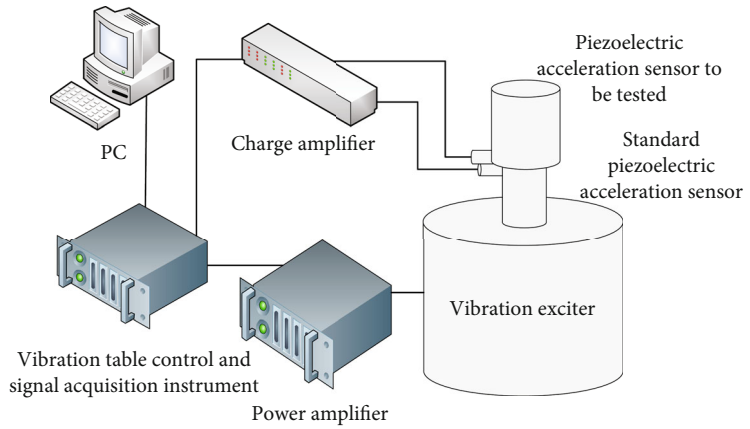

Figure 15: Schematic diagram of sensor calibration experiment test device.

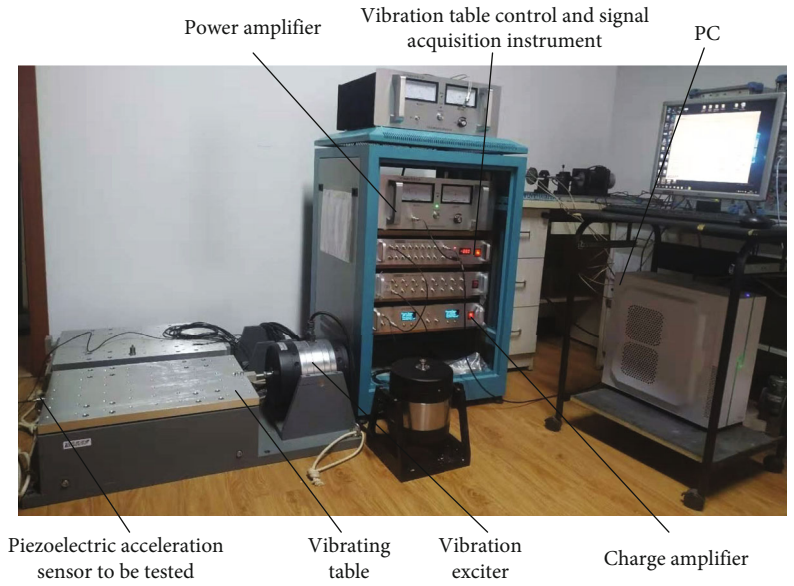

Figure 16: Physical diagram of sensor experimental test device.

frequency of 6250.6 Hz under the acceleration load of the sensor, and the stable working frequency of the sensor is 0-2083 Hz. In this frequency range, the frequency response curve of the sensor is approximately a straight line, which can be stably monitored by microseismic signals. According to Reference [32], the working frequency range of the sensor is 0 to 1/3 of the resonance frequency range. The simulation results verify the correctness of the above conclusion.

3.3. Piezoelectric Analysis. The charge sensitivity of the sensor is simulated based on the harmonic response analysis. Only the open-loop condition of the piezoelectric element is considered in the simulation calculation; that is, only the open-loop output potential of the piezoelectric element under acceleration load is calculated. The two surfaces of the piezoelectric element are set as zero potential constraint and voltage coupling constraint, respectively. Under the action of the external load, the voltage difference between two planes of the piezoelectric element is an amount to be determined [33]. The result of the piezoelectric analysis is shown in Figure 8.

Under the action of the acceleration load, the output voltage frequency diagram of the piezoelectric element is shown in Figure 9. The output voltage of the sensor is linear and stable in the range of 0-2083 Hz, and its charge sensitivity is 1635 pC/g.

3.4. Response Surface Optimization. Since the designed sensor contains many nonlinear features and geometric design variables, the Kriging model is used in response surface analysis, and the global approximation model is used in the metamodel [34]. Using the Kriging model, ten design variables are optimized through the response surface optimization method to determine which design variables will affect the performance of the designed sensor and how much its performance is improved compared to the reference sensor [35]. Therefore, three different cases are used to optimize the performance of the designed sensor, of which

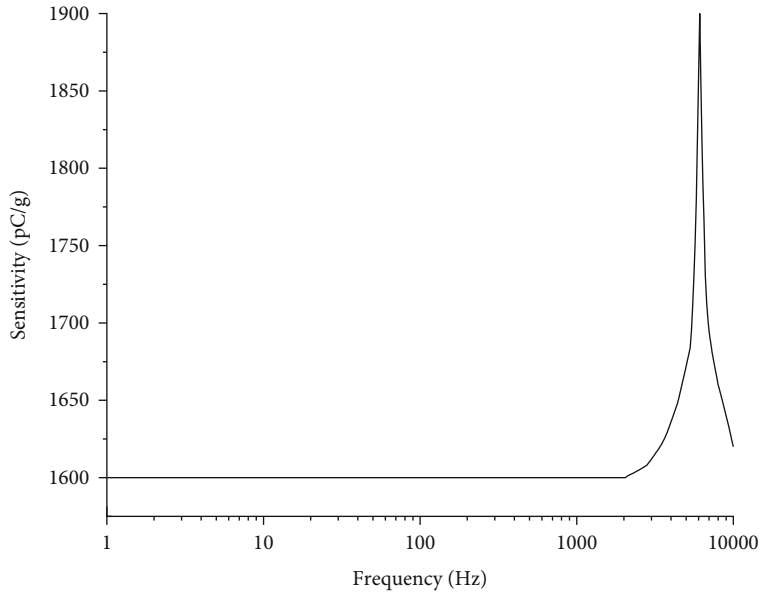

Figure 17: Charge sensitivity frequency response curve.

case 1 is to optimize the charge sensitivity at a constant resonant frequency (6250 Hz). The optimized voltage distribution is shown in Figure 10. Case 2 is to optimize the resonant frequency at a constant charge sensitivity (1635 pC/g). The optimized modal analysis result is shown in Figure 11. Finally, case 3 is used to optimize these two performances. The optimized voltage distribution and modal analysis results are shown in Figures 12 and 13. The optimized numerical analysis results in these three cases are shown in Table 4. Clearly, this optimization has successfully improved one performance (cases 1 and 2) or two performances (case 3).

As can be seen from Table 4, for case 1, the charge sensitivity increased by 18.96% (1945 pC/g), and for case 2, the resonant frequency increased by 9.46% (6841.9 Hz). For case 3, the charge sensitivity increased by 11.13% (1817 pC/g), and the resonance frequency increased by 3.54% (6471.6 Hz).

To study the influence of design variables on target performance in detail, Figure 14 shows the changes of ten design variables in three cases, and their sizes are standardized relative to the reference sensor. For case 1, the design variables that mainly affect the increase of charge sensitivity are $x_2, x_3, x_4, x_5, x_6, x_7, x_9$, and x_{10}. The height of the seismic mass increased by 9.1%; the thickness of the insulation sheet and the height of the conductive sheet decreased by 6.7% and 11.1%, respectively; the thickness and height of the piezoelectric element decreased by 20% and 12.5%, respectively; and the thickness of the base decreased by 22.2%. The influence of other design variables is not obvious (less than 5%). For case 2, the increased resonance frequency is mainly composed of $x_1, x_2, x_5, x_6, x_7, x_9$, and x_{10}. For example, the outer diameter of the seismic mass and the base decreased by 3.7% and 3.2%, respectively, while the height of the seismic mass increased by 8.7%. The remaining changed parameters are the same as in case 1. For case 3, the reason that the performance of both can be increased is that x_1 is increased by 1.5%, x_3 and x_4 are reduced by 6.7%, x_5 is reduced by 11.1%, x_6 is reduced by 20%, x_7 is reduced by 12.5%, x_8 is reduced by 4.5%, and x_9 is reduced by 13.3%.

As a result, the reduction in the thickness of the base and the reduction in the thickness and height of the piezoelectric element have a positive impact on both properties. Since the data of other design variables (seismic mass height and insulation sheet thickness) in Figure 14 show a positive impact on one performance and a negative impact on the other, these variables need to be controlled appropriately by selecting additions or decreases to meet the performance requirements. It is worth noting that the size of the seismic mass is the most obvious factor affecting performance, and the effect is just the opposite. This is proof of the conflict between resonant frequency and seismic mass sensitivity. The above analysis indicates that it is very significant to determine the optimal size of the seismic mass.

4. Results and Discussion

To test the performance of the designed sensor, a sensor experimental test device is built. According to international standards, when calibrating the piezoelectric acceleration sensor, it is necessary to adopt the vibration exciter to provide controllable excitation and record the output signal [36]. The setting of the piezoelectric acceleration sensor calibration experimental test device is shown in Figure 15. WS-5932/U160216-DA2 type vibration table control and signal acquisition instrument are adopted to generate a sinusoidal signal, which is amplified by the GF-500 type 500 W power amplifier and then exerted on the JZ-50 type vibration exciter to produce the required vibration. The WS-4601Z charge amplifier is adopted to amplify the electrical signals

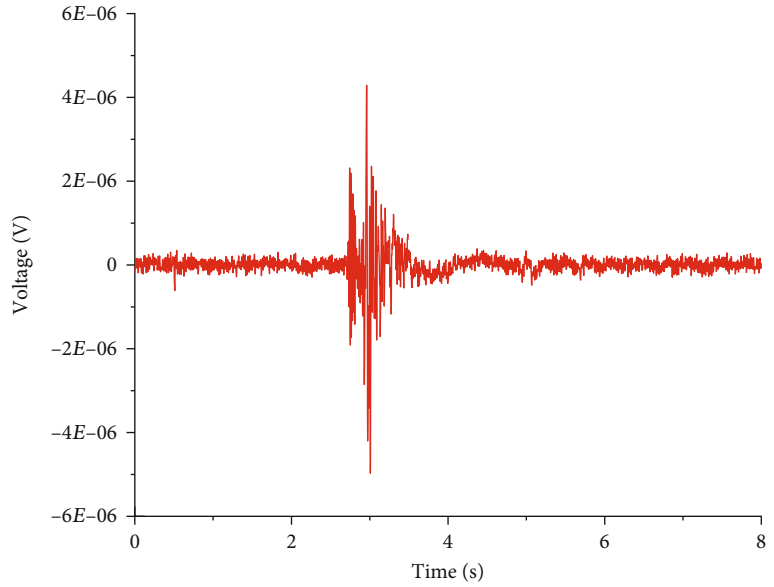

(a) The microseismic signal 1

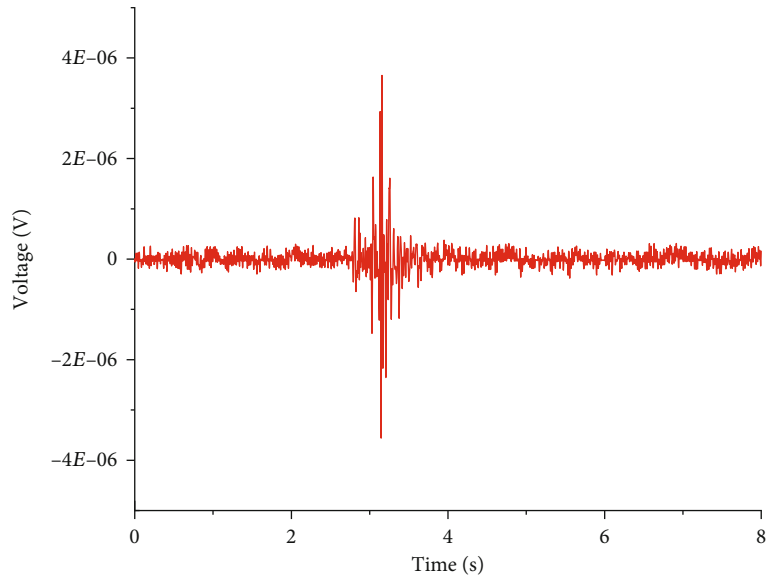

(b) The microseismic signal 2

Figure 18: Continued.

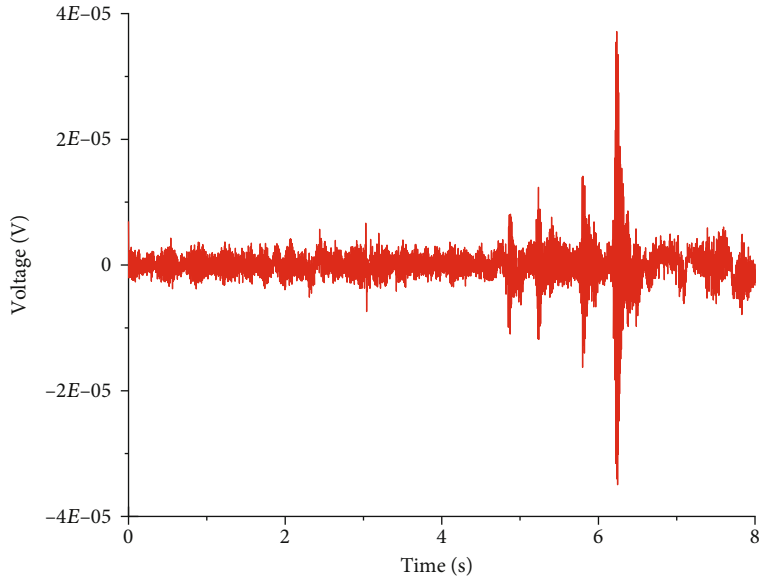

(c) The microseismic signal 3

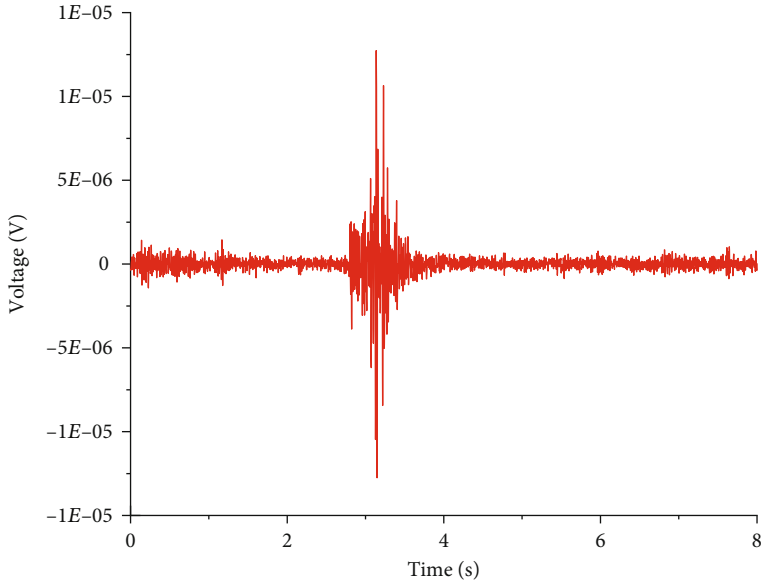

(d) The microseismic signal 4

Figure 18: Waveform of microseismic signals detected by the designed sensor.

from the standard piezoelectric acceleration sensor. The vibration signals detected by the designed sensor are converted into electrical signals through the piezoelectric elements and transmitted to the WS-2411Z charge amplifier. After signal conditioning, they are transmitted to the vibration table control and signal acquisition instrument. After A/D conversion, they are transmitted to a PC for data processing, and the sensitivity test curves of the piezoelectric acceleration sensor and the standard piezoelectric acceleration sensor are recorded.

The standard piezoelectric acceleration sensor is used to measure the acceleration of the vibration exciter. Its model is BK-8305, the charge sensitivity is 1.25 pC/g, and the working frequency is 1-10000 Hz. The back-to-back calibration method is used to measure the sensitivity of the tested sensor.

The experimental test device for the microseismic signal of the piezoelectric acceleration sensor is developed based on the calibration experimental device. Compared with the calibration experimental device, a new vibrating table directly connected to the vibration exciter is added, and the sensor is fixed on the vibrating table for the experimental test. The physical diagram is shown in Figure 16.

When testing the designed sensor, the steady-state sinusoidal excitation method is widely used in the world, which is provided by the vibration exciter. During the test, the sinusoidal signal is output by the vibration controller, amplified by the power amplifier, and then drives the vibrator to

make the measured sensor receive the vibration signal [37]. The charge sensitivity of the designed sensor is calibrated under an excitation signal of 1-10000 Hz. The calibration data is recorded by a computer, and the results are shown in Figure 17.

It can be seen from Figure 17 that the charge sensitivity of the designed sensor is 1600 pC/g, and the resonant frequency is 6150 Hz, so its effective working frequency is 0.1-2050 Hz. There are some errors between the experimental results and theoretical calculation or the finite element simulation. The main reason is that the simulation is set under the ideal conditions of the software without considering processing and assembly errors. In addition, in order to improve the sensitivity of the designed sensor, a more complex structure is adopted, and a certain working frequency range is sacrificed. The complex sensor structure will increase the difficulty of the processing and assembly of the sensor, resulting in large errors between the experimental results and the theoretical analysis or the simulation.

To verify the feasibility of the designed sensor to detect the microseismic signals, the vibration experiments are carried out on the platform shown in Figure 16. Four microseismic signals are selected for experimental verification. The vibration table is driven to vibrate by sending a microseismic signal to the vibration exciter. Then, the designed sensor is used for detection, and the results are shown in Figure 18. The results show that the designed sensor is feasible to detect microseismic signals and has the characteristics of a wide frequency range and high sensitivity.

5. Conclusions

In this paper, a piezoelectric acceleration sensor for microseismic monitoring based on a kind of triangular shear structure is designed and optimized. The piezoelectric element materials and other element materials of the sensor are determined. The modal analysis, resonance response analysis, and piezoelectric analysis of the designed sensor are carried out based on the finite element structural model. The experimental platform is built to verify the feasibility of the sensor to detect microseismic signals. The main conclusions can be drawn as follows:

(1) The natural frequency and sensitivity of the sensor are improved by improving the structure and selecting high-performance materials

(2) The reoptimized design of the reference sensor has successfully improved the performance, the resonant frequency is increased by 9.56%, and the charge sensitivity is increased by 18.96%

(3) The working frequency of the sensor is 0.1-2050 Hz, and the sensitivity is 1600 pC/g, which meets the frequency range and high sensitivity requirements of microseismic signal detection

Clearly, there is a lot of work to do in the future, including analysis of the background noise of the designed sensor, consideration of engineering application and verification in microseismic monitoring system, and further improvement of the working frequency and sensitivity of the piezoelectric acceleration sensor.

Data Availability

The data used to support the findings of this study are available from the corresponding author upon request.

Conflicts of Interest

We all declare that we have no conflict of interest in this paper.

Acknowledgments

This research was supported by the Key R & D Projects of Hebei Province under Grant 19275507D, Hebei Natural Science Foundation Project under Grant E2020402064, and Hebei Innovation Capability Improvement Plan Project under Grant 215676140H.

References

[1] Y. Jiang, Y. Pan, F. Jiang, L. Dou, and Y. Ju, "State of the art review on mechanism and prevention of coal bumps in China," *Journal of China Coal Society*, vol. 39, no. 2, pp. 205–213, 2014.

[2] L. Yuan, Y. D. Jiang, X. Q. He et al., "Research progress of precise risk accurate identification and monitoring early warning on typical dynamic disasters in coal mine," *Journal of China Coal Society*, vol. 43, no. 2, pp. 306–318, 2018.

[3] C. Peng, Y. Chen, Q. Chen et al., "A new type of tri-axial accelerometers with high dynamic range MEMS for earthquake early warning," *Computers & Geosciences*, vol. 100, pp. 179–187, 2017.

[4] N. Zeng, C. Z. Shi, M. Zhang, L. W. Wang, Y. B. Liao, and S. R. Lai, "A 3-component fiber-optic accelerometer for well logging," *Optics Communications*, vol. 234, no. 1-6, pp. 153–162, 2004.

[5] Y. M. Xing, S. H. Liu, and D. X. Wang, "Design and research on piezoelectric acceleration geophone," *Advanced Materials Research*, vol. 468-471, pp. 826–830, 2012.

[6] M. Li, Z. Lin, J. Liu, H. Lv, and L. Qin, "Principle study of a six-axis acceleration sensor," *Chinese Journal of Sensors and Actuators*, vol. 26, no. 9, pp. 1213–1218, 2013.

[7] H. Zhou, L. Hong, and Q. Cheng, "A low self-noise accelerometer based on piezoelectric bimorphs," *Journal of Chinese Inertial Technology*, vol. 28, no. 4, pp. 469–473, 2020.

[8] G. Xu, C. Wang, H. Yang, Y. Ma, and X. Chen, "Emulational analysis and design of anti-overload piezoelectric MEMS accelerometer for vibration monitoring of industrial equipment," *Instrument Technique and Sensor*, vol. 445, no. 2, pp. 28–32+55, 2020.

[9] Z. Qiu, J. Huang, and H. Hao, "Design and simulation on the suspension of MEMS sensor for low-frequency micro-seismic monitoring," *Mining Research and Development*, vol. 38, no. 11, pp. 113–118, 2018.

[10] A. T. Kollias and J. N. Avaritsiotis, "A study on the performance of bending mode piezoelectric accelerometers," *Sensors and Actuators A: Physical*, vol. 121, no. 2, pp. 434–442, 2005.

[11] D. Crescini, D. Marioli, E. Sardini, and A. Taroni, "Large bandwidth and thermal compensated piezoelectric thick-film acceleration transducer," *Sensors and Actuators A: Physical*, vol. 87, no. 3, pp. 131–138, 2001.

[12] L. P. Wang, R. A. Wolf, Y. Wang et al., "Design, fabrication, and measurement of high-sensitivity piezoelectric microelectromechanical systems accelerometers," *Journal of Microelectromechanical Systems*, vol. 12, no. 4, pp. 433–439, 2003.

[13] L. P. Wang, K. Deng, L. Zou, R. Wolf, R. J. Davis, and S. Trolier-McKinstry, "Microelectromechanical systems (MEMS) accelerometers using lead zirconate titanate thick films," *IEEE Electron Device Letters*, vol. 23, no. 4, pp. 182–184, 2002.

[14] K. Kim, S. Zhang, G. Salazar, and X. Jiang, "Design, fabrication and characterization of high temperature piezoelectric vibration sensor using YCOB crystals," *Sensors and Actuators A: Physical*, vol. 178, pp. 40–48, 2012.

[15] S. H. Choy, X. X. Wang, H. L. W. Chan, and C. L. Choy, "Study of compressive type accelerometer based on lead-free BNKBT piezoceramics," *Applied Physics A*, vol. 82, no. 4, pp. 715–718, 2006.

[16] P. A. Wlodkowski, D. Kan, and M. Kahn, "The development of high-sensitivity, low-noise accelerometers utilizing single crystal piezoelectric materials," *Sensors and Actuators A: Physical*, vol. 90, no. 1-2, pp. 125–131, 2001.

[17] C. Ai, X. Zhao, S. Li, Y. Li, Y. Bai, and D. Wen, "Fabrication and characteristic of a double piezoelectric layer acceleration sensor based on Li-doped ZnO thin film," *Micromachines (Basel)*, vol. 10, no. 5, p. 331, 2019.

[18] Q. Lu, J. Bai, K. Wang, and S. He, "Design, optimization, and realization of a high-performance MOEMS accelerometer from a double-device-layer SOI wafer," *Journal of Microelectromechanical Systems*, vol. 26, no. 4, pp. 859–869, 2017.

[19] W. R. Ali and M. Prasad, "Piezoelectric MEMS based acoustic sensors: a review," *Sensors and Actuators A: Physical*, vol. 301, p. 111756, 2020.

[20] S. Tadigadapa and K. Mateti, "Piezoelectric MEMS sensors: state-of-the-art and perspectives," *Measurement Science and Technology*, vol. 20, no. 9, p. 092001, 2009.

[21] T. Hou, H. Liu, J. Zhu et al., "Piezoelectric geophone: a review from principle to performance," *Ferroelectrics*, vol. 558, no. 1, pp. 27–35, 2020.

[22] Y. Xin, H. Sun, C. Guo et al., "Note: a novel cantilever beam for low-frequency high performance piezoelectric geophone," *The Review of Scientific Instruments*, vol. 88, no. 6, article 066105, 2017.

[23] M. K. Lee, S. H. Han, K. H. Park et al., "Design optimization of bulk piezoelectric acceleration sensor for enhanced performance," *Sensors (Basel)*, vol. 19, no. 15, p. 3360, 2019.

[24] S. Pyo, J. Kim, H. Kim, and Y. Roh, "Development of vector hydrophone using thickness-shear mode piezoelectric single crystal accelerometer," *Sensors and Actuators A: Physical*, vol. 283, pp. 220–227, 2018.

[25] J. C. Yu and C. B. Lan, "System modeling of microaccelerometer using piezoelectric thin films," *Sensors and Actuators A: Physical*, vol. 88, no. 2, pp. 178–186, 2001.

[26] A. Erturk and D. J. Inman, "Issues in mathematical modeling of piezoelectric energy harvesters," *Smart Materials and Structures*, vol. 17, no. 6, p. 065016, 2008.

[27] C. C. Hindrichsen, J. Larsen, E. V. Thomsen, K. Hansen, and R. Lou-Møller, "Circular piezoelectric accelerometer for high band width application," in *Proceedings of the 2009 IEEE Sensors*, pp. 475–478, Christchurch, New Zealand, 2009.

[28] C. Liu and Z. Fang, "Response surface method for complex mechanical assembly," *Journal of Xi'an Jiaotong University*, vol. 52, no. 9, pp. 28–36, 2018.

[29] X. Xu, Y. Li, G. Wang, X. Sun, and Y. Sun, "Design of six-axis force piezoelectric sensor with spoke structure," *Optics and Precision Engineering*, vol. 28, no. 12, pp. 2655–2664, 2020.

[30] B. Tian, H. Liu, N. Yang, Y. Zhao, and Z. Jiang, "Design of a piezoelectric accelerometer with high sensitivity and low transverse effect," *Sensors (Basel)*, vol. 16, no. 10, p. 1587, 2016.

[31] A. Sheikhaleh, K. Abedi, and K. Jafari, "A proposal for an optical MEMS accelerometer relied on wavelength modulation with one dimensional photonic crystal," *Journal of Lightwave Technology*, vol. 34, no. 22, pp. 5244–5249, 2016.

[32] D. Zhu, N. Wang, and M. Huang, "The analysis of the frequency response characteristics of the piezoelectricity acceleration geophone apllied to seismic exploration," *Journal of Railway Science and Engineering*, vol. 8, no. 5, pp. 113–118, 2011.

[33] Y. Yuan, D. Wang, X. Li et al., "Design of high sensitive piezoelectric accelerometer for nuclear power status monitoring," *Piezoelectrics & Acoustooptics*, vol. 41, no. 1, pp. 49–52, 2019.

[34] D. Huang, T. T. Allen, W. I. Notz, and N. Zeng, "Global optimization of stochastic black-box systems via sequential kriging meta-models," *Journal of Global Optimization*, vol. 34, no. 3, pp. 441–466, 2006.

[35] Z. Mohammed, W. A. Gill, and M. Rasras, "Modelling and optimization of inertial sensor-accelerometer," in *Outlook and Challenges of Nano Devices, Sensors, and MEMS*, pp. 331–345, Springer, 2017.

[36] H. Nozato, A. Oota, T. Ishigami, and T. Usuda, "The methods for the calibration of vibration pick-ups by laser interferometry: part V. Uncertainty evaluation on the ratio of transducer's peak output value to peak input acceleration in shock calibration," *Measurement Science and Technology*, vol. 22, no. 12, p. 125109, 2011.

[37] Y. Li, Y. Xu, J. Zhu et al., "Design, assembly and testing of a novel piezoelectric geophone based on PVDF film," *Integrated Ferroelectrics*, vol. 211, no. 1, pp. 69–81, 2020.

Hindawi
Geofluids
Volume 2022, Article ID 4316878, 17 pages
https://doi.org/10.1155/2022/4316878

Research Article

Study on Hydraulic Connection and Seepage Law of Goaf Groups in Coal Mine Underground Reservoir

Wei Qin

State Key Laboratory of Coal Resources and Mine Safety, China University of Mining and Technology, Xuzhou, Jiangsu Province 221116, China

Correspondence should be addressed to Wei Qin; qw198427@163.com

Received 22 January 2022; Accepted 1 March 2022; Published 24 March 2022

Academic Editor: Basim Abu-Jdayil

A coal mine underground reservoir, composed of a large number of goaf groups, is effective in achieving the protective utilization of coal mine water. Mastering the hydraulic connection between the goaf groups and the law of seepage is the key to the design and safe operation of coal mine underground reservoirs. Coal/rock sample seepage tests were conducted in Wanli No. 1 Mine in the Shendong mining area according to the evolution law of the lateral supporting pressure of the coal pillars. From the tests, the function of vertical stress in relation to the permeability of coal/rock samples was obtained and the distribution law of permeability of porous media in the goaf was revealed. On this basis, the computational fluid dynamics (CFD) numerical calculation of seepage properties of the coal/rock pillars was conducted. The results show that with the decrease of water level in the goaf and the increase of coal pillar width, the flow range and flow velocity keep decreasing. At the water level of 18.65, 28.65, and 38.65 m, the critical coal pillar widths for the goaf water to penetrate into the adjacent goaf are 30, 50, and 70 m, respectively. When the coal pillar width is less than 10 m, the water can bypass the elastic core area at the bottom coal seam to the adjacent goaf area; when the width exceeds 20 m, the water cannot enter the adjacent goaf area through the bottom coal pillar. On the basis of CFD simulation study on seepage properties of coal/rock pillars between goafs, this paper conducts calculations for all the goafs in the 4-2 coal-panel block of Wanli No. 1 Mine and reveals the seepage path and seepage law in the underground reservoir of this mine.

1. Introduction

An underground reservoir, formed by underground pores in sand and gravel, rock cracks or karst caves in a certain range, has the advantages of large storage capacity, small evaporation loss, and not occupying land surface. Japan's Nagasaki has built the world's first underground reservoir, though the storage capacity is only 9,000 m^3 [1]. The aquifer storage and recovery (ASR) program implemented in the United States stores water by preinjecting it into the aquifer and extracts it when needed [2, 3]. Since the 1950s, Amsterdam, the Netherlands, has been diverting water from the Rhine River to canals and ditches on natural sand dunes to replenish groundwater [4]. These practices can shed light on water resource protection in western China where the ecological environment is fragile, especially areas with large-scale coal mining activities. The traditional water-preserving mining technology adopts the "blocking method" to protect the aquiclude, but this technology greatly limits the mining efficiency and recycling rate of coal mines. For this reason, Shenhua Group put forward a new concept of "diverting, storing, and utilizing water" with coal mine underground reservoirs to achieve water resource protection and utilization [5].

Wanli No. 1 Mine, located in Dongsheng District, Ordos City, Inner Mongolia, is in a typical arid and semiarid area with a fragile ecological environment. In view of this, water conservation is introduced to build underground reservoirs that have been adopted in the Shendong mining area. An underground reservoir water conservation project was implemented in the goaf of south and north wings of coal panel No. 4-2, where some coal pillars were left between adjacent goafs after the mining of working face. These structures had a significant impact on the hydraulic connection of

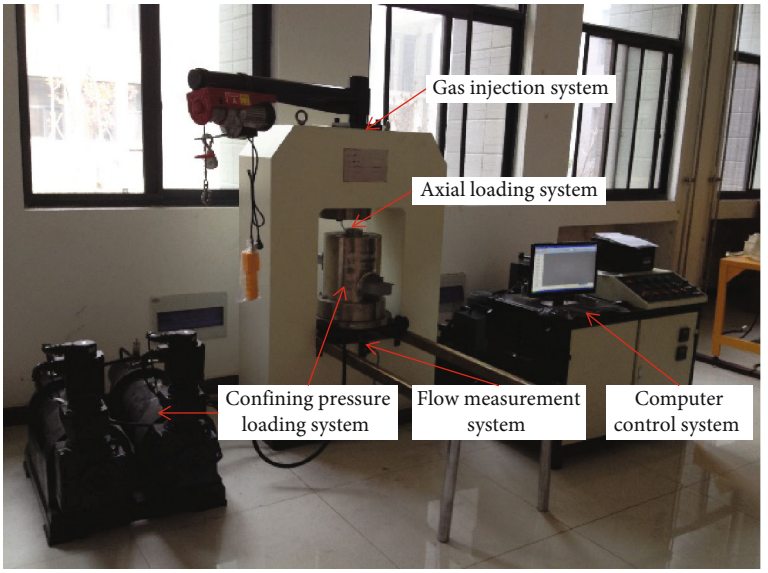

Figure 1: Three-axis servo seepage testing machine.

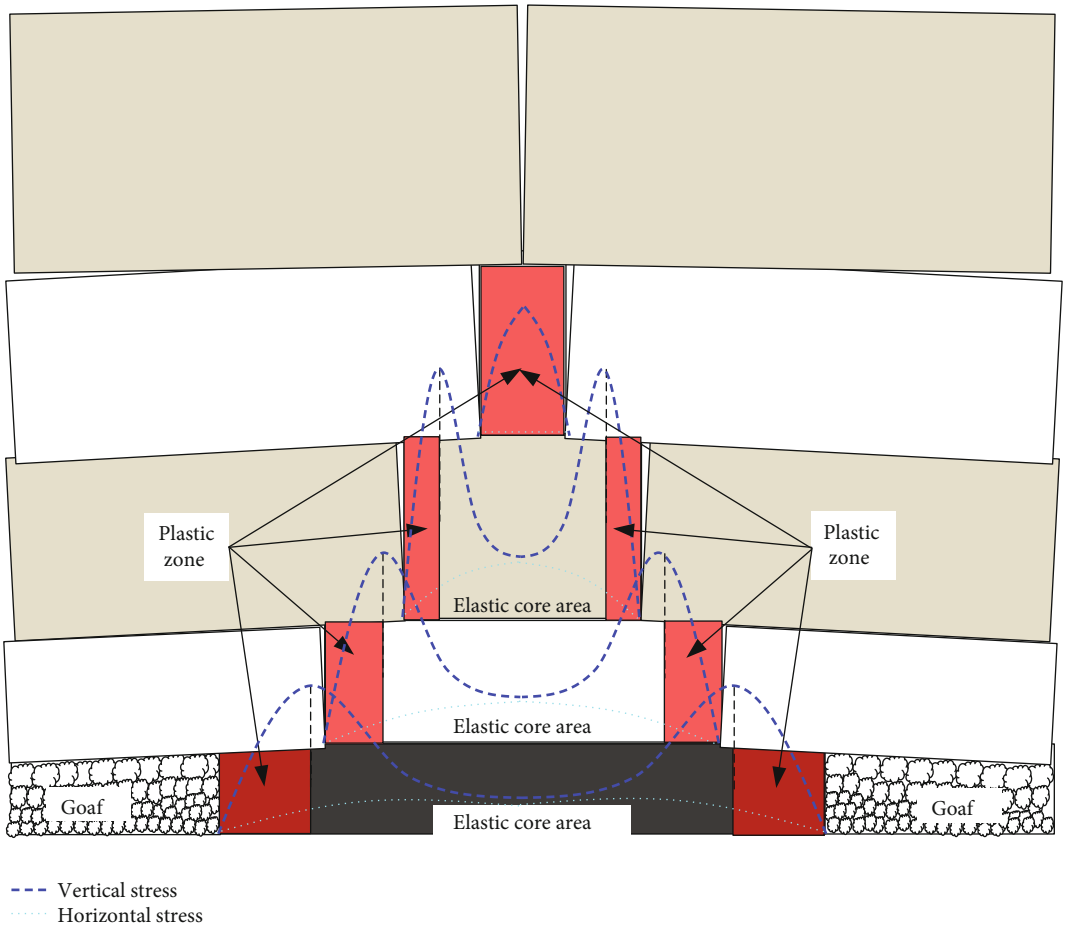

Figure 2: Vertical stress distribution of coal/rock pillar from No. 4-2.

this area. Scholars from China and abroad have, at present, studied the seepage properties of fractured rock from both theoretical and practical perspectives. Ma systematically studied the properties of broken rockmass and saturated broken rockmass, including the swelling and permeability properties, porosity compaction, and the deformation

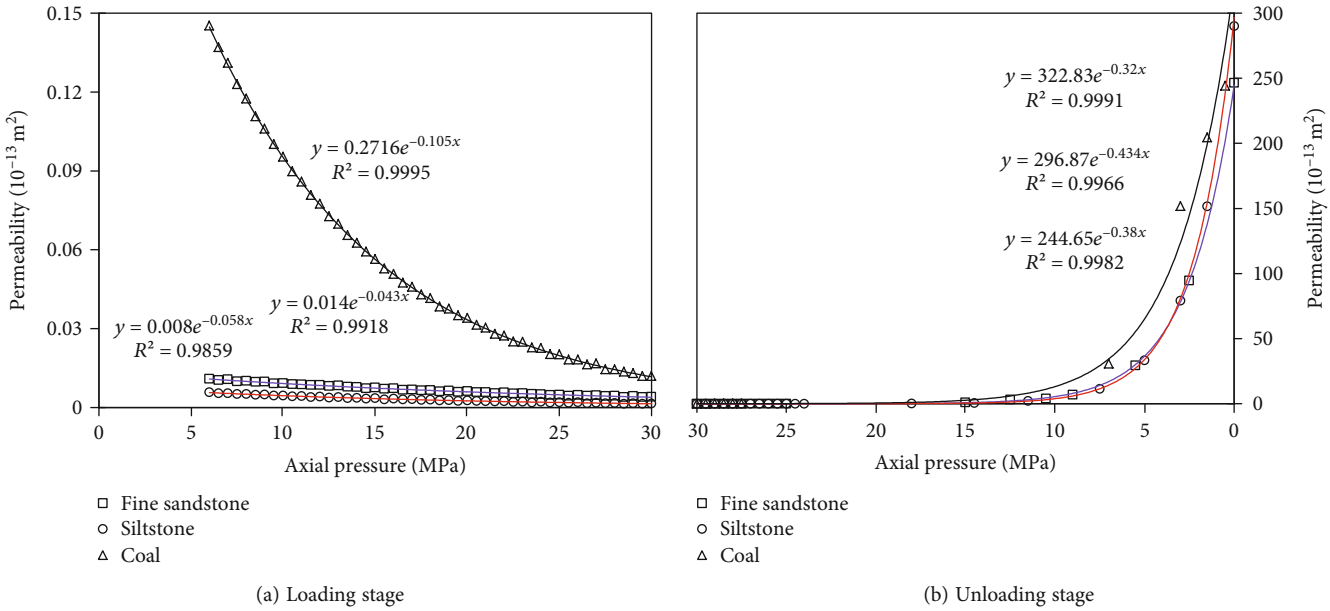

Figure 3: Curves of permeability and axial pressure. (a) Loading stage. (b) Unloading stage.

Table 1: Fitting function of coal/rock sample permeability and axial pressure.

Lithology	Permeability in loading stage (1×10^{-13} m^2)	Permeability in unloading stage (1×10^{-13} m^2)
Coal	$0.2716e^{-0.105x}$ $R^2 = 0.9995$	$322.83e^{-0.320x}$ $R^2 = 0.9991$
Fine sandstone	$0.014e^{-0.043x}$ $R^2 = 0.9918$	$244.65e^{-0.380x}$ $R^2 = 0.9982$
Siltstone	$0.008e^{-0.058x}$ $R^2 = 0.9859$	$296.87e^{-0.434x}$ $R^2 = 0.9966$

modulus. He further studied seepage property of broken rock in the goaf with numerical simulation [6]. Yang et al. suggested that water flow should experience three physical processes during the water inrush after the mining rockmass failure, i.e., Darcy laminar flow in the aquifer, non-Darcy high-speed flow in the rockmass, and the Navier-Stokes turbulent flow in the roadway [7, 8]. Based on the key layer theory of rock strata control studies, Cao et al. examined the properties of water flow in the fracture and its main channel distribution model [9] from the perspective of fracture pattern and fracture distribution in the overlaying rockmass. In searching for methods preventing water damage in the abandoned goaf of Yangquan No. 3 Mine, Xu et al. focused on predicting the roof water-conducting crack in the lateral boundary of the goaf and proposed a method to judge the lateral boundary of the roof water-conducting crack in relation to the scale of horizontal deformation [10]. Fink et al. studied the permeability properties of shale under the influence of both slip flow and pore elastic effects in the range of large pore pressure. They established a permeability model taking slip flow and pore elastic effects into account [11]. Ghanizadeh et al. first revealed that the permeability of early Jurassic shale in northern Germany decreased nonlinearly with the increase of effective stress [12].

The existing studies on seepage in the goaf mainly focus on the prevention and control of water hazards, but quite little has been done on the hydraulic connection, the seepage law, and the seepage path between the goaf of coal mine underground reservoirs. Therefore, taking the Wanli No. 1 Mine in the Shendong mining area as the engineering background, this study designed tests according to the evolution law of the lateral supporting pressure of the coal pillars in the area and conducted seepage tests of the coal/rock samples to obtain the function of the coal/rock permeability with the change of vertical stress. Following that, the CFD numerical calculation of the seepage properties in the goaf area was conducted, which revealed the hydraulic connection, the seepage law, and the seepage path between the adjacent goaf. The results could provide guidance for optimizing the design of coal mine underground reservoirs and hence ensuring the safe operation of them.

2. Coal/Rock Pillar Seepage Test

2.1. Test Equipment. In order to study the law of permeability change of coal pillars and its overlaying rock with coal/rock stress in Wanli No. 1 Mine, a three-axis servo seepage testing machine (Figure 1) was used for detecting coal/rock deformation under seepage action. It consists of five parts, namely, confining pressure loading system, axial loading system, gas injection system, flow measurement system, and computer control system.

2.2. Test Design. During mining of a coal seam, the variation in stress in a coal/rock mass significantly influences the deformation and failure characteristics of the coal/rock mass itself. Figure 2 shows how the variation of the stress field

No.	Thickness (m)	Depth (m)	Lithology	Position of key strata	Columnar section
27	10.59	10.59	Coarse sandstone		
26	6.21	16.80	Coarse sandstone		
25	8.05	24.85	Coarse sandstone		
24	1.55	26.40	Coal		
23	0.75	27.15	Siltstone		
22	1.10	28.25	Coal		
21	1.15	29.40	Siltstone		
20	1.20	30.60	Coal		
19	3.20	33.80	Siltstone		
18	4.60	39.40	Fine sandstone		
17	4.10	42.50	Siltstone		
16	2.45	44.95	Coal		
15	6.70	51.65	Siltstone		
14	1.05	52.70	Coal		
13	1.35	54.05	Siltstone		
12	2.10	56.15	Fine sandstone		
11	2.95	59.10	Siltstone		
10	7.90	67.00	Fine sandstone		
9	3.27	70.27	Medium sandstone		
8	6.73	77.00	Coarse sandstone		
7	2.70	79.70	Fine sandstone		
6	1.90	81.60	Siltstone		
5	1.20	82.80	Fine sandstone		
4	2.15	84.95	Coal		
3	21.05	106.00	Siltstone	Primary key stratum	
2	0.60	106.60	Fine sandstone		
1	3.95	110.55	Siltstone	Secondary key stratum	
0	5.10	115.65	Coal		

Figure 4: Key strata distinguishing results of ZK1416 borehole.

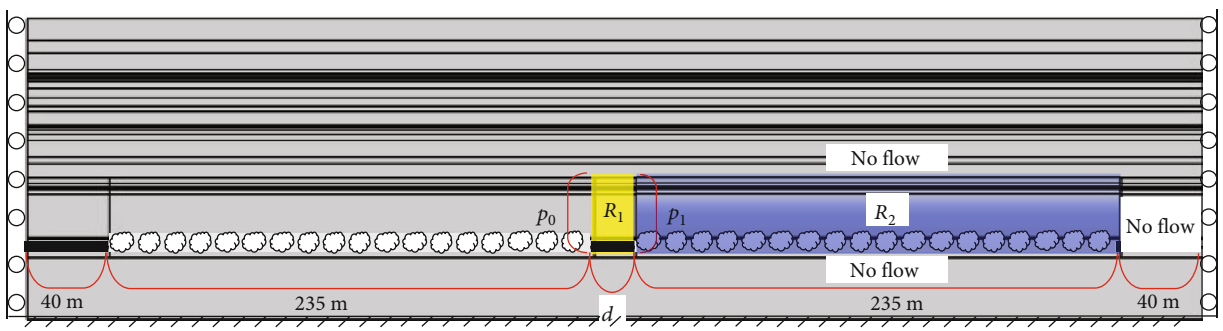

Figure 5: Geometric structure model.

Table 2: Parameter table of the model.

Parameter name	Coal	Fine sandstone	Siltstone	Water	Source
Elastic modulus (MPa)	700	953	995	—	Laboratory data
Poisson's ratio	0.28	0.26	0.22	—	Laboratory data
Density (kg·m^{-3})	1400	2570	2590	1000	Laboratory data
Yield stress (MPa)	6	14×10^6	17×10^6	—	Laboratory data
Dynamic viscosity (Pa·s)	—	—	—	1.01×10^{-3}	Laboratory data [15]
Porosity	0.05	0.03	0.03	—	Laboratory data [15]

Table 3: Simulation schemes.

Water level (m)	Coal pillar width (m)	Water level (m)	Coal pillar width (m)	Water level (m)	Coal pillar width (m)
18.65	10	28.65	10	38.65	10
18.65	20	28.65	20	38.65	20
18.65	30	28.65	30	38.65	30
18.65	40	28.65	40	38.65	40
18.65	50	28.65	50	38.65	50
18.65	60	28.65	60	38.65	60
18.65	70	28.65	70	38.65	70

influences the distribution of mining-induced fractures after mining of the coal seam. After the coal seam is mined, the stresses in the surrounding rock are redistributed. From the center of the coal pillar to both sides of the coal pillar, the stress of coal and rock gradually changes from the triaxial stress state to the uniaxial stress state. The bearing capacity of the coal/rock mass near the coal pillar boundary decreases, and the stress is transferred to the interior of the coal/rock pillar, forming lateral abutment pressure. Under the effect of lateral abutment pressure, plastic failure occurs in the coal/rock masses, significantly raising the permeability of the coal masses. As shown in Figure 2, the coal pillar in the No. 4-2 Coal Panel of Wanli No. 1 Mine (henceforth referred to as "No. 4-2") is about 20 m in width, with an elastic core area in the middle and a certain length of plastic zones on both sides. The permeability of the plastic failure zone is high, meaning that water in the goaf can easily penetrate it. Similarly, the permeability of the elastic core area is comparatively low, which means water on one side can only pass through the coal/rock pillar to the other side when the pressure discrepancy is large enough. Due to the narrow width of the upper rock pillar, the whole rock pillar is in a plastic state, and the elastic core area disappears.

The obtained coal/rock sample from No. 4-2 was cut and processed into specimens with a diameter of 50 mm and a height of 100 mm. The change of vertical stress was simulated by loading and unloading of axial pressure, and the change of horizontal stress was simulated by loading and unloading of confining pressure. Air tightness between the airway system, and the sample was checked before the test. A specimen coated with silicone rubber and enclosed within a heat shrinkable tube was put into the seepage experiment machine. Axial pressure was applied slightly first to press the specimen, then oil was injected to remove the air in the pressure chamber, and the oil return valve was closed. In the first stage of the test, the axial pressure and confining pressure of the coal/rock sample were loaded at a rate of 0.01 MPa/s to 6 MPa; in the second stage, the confining pressure (6 MPa) was kept constant, and the axial pressure was loaded to 30 MPa at a rate of 0.01 MPa/s; in the third stage, the axial pressure and confining pressure are both unloaded at the speed of 0.01 MPa/s, until the coal/rock sample is destroyed. In the second stage of the test process, that is, when the axial pressure and the confining pressure are both at 6 MPa, the pressure relief valve was adjusted to stabilize the cylinder pressure at 1 MPa, and then, the pipeline valve was opened. After the flow rate was stable, the rate was recorded. During the test, the flow rate was recorded for every 0.5 MPa change in axial pressure.

2.3. Test Results. Permeability is an important parameter in the law of solid-liquid coupling seepage. According to Darcy's law, the permeability K of the sample can be expressed as [13]

$$K = \frac{QL\mu}{[A(P1 - P2)]}, \tag{1}$$

where K is permeability, m^2; Q is helium flow rate, m^3/s; L is height of the coal sample, m; μ is helium dynamic viscosity (18.9 μPa·s); A is cross-sectional area of the coal sample, m^2; P_1 is inlet gas pressure, Pa; P_2 is outlet gas pressure (0.1 MPa).

By taking the specimen parameters in this test and the helium gas flow data into equation (1), the relationship was obtained between coal/rock permeability and axial pressure in pressure-loading and pressure-unloading stages, as shown in Figure 3.

The coal/rock permeability was closely related to the coal/rock deformation and damage. As shown in Figure 3(a), when axial pressure increases while confining pressure is fixed, the gas flow channel is closed, and the coal/rock permeability and the gas flow rate decreases gradually. Therefore, the permeability is the lowest when the lateral support pressure of the coal pillar is at its peak position. Compared with rock sample, the initial permeability of coal sample is higher, but when axial pressure increases, the drop of coal permeability is also greater due to its softness and the compaction of its internal pores. Figure 3(b) shows that with the decrease of axial pressure and confining pressure, the

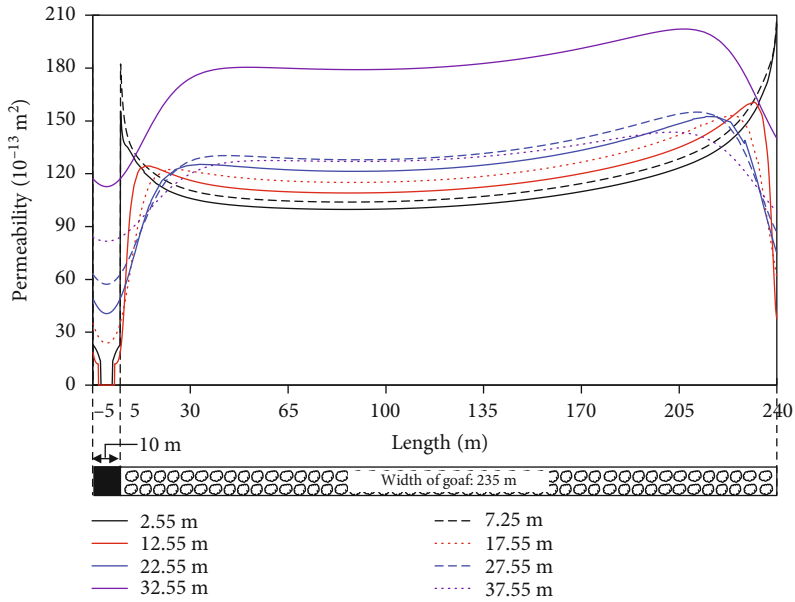

(a) Coal pillar width is 10 m

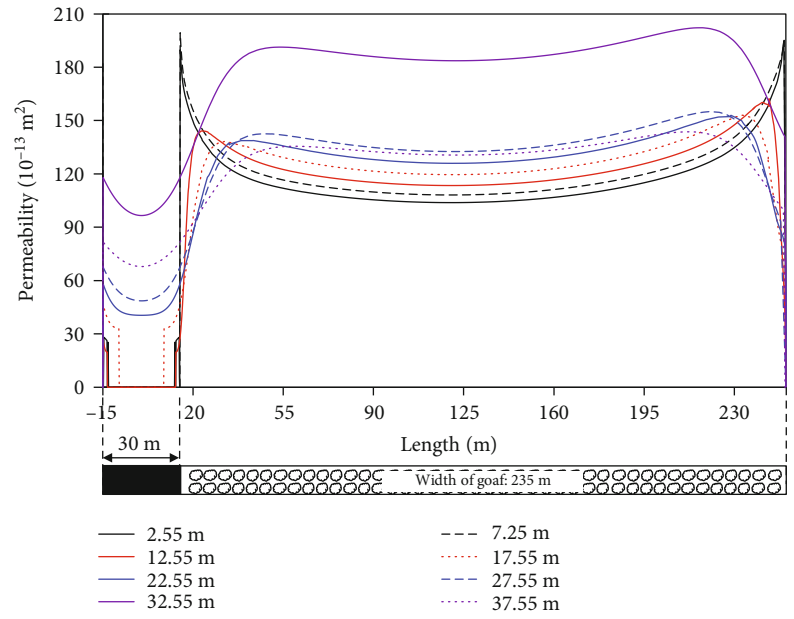

(b) Coal pillar width is 30 m

Figure 6: Continued.

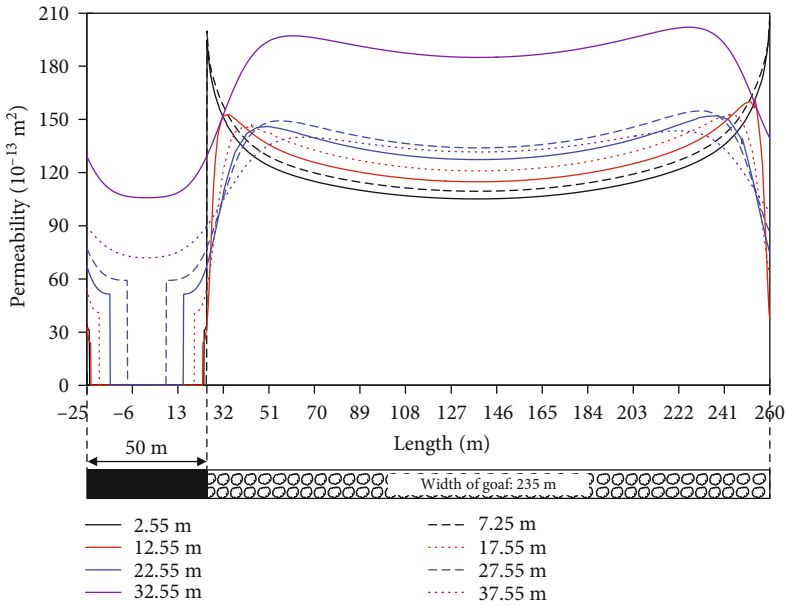

(c) Coal pillar width is 50 m

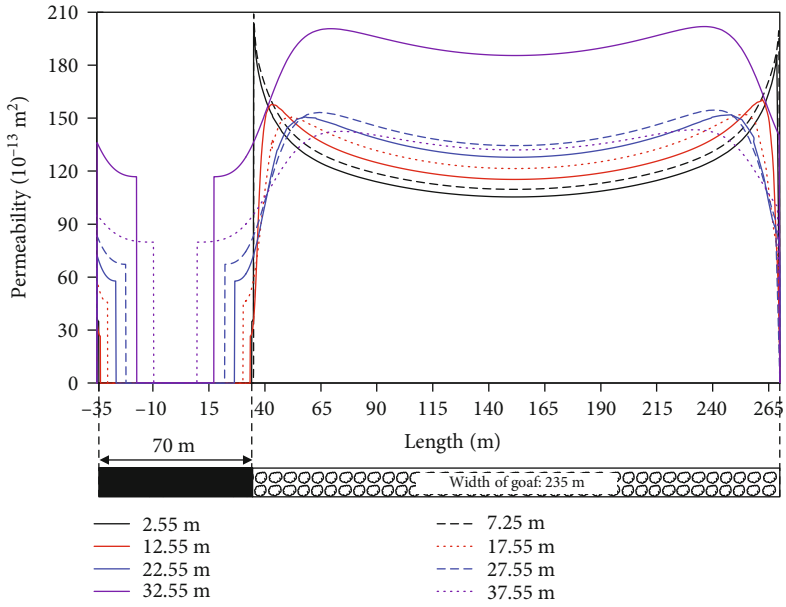

(d) Coal pillar width is 70 m

Figure 6: Permeability distribution curves at different coal pillar widths. (a) Coal pillar width is 10 m. (b) Coal pillar width is 30 m. (c) Coal pillar width is 50 m. (d) Coal pillar width is 70 m.

permeability of coal/rock samples continues to increase. In the early stage of the unloading stage, due to the high confining pressure, the coal/rock sample still maintains its strength, with a slight permeability increase. In the later stage of the unloading stage, featured with the low confining pressure, the coal/rock sample becomes unstable. After reaching its strength limit, its permeability increases sharply. After the unstable state, the scale of increase in permeability of the coal sample is the smallest, only 263 times higher than its minimum permeability, while that of the siltstone is the largest, about 139,519 times higher than its own minimum value. In the pressure loading and unloading stages, the relationship between coal/rock sample permeability and axial pressure can be fitted with an exponential function, and the fitting results are shown in Table 1.

3. CFD Numerical Calculation of Seepage Properties of the Coal/Rock Pillar

3.1. Establishment of Numerical Calculation Model

3.1.1. Geometric Model and Boundary Conditions. Strata of different hardness and thickness may play two controlling roles by affecting part of the strata above or the whole strata

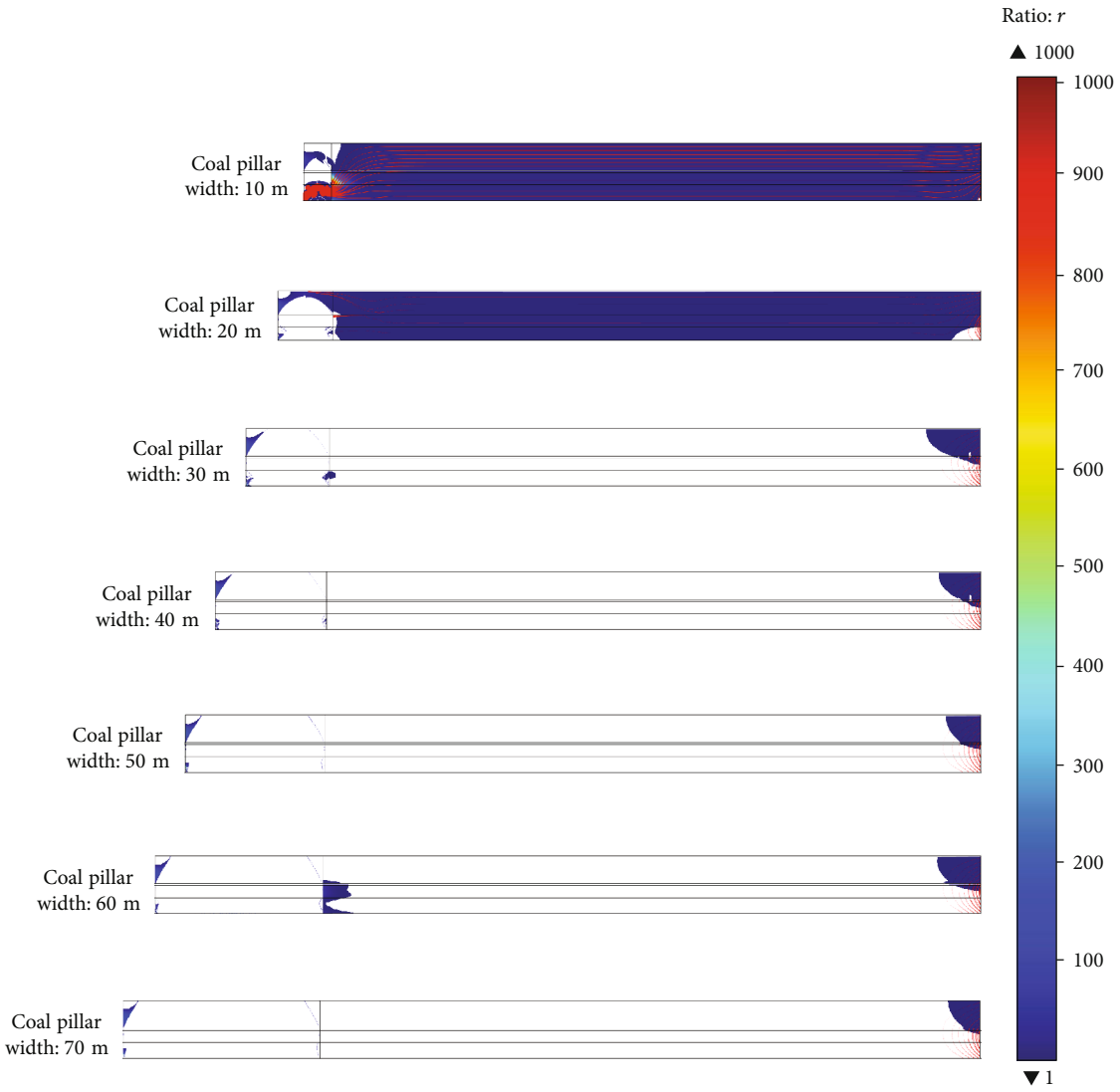

(a) Water level at 18.65 m

Figure 7: Continued.

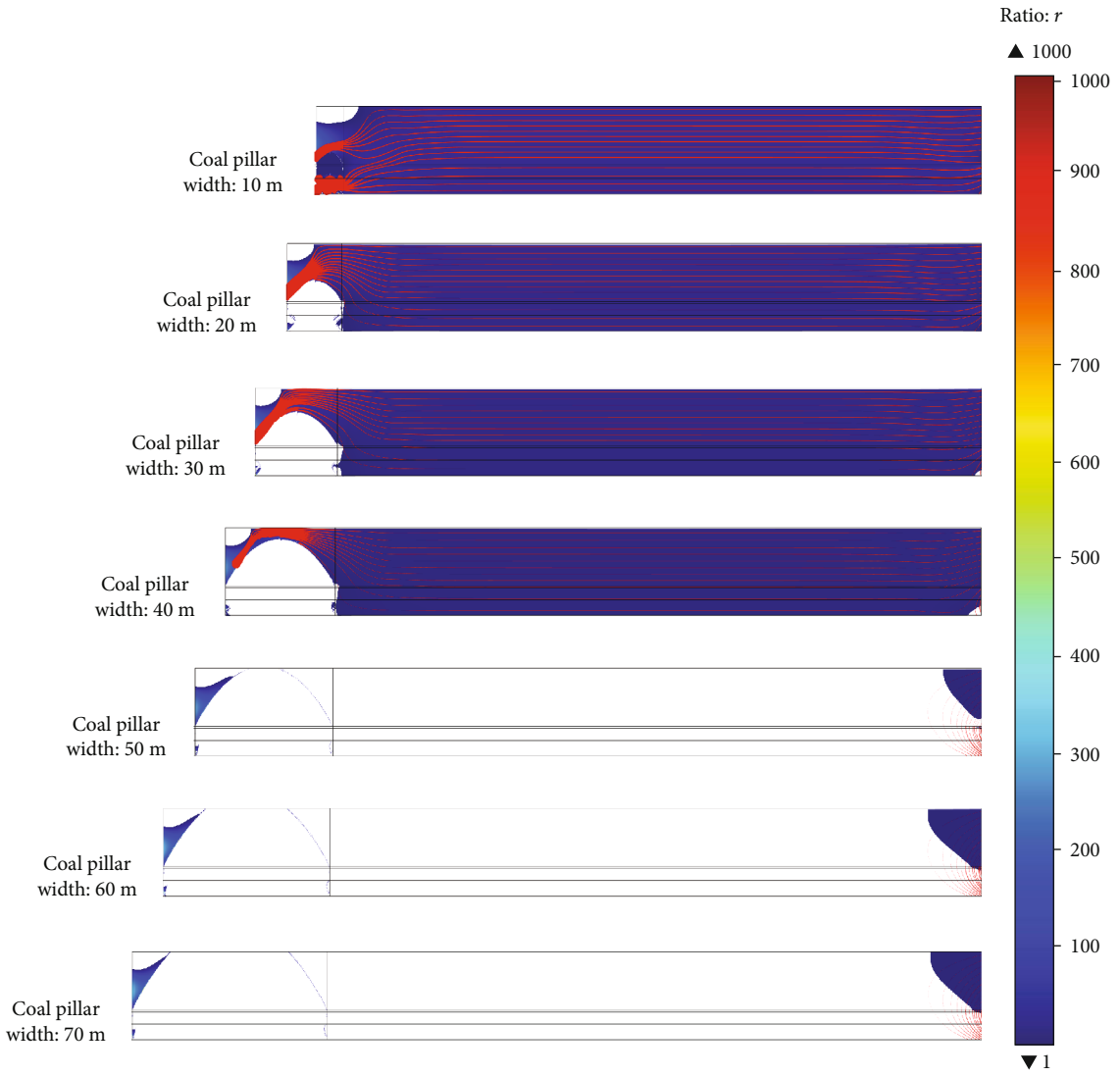

(b) Water level at 28.65 m

Figure 7: Continued.

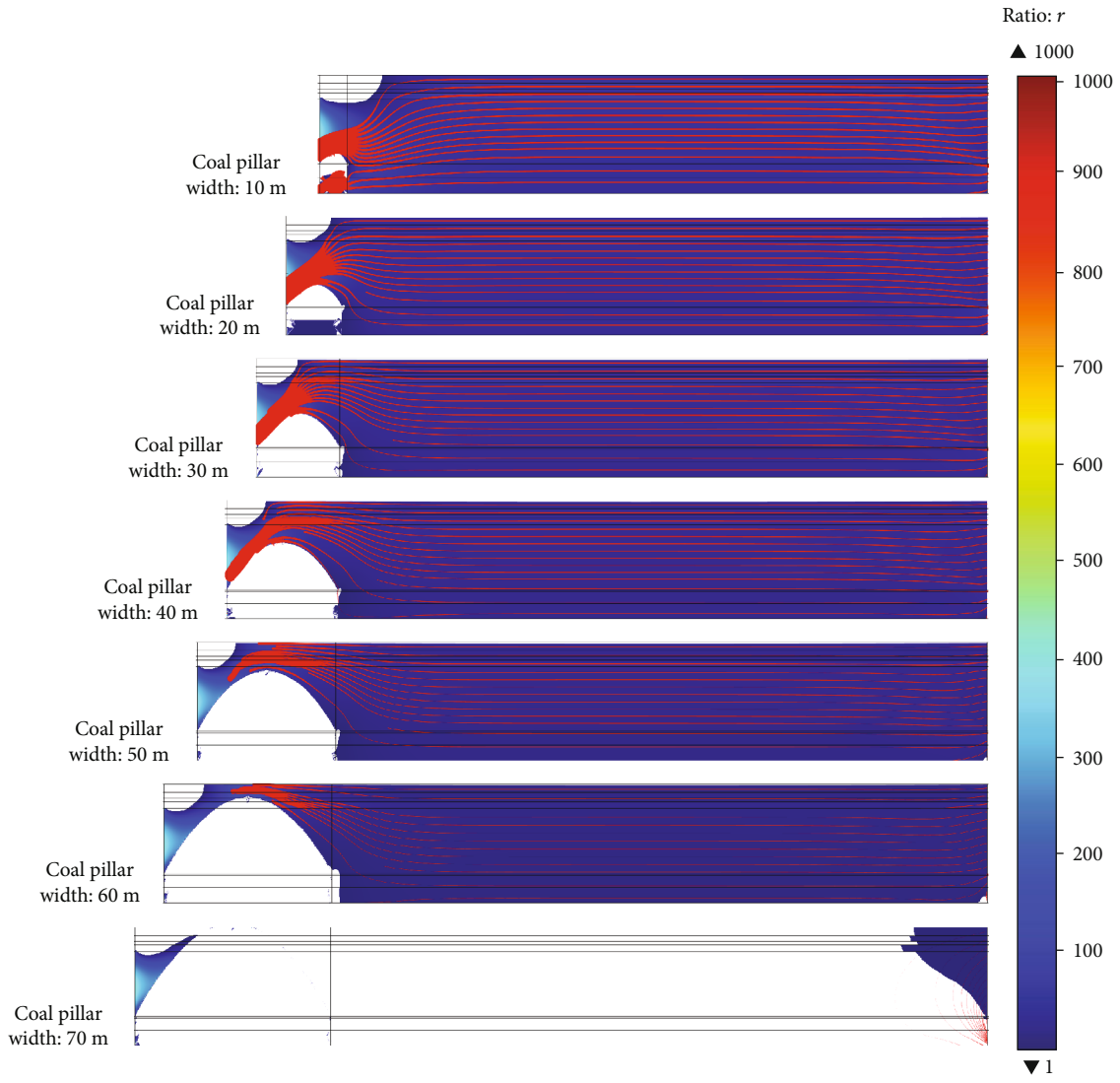

(c) Water level at 38.65 m

FIGURE 7: Cloud map of ratio r and water trace of goaf at different water levels and coal pillar widths. (a) Water level at 18.65 m. (b) Water level at 28.65 m. (c) Water level at 38.65 m.

above, where the former is called the secondary key stratum and the latter the primary key stratum [14]. The sample in this simulation is a coal pillar from a section of 20 m in width between goaf No. 42111 and 42101 of Wanli No. 1 Mine. According to the ZK1416 borehole in the above area, the Key Strata Distinguishing software (KSPB) is used to examine the key strata of the overlaying rock in this area. The result is shown in Figure 4.

According to Figure 4, we established a goaf model (Figure 5) with a geometric structure of 115.65 m in height and 550 m in length. In terms of solid mechanics calculations, the top interface of the model is a free boundary, the side boundaries are roller bearing boundaries, and the bottom interface a fixed boundary. In terms of fluid calculation, the target areas of this model are R_1 and R_2, where R_1 is a coal/rock pillar with its left boundary pressure at $p_0 = 0$ Pa and R_2 is the goaf area with its water level being h. So the pressure on the left is $p_1 = \rho g h = [1000 \times 9.8 \times (h - y)]$ Pa. Assuming that the water ratio of the initial state of R_1 area is 0 with an initial pressure of 0 Pa, and the initial water level of R_2 area is h, and the initial water pressure of the area is $[1000 \times 9.8 \times (h - y)]$ Pa. The permeability is determined according to Table 1.

The parameter values are shown in Table 2.

3.1.2. Simulation Schemes. The model plans to calculate the width d of the coal pillar in this section and the water level h in R_2 area. According to the abovementioned plan, the orthogonal simulation schemes are designed by setting the water level in R_2 area at 18.65, 28.65, and 38.65 m and

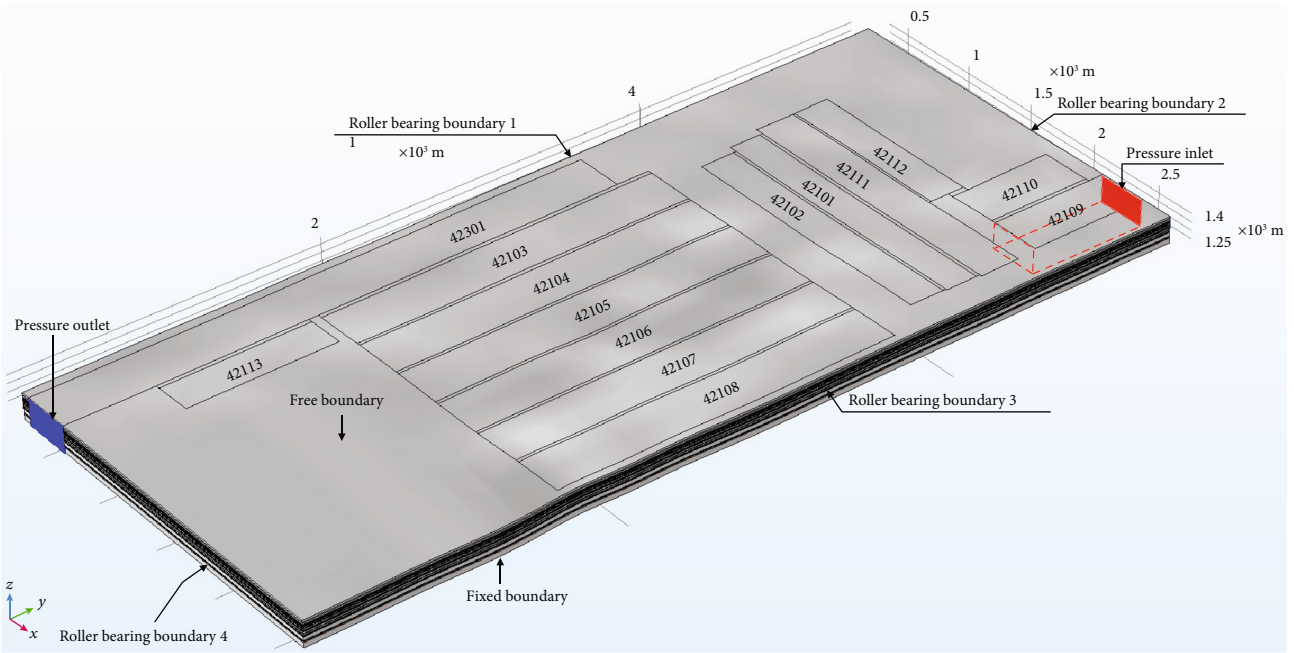

Figure 8: Geometric structure model.

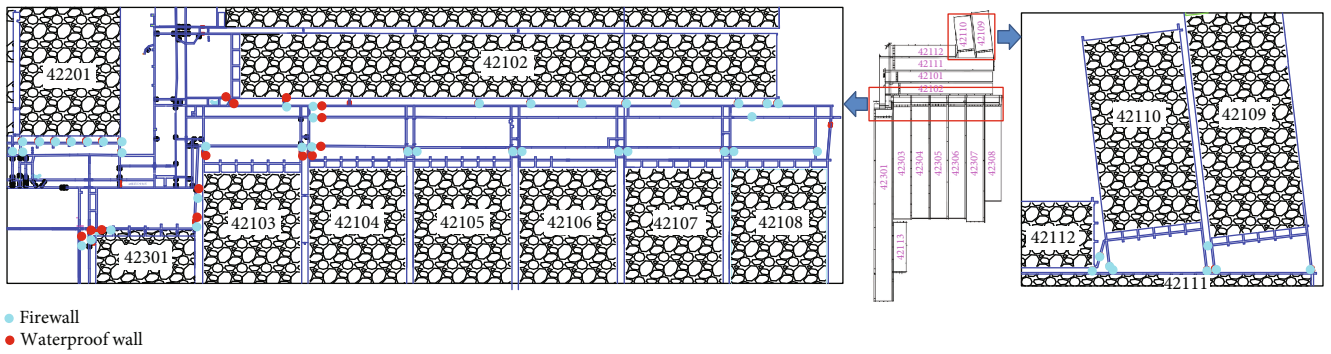

Figure 9: Map of firewalls and waterproof walls in the south and north wings of goafs in No. 4-2.

the coal pillar width d at 10, 20, 30, 40, 50, 60, and 70 m. The simulation schemes are shown in Table 3.

3.2. Analysis of Simulation Results

3.2.1. Distribution Law of Permeability in Goaf. By arranging survey lines at 2.55, 7.55, 12.55, 17.55, 22.55, 27.55, 32.55, and 37.55 m from the coal seam floor along the coal seam inclination, the permeability of each point was obtained and hence the changing pattern (Figure 6) of permeability of the overlaying rock coal pillars at different widths. It shows that stress on the coal/rock in the goaf has a significant impact on permeability, which is mainly manifested in the following five aspects:

(1) When the coal pillar width is 10 m, the permeability below 12.55 m of the survey line drops sharply because the original fractures of the rockmass are compacted, which indicates that the area below 12.55 m is an elastic core area with extremely low permeability. As the coal pillar width increases, the permeability at higher survey lines drops significantly too, indicating that the height of the elastic core area is increasing. The permeability of the elastic core area of the rock pillar is between 8.7×10^{-15} and 1.6×10^{-15} m^2 and that of the coal pillar is between 4.4×10^{-16} and 6.3×10^{-16} m^2

(2) The permeability of the rock above the elastic core area is relatively high, and the coal/rock body in this range is destroyed due to the reduction of horizontal stress. When the coal pillar width is 10 m, the permeability below 12.55 m is low, but the permeability above 17.55 m is higher, which indicates that the lateral boundaries of the water-conducting fractures on both sides of the coal pillar meet at the height

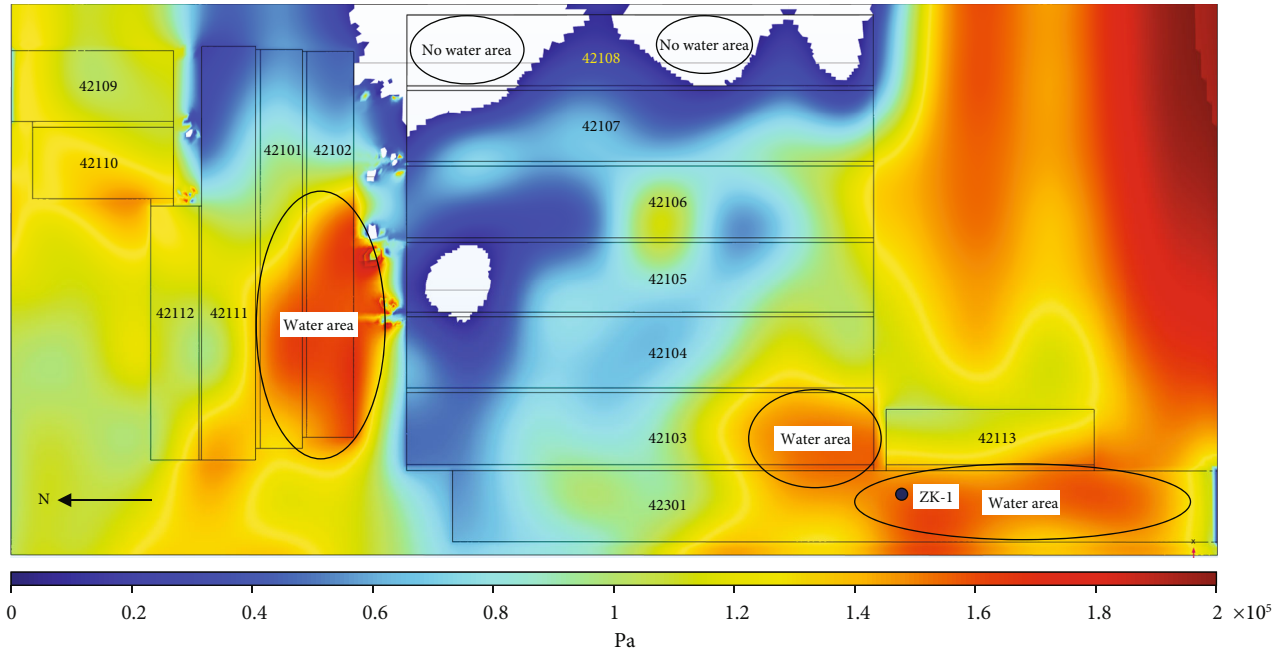

Figure 10: Cloud diagram of the pressure distribution on the floor of the goaf in No. 4-2.

between 12.55 m and 17.55 m from the coal seam floor. As the coal pillar width increases, the permeability in the plastic failure zone increases slightly, and the permeability in this range is between 3.2×10^{-13} and 1.35×10^{-11} m^2

(3) Under the support of the coal pillar, the coal/rock near the mining boundary is not fully compacted, and the permeability in this area is relatively high. Because the coal pillar width is 10 m which is smaller than boundary coal pillar width (40 m) in the model, the permeability above the goaf is distributed asymmetrically. As the coal pillar width increases, the above phenomenon gradually disappears with the permeability starting to distribute symmetrically. The peak permeability near the mining boundary is between 1.05×10^{-11} and 1.28×10^{-11} m^2

(4) In contrast with the coal/rock naturally deposited near the mining boundary of goaf, the permeability of the fractured coal/rock in the middle and lower parts of the goaf is relatively low, because it is recompacted. But such permeability (1.05×10^{-11} ~1.28×10^{-11} m^2) is still greater than that of the coal pillar in the plastic failure zone

(5) Affected by the mining of the lower coal seam, the stress of the upper coal/rock is relieved, but permeability of the coal/rock is increased. However, as the degree of stress unloading on the coal in this area is less than that on the coal near the mining boundary, its permeability (1.3×10^{-11}~1.8×10^{-11} m^2) is lower than that of the latter area, but significantly higher than the fractured coal/rock in the middle and lower parts of the goaf

In summary, the order of coal/rock permeability in the goaf is: natural accumulation area near the mining boundary > low stress area in the middle and upper part of the goaf > recompaction area in the middle and lower part of the goaf > plastic failure zone above the coal pillar > the elastic core area in the middle of the coal/rock pillar. From the perspective of the overall distribution of coal/rock permeability in the goaf, the boundary area is connected to the high permeability area in the middle and upper part of the goaf, forming a round hat-shaped structure in space, which corresponds to the "O-shape" theory and the "ellipse parabolic zone" theory in mining cracks studies.

3.2.2. The Law of Fluid Movement in the Goaf. The pressure gradient dp is the ratio of the pressure difference between two points in the flow area to the distance between them. According to the theory of fluid seepage in porous media, water seepage in the coal happens at a certain starting dp. The starting dp of seepage in coal/rock can be expressed as [16]:

$$G = 2.306 \times 10 - 1\, k^{-1.096}. \quad (2)$$

In this formula, G is the starting dp, Pa/m; k is permeability, $10^{-3}\,\mu$m^2, which can be obtained through tests.

When $dp < G$, the water body is in a static state; when $dp > G$, the water body is in a flowing state. The ratio r of dp to G in the fluid calculation range is derived, and the flowing area, where $r > 1$, is colored and labeled, while the static area, where $r < 1$, is not colored and labeled. So we obtained the cloud map of r and fluid streamline distribution of different water levels and different coal pillar widths (Figure 7). The red lines in Figure 7 represent the

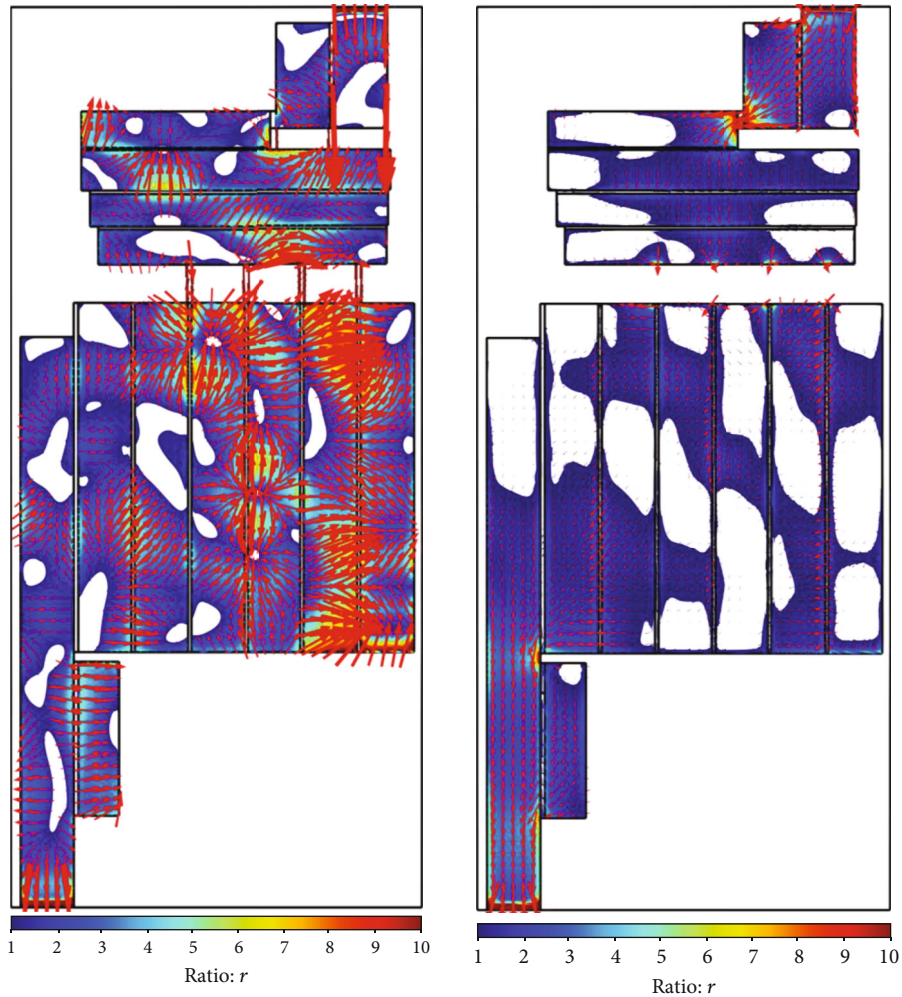

(a) The range of 0 ~ 5.1 m from the coal seam floor (b) The range of 15~20 m from the coal seam floor

Figure 11: Continued.

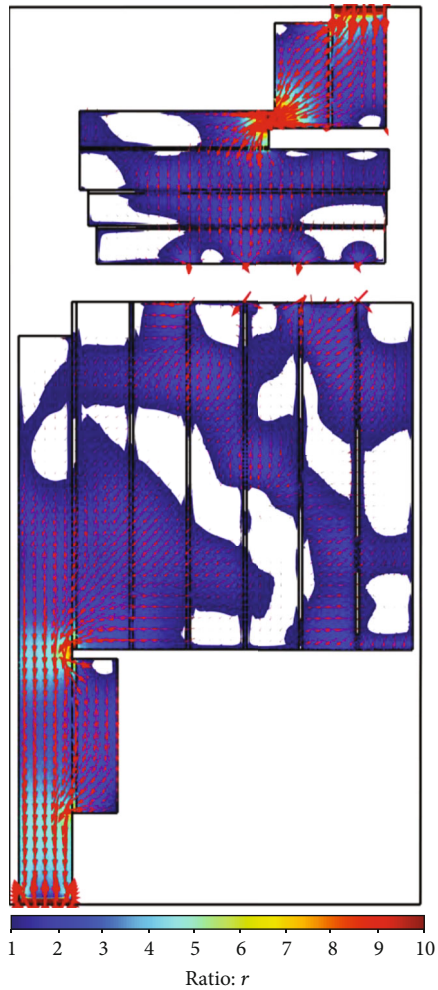

(c) The range of 25~30 m from the coal seam floor

FIGURE 11: The r value cloud map and flow direction above the coal seam floor. (a) The range of 0 ~ 5.1 m from the coal seam floor. (b) The range of 15~20 m from the coal seam floor. (c) The range of 25~30 m from the coal seam floor.

water flow in the goaf, and the thickness of the line represents the seepage velocity.

(1) Figure 7(a) indicates that when the water level is at 18.65 m and the coal pillar width is 10 m, both the goaf and the coal pillar are flowing areas. However, the rock above the coal pillar forms an elastic core area, also called static zone. In addition, when the coal pillar width is 20 m, in the upper part of the elastic core area where $r > 1$, the water in the goaf overflows the elastic core area. When the coal pillar width exceeds 30 m, in most fluid calculation areas where $r < 1$, the water in the goaf is in a static state

(2) According to Figure 7(b), when the water level is at 28.65 m and the coal pillar width is 20 m, the coal pillar becomes a static area, and the water in the goaf can only move above the elastic core area of the rock pillar to the adjacent goaf. When the coal pillar width increases to 50 m, the coal/rock pillar and the goaf almost entirely become static areas, and there is only downslope flow on the left side of the elastic core area

(3) It can be seen from Figure 7(c) that when the water level is at 38.65 m and the coal pillar width is 20 m, a flowing zone appears in the coal pillar, but it is blocked by the static zone, so continuous seepage is not actually formed. When the coal pillar width increases to 70 m, the static zone cuts off the entire seepage area, and there is almost no water flow in the goaf

The coal pillar width in No. 4-2 was 20 m. During the mining process, water once flowed in from adjacent goafs. When the water level of the adjacent goaf became lower than 18 m, the water influx decreased and gradually stopped, indicating that when the coal pillar width is 20 m, the critical water level is 18 m, which is consistent with the numerical calculation results in Figure 7(a).

4. CFD Numerical Calculation of Seepage Law in the Goafs of Wanli No. 1 Mine

In order to rationally design coal mine underground reservoirs and ensure the safe operation of them, it is necessary to understand clearly the seepage law and seepage path of the water in goaf. So, we conducted CFD numerical calculations for the whole goaf groups of No. 4-2. After assigning values to the permeability of the overlaying rock in the goaf with coupling function of coal/rock permeability and vertical stress obtained from the seepage test, the seepage law and seepage path in the underground reservoir was finally obtained.

4.1. Establishment of Numerical Calculation Model

4.1.1. Geometric Model and Boundary Conditions. First, a three-dimensional surface was generated according to the elevation points from the floor of No. 4-2, and then, the three-dimensional surface was scanned vertically to produce a geometric structure model (Figure 8). This model was 2400 m in width, 4150 m in length, and 115.65 m in thickness, including 14 goafs with 13 coal pillars between them. Next, the elastoplastic calculation module was chosen for the simulation of solid mechanics calculation, in which the top interface of this model was considered a free boundary, the sides around the model as roller bearing boundaries, the bottom interface of the model as a fixed boundary, and the internal boundaries of the model as free boundaries. In terms of fluid calculation, since the water level at the outer boundary of the goaf in goaf No. 42109 was 35 m, the pressure at this inlet boundary was assigned $P1 = \rho gh = [1000 * 9.8 * 35]$ Pa. As lateral boundary of goaf No. 42301 was open to the atmosphere, it was set as pressure outlet with a pressure of 0 Pa. In addition, it was assumed that except for working face No. 42109, the initial water ratio of other areas of the model was 0, and the initial pressure was 0 Pa.

This model can investigate the spatial distribution of seepage law and seepage path of reservoir water (the values for the parameters were shown in Table 2). Assuming that the seepage in the overlaying area of the goaf complies with Darcy's law, the permeability of overlaying rock can be determined according to the coal/rock permeability and axial stress fitting function in Table 1. The coal pillar width (in Figure 9) between the south and north wings of No. 4-2 is about 210 m, much longer than the critical width of 70 m, which means that the water in the goaf will not flow into the adjacent goaf. That is to say, the south and north goaf of No. 4-2 are separated by coal pillars. However, there are roadways connecting the south and north wings, as shown in Figure 9. The red dots in Figure 9 are waterproof walls with great strength and good airtightness. Therefore, goaf No. 42301 and 42103 in the south wing cannot be connected to goaf No. 42102 in the north wing. The blue dots in Figure 9 are firewalls used as temporary walls with fairly poor airtightness. Therefore, goafs No. 42104, 42105, 42106, 42107, and 42108 in the south wing and No. 42102 in the north wing are connected to each other, and goafs No. 42110, 42109, and 42111 are connected as well.

4.2. Analysis of Simulation Results

4.2.1. The Distribution Law of Water Pressure on the Floor of the Goaf. A cloud diagram of the pressure distribution on the floor of the goaf (Figure 10) shows that the coal pillar width between the south and north wings is very large. The northern floor of the coal pillars is under high water pressure of 194 kPa with a water level at 19.4 m, due to the blocking of boundary coal/rock pillars. Similarly, the floor at the northern boundary of No. 42301 is also under high water pressure of 163 kPa with a water level at 16.3 m. In addition, the ground drilling ZK-1 on No. 42301 working face reveals that the water level here is 15 m, which is consistent with the calculation results of this model, indicating that the model parameters are selected reasonably and the simulation results are accurate and reliable.

4.2.2. Seepage Law in Goaf Groups. In order to obtain the seepage law in goaf groups, the ratio r of the dp in the area to the dp at the starting point is calculated. If $r > 1$, it means that the fluid dp is greater than the starting dp, and the water in the goaf is in a flowing state; if $r < 1$, it indicates that the fluid dp is less than the starting dp, and the water in the goaf is in a static state.

(1) The r value cloud diagram and the flow direction within 0 ~ 5.1 m from the coal seam floor (see Figure 11(a)) reveal that the coal pillars permeability both in the section and at the boundary of the goaf is low, and the fluid is in a static state as $r < 1$. Such phenomenon appears only in the compaction zone in the middle of part of the goaf, while within the goaf, the flow range at the height of 0 ~ 5.1 m is relatively large. As to fluid movement, the water may flow in completely different directions, such as either flowing from the surroundings to the center point or vice versa. The main reason for this is the force of gravity, which means, within 0 ~ 5.1 m from the coal seam floor, gravity plays a dominant role in the direction of fluid movement, and the water normally moves from a high position to a lower one. In addition, due to high permeability of the roadways, the flow velocity in the lanes is quite high

(2) Figure 11(b) shows the r value cloud map and the flow direction within 15-20 m from the coal seam floor. The result shows that the water level in the goaf begins to exceed the height of the elastic core,

and the fluid in it flows from the high-pressure area to the low-pressure area under *dp*

(3) Figure 11(c) shows the *r* value cloud diagram and the flow direction within 25-30 m from the coal seam floor. The result shows that, compared with that of 15-20 m, the range of water flow is enlarged, which shows that the permeability at the 25-30 m layer is large, and the flow velocity in the goaf is high

(4) The seepage path in Wanli No. 1 Mine is: 42109-42110-42112-42111-42101-42102- roadway connecting the north and south wings-"O" ring fissure zone of 42108, 42107, 42106, 42105, 42104, and 42103-42301-42113

5. Conclusions

(1) A coal/rock sample was collected from No. 4-2 of Wanli No. 1 Mine, and tests were designed based on the evolution laws of the lateral supporting pressure on coal pillars. Through tests on a three-axis servo seepage testing machine, the permeability of the coal/rock pillar was obtained as a function of the vertical stress, which provides a basis for studying the seepage properties of the coal/rock pillars between adjacent goafs of the underground reservoir

(2) CFD simulation on seepage properties of coal/rock pillar showed that as the water level in the goaf decreased and the coal pillar width increased, the water flow range and flow velocity continued to decrease. At the water level of 18.65, 28.65, and 38.65 m, water could enter adjacent goaf when coal pillar widths were of 30, 50, and 70 m, respectively. In addition, when the coal pillar width was 10 m, the coal pillar was penetrated by high permeability area, and water in the goaf could bypass the elastic core area through coal pillars at the bottom to the adjacent goaf. As the coal pillar width increases, water could no longer enter the adjacent goaf through the coal pillar at the bottom

(3) A seepage model for the goaf groups of underground reservoirs was established and numerical calculations performed. The results were verified by the in situ water level data. Numerical calculation results showed that at the height of 0 ~ 5.1 m from the coal seam floor, water in the goaf flowed from a higher place to a low one under gravity. At the height of 15~20 m from the floor, water in the goaf flowed from high-pressure area to low-pressure area under the pressure gradient. At the height of 25~30 m from the floor, water in the goaf flowed at a high velocity in a wide range, as this area's permeability was high. Based on the seepage area and seepage direction on different layers of the goaf, the seepage path of the underground reservoir in Wanli No. 1 Mine was obtained

Data Availability

All relevant data are available from FigShare, under the DOI: (https://figshare.com/s/e72c1f8e7c8ed0bcf963).

Conflicts of Interest

The authors declare that there is no conflict of interest regarding the publication of this paper.

Acknowledgments

We thank X. Chen for assistance with the experiments and Y. Dong for valuable discussion. Financial support for this work was provided by the Independent Research Project of State Key Laboratory of Coal Resources and Safe Mining (No. SKLCRSM19X009) and the National Natural Science Foundation of China (No. 52174212).

References

[1] S. K. Gupta, C. R. Cole, and G. F. Pinder, "A finite-element three-dimensional groundwater (FE3DGW) model for a multiaquifer system," *Water Resources Research*, vol. 20, no. 5, pp. 553–563, 1984.

[2] F. Getchell and D. Wiley, "Artificial recharge enhances aquiter capacity," *Water/ Engineering and Management*, vol. 142, no. 11, pp. 2–25, 1995.

[3] M. K. Jha, K. Chikamori, and Y. Kamii, "Effectiveness of the Kamo river for artificially recharging the Takaoka aquifer, Tosa city, Japan," *International Agricultural Engineering Journal*, vol. 7, no. 2, pp. 87–108, 1998.

[4] A. Jonoski, Y. Zhou, J. Nonner, and S. Meijer, "Model-aided design and optimization of artificial recharge-pumping systems," *Hydrological Sciences Journal*, vol. 42, no. 6, pp. 937–953, 1997.

[5] D. Gu, "Theory framework and technological system of coal mine underground reservoir," *Journal of China Coal Society*, vol. 40, no. 2, pp. 239–246, 2015.

[6] Z. Ma, *Research on the superhigh-water packing materialand filling mining technology and their application*, China University of Mining and Technology, Xuzhou,China, 2003.

[7] T. Yang, S. Chen, W. Zhu, Z. Meng, and Y. Gao, "Water inrush mechanism in mines and nonlinear flow model for fractured rocks," *Chinese Journal of Rock Mechanics and Engineering*, vol. 27, no. 7, pp. 1411–1416, 2008.

[8] T. H. Yang, W. H. Shi, S. C. Li, X. Yang, and B. Yang, "State of the art and trends of water-inrush mechanism of nonlinear flow in fractured rock mass," *Journal of China Coal Society*, vol. 41, no. 7, pp. 1598–1609, 2016.

[9] Z. Cao, J. Ju, and J. Xu, "Distribution model of water-conducted fracture main channel and its flow characteristics," *Journal of China Coal Society*, vol. 44, no. 12, pp. 3719–3728, 2019.

[10] G. Xu, J. L. Xu, W. Y. Lu, and D. Y. Fan, "Lateral boundary prediction of water conducting fracture formed in roof and its application," *Chinese Journal of Geotechnical Engineering*, vol. 32, no. 5, pp. 724–730, 2010.

[11] R. Fink, B. M. Krooss, Y. Gensterblum, and A. Amann-Hildenbrand, "Apparent permeability of gas shales-superposition of

fluid-dynamic and poro-elastic effects," *Fuel*, vol. 199, pp. 532–550, 2017.

[12] A. Ghanizadeh, A. Amann-Hildenbrand, M. Gasparik, Y. Gensterblum, B. M. Krooss, and R. Littke, "Experimental study of fluid transport processes in the matrix system of the European organic-rich shales: II. Posidonia Shale (Lower Toarcian, northern Germany)," *International Journal of Coal Geology*, vol. 123, pp. 20–33, 2014.

[13] J. P. Tang, Y. S. Pan, C. Q. Li, and Q. SHI, "Experimental study of desorption and seepage of coal-bed methane under solid-fluid coupling," *Journal of China University of Mining & Technology*, vol. 35, no. 2, pp. 274–278, 2006.

[14] Z. Li, S. Yu, W. Zhu et al., "Dynamic loading induced by the instability of voussoir beam structure during mining below the slope," *International Journal of Rock Mechanics and Mining Sciences*, vol. 132, article 104343, 2020.

[15] G. Z. Hu, J. L. Xu, H. T. Wang, Z. Y. Jin, and R. L. Wu, "Research on a dynamically coupled deformation and gas flow model applied to low-permeability coal," *Journal of China University of Mining & Technology*, vol. 40, no. 1, pp. 1–6, 2011.

[16] F. Hao, L. Cheng, and C. Li, "Study on threshold pressure gradient in ultra-low permeability reservoir," *Journal of Southwest Petroleum University*, vol. 28, no. 6, pp. 29–32, 2006.

Hindawi
Geofluids
Volume 2022, Article ID 2951634, 15 pages
https://doi.org/10.1155/2022/2951634

Research Article

Distribution Law of In Situ Stress and Its Engineering Application in Gateroad Maintenance: A Case Study

Guangchao Zhang,[1,2] You Li,[1] Guangzhe Tao,[1] Miao Chen,[1] Ruihua Xu,[2] Hanqing Guo,[2] Devkota Bidit,[1] Guanglei Zhou,[1] Zhi Qu,[1] and Hao Zuo[1]

[1]*College of Energy and Mining Engineering, Shandong University of Science and Technology, Qingdao 266590, China*
[2]*Shandong Energy Group Co., Ltd., Jinan 250014, China*

Correspondence should be addressed to You Li; liyou0239@163.com and Guangzhe Tao; tgz17854282741@163.com

Received 22 November 2021; Accepted 5 February 2022; Published 3 March 2022

Academic Editor: Gangwei Fan

In this study, the stress relief method of hollow inclusion and mathematical-statistical analysis are used to study the in situ stress distribution law of the Guotun coal mine, and the optimization strategy of roadway support is put forward. The test site is located in the city of Heze, Shandong Province, China. The main conclusions included the following: (1) among the three large-scale tectonic movements experienced by the Guotun coal mine, the middle Yanshan period has the strongest impact on it. According to the geological evolution process, it is preliminarily inferred that the maximum principal stress direction of the Guotun coal mine is northwest by west to southeast by east (NWW~SEE). (2) Compared with the surrounding mines, the average value of the maximum principal stress in the Guotun coal mine is slightly higher, and there is a significant difference in the direction of in situ stress. The arc structure within the mine is the main reason for the deflection of the stress direction. (3) The lateral pressure coefficients K_H, K_h, and K_{av} show a nonlinear distribution with increased depth, and the three coefficients have a decreasing trend. The value of the stress gradient in the Guotun coal mine is greater when it is compared with the surrounding mines. (4) Field tests show that the new strategy proposed in this study is effective, which provides a good reference for engineering practice under similar geological conditions.

1. Introduction

In situ stress is the fundamental force that causes the deformation and failure of the surrounding rock in underground caverns, civil buildings, slopes, and other geotechnical engineering structures [1, 2]. With the increase in the energy demand in China, coal mining has entered a state of deep mining [3]. Due to the higher mining intensity and the more complex distribution of in situ stress, large deformation of the deep gateroad, damage of the support structure, and other disasters that frequently occur [4, 5], a basic consensus has been reached in the mining industry that the design of mining gateroad and control of surrounding rock deformation should start with in situ stress measurement and analysis [6, 7].

To date, a number of studies have been conducted to investigate in situ stress measurement methods and equipment, field measurement, and its distribution law in China. For example, Cai et al. [8] proposed a device for in situ stress measurement based on complete temperature compensation and further put forward the calculation method for in situ stress. Kang et al. [9] presented a small-aperture hydraulic fracturing in situ stress measurement method and applied it in Luan, Jincheng, Fenxi, and other mining areas in China. Wang et al. [10] performed field monitoring to investigate the in situ stress distribution law of the Ping ding shan mining area. Synn et al. [11] analyzed the regional in situ stress pattern using 460 stress measurement data at about 100 test sites in Korea. A theoretical model was used to explain the effect mechanism of in situ stresses on crack propagation due to blasting by Yi et al. [12], and they supposed that the high in situ stresses can influence the crack propagation in the far field. Yang et al. [13] analyzed the stability of the hydrocarbon wells, by measuring the value of

the in situ stress in the South Pars field. All these studies have improved our understanding of the in situ stress measurement and its engineering application.

tAt present, there are hundreds of measurement technologies in the world, which can be divided into three categories according to the measurement principle. The first is the mechanical method based on the measurement of strain and deformation in the rock mass, such as the stress recovery method, stress relief method, and hydraulic fracturing method. The second type is the geophysical method based on measuring the changes in acoustic emission, acoustic wave propagation law, resistivity, or other physical quantities in the rock mass. The third type is to determine the stress direction according to the information provided by geological structure and underground rock mass failure. Among them, the stress solution method and hydraulic fracturing method are widely used, and the other methods can only be used as auxiliary methods. Hydraulic fracturing method and hollow inclusion casing drilling method have been widely used and have been successfully commercialized. These two methods are also the key methods recommended by the International Committee on rock mechanics test methods in 2003.

It is well known that the distribution of in situ stress is closely related to the geological structure and exhibited evident regional distribution characteristics [13–17]. The Guotun coal mine is located in the southwest of Shandong province, with a complex geological structure and a maximum mining depth of 900 m. With the progress of mining activities in the mine, the deformation and damage phenomena often occur in the gateroad, which has seriously affected the safe and efficient production of the mine. In addition, no systematic in situ stress test has been carried out in the mining area currently under mining. Therefore, it has become an urgent problem to study the in situ stress of the Guotun coal mine and improve the relevant support scheme.

The objective of this study is to develop a better understanding of the distribution characteristics of in situ stress and its engineering application in the Guotun coal mine. This study is organized as follows: in Section 1, the analysis of the geological structure evolution process and in situ stress direction was first presented. In Section 2, the process of in situ stress measurement is described in detail, and according to the result curve, the magnitude and direction of the in situ stress field are revealed. The variation law of principal stress and the lateral pressure coefficient with depth are discussed in this study. In Section 3, the control measures for large deformation of gateroad were proposed in the Guotun coal mine, and its validity was verified by a field application. The results presented in this study have important theoretical and practical implications for the exploitation of coal resources and the construction of gateroad engineering structures in the Guotun coal mine.

2. Engineering Background and In Situ Stress Direction Prediction

2.1. Engineering Geology Conditions. The Guotun coal mine is located in 3~17 km south of Yuncheng county in Heze city, Shandong Province, and the mine center is about 10 km away from Yuncheng county. It is the second pair of large modern mines planned and constructed in Juye coalfield and is currently the important coal resource-producing area in Shandong province. The mine covers an area of 69.33 km^2, with geological reserves of 475 million tons and recoverable reserves of 165 million tons. The current mining seam is #3 coal seam, with an average thickness of 4.73 m. The average buried depth of the main coal seam is 808 m. The thickness of the overlying Cenozoic stratum in the minefield is 530~650 m, mainly composed of clay, sandy clay, and sand. The roof of the coal seam is mainly fine sandstone and mudstone, with an average thickness of 7.5 m, which is a relatively stable rock stratum; the coal seam floor is mainly composed of mudstone and carbonaceous mudstone, with an average thickness of 8.37 m, which is a stable rock stratum. The structural complexity of the Guotun coal mine is medium, mainly monoclinic structure with north-south strike and east dip; the east boundary of the mine is Tianqiao fault, and the west boundary is coal seam outcrop; the stratum is gentle in the west and south and steep in the north and east. The main faults and folds of the mine are shown in Table 1.

2.2. Evolution Law of the Geological Structure and Principal Stress Direction Analysis. The geological structure of the Guotun coal mine is mainly controlled by the Juye mining area. In geological history, the Guotun coal mine has mainly experienced three large-scale tectonic movements, namely, Indosinian movement, Mid-Yanshan movement, and Late Yanshan movement [16]. The influence of geological tectonic movement on in situ stress field is different in each period.

The first stage was Indosinian movement, which led to strong fold uplift and fault movement in the whole coal accumulation basin in North China. The collision between the north and south continental blocks in the E-W direction formed E-W folds and faults, such as Yuncheng fault and Heze fault. The tectonic movement in this period formed the boundary of the Guotun coal mine.

The second stage is the Middle Yanshanian period. Due to the combined action of lateral tension of mantle plastic flow and plate edge compression, N-W compression weakens, and S-N normal faults controlling the occurrence of coal measure strata are widely developed. The tectonic movement in this period formed Xiangyang, Wangdong, Balihe, and other faults. These faults cut the interior of the Guotun mine and have a severe impact on the geological structure of the whole Guotun mine. Up to now, it is still the main geological structure of the Guotun coal mine.

The third stage was the Late Yanshanian period. When the plate extrusion replaced the mantle stress, the Guotun coal mine block was subjected to the extrusion and offset as a whole, gradually forming an arc structure. Then, it was subjected to the tension and torsion of many different rotation directions, forming a large number of uplifts, such as Balihe anticline and Guotun syncline.

At the present stage, the Guotun coal mine is mainly controlled by Tianqiao, Tianqiaozhi, Hongmiao, Balihe,

Table 1: List of main structures of Guotun coal mine.

Number	Name of the geological structure	Extension length (m)	Fault occurrence/Range (m)		
			Fault throw	Dip	Dip angle
1	Tianqiao fault	7.5	>500 m	East	70°
2	Balizhuang fault	12	0~150 m	West	70°
3	Balihe fault	10	0~150 m	West	70°
4	Dongdong fault	6.5	0~40 m	East	70°
5	Xiangyang fault	4.5	0~150 m	West	70°
6	Houying fault	3	170 m	West	70°
7	Dingguantun anticline	15	2~150 m		
8	Balihe anticline	15	20~80 m		
9	Dinglichang syncline	15	20~240 m		
10	Guotun syncline	15	50~300 m		

Xiangyang, Dongzhang, Balizhuang, Houxin, and other structures, which indicated that the Guotun coal mine is obviously affected by the compressive stress in the NW-SE direction. From the above analysis, it can be concluded that the main stress direction of the coal mine should be NWW-SEE, as shown in Figure 1.

3. The In Situ Stress Measurement and Its Distribution Characteristics in Guotun Coal Mine

3.1. In Situ Stress Measurement

3.1.1. The Selection of Measuring Equipment and Point Location. The "recommended method for determining rock stress" was promulgated by the committee on test methods of the international society for rock mechanics in 1987. They confirmed the following four measurement methods as recommended methods: flat-jack method, hydraulic fracturing method, USBM borehole diameter deformation gauge method, and CSIRO hollow inclusion strain gauge method. The hollow inclusion stress resolution method is the best method to obtain the three-dimensional stress state. Therefore, the hollow inclusion stress solution method is selected for this in situ stress measurement. The main equipment diagram is shown in Figure 2 that mainly includes the following:

(i) The hollow inclusion triaxial stress meter *KX-2011*: its outstanding advantages are that the bonding quality between the stress gauge and the hole wall rock is great, and the measurement error caused by the temperature difference is eliminated.

(ii) The mine pressure monitoring substation KJF327-F: the accuracy can reach 0.1%, and the lowest strain difference is $1\,\mu\varepsilon$, sensitivity coefficient is 0.001~999.999.

(iii) The other equipment includes confining pressure calibrator, strain gauge driver, and data processing software.

The selection of measuring points shall meet the following requirements. First, it needs to be representative, and it is necessary to avoid goaf and the complex geological structure. Second, consideration must be given to production, staff safety, the impact of measurement, and the production processes. Third, the borehole must be located in the same rock stratum. Based on the above selection principles, combined with the geological mining conditions and engineering practice background of the Guotun coal mine, five measuring points are finally selected, as shown in Figure 3. The technical characteristics of each measuring point are shown in Table 2.

3.1.2. Measurement Process and the Key Steps. The research team conducted a detailed in situ stress analysis in the No. 234 mining area of the Guotun coal mine from 2019 to 2020. The measurement process and the key steps are shown in Figure 4 as follows:

Step 1. Drilling geological holes. First, a large measuring hole is drilled with a hole depth of 1.5~2 times the gateroad width and a diameter of 130 mm. Then, a conical drill bit is used to drill a conical variable diameter guide hole with a depth of 6~8 cm. Finally, a small drill bit is used with a diameter of 36 mm to drill a measuring hole with a hole depth of 35~40 cm.

Step 2. Install the stress gauge. First, the drilling hole is cleaned with cotton yarn, hole washer, and acetone. Then, epoxy adhesive is prepared in proportion and the length of the small hole is measured. Finally, the stress meter, positioner, and guide rod are installed in sequence, and finally, the conductor is protected.

Step 3. Measure the hole parameters. First, the positioner and guide rod are taken out in turn. Then, the azimuth and dip angles of the borehole are measured by the standard geological compass.

Step 4. Stress relief. First, the strain gauge is checked. Then, the release distance is marked and the drill is started. Next, the drilling rig is pushed while injecting water and data acquisition is carried out. Finally, when the reading of the strain gauge tends to be stable, releasing is stopped and the core is taken out with a stress gauge.

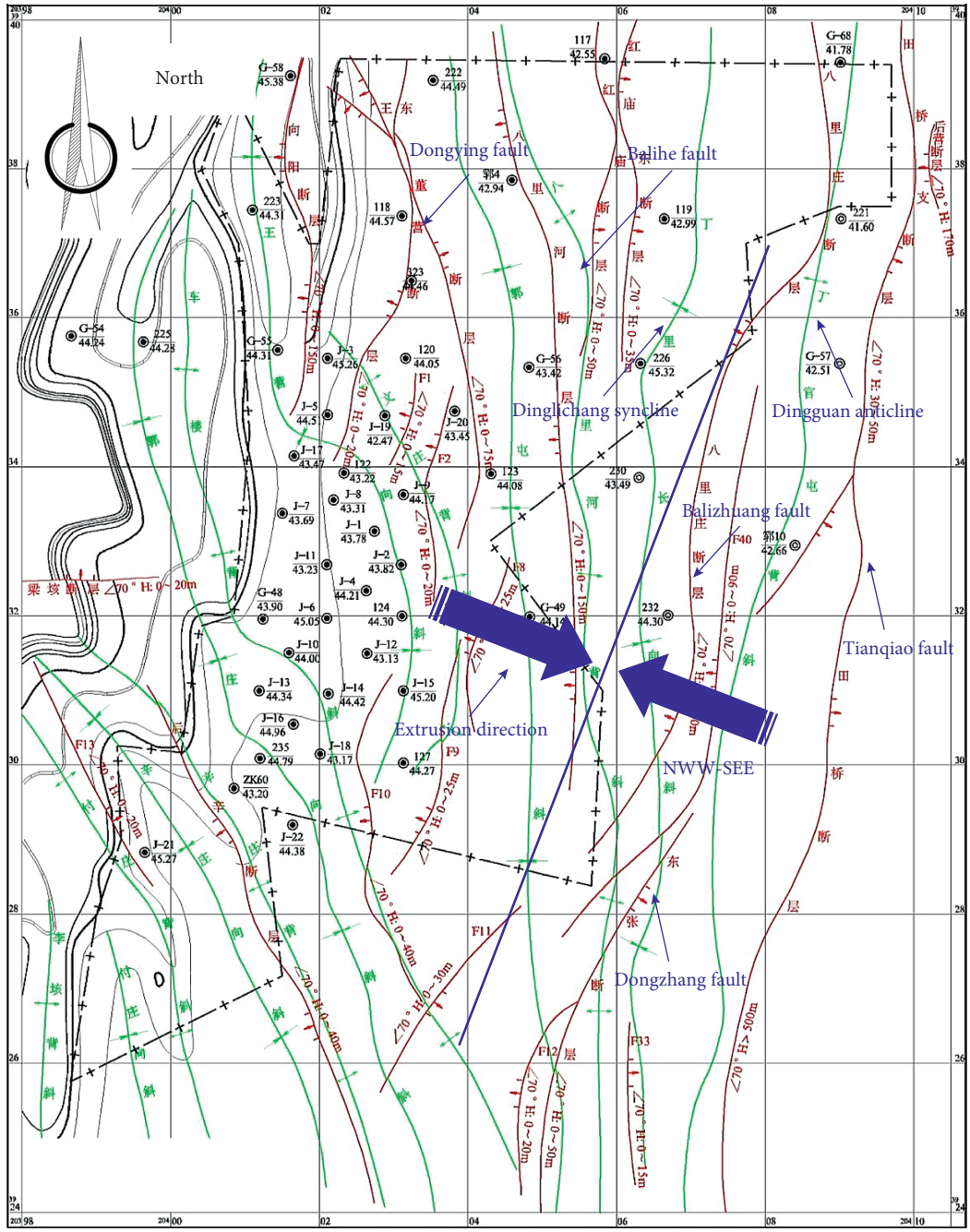

Figure 1: Analysis diagram of main stress direction of Guotun coal mine.

Figure 2: Main equipment for in situ stress measurement.

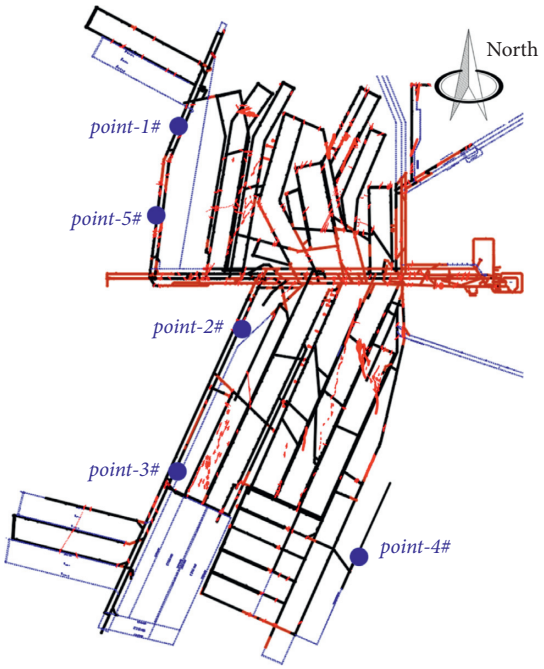

Figure 3: Location distribution of measuring points.

Table 2: Technical characteristics of measuring points.

Point number	Measuring point position	Hole depth (m)	Buried depth (m)	Azimuth (°)	Dip angle (°)	Elastic modulus	Poisson ratio	Mounting angle
1#	Third area gateroad	6.7	768	128	3.5	22700	0.29	0°
2#	Gateroad #2310	7.8	770	236	3.5	19800	0.20	0°
3#	Gateroad #2305	8.5	782	134	4	23800	0.26	0°
4#	Fourth area gateroad	8.2	801	131	5	19300	0.19	0°
5#	Third area #3303	7.6	795	124	3.5	28700	0.29	0°

(a) (b) (c)

Figure 4: Continued.

(d)

Figure 4: Key steps of field measurement. (a) Drill holes, (b) install stress gauge, (c) measure parameters, and (d) stress relief.

3.2. Measurement Results and Analysis of the In Situ Stress Data

3.2.1. In Situ Stress Measurement Results. Based on the strain values obtained from the above in situ stress measurement process and combined with the laboratory test, we got the $Y(n)$ curve, as shown in Figure 5. According to the stress relief curve, the stress relief process can be roughly divided into three stages [13].

In the first stage, when the stress relief surface does not reach the section where the strain gauge is located, the strain value monitored by each channel is small, which can be understood as the stress transfer of surrounding rock caused by the "excavation effect."

In the second stage, when the stress relief surface passes through the section where the strain gauge is located, the strain value gradually increases until it reaches the maximum value.

In the third stage, after the stress relief surface passes through the section where the strain gauge is located, the strain value monitored by each channel decreases to varying degrees and finally tends to be stable. The stable data are the initial strain data at the measured borehole.

The measurement results are processed by a computer program. It is a special in situ stress measurement and calculation program for hollow inclusion stress relief method designed by the Institute of Geomechanics, Chinese Academy of Geological Sciences in 2003. Its main interface is shown in Figure 6. The summary of calculation results is shown in Table 3.

3.2.2. Analysis of In Situ Stress Distribution. Based on the measured and existing data (a total of 9 measuring points) in the Guotun coal mine, this study analyzed the in situ stress field including its size and the direction variation law.

Distribution Characteristics of Principal Stress. According to the statistical analysis of the obtained in situ stress data, the maximum principal stress of the Guotun coal mine is 30.99 MPa~56.56 MPa, with an average of 38.77 MPa. [18, 19] The intermediate principal stress is 19.17 MPa~27.85 MPa, with an average of 22.01 MPa. The minimum principal stress is 12.06 MPa~19.08 MPa, with an average of 15.95 MPa. The principal stress values of each measuring point are summarized on the grid, as shown in Figure 7.

Further analysis indicated that the Guotun coal mine is dominated by horizontal tectonic stress, and the types of in situ stress field are $\sigma_{H>}\sigma_{v>}\sigma_h$. This strike-slip stress state is conducive to the preparation and activity of strike-slip faults. In addition, the stress values of all measuring points are above 30 MPa, belonging to the ultra-high stress area, and the stress gradient is 4.81 MPa/100 m, which is larger than the surrounding mines. This may be attributed to the complex folds, faults, and other geological structures within the scope of the Guotun coal mine. Therefore, special attention should be paid to a series of stope dynamic phenomena caused by high stress.

Distribution Characteristics of Maximum Horizontal Principal Stress Direction. Figure 8 is a rose diagram of the dominant direction of the maximum horizontal principal stress in the Guotun coal mine. Statistics show that the dominant direction is distributed at 117°~134°, with an average of 123°, which is completely consistent with the macroanalysis results (NWW-SEE).

Therefore, it can be determined that the direction of in situ stress field in the Guotun coal mine is N57°W. As can be seen from Figure 8, compared with the whole Shandong region, the maximum principal stress direction of the Guotun coal mine is within a reasonable range [20]. Compared with the adjacent mines (Yuncheng and Zhaolou), the adjacent mines are near E-W, while the direction of the Guotun coal mine deflects to the WN-ES. Based on the further analysis, we can infer that the main reason for the deflection to the WN-ES direction is a large number of arc structures (including folds and faults), which protrudes to the southeast, as shown in Figure 9.

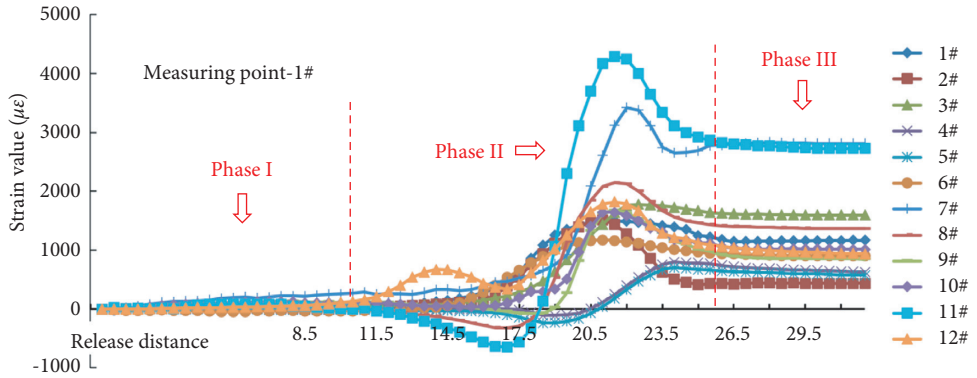

(a)

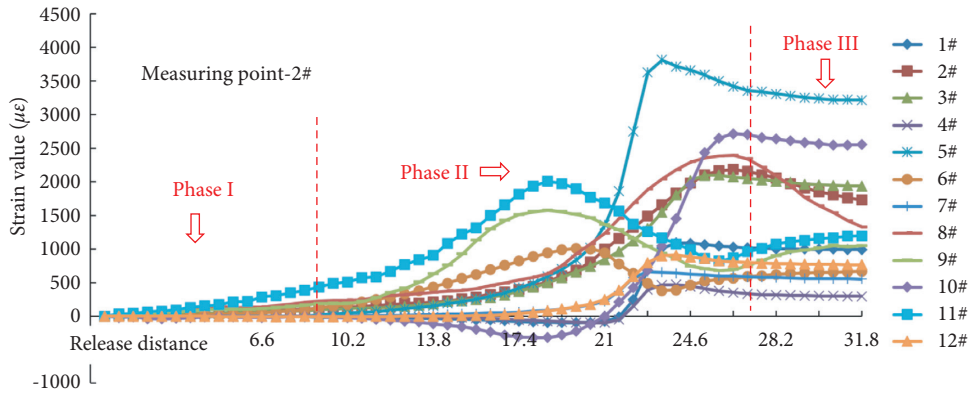

(b)

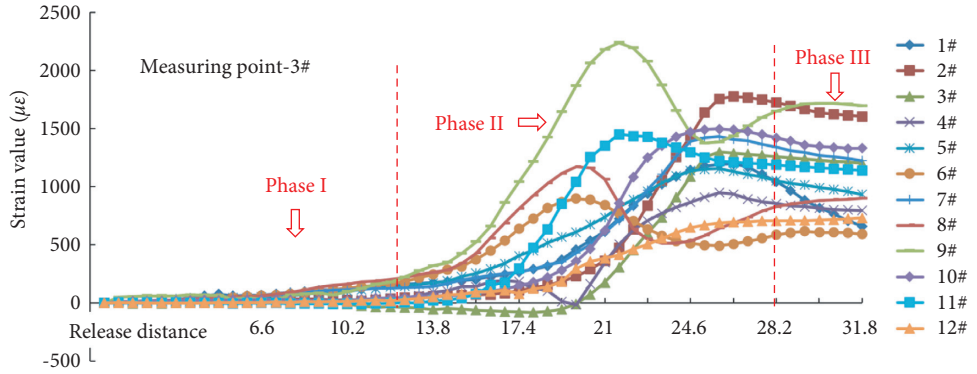

(c)

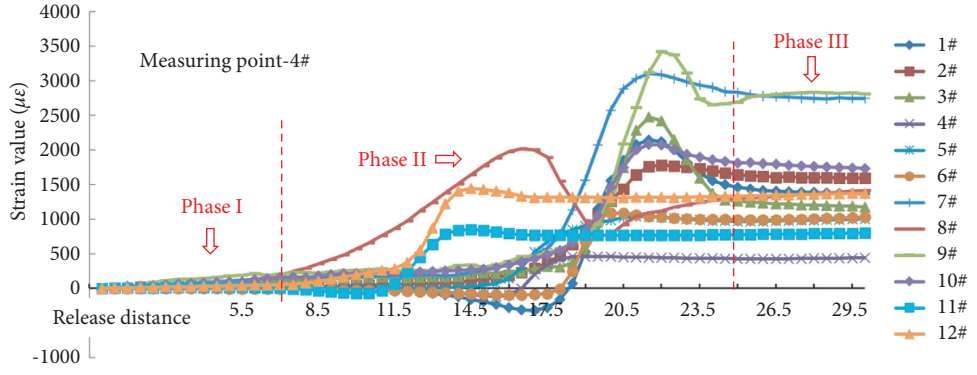

(d)

Figure 5: Continued.

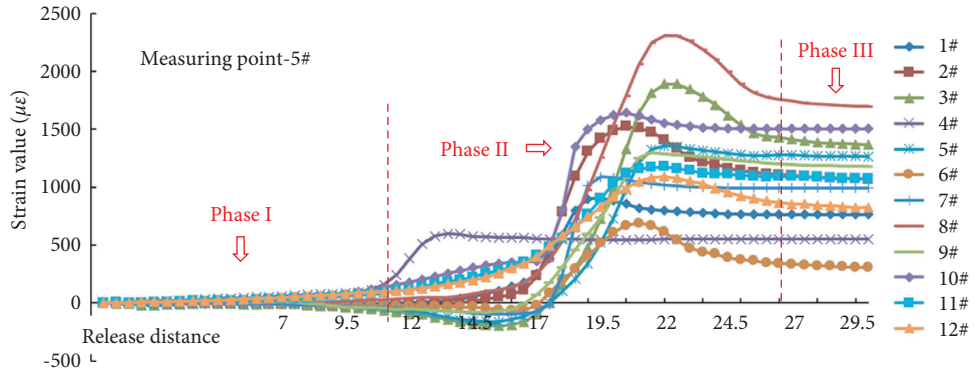

(e)

Figure 5: Stress relief curve.

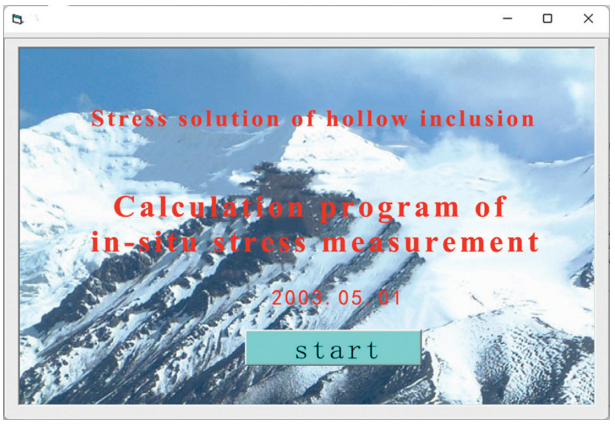

Figure 6: The main interface of in situ stress calculation program.

Table 3: Summary of measurement results.

Number	Measuring point position	Principal stress	Value (MPa)	Dip angle	Azimuth
1#	Third area gateroad	σ_1	39.48	6°	122°
		σ_2	21.35	83°	63°
		σ_3	19.08	1°	212°
2#	Gateroad #2310	σ_1	35.04	−11°	219°
		σ_2	19.96	62°	73°
		σ_3	12.06	25°	134°
3#	Gateroad #2305	σ_1	35.02	3°	134°
		σ_2	19.17	70°	36°
		σ_3	14.39	19.7°	225°
4#	Fourth area gateroad	σ_1	33.86	24°	126°
		σ_2	20.01	61°	18°
		σ_3	15.09	14°	223°
5#	Third area #3303	σ_1	42.54	−6°	117°
		σ_2	23.72	−78°	6°
		σ_3	18.73	−9°	208°

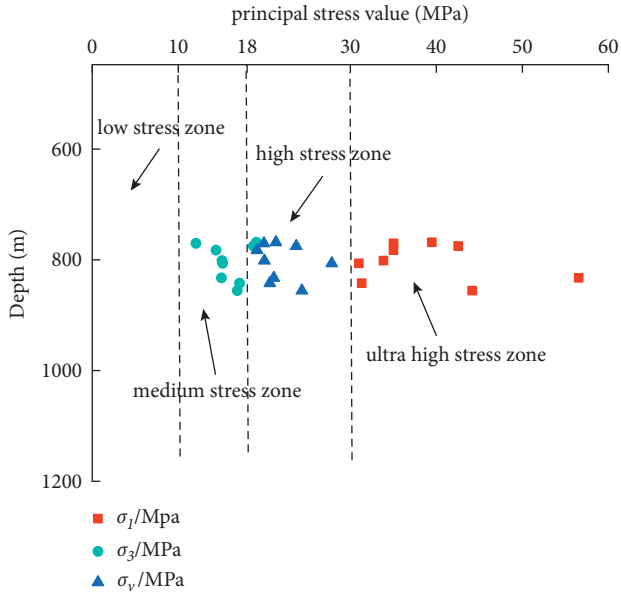

Figure 7: Distribution of principal stress.

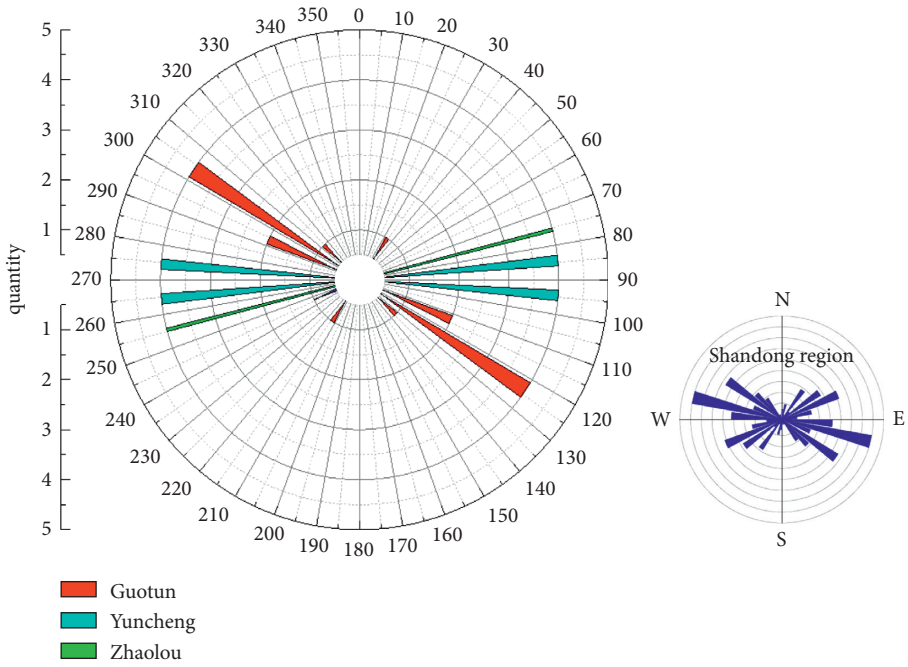

Figure 8: Rose diagram of the maximum principal stress [16].

Variation Law of Principal Stress with Depth. The maximum, minimum, and vertical principal stresses with the corresponding depth of each measurement point were plotted in Figure 10.

The least square method was used for linear regression fitting. The fitting results are as follows:

$$\sigma_1 = 0.0453H + 14.419\left(R^2 = 0.90182\right), \quad (1)$$

$$\sigma_2 = 0.0293H + 15.077\left(R^2 = 0.91381\right), \quad (2)$$

$$\sigma_3 = 0.0278H + 19.685\left(R^2 = 0.92271\right), \quad (3)$$

where H is the depth (m), and R^2 is the correlation coefficient.

From equations (1)–(3), it can be concluded that a great fitting effect was obtained by the three main stress fitting equations with the correlation coefficient R^2 of greater than 0.9. It can be also seen in Figure 10 that the principal stress value approximately linearly increases with the depth, and the maximum principal stress is slightly discrete. This may be

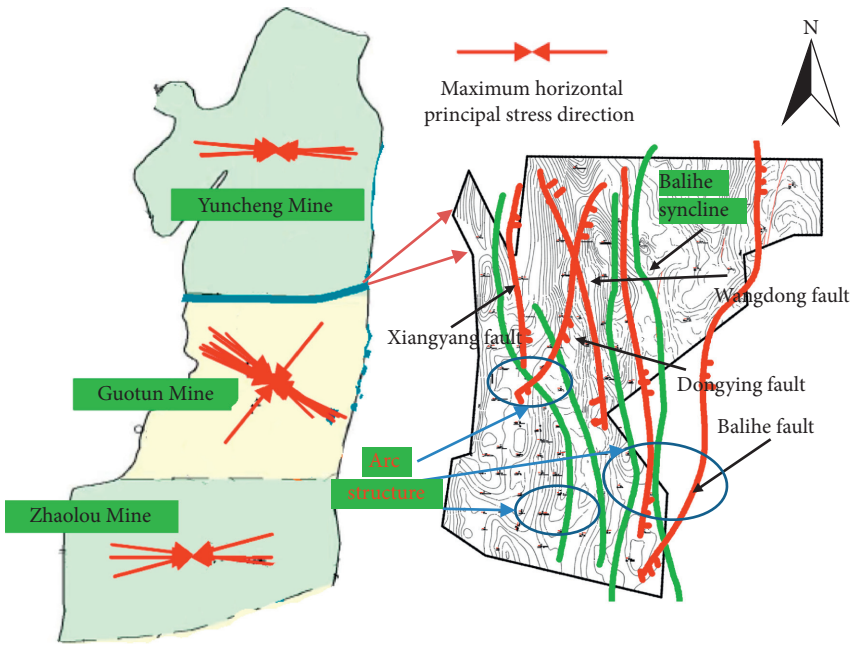

Figure 9: Directional distribution of the maximum horizontal principal stress.

caused by the differences in the geological structure and rock stratum characteristics in different degrees of the local range.

In the process of actual measurement, due to the unpredictability of the lithology of the measured rock mass and its fracture development degree, there will inevitably be errors in the measurement results. So, in order to verify the accuracy of the measurement results, the principal stress fitting results of the Guotun coal mine are compared with the surrounding coal mines, as shown in Table 4. It can be inferred that the variation trend of σ_H and σ_h between the Guotun coal mine and the Zhaolou coal mine shows a great consistency on the whole, but the Guotun's stress gradient (slope of the fitting curve) is relatively large. Compared with the Yuncheng coal mine, the two regression equations are quite different, which may be caused by the different amount of data and statistical depth used in regression analysis.

Variation of the Lateral Pressure Coefficient with Depth. The lateral pressure coefficient is an important characterization of the in situ stress state, and its size has a very important reference value for the design, construction, and maintenance of mine gateroad engineering [23, 24]. In this study, the ratios of σ_H to σ_v, σ_h to σ_v, and $\sigma_{(H+h)/2}$ to σ_v are denoted as K_H, K_h, and K_{av}. They were used to analyze the variation law of the in situ stress state with depth. The curve function $K = a/H + b$ was used for regression fitting, and the results are as follows:

$$K_H = \frac{72.71}{H + 1.57}, \tag{4}$$

$$K_h = \frac{56.54}{H + 0.63}, \tag{5}$$

$$K_{av} = \frac{101.21}{H + 1.12}. \tag{6}$$

Figure 11 shows the fitting curves of three lateral pressure coefficients varying with depth. It can be concluded that the distribution of K_H, K_h, and K_{av} shows a great regularity. According to the statistical results, the value of K_H is 1.11–2.68, with an average of 1.78, the K_h value is 0.54–0.89, with an average of 0.73, and the K_{av} is 0.83–1.70, with an average of 1.26. In general, with increased depth, the values of the three lateral pressure coefficients have a decreasing trend. From formulas (4)~(6), it can also be inferred that K_H, K_h, and K_{av} are likely to approach 1.57, 0.63, and 1.12, respectively.

4. Surrounding Rock Control Measures and Application

The stability of roadway surrounding rock is mainly affected by horizontal stress and can be divided into three areas: first, slightly affected areas; second, medium impact area; and third, seriously affected areas. The roadway parallel to the maximum horizontal stress direction is the least affected, and the surrounding rock stability is the best. For the roadway intersecting with the maximum horizontal stress direction at an acute angle, the surrounding rock deformation tends to a certain side of the roadway, and the surrounding rock stability is general. The roadway perpendicular to the maximum horizontal stress direction is most affected by horizontal stress, and the stability of surrounding rock is the worst.

In engineering practice, correctly handling the relationship between gateroad support design and in situ stress is an important guarantee for the safe mining of coal mine [25, 26]. The above-measured results and distribution law provide a detailed and reliable basis for gateroad mining layout and support scheme design. In this study, optimizing mining layout and strengthening support were proposed and

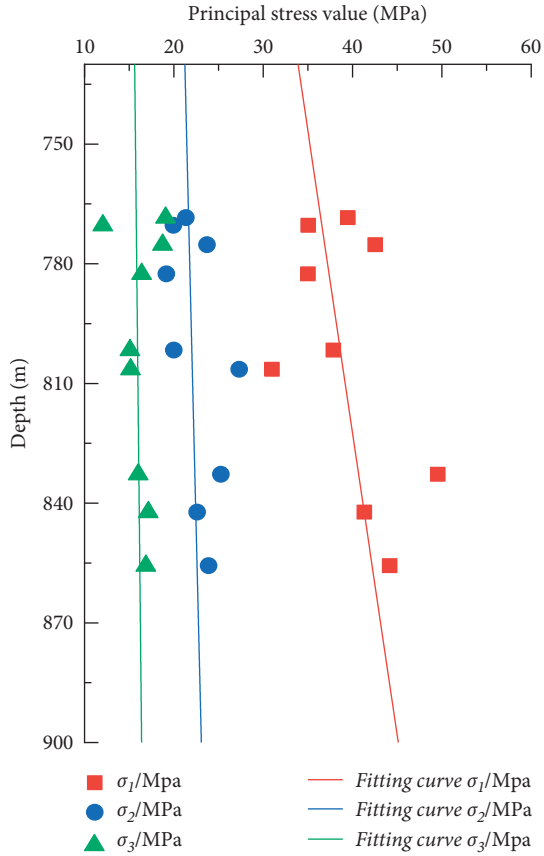

Figure 10: Fitting curve of principal stress with buried depth.

Table 4: Comparison of principal stress variation with depth between Guotun and other mines.

σ_H	σ_h	σ_v	Mine	Source
$0.0453H + 14.419$ ($R^2 = 0.90182$)	$0.0278H + 19.685$ ($R^2 = 0.92271$)	$0.0293H + 15.077$ ($R^2 = 0.91381$)	Guotun	This paper
$0.0384H + 4.78$ ($R^2 = 0.7918$)	$0.0276H + 4.34$ ($R^2 = 0.8960$)	–	Zhaolou	Chen et al. [21]
$0.3256H - 235.299$ ($R^2 = 0.9503$)	$0.1250H - 84.191$ ($R^2 = 0.8121$)	$0.2256H - 161.199$ ($R^2 = 0.9942$)	Yuncheng	Peng et al. [22]

carried out field application, based on the distribution law of in situ stress in the Guotun coal mine.

4.1. Control Measures for Large Deformation of Gateroad. First, working face 3301 is one of the typical working faces being mined. One of the measuring points of this in situ stress measurement is selected near the working face. Second, the overburden of working face 3301 has the typical stratigraphic characteristics of the Guotun coal mine. Therefore, gateroads of working face 3301 are selected as the site for the field application of the support scheme in this study.

The detailed technology parameters should be determined based on the existing economic and technical conditions, relevant theories, and engineering practice. Taking the working face 3301 of the Guotun coal mine as an example, the coal seam has stable occurrence, simple structure, and average thickness of 5.65 m. The roof is mainly fine and siltstone, and the floor is mainly mudstone and siltstone. A rectangular gateroad with width of 4.6 m, height of 4.3 m, and net sectional area of 19.78 m^2 is used for solid coal or semicoal rock excavation. The specific control measures are as follows:

4.1.1. Optimizing Mining Layout. First, the gateroads should be excavated along the direction of the maximum principal stress or at an acute angle with it as far as possible. It means that the gateroad in the Guotun coal mine should be arranged along the N57W direction as far as possible. Considering the specific engineering geological and construction conditions of the working face 3301, the angle between the direction of excavation and the maximum principal stress is set to 8 degrees. The specific layout of gateroad is shown in Figure 12.

Second, the gateroad layout should avoid large geological structures (fault, fold, and collapse column) as far as possible.

4.1.2. Strengthen the Support Scheme. First, the anchor bolts. Anchor bolts with yield strength greater than 500 MPa and easy to install shall be selected to enhance the adaptability to

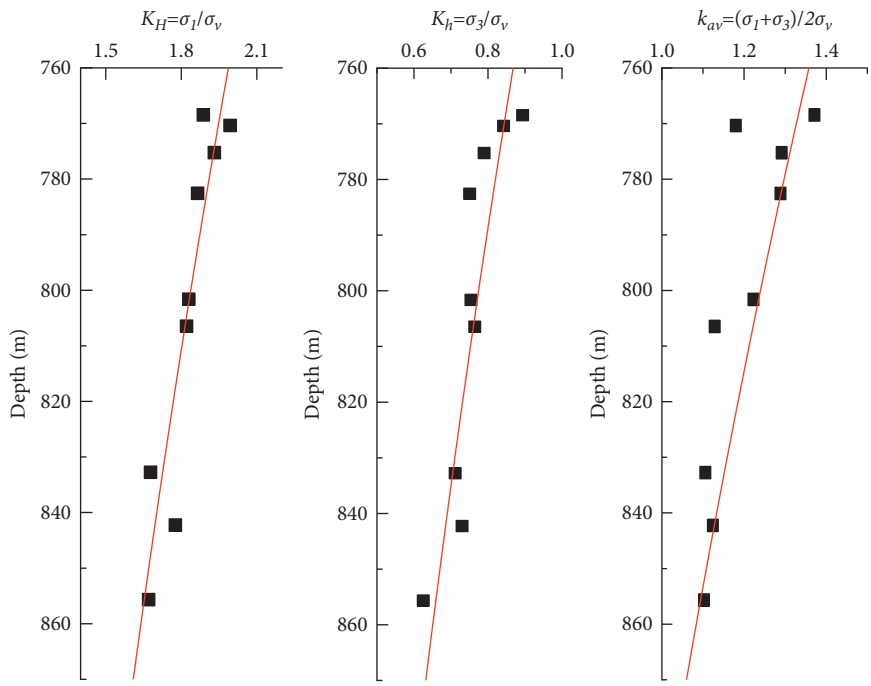

Figure 11: Relationship between lateral pressure coefficient and buried depth.

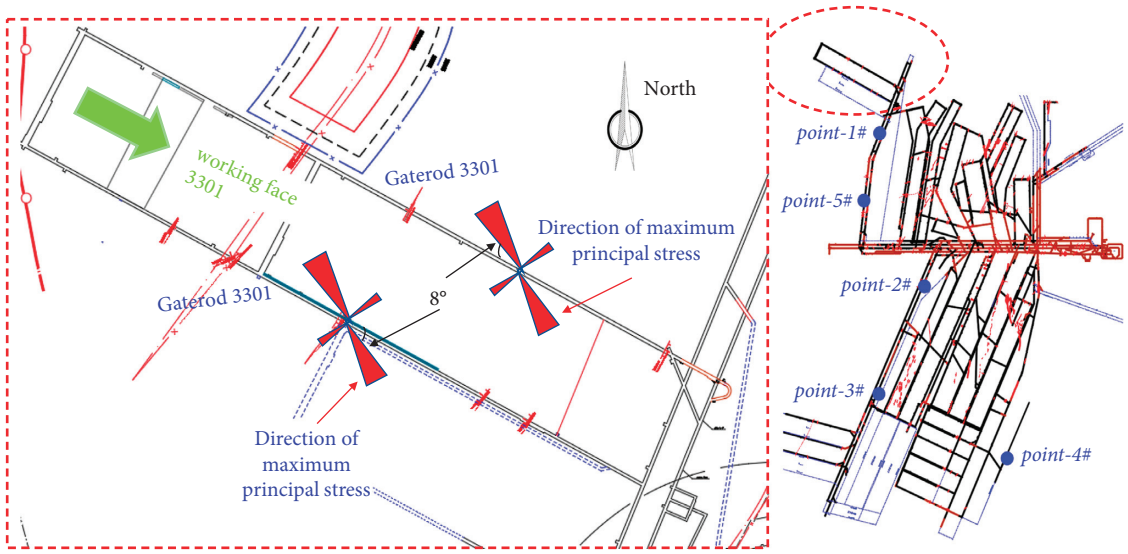

Figure 12: General layout of gateroad at working face 3301.

roof and coal wall. Especially for broken surrounding rock, when there are local irregularities, the ribs and roof can be smoothly pasted. Six left-handed high-strength prestressed bolts with a 20 mm diameter, a 2,400 mm length, and 500 MPa tensile strength were used in the roof. Five right-hand threaded steel bolts without longitudinal reinforcement with 20 mm in diameter and 3,300 mm in length were installed in the two ribs of the gateroad. All the bolts were installed with a spacing of 900 mm × 900 mm, a capsule resin K2370, and a 150 mm × 150 mm × 10 mm anchor bolt tray [27–31].

Second, the anchor cable. The type of 1 × 19# high-strength anchor cable is chosen, which can make the anchor cable to have better diffusion prestressing effect in the preloading stage and strong antideformation ability in the working stage. Three left-handed steel strand anchor cables with a 22 mm diameter and 8 m length are used in the gateroad roof. The anchor cable beam is processed with 14# channel steel (yield strength limit 235 MPa). All the bolts were installed with a spacing of 1,800 mm × 900 mm and two capsule resin K2370 [32–35]. The large diameter thickened anchor cable tray (bearing capacity 560 kN) is used with the

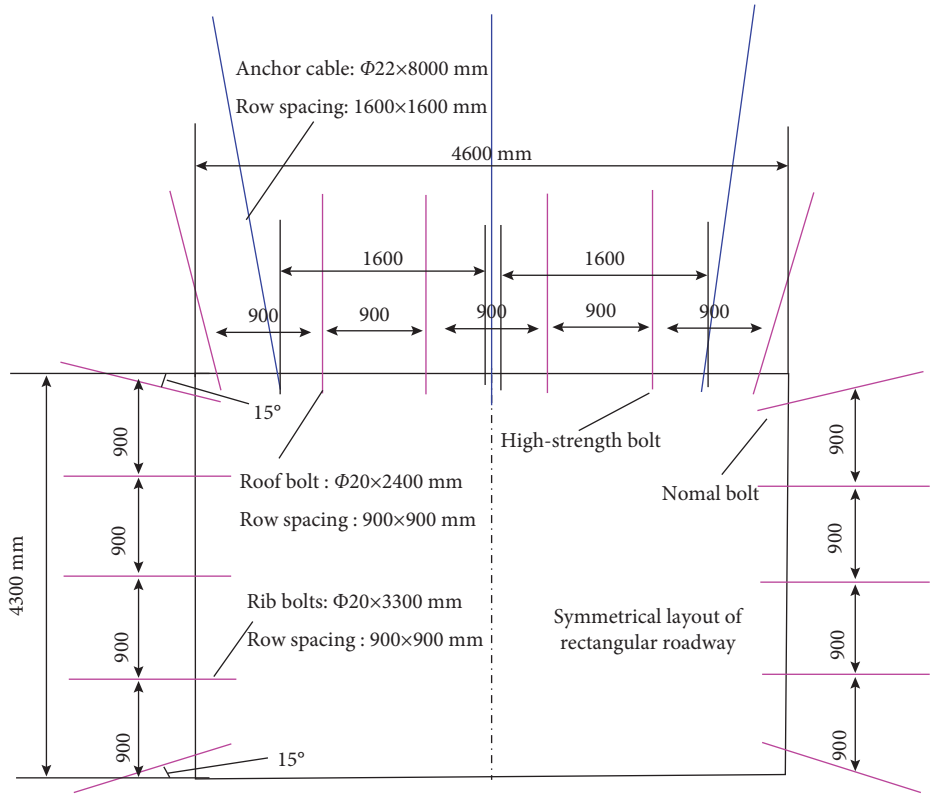

Figure 13: Support scheme 3301.

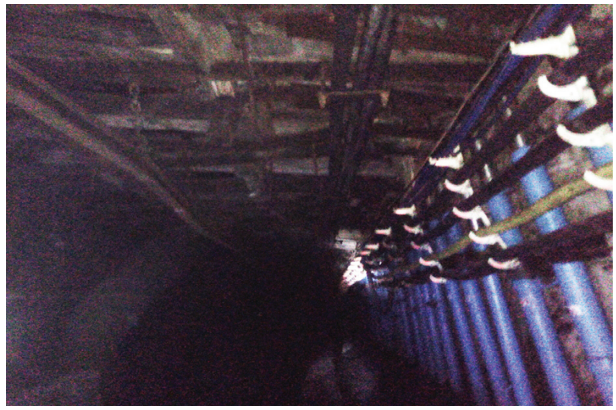

Figure 14: Roof support effect of working face 3301.

size of 150 mm × 150 mm × 10 mm, and the anchor cable layout is "3-2-3."

Third, protection of the gateroad surface. The gateroad surface is protected by metal mesh and high-strength impact-resistant woven mesh at the same time, which can effectively prevent the roof from breaking and falling. Gateroad roof and two sides can be laid Φ 6 mm × 1,100 mm × 2,000 mm metal mesh (yield strength 380 MPa) and high-strength tensile plastic, with plastic mesh inside and metal mesh outside. The plastic mesh shall be overlapped for 100 mm, a buckle shall be connected every 300 mm, and the mesh wire shall be 12# iron wire. The specific support scheme is shown in Figure 13.

4.2. Analysis of Surrounding Rock Control Effect. After the above layout method and support scheme are used in the mining gateroad of working face 3301, we use the roof separation instrument to monitor the displacement of relevant areas. The monitoring results show that the deformation of two ribs and the roof was within the control range. During the gateraod excavation, the deformation of both ribs and the roof was within the control range. The cumulative subsidence of the roof was 200 mm, the two ribs' convergence was 200 mm, and there was no floor heave. During the panel retreat period, the deformation of the gateroad slightly increased, and the overall deformation is always at a low level. The roadway could meet the

requirements of the ventilation and normal mining of the working face. The field support effect is shown in Figure 14.

5. Conclusions

This study mainly focuses on the distribution law of in situ stress field in the Guotun coal mine, and the specific control measures for surrounding rock are presented. The main conclusions are as follows:

(1) Among the three large-scale tectonic movements experienced by the Guotun coal mine, the middle Yanshan period has the strongest impact on it. According to the geological evolution process, it is preliminarily inferred that the maximum principal stress direction of the Guotun coal mine is NWW~SEE.

(2) The field measurement results show that the average maximum principal stress of the Guotun coal mine is 38.77 MPa, and the direction is 123 (N57W). Compared with the adjacent mines, the NW deflection is obvious, which is mainly caused by the arc structure within the mine.

(3) The type of in situ stress field in the Guotun coal mine is $\sigma_H > \sigma_v > \sigma_h$. The average stress gradient is 4.81 MPa/100 m. The maximum principal stress linearly increases with the depth and is larger than the surrounding mines. The lateral pressure coefficients K_H, K_h, and K_{av} are likely to approach 1.57, 0.63, and 1.12, respectively.

(4) The field test shows that the large deformation control measures proposed in this study to optimize the mining layout and strengthen the support have significant effects.

Data Availability

The data used to support the findings of this study are included in the article.

Conflicts of Interest

There are no conflicts of interest regarding the publication of this paper.

Acknowledgments

This is work was supported by the National Natural Science Foundation of China (nos. 51904164 and 52004145) and the Natural Science Foundation of Shandong Province (ZR2018QEE001 and ZR2020QE119).

References

[1] T. Bai, H. Yang, X.-B. Chen, S. C. Zhang, and Y. S. Jin, "In-situ monitoring and reliability analysis of an embankment slope with soil variabilit," *Geomechanics and Engineering*, vol. 23, no. 3, pp. 261–273, 2020.

[2] Ł. Bednarek and T. Majcherczyk, "An analysis of rock mass characteristics which influence the choice of support," *Geomechanics and Engineering*, vol. 21, no. 4, pp. 371–377, 2020.

[3] H.-P. Kang, B.-D. Yi, F.-Q. Gao, and H.-W. Lv, "In-situ stress database and its distribution in China's coal mines," *Journal of China Coal Society*, vol. 44, no. 1, pp. 23–33, 2019.

[4] K. Bandyopadhyay, J. Mallik, and T. Ghosh, "Dependence of fluid flow on cleat aperture distribution and aperture–length scaling: a case study from Gondwana coal seams of Raniganj Formation, Eastern India," *International Journal of Coal Science & Technology*, vol. 7, no. 1, pp. 133–146, 2020.

[5] A. J. Das, P. K. Mandal, P. S. Paul, and R. K. Sinha, "Generalised analytical models for the strength of the Inclined as well as the flat coal pillars using rock mass failure criterion," *Rock Mechanics and Rock Engineering*, vol. 52, no. 10, pp. 3921–3946, 2019.

[6] L.-Y. Huang, S.-X. Yang, X.-F. Cui, Q.-C. Chen, and R. Yao, "Analysis of characteristics of measured stress and stability of faults in North China," *Chinese Journal of Geophysics*, vol. 36, no. 1, pp. 204–213, 2013.

[7] Y. M. Cheng, J. A. Wang, G. X. Xie, and W. B. Wei, "Three-dimensional analysis of coal barrier pillars in tailgate area adjacent to the fully mechanized top caving mining face," *International Journal of Rock Mechanics and Mining Sciences*, vol. 47, no. 8, pp. 1372–1383, 2010.

[8] M.-F. Cai, Q.-F. Guo, Y. Li, Z.-F. Du, Z.-F. Du, and J.-H. Liu, "Geostress measurement and its application in pingmei mine," *Chinese Journal of Engineering*, vol. 35, no. 11, pp. 1399–1406, 2013.

[9] H.-P. Kang, T.-M. Jiang, X. Zhang, and L. Yan, "Research and application of in-situ stress field in Jincheng mining area," *Chinese Journal of Rock Mechanics and Engineering*, vol. 28, no. 1, pp. 1–8, 2009.

[10] Y.-C. Wang, H.-W. Jing, K.-F. Chen, and L.-Y. Wei, "Research on in-situ stress distribution and spatial zoning in Pingdingshan mining area," *Chinese Journal of Rock Mechanics and Engineering*, vol. 33, no. s1, pp. 2620–2627, 2014.

[11] J.-H. Synn, C. Park, and B.-J. Lee, "Regional distribution pattern and geo-historical transition of in-situ stress fields in the Korean peninsula," *Tunnel and Under Ground Space*, vol. 23, no. 6, pp. 457–469, 2013.

[12] C.-P. Yi, D. Johansson, and J. Greberg, "Effects of in-situ stresses on the fracturing of rock by blasting," *Computers and Geotechnics*, vol. 104, no. 1, pp. 321–330, 2017.

[13] J.-C. Yang, X.-D. Li, K.-W. Liu, and Z.-X. Liu, "Stress initialization methods for dynamic numerical simulation of rock mass with high in-situ stress," *Journal of Central South University*, vol. 27, no. 10, pp. 3149–3162, 2020.

[14] T. Hijazo and L. I. G. D. Vallejo, "In-situ stress amplification due to geological factors in tunnels: the case of Pajares tunnels, Spain," *Engineering Geology*, vol. 13, no. 20, pp. 137-138, 2012.

[15] H. Yavuz, "An estimation method for cover pressure re-establishment distance and pressure distribution in the goaf of longwall coal mines," *International Journal of Rock Mechanics and Mining Sciences*, vol. 41, no. 2, pp. 193–205, 2004.

[16] P. Li, Q.-F. Guo, H.-T. Liu, and X.-Q. Jiang, "Analysis on the characteristics of current in-situ stress field and stress accumulation level in Shandong province," *Chinese Journal of Rock Mechanics and Engineering*, vol. 36, no. 9, pp. 2220–2231, 2017.

[17] Y.-H. Wang, X.-F. Cui, X.-P. Hu, and F.-R. Xie, "Study on the stress state in upper crust of China mainland based on in-situ stress measurements," *Chinese Journal of Geophysics*, vol. 55, no. 9, pp. 3016–3027, 2012.

[18] E. Komurlu, A. Kesimal, and R. Hasanpour, "In situ horizontal stress effect on plastic zone around circular underground openings excavated in elastic zones," *Geomechanics and Engineering*, vol. 8, no. 6, pp. 783–799, 2015.

[19] J. A. Smith, H. L. Ramandi, C. Zhang, and W. A. Timms, "Analysis of the influence of groundwater and the stress regime on bolt behaviour in underground coal mines," *International Journal of Coal Science & Technology*, vol. 6, no. 2, pp. 286–300, 2019.

[20] G. Jepson, R. C. King, S. Holford, A. H. E. Bailey, and M. Hand, "In situ stress and natural fractures in the carnarvon basin, north west shelf, Australia," *Exploration Geophysics*, vol. 50, no. 5, pp. 514–531, 2019.

[21] M. Chen, S.-Q. Yang, P.-G. Ranjith, and Y.-C. Zhang, "Cracking behavior of rock containing non-persistent joints with various joints inclinations," *Theoretical and Applied Fracture Mechanics*, vol. 109, no. 1, pp. 1–16, 2020.

[22] H. Peng, X.-M. Ma, and J.-J. Jiang, "In situ stress measurement and stress field study of 1000 m deep hole hydraulic fracturing in Zhaolou coal mine," *Chinese Journal of Rock Mechanics and Engineering*, vol. 30, no. 8, pp. 1638–1645, 2011.

[23] J.-K. Li, G. Li, and Z.-J. Tian, "Application of hollow inclusion in in-situ stress test in Yuncheng coal mine," *Industrial Safety and Environmental Protection*, vol. 45, no. 4, pp. 15–19, 2019.

[24] M. Shabanimashcool and C. C. Li, "Analytical approaches for studying the stability of laminated roof strata," *International Journal of Rock Mechanics and Mining Sciences*, vol. 79, no. 1, pp. 99–108, 2015.

[25] M. M. Mohammed, H. Roslan, and S. Firas, "Assessment of rapid impact compaction in ground improvement from in-situ testing," *Journal of Central South University*, vol. 20, no. 3, pp. 786–790, 2013.

[26] G.-L. Zhou, T. Xu, M. J. Heap et al., "A three-dimensional numerical meso-approach to modeling time-independent deformation and fracturing of brittle rocks," *Computers and Geotechnics*, vol. 117, no. 1, Article ID 103274, 2020.

[27] Y. Sun, J. Zuo, M. Karakus, L. Liu, H. Zhou, and M. Yu, "A new theoretical method to predict strata movement and surface subsidence due to inclined coal seam mining," *Rock Mechanics and Rock Engineering*, vol. 54, no. 6, pp. 2723–2740, 2021.

[28] W.-L. Shen, G.-C. Shi, Y.-G. Wang, J.-B. Bai, R.-F. Zhang, and X.-Y. Wang, "Tomography of the dynamic stress coefficient for stress wave prediction in sedimentary rock layer under the mining additional stress," *International Journal of Mining Science and Technology*, vol. 31, no. 6, pp. 653–663, 2021.

[29] G.-C. Zhang, C.-W. Zang, M. Chen, and T. Guangzhe, "Ground response of entries driven adjacent to a retreating longwall panel," *International Journal of Rock Mechanics and Mining Sciences*, vol. 138, no. 11, Article ID 104630, 2021.

[30] G. C. Zhang, Z. J. Wen, S. J. Liang et al., "Ground response of a gob-side entry in a longwall panel extracting 17 m-thick coal seam: a case study," *Rock Mechanics and Rock Engineering*, vol. 53, no. 2, pp. 497–516, 2019.

[31] F. Cui, C. Jia, X.-P. Lai, and J.-Q. Chen, "Study on the evolution characteristics and stability of overburden structure in upward mining of short distance coal seams with strong burst tendency," *Chinese Journal of Rock Mechanics and Engineering*, vol. 39, no. 03, pp. 570–521, 2020.

[32] G.-C. Zhang, F.-L. He, H.-G. Jia, and Y.-H. Lai, "Analysis of gateroad stability in relation to yield pillar size: a case study," *Rock Mechanics and Rock Engineering*, vol. 50, no. 05, pp. 1263–1278, 2017.

[33] X. Li, G. Zhang, G. Tao et al., "Ground behaviors analysis of a stope covered by the thin bedrock and large-thick alluvium: a case study," *Shock and Vibration*, vol. 2022, Article ID 4759416, 14 pages, 2022.

[34] J.-H. Chen, P. Liu, H.-B. Zhao, C. Zhang, and J.-W. Zhang, "Analytical studying the axial performance of fully encapsulated rock bolts," *Engineering Failure Analysis*, vol. 128, no. 1, pp. 1–16, 2021.

[35] J.-H. Chen and D.-Q. Li, "Numerical simulation of fully encapsulated rock bolts with a tri-linear constitutive relation," *Tunnelling and Underground Space Technology*, vol. 120, no. 1, pp. 1–13, 2022.

Hindawi
Geofluids
Volume 2022, Article ID 2892964, 22 pages
https://doi.org/10.1155/2022/2892964

Research Article

Water Supply and Regulation of Underground Reservoir in Coal Mine considering Coal-Water Occurrence Relationship

Mingbo Chi[1,2], **Zhiguo Cao**[1,2], **Quansheng Li**[1], **Yong Zhang**[1,2], **Baoyang Wu**[1,2], **Bao Zhang**[1,2], **Yi Yang**[1,2] and **Xiaoqing Liu**[1,3]

[1]*State Key Laboratory of Water Resource Protection and Utilization in Coal Mining, Beijing 100011, China*
[2]*National Institute of Clean-and-Low-Carbon Energy, Beijing 102209, China*
[3]*Shenhua Shendong Technology Research Institute, Shaanxi 719315, China*

Correspondence should be addressed to Mingbo Chi; mingbo.chi@chnenergy.com.cn
and Zhiguo Cao; zhiguo.cao@chnenergy.com.cn

Received 22 November 2021; Accepted 27 December 2021; Published 22 January 2022

Academic Editor: Afshin Davarpanah

Water supply prediction and control is one of the key issues in exploitation of coal mine underground reservoirs (CMUR). In order to investigate the water supply for underground reservoirs in coal mines, the aquifers were classified into three types (types I, II, and III) according to the relative location of aquifers. The discrete element fluid structure coupling numerical simulation model is constructed according to the classification results. The numerical simulation parameters are inversed based on the surface subsidence data and the advance support pressure, and then, the disturbed characteristics and water pressure variation law of different types of aquifers are studied. The research results show that the maximum water inflow of type III, type II, and type I aquifers is 739 m^3/h, 377 m^3/h, and 279 m^3/h, respectively. The dynamic calculation process of underground reservoir capacity under mining disturbance is refined, and the regulation and storage methods of underground reservoir are preliminarily put forward.

1. Introduction

With the implementation of China energy strategy, the western mining area has become the "main battlefield" for the development and utilization of coal resources. The output and reserves of coal in the five western provinces (Shanxi, Shaanxi, Mongolia, Ningxia, and Xinjiang) account for more than 70% of the national total, while their water resources account for only 3.9% of the total. Under the background characterized by "rich coal, poor water, and weak ecology," water resources have become a "bottleneck" restricting the development of coal industry in China western areas. The "ecological loss" derived from traditional extensive mining far exceeds the "economic value" created by coal development. The ecological environment problem, especially the water resources protection in western mining areas, has become the major problem faced by the coal industry [1–4]. According to statistics, China's annual output of mine water is about 8 billion tons, of which 6 billion tons are wasted, which accounts for about 60% of the industrial and civilian water. If the mine water can be fully utilized, there will be abundant water for downstream coal processing [1, 5–7]. Therefore, "protection and utilization of mine water" has become a strategic requirement for sustainable development as well as an important prerequisite for the green development of coal resources.

At present, many scholars have carried out extensive theoretical researches and engineering practices on "water-preserved mining." From the perspective of "blocking, interception and drainage," a lot of researches have been conducted on mining-induced fissures and rock movement in order to master the development law of mining-induced fissures and investigate the impact of coal mining on water resources. Through theoretical analyses, experimental researches, and engineering practices, researchers have put forward theoretical and engineering technical means such

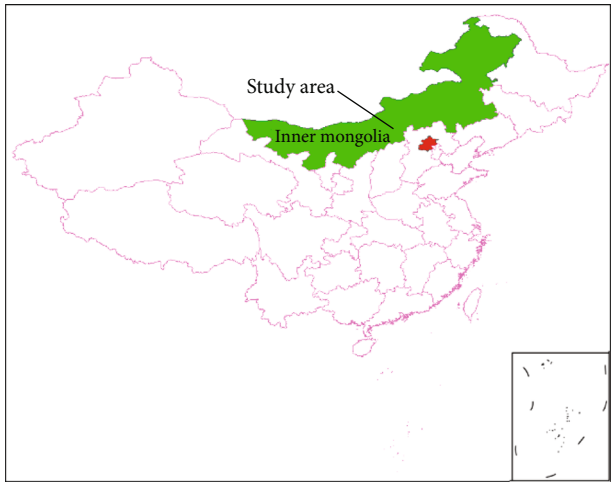

(a) Location map of the study area

(b) Supplement a map with water

(c) Scarce vegetation

Figure 1: Overview of study area.

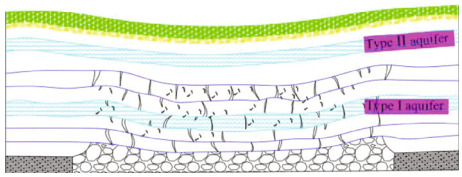

(a) Lower limit aquifer (type I aquifer)

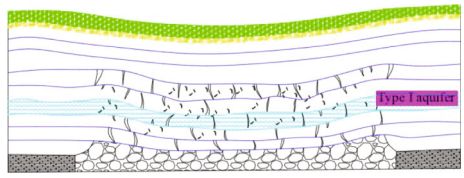

(b) Upper limit aquifer (type II aquifer)

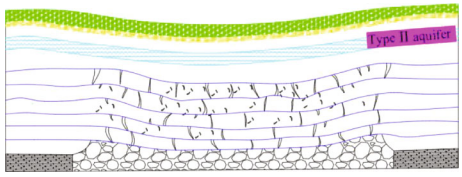

(c) Mixed aquifer (type III aquifer)

Figure 2: Generalized classification of coal-water occurrence relationship in shallow coal seam.

as height-limiting mining, mining with filling, and ground water storage in order to avoid or reduce the degree of damage to water resources caused by mining and thereby solve the contradiction between coal mining and ecological environment [8–11]. However, these mining protection methods and technologies have certain limitations. For example, height-limiting mining reduces the coal recovery rate and causes the waste of resources; ground water storage is limited due to the problems such as insufficient water storage space and high costs of water storage. In addition, there are still theoretical and technical difficulties in the study on the relationship between the development of mining-induced fissures and the destruction of aquifers, which are also key issues to be addressed in the protective exploitation of water resources.

After more than 20 years of scientific and technological researches and engineering practices, Gu Dazhao first proposed the concept of "diversion, storage and use" for underground reservoirs in coal mine. At present, more than 30 underground reservoirs have been successfully constructed in the Shendong mining area, with an annual water storage capacity of about 32 million m^3, which contributes a lot to the ecological development, industrial production, and domestic water use in the mining area [1]. After years of researches and explorations, the academic community has carried out a large number of theoretical and engineering

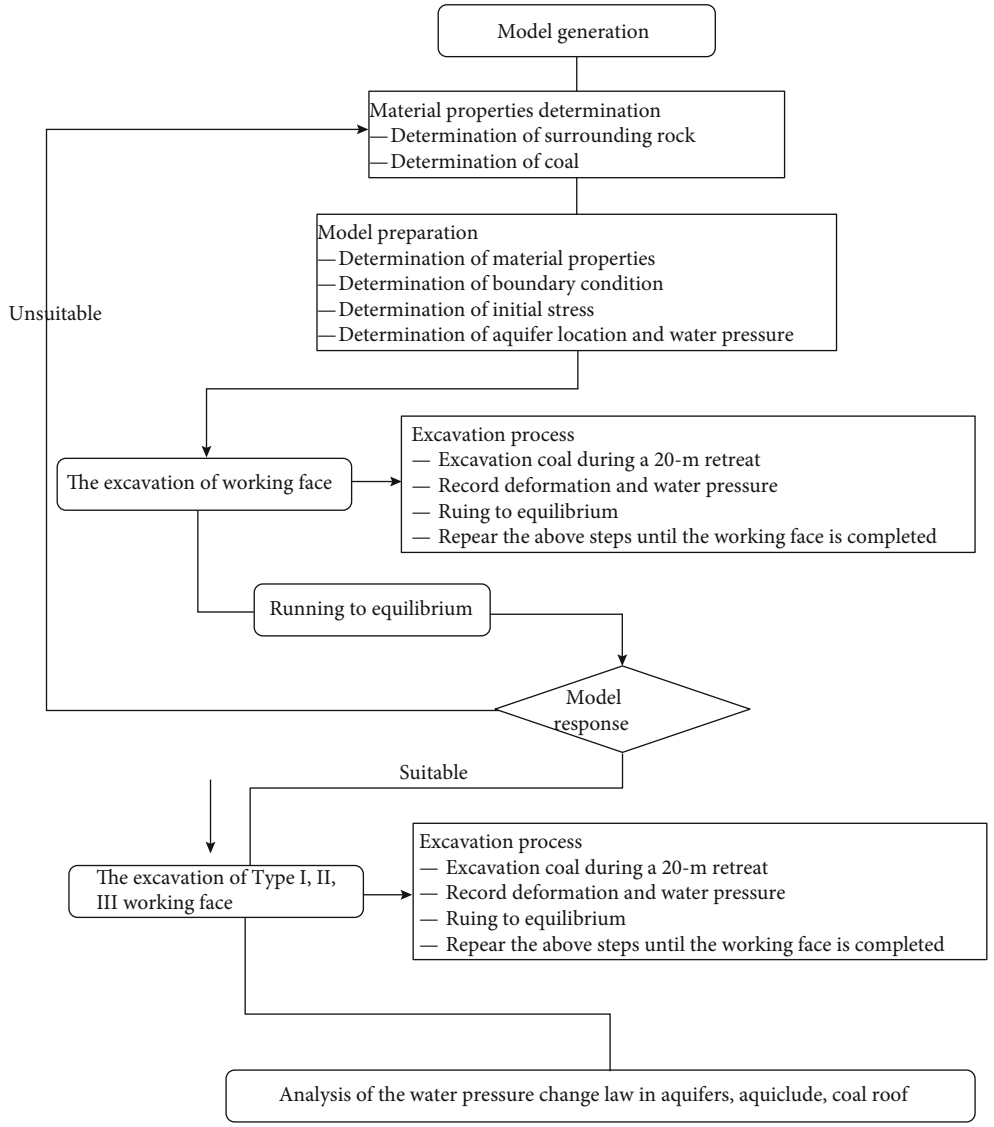

Figure 3: Flow chart of numerical simulation.

Table 1: Physical and mechanical parameters of rock stratum.

Types of rocks	Bulk density kN/m^3	Compressive strength σ_t/MPa	Internal friction angle	Cohesion	Elastic modulus E/GPa	Poisson's ratio μ	Permeability coefficientc m/s
Aeolian sand	15.8	—	20	0.02	—	—	1×10^{-9}
Conglomerate	23.9	45.3	39	7.10	33	0.25	3×10^{-4}
Sandy mudstone	22.4	22.8	38	6.32	23	0.28	1×10^{-11}
Siltstone	23.5	40.6	38	7.07	35	0.25	2×10^{-7}
Coal	15.1	6.60	30	2.00	14	0.22	1×10^{-6}
Mudstone	22.3	20.7	29	5.55	20	0.30	3×10^{-10}
Fine sandstone	23.4	6.60	38	6.46	13	0.22	1×10^{-8}

practices on site selection for underground reservoir, body design of reservoir dam, and reservoir design. Key technologies such as water source prediction, reservoir site selection, and storage capacity design have been put forward to guarantee the safety of reservoir operation. It is worth noting that water source prediction is the basic prerequisite for the

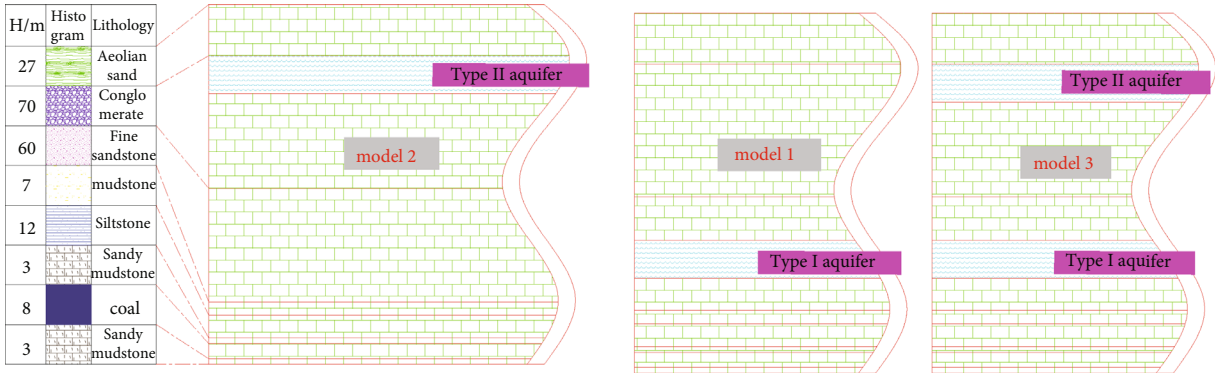

(a) Composite borehole histogram (b) Type I (c) Type II (d) Type III

Figure 4: Generalization model for numerical simulation.

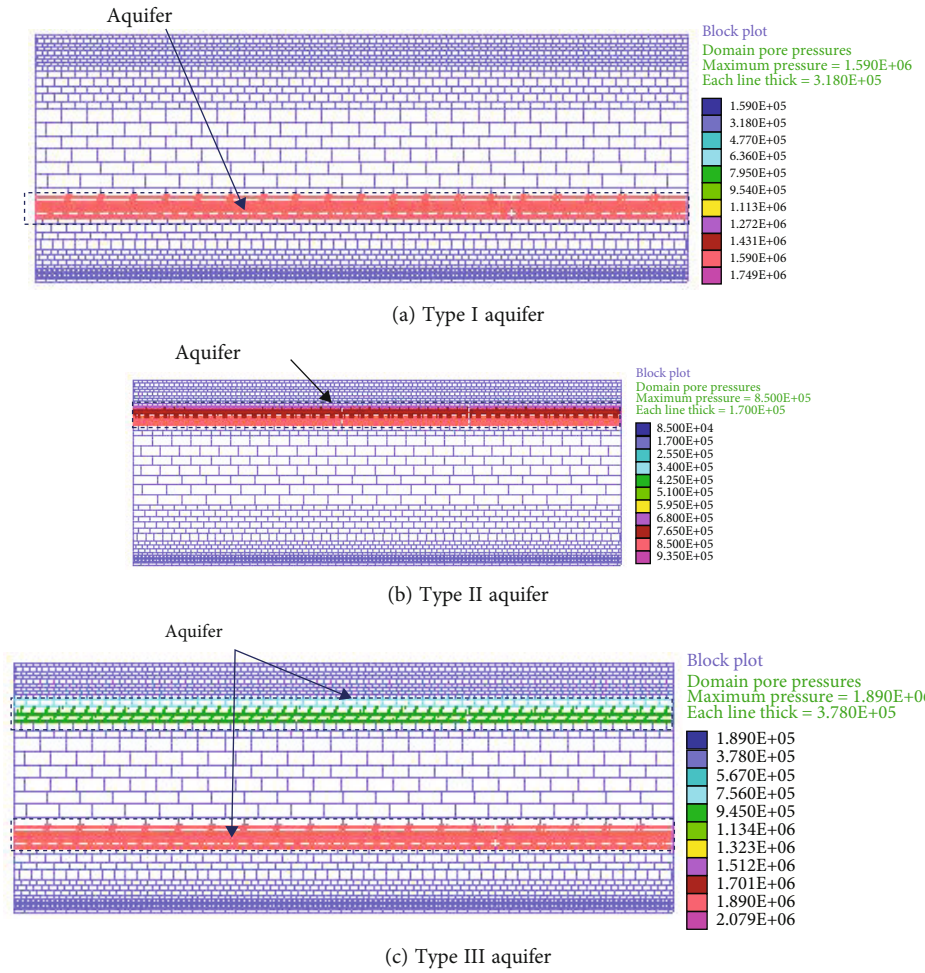

(a) Type I aquifer

(b) Type II aquifer

(c) Type III aquifer

Figure 5: Numerical modeling.

construction of underground reservoirs in coal mine, which includes two aspects: groundwater migration law research and groundwater volume prediction. Mine water inflow is the basis of a series of water storage activities in goaf such as underground reservoir capacity design, safe operation of underground reservoir, and mine water supply [12–17]. At present, water source prediction is mainly based on the actual monitoring data of mine water inflow. In fact, most of the water sources of underground reservoirs derive from the overlying aquifer of the coal seam, which is closely related to the law of disturbance of the aquifer. Therefore, determining the change law of aquifer under the influence

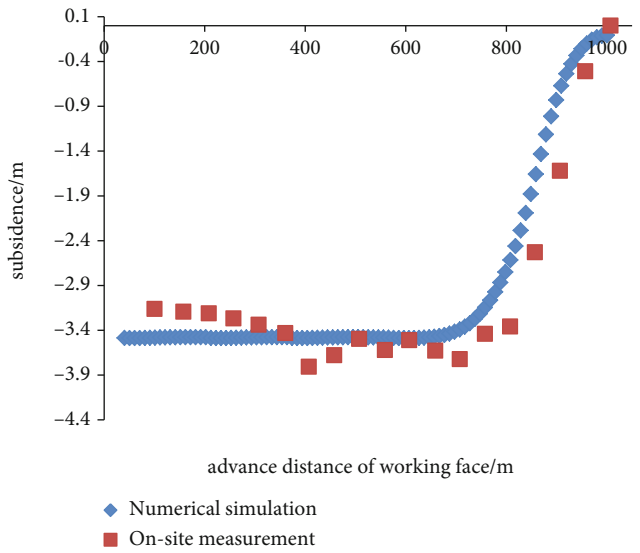

Figure 6: Comparison of surface subsidence data and simulation results.

of mining is the basis for the study of reservoir water sources. In addition, coal seams in the western mining areas are typically characterized with shallow burial depth, big thickness, variable aquifer locations, and uncertain aquifer layers [18, 19], which brings big problems in the prediction of underground reservoir water sources.

Taking the Bulianta coal mine in Shendong mining area as example, this study presents fluid-solid coupling numerical analysis by using UDEC discrete element simulation software, studies the aquifer change law under the impact of mining, comparatively studies the water pressure changes of aquifers in different models, analyzes the water source of the underground reservoir, and proposes the water source control method for underground reservoir. The research results carry academic significance for accurately predicting the water source of underground reservoirs in coal mines.

2. Generalized Classification of "Coal-Water" Occurrence Relationship in Shallow Coal Seams

2.1. Analysis of Main Factors Influencing Aquifer Changes under Mining Action. After the coal seam is mined, the original balance state of the rock layer is destroyed, which leads to the deformation of the overlying rock mass and the generation of mining-induced fissures, resulting in the change of permeability of the overlying coal seam (Figure 1). On this basis, the mining-induced fissures continue to expand under the "mining stress-water" coupling effect, which eventually become a channel for water loss, causing water resources to flow to the goaf. In fact, there are two necessary conditions for water resources derived from aquifers to enter the goaf: one is that the mining-induced fissures communicate with the aquifer, and the other is that the fissures develop into water-conducting fissures. When either of the two conditions is not satisfied, loss of water resources in the aquifer will not be resulted. For example, when the overlying rock is soft rock or contains kaolin, illite, and other water-swelling minerals, the water-conducting fissures will gradually close after a certain period of time; the water level of the aquifer will gradually recover, so that the loss of water resources will gradually decrease. Therefore, water-conducting fissure zone is one of the main factors causing the change of aquifers. In the research process, it is necessary to consider the development height of the fissures and also analyze whether the fractures can develop into water-conducting channels. Only when the fissures communicate with the aquifer and develop into water-conducting channels, it will impose threat to the aquifer, which is very important for water supply during the construction of underground reservoirs in coal mines.

Regarding the problem of mining-induced fissures, many scholars have conducted a lot of researches by theoretical analysis and simulation deduction. It is believed that the main factors influencing mining-induced fractures are coal seam depth, mining thickness, mining speed, etc. The calculation formula and judgment standard of fissure development height have been put forward [11, 20–23]. Where roof lithology, burial depth, and lithological conditions can be regarded as internal factors affecting the development of water-conducting fissure zone, while mining height and working face size can be regarded as external factors. Factors such as mining thickness and mining speed affect the degree of roof rock destruction (fissure development), while roof lithology and combination means determine its ability to "resist" mining disturbances. According to the mining-induced damage on aquifer, impacts of mining-induced fissures on the aquifer can be classified into three cases. First, mining-induced fissures will not damage the stability of the aquifer; that is, it will not cause the loss of water resources in the aquifer. Second, mining-induced fissures destroy the aquifer stability, but after a period of time, the aquiclude gradually recovers its water-proof capacity, and the fissures lose the function of water conduction. Although there is a certain loss of water in the aquifer, the stability of the aquifer is not affected. Third, mining-induced fissures cause irreversible damage to the aquifer, and mining-induced fissures become seepage channels, so that a large amount of water resources flow to the goaf [4, 20]. The main factor affecting the occurrences of the above three cases is the relationship between the development height of the water-conducting fissures and the occurrence location of the aquifer. Due to the shallow burial depth and great thickness of coal seams in western mining areas, fissures will develop to the surface after coal seams are mined. Therefore, its impact on aquifers basically accords with the second and third cases, causing a lot of waste of water resources. The construction purpose of underground reservoirs in coal mines is to introduce mine water into the goaf, so that it can be used after being sealed and fully purified. Therefore, it is necessary to generalize the classification of the occurrence modes of aquifers, link them with the development of mining-induced fissures, and then study its disturbance characteristics under different conditions to provide a basis for the prediction of water source in underground reservoirs.

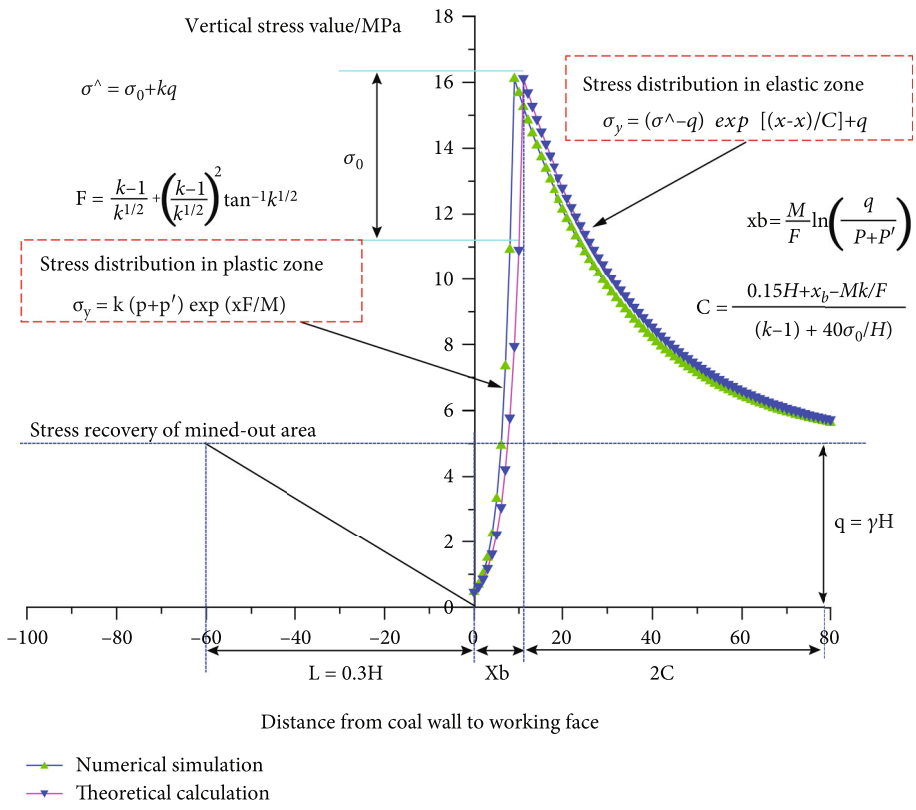

Figure 7: Distribution characteristics of abutment pressure in working face.

Table 2: Wilson's theoretical formula parameters.

Coal seam thickness/m	Buried depth/m	Triaxial stress factor	Lateral supporting pressure at the coal wall/MPa	Hydrostatic pressure/MPa	Uniaxial compressive strength/MPa	Uniaxial compressive residual strength/MPa
5	200	2.3	0	5	5	0.2

2.2. Generalized Classification of Coal-Water Relationship. Over the years, many scholars have carried out a large number of studies on the movement law of the overburden strata in shallow coal seams. It is concluded that the movement of the overburden strata in shallow coal seams has obvious "two belt" divisions in the vertical direction, and the disturbance characteristics of coal mining on aquifers are studied according to the development laws of the "two belts." In fact, the location of aquifer varies with the influence degree of mining. For underground reservoirs in coal mine, the aquifers at different locations provide varying degrees of recharge to the reservoir after mining disturbances. Considering this, this paper classifies the relationship between the aquifer location and the development height of the "two belts", and generalizes the aquifers into three types (as shown in Figure 2).

Type I aquifer: the lower aquifer, which is located between the caving zone and the fissure zone. When the aquifer is located at this position, the mining-induced fissures directly destroy the stability of the aquifer; the fissures communicate with the aquifer and become the main channel allowing the water source of the aquifer to flow to the goaf.

Type II aquifer: the upper aquifer, which is located above the fissure zone. This type of aquifer is less affected by fissure development than type I. Mining-induced fissures have not developed to the aquifer or have less impact on the stability of the aquifer. Water resources in the aquifer will flow downwards only when fissure penetrates the aquifer and forms a water-conducting channel.

Type III aquifer: mixed type aquifer, which coexists with type I aquifer and type II aquifer. Generally, this type of aquifer is dominant in the process of coal seam excavation. Different mining methods and geological conditions have greatly different effects on the aquifers, and the water supply to underground reservoirs in coal mine is also different.

Type I and type II aquifers are collectively referred to as single type aquifer. It can be determined that the water source of the underground reservoir basically comes from this type of aquifer. Type III aquifer is a combination of the other two types of aquifers. In the case of Type III aquifer, the water source of the underground reservoir is supplied by two or more aquifers. Since type I aquifer is in the fissure zone, the destruction degree is larger compared to type II. Therefore, type I aquifer may become the main water source for underground reservoirs. In order to clarify the recharge of aquifers to the underground reservoirs under different conditions, it is necessary to analyze the failure

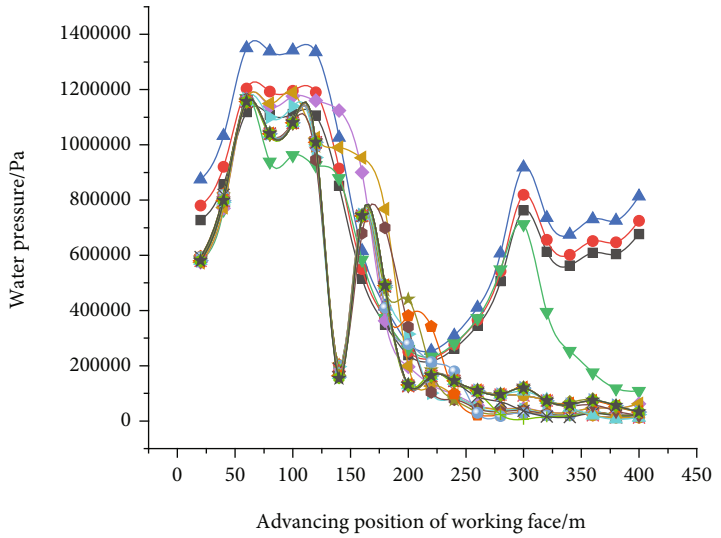

(a) Lower aquifer of model 1

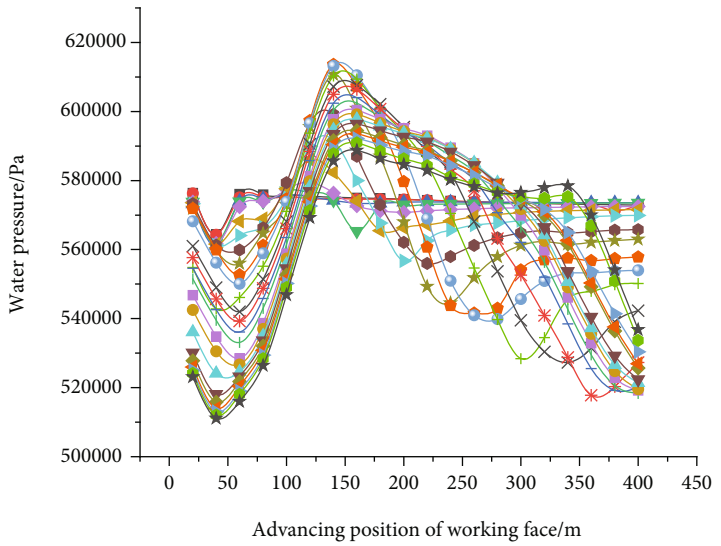

(b) Lower aquifer of model 2

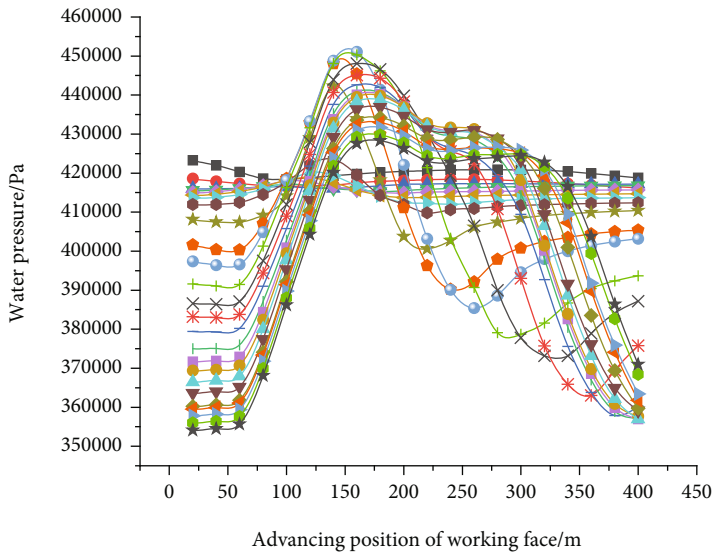

(c) Model 3 (type II aquifer)

Figure 8: Continued.

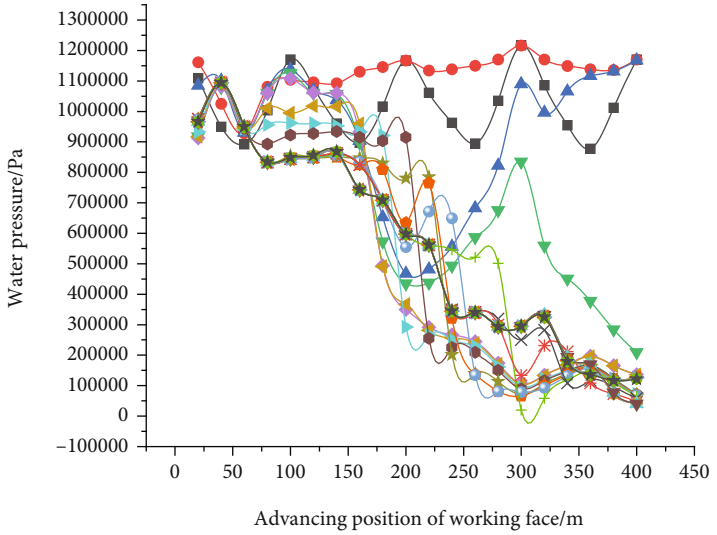

(d) Model 3 (upper part of type I aquifer)

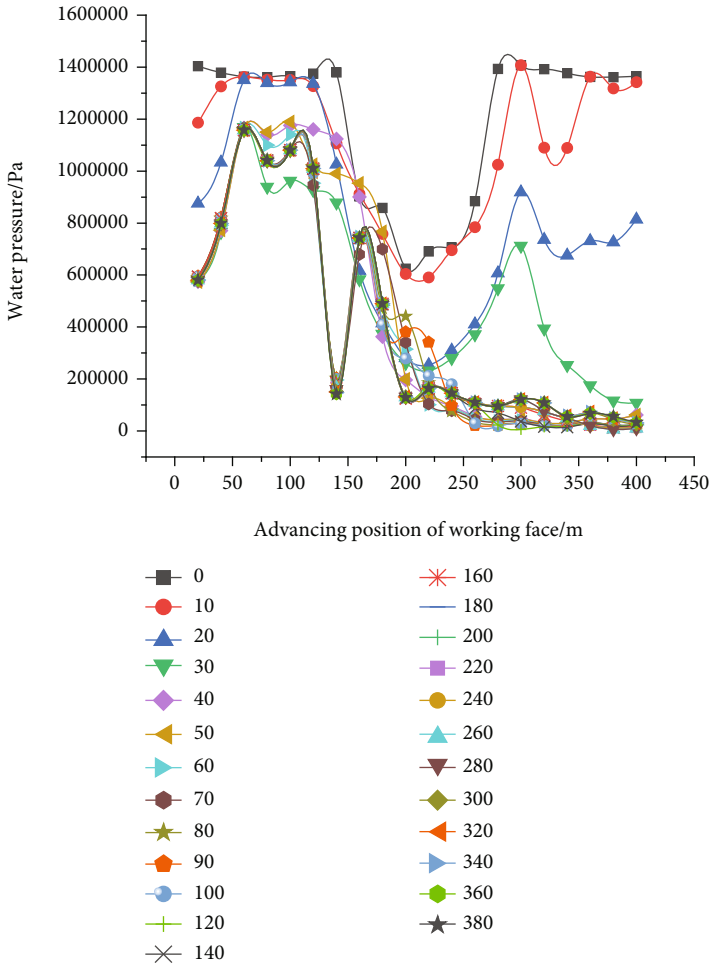

(e) Model 3 (lower part of type I aquifer)

Figure 8: Variation law of water pressure in aquifer.

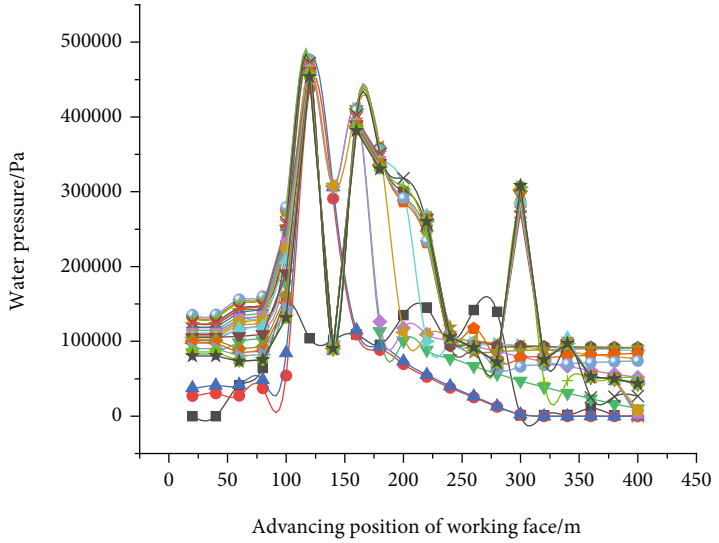

(a) The upper part of coal seam in model 1

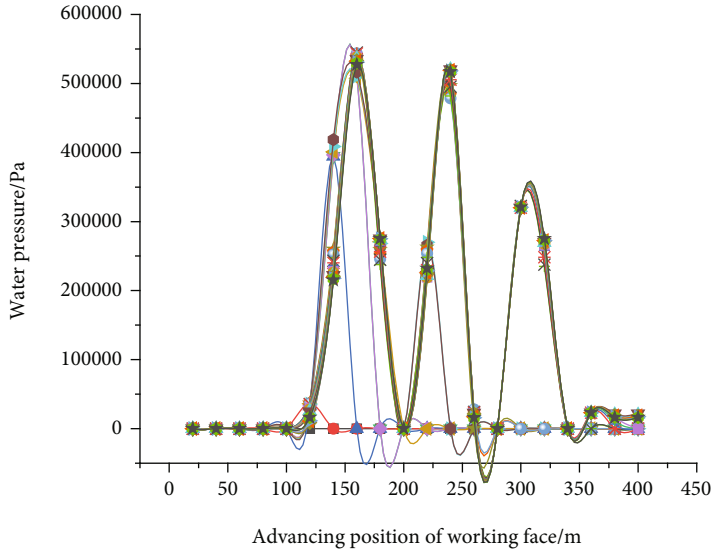

(b) The upper part of coal seam in model 1

Figure 9: Continued.

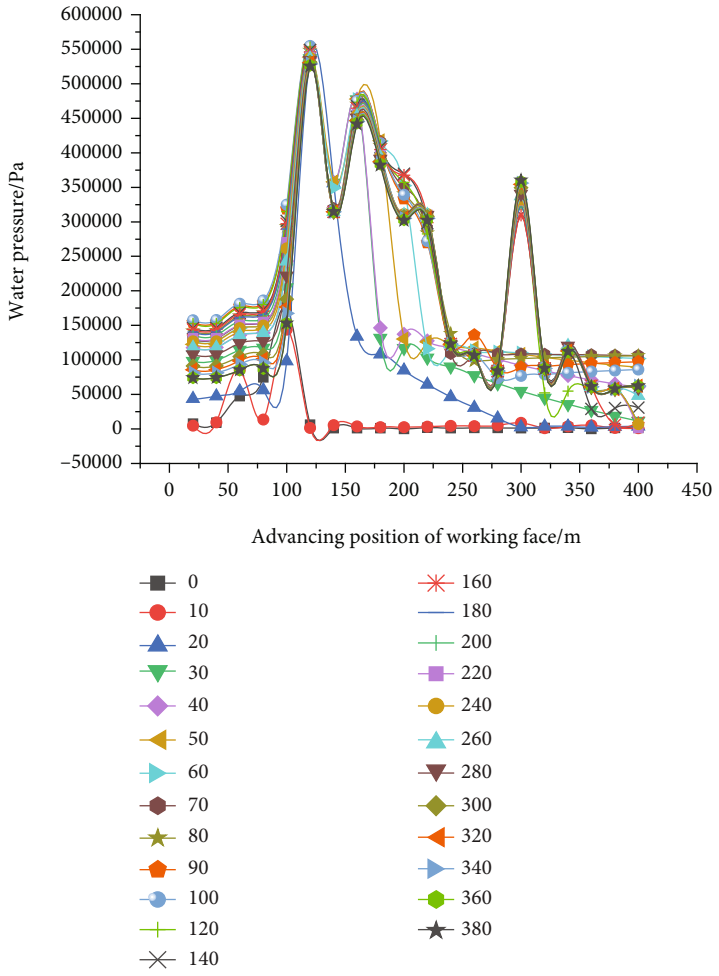

(c) The upper part of coal seam in model 1

Figure 9: Variation law of water pressure at coal roof.

characteristics of various types of aquifers under the influence of mining.

3. Numerical Model and Result Analysis

The Discrete Element Method (DEM) believes that the rock mass is composed of rock blocks and discontinuous surfaces between the blocks. DEM can be used to describe the geometric characteristics (fracture length, inclination, opening degree, spacing, etc.) of rock mass cracks more truthfully. Therefore, the DEM-based numerical calculation method has been widely used in the study of the hydraulic characteristics of rock (body) fissures.

In the simulation process, the mechanical deformation of the joint will affect the hydraulic opening of the joint. The hydraulic opening of the joint is calculated by the following formula.

$$\begin{aligned} a &= a0 + \triangle a, \\ \triangle a &= \frac{\sigma n}{kn}, \end{aligned} \tag{1}$$

where a_0 is the joint opening in the zero-stress state, σ_n is the normal stress acting on the joint, k_n is the stiffness of the joint, and a_{res} is the residual hydraulic opening of the joint.

In the process of stress change, the crack opening changes, the flow rate of each node changes, and the pore pressure of the original domain also changes. The pore pressure of the new area can be calculated by following formula:

$$P = P_0 + K_w Q \frac{\triangle t}{V} - K_w Q \frac{\triangle V}{V}, \tag{2}$$

where P is the updated regional pressure, Pa; P_0 is the original regional pressure, Pa; K_w is the bulk modulus of the fluid, MPa; Q is the total flow rate of the regional interconnection joints, m^2/s; $\Delta V = V - V_0$, $V_m = (V + V_0)/2$, V, and V_0 are the areas of the new and old regions, respectively; and Δt is the time step.

3.1. Establishment of Numerical Model Based on Generalized Classification. Bulianta Coal Mine is located in the central part of Shendong Mining Area. The main coal seam is No. 1^{-2}, with the average thickness of the coal seam of 7.44 m, so one-time full-thickness mining technology is adopted.

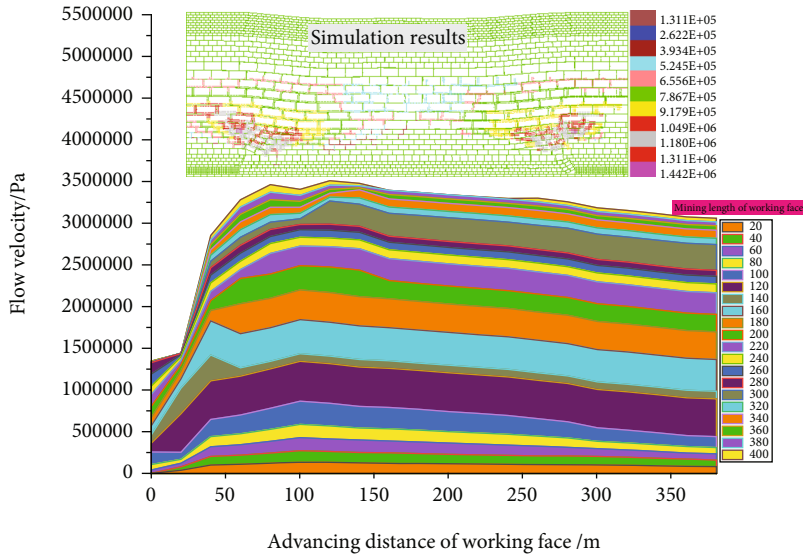

(a) Model 1

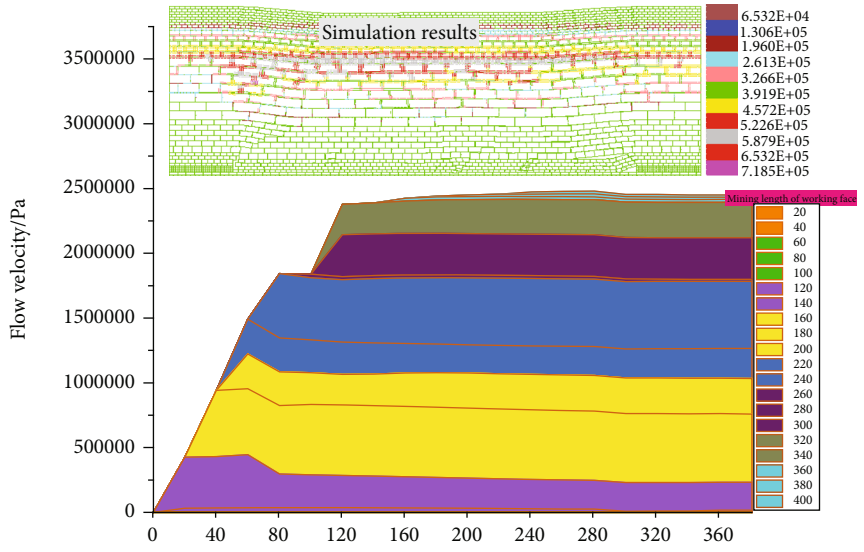

(b) Model 2

Figure 10: Continued.

(c) Model 3

Figure 10: Variation law of water pressure at coal roof with the advancement of working face.

There are mainly two aquifers in the upper part of the coal seam, namely the Quaternary aquifer and the Zhidan Group aquifer of the Lower Baixi System. The aquiclude is located on the top of the Yan'an Formation in the Lower Jurassic, and its lithology is mainly composed of mudstone and sandy mudstone. In order to analyze the water source problems during the construction of underground reservoirs after the mining of No. 1^{-2} coal seam, it is necessary to study the change law and recharge law of water source in the aquifer under the action of mining. In view of this, this paper uses the discrete and fluid model of the UDEC software (Figure 3) to conduct numerical simulation analysis based on the occurrence status of No. 1^{-2} coal seam and aquifer in Shendong Bulianta Coal Mine. A numerical analysis model is constructed to analyze the influence of coal mining on the aquifer as well as the influence of mine water occurrence modes on the water source of underground reservoirs. The physical and mechanical parameters of each rock layer of the model are shown in Table 1 [24, 25]. The size and basic parameters of each rock layer are selected as follows:

① Model size: according to the average burial depth of No. 1-2 coal seam, the model height is set to 190 m; at the same time, considering the boundary effect and the full mining effect during the advancement of the working face, coal pillars with length of 60 m are arranged on the left and right sides, and the model length is set to 500 m; excavation step distance is set to 10 m/step. ② Selection of mining height: based on the actual mining thickness of No. 1-2 coal seam, the mining height is set to 8 m. ③ Aquifer: according to the above generalized model, a total of 3 sets of models are set up based on the aquifer location. Model 1 and model 2 are given a set of aquifers, namely, type I and type II aquifers, model 3 has two aquifers, and the aquifer thickness for the three types of models is set to 20 m, as shown in Figure 4. The modeling results are shown in Figure 5; ④ monitoring line layout: during the simulation, the monitoring lines are arranged in the lower part of the aquifer (the upper and lower parts of the type I aquifer in model 3), the lower part of the aquiclude, and the upper part of the coal seam. The change characteristics of water pressure and water velocity during the excavation process are monitored, and the aquifer water level change law, seepage path, and other related information are inverted according to the change characteristics of water pressure.

The leading-support stress distribution of working face is obtained based on numerical calculation model, and ground surface displacement subsidence curve is plotted based on Wilson's theoretical calculations and field measured data (Figures 6 and 7). The error rate of the ground settlement monitoring data is 7.95%, and the error rate of the leading-support peak stress is 1.86%. The deviation between the numerical simulation model and the actual measurement and theoretical calculations are within 10%, showing good consistency. The calculation method of the specific values refers to the calculation method using the Wilson theory [26–28] formula. The parameters required in the theoretical formula when the mining height is 5 m are summarized in Table 2.

3.2. Disturbance Characteristics of Aquifer under Mining. According to the characteristics of water pressure change at the measuring point, the characteristics of the aquifer change under the mining action can be obtained. Through studying the dynamic changes of the water pressure before and after mining, we can obtain the change characteristics of the water resources under the mining action, understand the water pressure change laws of aquifers, aquiclude, and coal roofs, respectively, and then grasp the disturbance characteristics of different types of aquifers under mining.

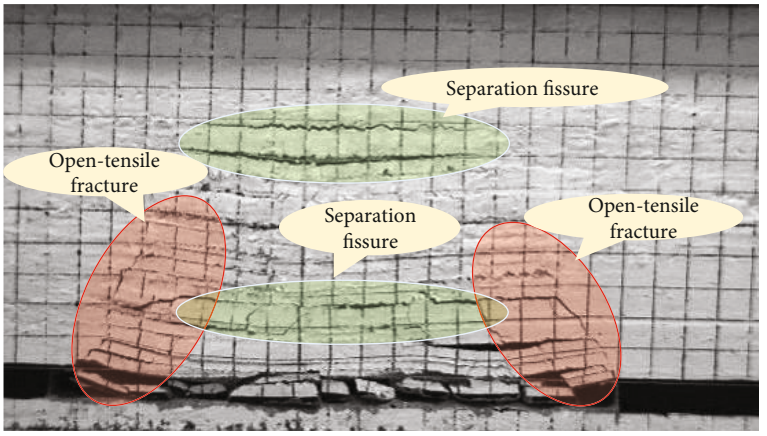

(a) The development characteristics of fissures when mining to the middle

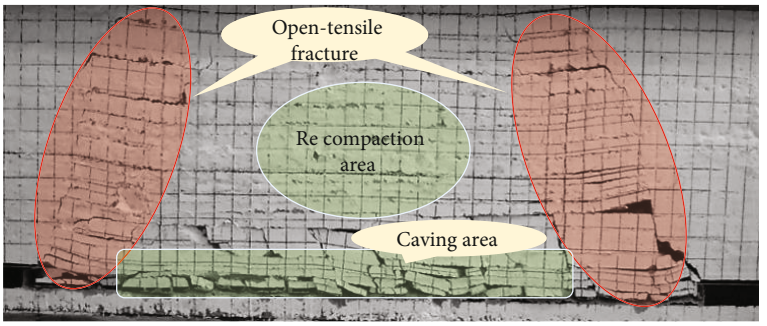

(b) The development characteristics of fissures after mining in the working face

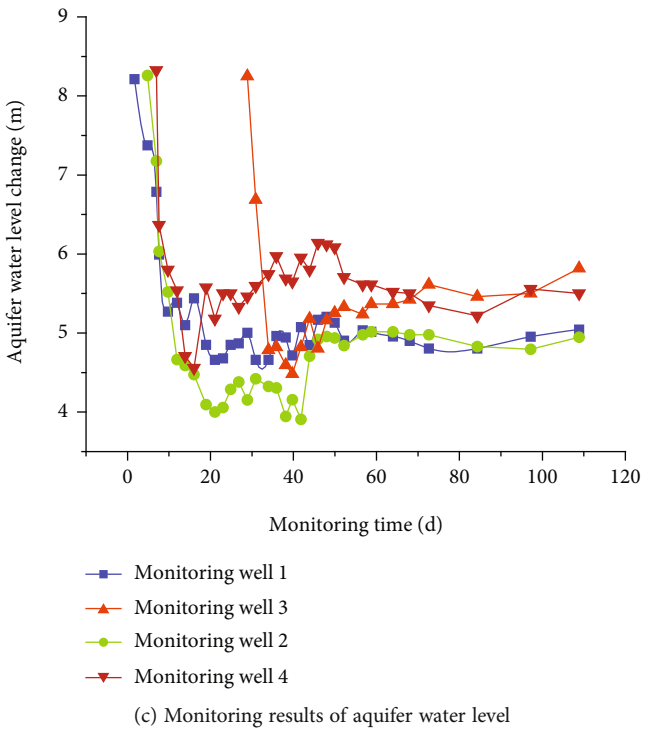

(c) Monitoring results of aquifer water level

Figure 11: Comparison and verification of simulation and on-site monitoring results.

3.2.1. Analysis of the Change Law of Water Pressure in Aquifers. The direct reason why coal mining has an impact on the aquifer is that the fissures become water-conducting channels, and the mining-induced fissures continue to open and close during the advancement of the working face. In this process, the mining-induced fissures will increase the water pressure in the overburden strata and reduce alternating changes. From the simulation results (Figure 8), it can be

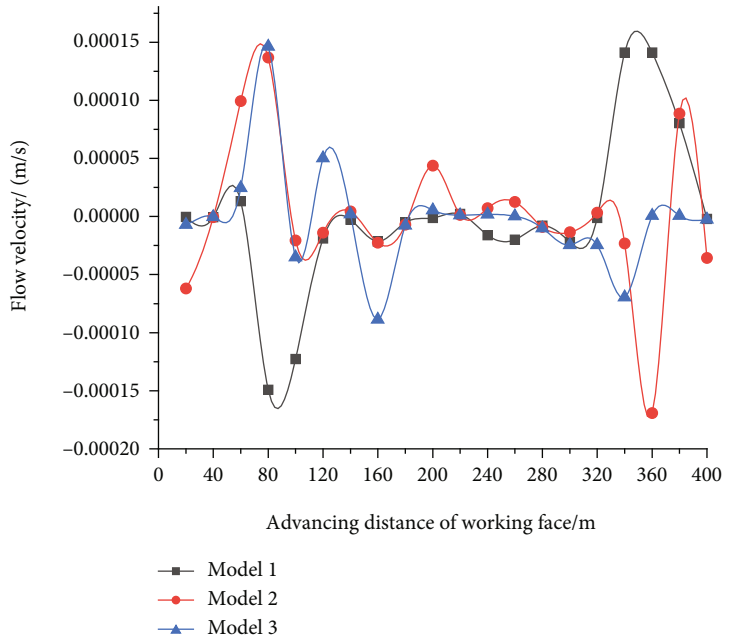

Figure 12: Variation law of roof water velocity of each model.

seen that after the mining of the working face, the water pressure at different locations in aquifers shows the tendency of increasing or decreasing, and as the distance between the coal seam and the aquifer increases, the magnitude of the change tends to decrease. In the case of type III aquifer, the water pressure in the lower aquifer changes more significantly than that in the case of type II aquifer, and the upper water pressure in the lower aquifer also changes as the working face advances. When the working face advances to about 100 m, the water pressure exhibits big fluctuations, indicating that the lower limit aquifer is "recharged" by the upper limit aquifer. In the case of type II aquifer (model 2), as the distance between the aquifer and the coal seam is greater than that in the case of type I aquifer, it is more affected by mining, and the water pressure at the same location changes earlier than that in the case of type I aquifer.

From the simulation results, it can be known that the aquifers at different locations present certain time effect. In general, there is a change characteristic of decrease→increase→decrease→recovery. The water resources located in the upper aquifer "migrate" along the mining-induced fissures to the lower rock layer or aquifer; when the aquifer is located in the upper part (type I), it is greatly affected by mining, and the disturbance time is later compared to type II aquifer; when the aquifer is type II or type III, the lower aquifer is greatly disturbed with serious water loss. In particular, when the aquifer is type III aquifer, the lower part of type II aquifer shows great water pressure changes, with more serious water loss, providing abundant water supply for underground reservoirs.

3.2.2. Analysis of the Change Law of Water Pressure in the Aquiclude. The change of water pressure in the aquiclude also reflects dynamic evolution of the fissures during coal seam mining as well as the strength of water resistance to a certain extent. According to the simulation results, the location of the aquifer greatly affects water pressure change in the aquiclude. As the distance between the two increases, the water pressure change in the aquiclude becomes smaller, and the time for the occurrence of water pressure change is slightly delayed. When the working face advances to about 180-200 m, the change law of water pressure basically tends to be stable, showing periodic fluctuations.

In the case of type III aquifer, the aquiclude has greater change amplitude and more significant increase of water pressure than the other two cases. In the case of type II aquifer, a stable "water gushing point" is formed about 100 m away from the open-off cut. It can be judged that the mining-induced fissure has the largest opening at this point, and the water source of the aquifer constantly flows to the goaf. Despite the great water resource flow at this point, the water pressure in the mining-induced fissure is small. In the case of type I aquifer, after the coal seam mining destroys the aquifer, water resources continue to flow to the lower rock layer and enter the goaf along the fissure of the aquiclude. In general, as the distance between the coal seam and the aquifer decreases, there is an increasingly serious loss of water resources in the aquifer, and the change law of water pressure becomes more and more complicated during the advancement of the working face. The farther away the occurrence location of aquifer is from the coal seam, the smaller the water pressure change is, and the longer the time will be. The difference in the water pressure change reflects the fissure opening degree or the strength of the water conductivity in the aquifer. The closer the distance between the aquifer and the coal seam, the more serious the loss of water resources after the mining-induced fissure destroys the aquifer, and the more stable the water supply to the underground reservoir. On the contrary, when the

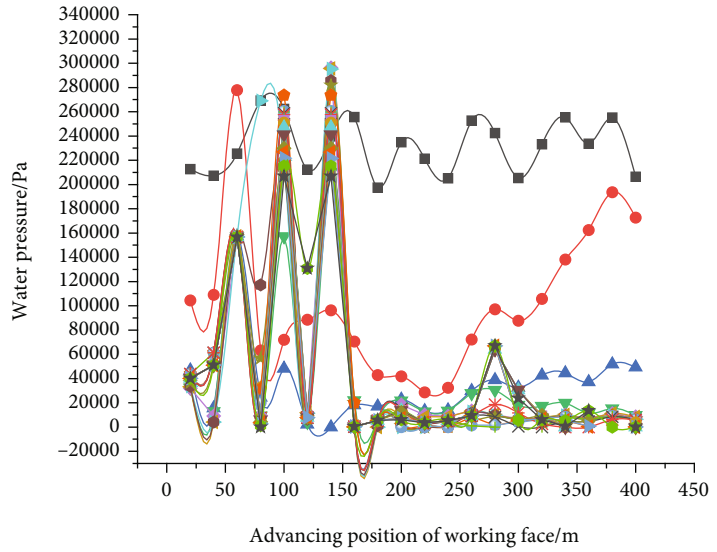

(a) The lower part of model 1 aquifer

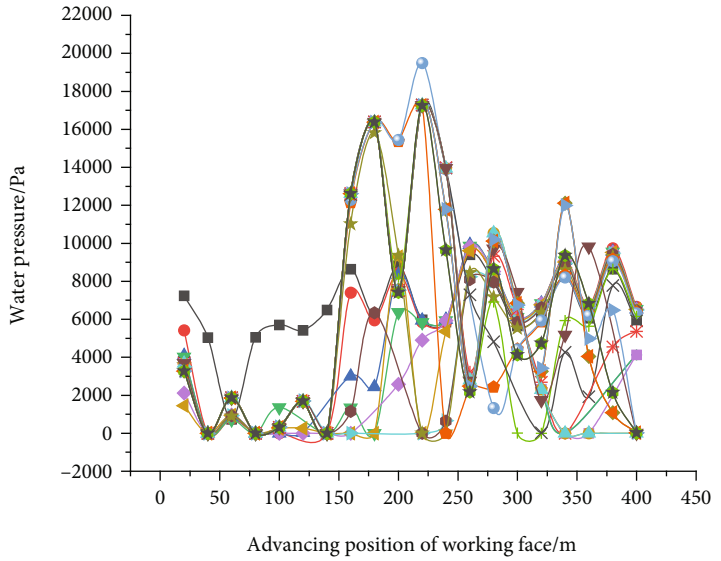

(b) The lower part of model 2 aquifer

Figure 13: Continued.

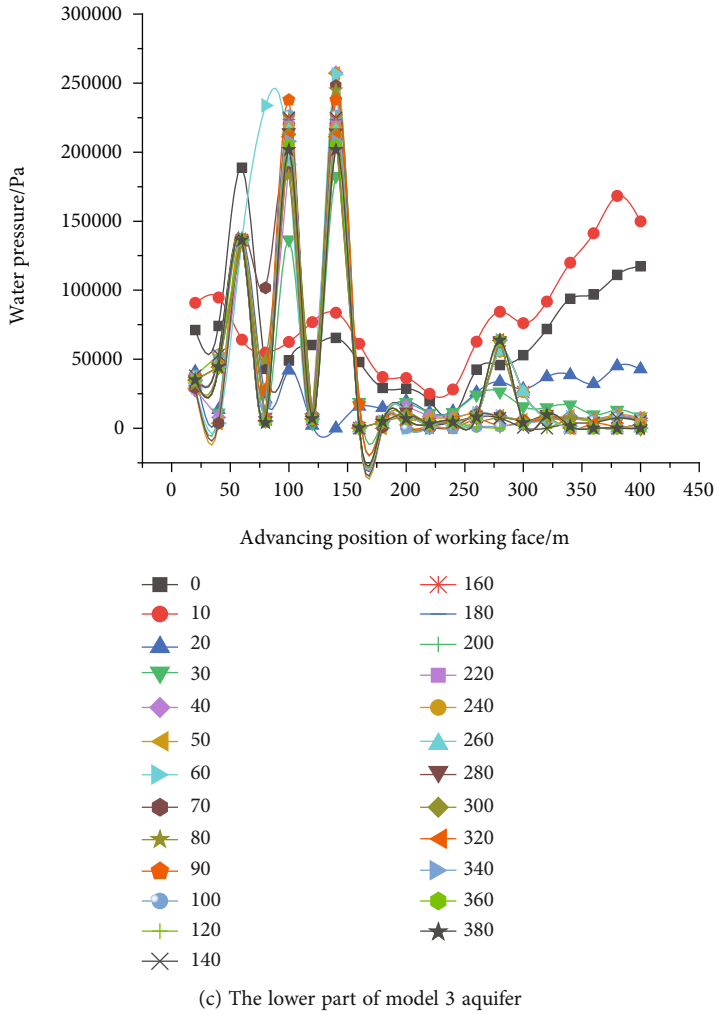

(c) The lower part of model 3 aquifer

Figure 13: Variation law of water pressure in aquiclude.

aquifer is far away from the coal seam, due to the action of the bedrock between the aquifer and the aquiclude, part of the water resources will be stored by the bedrock fissure (cracks) rather than flowing to the goaf, so that the underground reservoir cannot be steadily recharged.

3.2.3. Analysis of the Water Pressure Change Law at Coal Roof. In order to characterize the degree of water supply to underground reservoirs by different types of aquifers, the changes in water pressure at coal roof are analyzed. Based on the change law of water pressure in the aquiclude, it can be seen that the change law of water pressure at coal roof varies significantly with the occurrence forms of coal seam and aquifer as well as distance between the two. In model 3, the change amplitude and increase intensity of water pressure at coal roof are greater compared to the other two models. The change law is similar to that of model 1 (type II aquifer), but the change range of water pressure is bigger compared to model 1, which means that when the aquifer is a mixed type aquifer; the water source at the coal roof is "recharged" by the two aquifers. The main source for recharging is provided by the lower aquifer, and the water pressure change at coal roof is not a simple superposition of the change values of the water pressure in the two models, which also verifies to a certain extent that part of the water source in the upper aquifer will be stored in the fissure along with the opening and closing of the bedrock fissure.

After the mining of the working face is completed, the water pressure at the open-off cut and the stop line of the working face remains basically stable, and the water pressure in the middle of the working face increases and decreases periodically, indicating that the fissures at both ends of the working face have a greater degree of opening, which becomes a stable water gushing point. However, in the middle part, the fissure is closed due to the recompaction of the rock formation, and the upper part is constantly recharged by water, showing a periodic water pressure change of increase→decrease→increase.

The change of water pressure at coal roof can directly reflect the damage degree of different types of aquifers under mining as well as the water supply capacity of underground reservoirs in coal mine. From Figure 9, it can be found that the water supply capacity of the underground reservoir is directly related to the "coal-water" occurrence relationship. When it is closer to the coal seam, the recharge capacity is stronger, and the downward flow time of water resources is relatively advanced. When there are multiple aquifers above

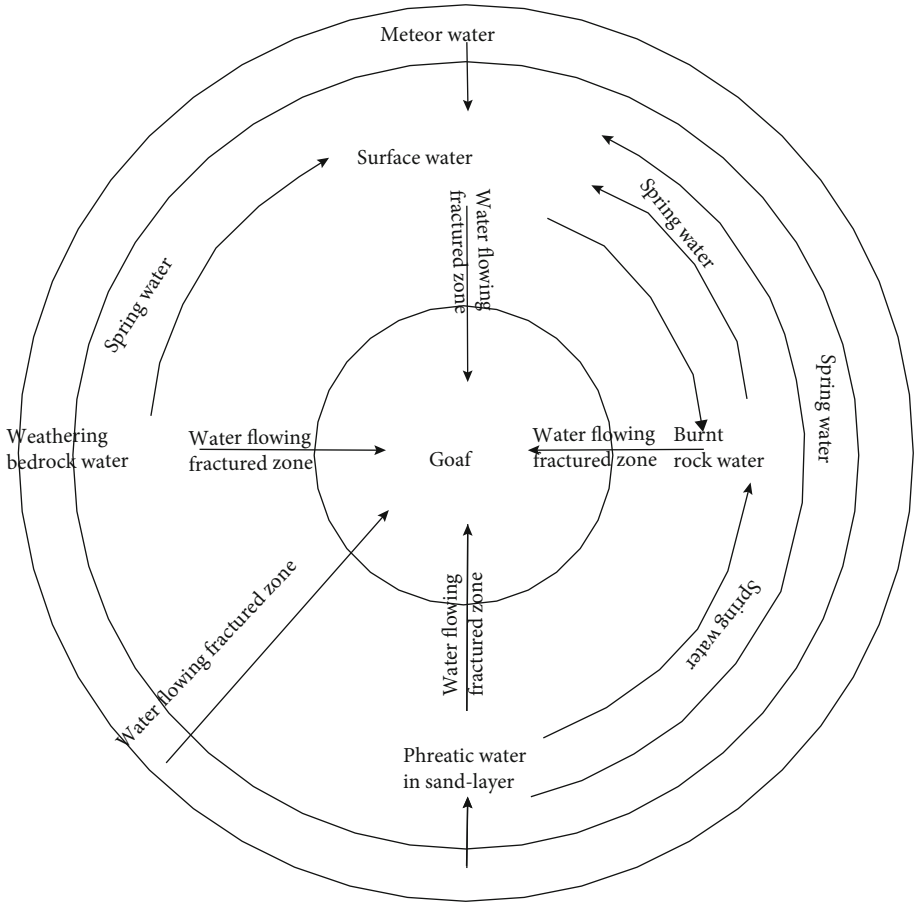

(a) Water supply source in goaf

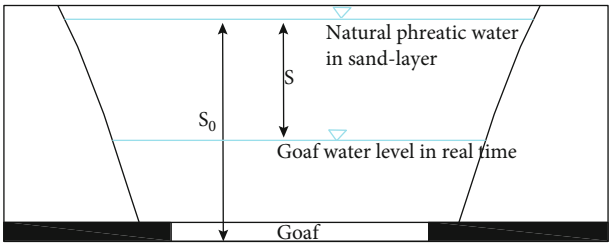

(b) Schematic diagram of water storage in goaf

Figure 14: Continued.

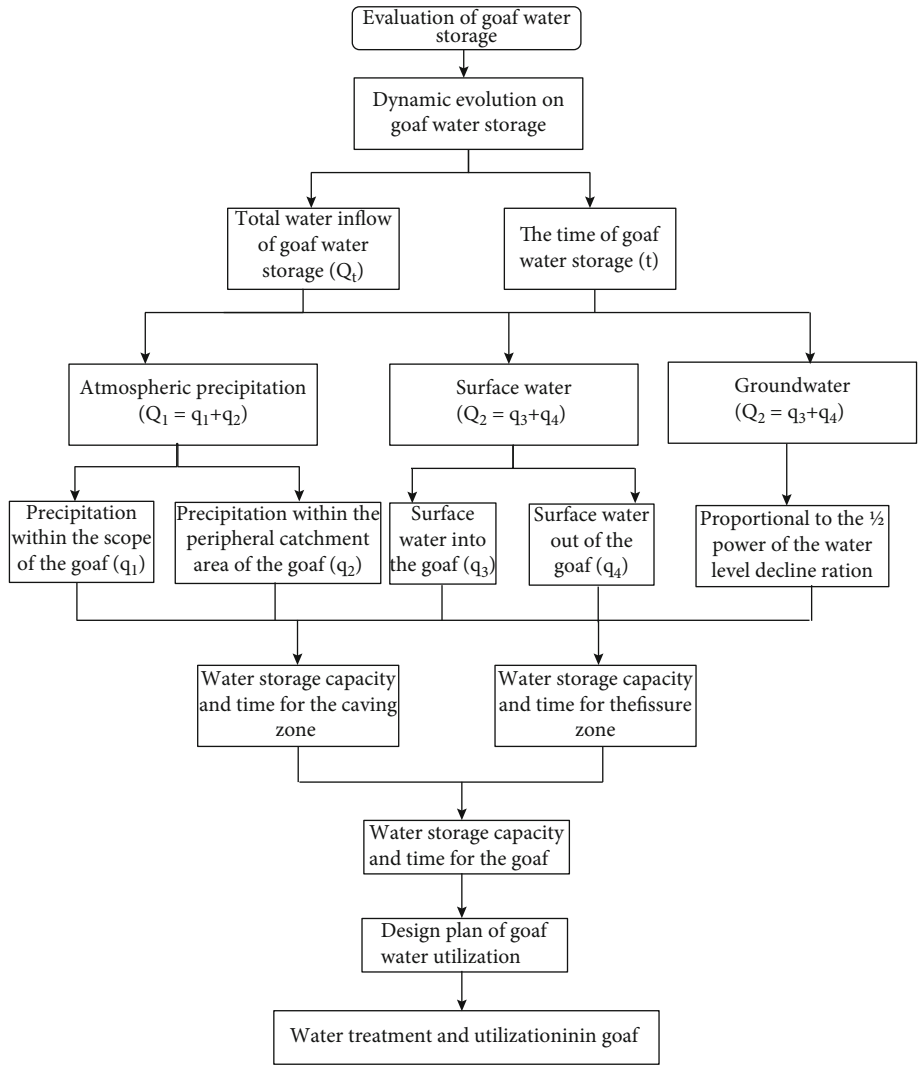

(c) Reserve calculation process

Figure 14: Flowchart of evaluation of water storage in goaf.

the coal seam, the aquifer located between the caving zone and the fissure zone is the main "supply aquifer" for the underground reservoir, and the aquifer above it continuously replenishes the lower aquifer under the influence of fissure.

3.3. Water Source Prediction of Underground Reservoirs under Different Coal-Water Occurrence Relationships. The water source of underground reservoirs mainly comes from the water resources in the aquifer. After the coal seam is mined, there will be stable water outlets at the open-off cut and stop line. The mining-induced fissures generated in this area have big openings and become one of the stable water sources for underground reservoirs. From the simulation results, the changes in water pressure at coal roof reflect the recharge status of underground reservoirs by aquifers. In order to further analyze the degree of water supply to underground reservoirs provided by different types of aquifers, the water pressure at coal roof is analyzed.

It can be seen from Figure 10 that, in models 2 and 3, there are obvious areas where water pressure increases at both ends of the working face, while in model 1, the water pressure at both ends of the working face does not change significantly, and the water pressure in the lower aquifer shows a hump-shaped distribution. Different types of aquifers show great differences in the cumulative increase trend of coal roof during the advancement of working face. The overall degree of change is ranked as model 3 > model 2 > model 1, indicating that the coal-water occurrence relationship has a great influence on the water source of underground reservoirs. The farther the aquifer is from the coal seam, the more unstable the recharge to the underground reservoir.

In order to verify the rationality of the numerical simulation, the numerical simulation results were compared with the physical simulation results and on-site monitoring results. The results show that the main "outlet points" derived from physical simulation and numerical simulation are near the open-off cut, and the fissure (water gushing channels) is developed in the tensioned fissure zone above the two ends of the working face [29]. The separation

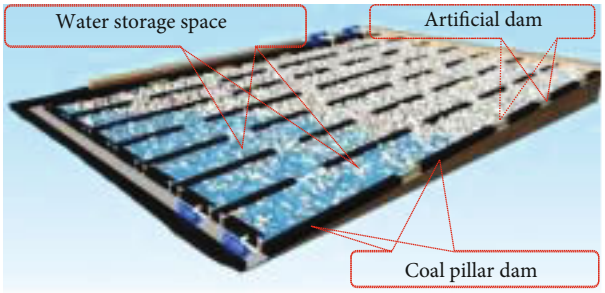

(a) Schematic diagram of underground reservoir in coal mine

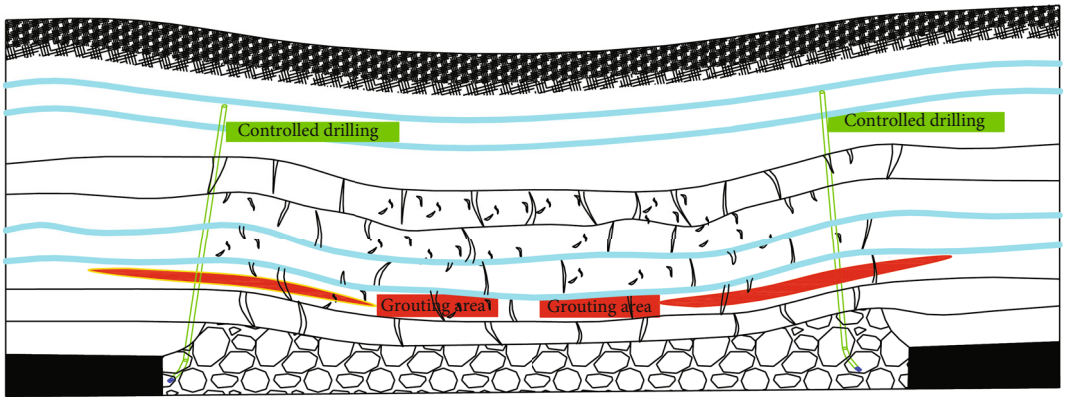

(b) Schematic diagram of adjustment measures

Figure 15: Schematic diagram of control method of groundwater reservoir water source based on generalization model.

fissures or horizontal fissures appear just above the working face during the mining process. With the advancement of working face, this part of the fissures is compacted and reclosed, causing the loss of water diversion capability. By comparison with the numerical simulation results, it can be found that great increase of water pressure also appears in the tensile fissure zone at the upper ends of the working face, and there is small water pressure change in the upper compaction zone of the working face. Therefore, the numerical simulation results are basically consistent with the actual results. By analyzing the on-site monitoring results of the aquifer water level (Figure 11(c)), it can be seen that with the advancement of the working face, the water pressure in the aquifer shows a tendency of decrease → recover → stabilize, which is consistent with the numerical simulation results.

In order to quantitatively analyze the recharging of underground reservoirs by different types of aquifers, according to Darcy's law calculation method, the water inflow V has a relationship with water flow velocity v, water flow channel area S, and time t, as shown in Equation (3).

$$V = \sum v \cdot dS, \tag{3}$$

where V is the water inflow, m^3/h; v is the water flow velocity, m/s; and S is the cross-sectional area of the water flowing through the rock formation (the coal roof is along the inclination direction of the working face), m^2. The monitoring results of the water flow velocity in the monitoring point are shown in Figure 12.

Based on the development degree of the main fissures in the mining process and according to the actual width of the working face, the cross-sectional area of seepage is calculated, and the water inflow results of the three models are finally calculated as well, as shown in Figure 13. The working face width is within the range of 200~300 m, and the water inflow of each model is obtained. Model 3 has the largest water inflow, which is about 493~739 m^3/h; model 2 has the smallest water inflow, which is about 252~377 m^3/h; the water inflow of model 1 is between the two, which is 186~279 m^3/h. According to the actual occurrence status of the aquifer, the Bulianta Coal Mine can be classified as type III aquifer. According to the analogy method and actual measurement results, the actual water inflow during the mining process of the No. 1^{-2} coal seam is 400 m^3/h by average, which is similar to the simulated value.

4. Water Source Regulation and Storage Method for Underground Reservoir in Coal Mine considering Coal-Water Occurrence Relationship

Flowchart of evaluation for water storage in goaf is shown in Figure 14 [1].

$$\begin{aligned} Q_1 &= q_1 + q_2, \\ q_1 &= F \cdot \alpha_1 \cdot h, \\ q_2 &= F_1 \cdot \alpha_2 \cdot h, \end{aligned} \tag{4}$$

where F is the area of the goaf, m^2; α_1 is the precipitation infiltration coefficient of the goaf; F_1 is the peripheral catchment area of the goaf, m^2; α_2 is the precipitation infiltration coefficient in the peripheral catchment area of the goaf; and h is the precipitation intensity of the study area, m/d.

$$Q_2 = q_3 + q_4, \tag{5}$$

where q_3 is the flow of the surface water into the goaf, m^3/d, and q_4 is the flow of surface water out of the goaf, m^3/d.

The recharge amount of the underground aquifer for the goaf is related to goaf water storage level. The groundwater inflow is directly proportional to the 1/2 power of decline ratio of the water level, which can be calculated by the following formula:

$$Q_3 = Q_0\sqrt{\frac{S}{S_0}}, \tag{6}$$

where Q_0 is the water inflow of the goaf before enclosure, m^3/d; S_0 is the drawdown of the phreatic water level before goaf closure, m; and S is the drawdown of the phreatic water level in the goaf water storage, m (Figure 14).

The time dt of goaf water storage presents the drawdown change dS of phreatic water level, so:

$$\left(Q_1 + Q_2 + Q_0\sqrt{\frac{S}{S_0}}\right)dt = F\mu_2 ds, \tag{7}$$

where μ_2 is the specific yield of the goaf caving zone; assuming $K_1 = Q_1 + Q_2$, $K_2 = Q_0/S_0$^1/2, following formula can be obtained through integration:

$$t = \frac{2F\mu_2}{K_2^2}\left[K_2\left(\sqrt{S_0} - \sqrt{S}\right)\right] - K_{\ln}\frac{K_1 + K_2\sqrt{S_0}}{K_1 + K_2\sqrt{S}}. \tag{8}$$

According to the generalized model of the "coal-water" relationship and the results of numerical analysis, different forms of water source control methods are proposed to ensure that the underground reservoirs have sufficient water supply while the water inflow does not exceed the storage capacity. According to the water supply types of underground reservoirs, they are divided into single-type water sources and mixed-type water sources. The single-type water sources include type I aquifers and type II aquifers, and the mixed aquifers are type III aquifers. The specific regulation and storage method are designed as follows:

(1) Category I (lower aquifer)

Since the aquifer is located within the fissure zone, the aquifer is greatly damaged by coal mining, and the water source of the aquifer directly enters the goaf. The predicted water inflow volume V_1 is used as the water source recharge of the underground reservoir, which is compared with reservoir capacity V. There are following two situations involved. In case 1, $V > V_1$, that is, the aquifer recharge exceeds the designed underground reservoir capacity; the control method is to grout at the bottom of the aquifer above the cut-off line and the stop line to plug the main water-conducting fissures, reduce the mine water inflow, connect the aquifer to the underground reservoir through drilling, arrange water valves in the roadway near the reservoir, adjust the water volume, thereby achieving the purpose of adjusting the water volume of the reservoir (as shown in Figure 15). In case 2, $V < V_1$, the water inflow of the aquifer is smaller than the designed reservoir capacity. The boreholes arranged in case 1 are used to increase water inflow to the reservoir, and the water source of the underground reservoir is controlled according to the actual water inflow.

(2) Category II (upper aquifer)

Since this kind of aquifer is far from the coal seam, it is less disturbed and has relatively weak ability to recharge the underground reservoir. When the aquifer water supply meets the reservoir capacity requirements, no large-scale water inrush will occur. When the aquifer water volume does not meet the reservoir capacity requirements, the aquifer can be communicated with the underground reservoir by drilling holes, and devices such as valves can be installed at the pipeline end, in order to guarantee the ecological, production, and domestic water requirement of the mining area in the underground reservoir. Water sources such as aquifers and surface water are introduced into underground reservoirs to ensure the recharge for underground reservoirs. When the water inflow is greater than the designed capacity of underground reservoir, the method of grouting should be taken to block the main water-conducting fissures for type I aquifers.

(3) Category III (contains both upper and lower aquifers)

When the aquifer above the coal seam has both upper and lower aquifers, there is relatively big reservoir water supply. Where type I aquifer is the main source of recharge for the underground reservoir. In order to control the water source of the underground reservoir within a reasonable range, type I aquifer is regarded as the main aquifer, and type II aquifer is subject to auxiliary control according to the amount of water inflow. Grouting and water pipe control are carried out simultaneously for the two types of aquifers to ensure that water inflow matches the storage capacity of underground reservoirs.

5. Conclusion

(1) Aiming at the core issue of water supply for underground reservoirs in coal mines, this paper clarifies that the development of water-conducting fissures in aquifers and the formation of water-conducting channels are the key factors leading to the loss of water resources in the aquifer. Based on the occurrence location of aquifer and the development height

of water-conducting fissure zone, the overlying aquifer of the shallow coal seam is generalized into three types, including the lower aquifer locating between the caving zone and the fissure zone, the upper aquifer locating above the fissure zone, and the mixed aquifer consisting of the above two

(2) Numerical simulation results show that in the process of coal mining, the water pressure of the aquifer presents a variation of decrease→increase→decrease→recovery and shows a certain time effect. When the occurrence location of aquifer is farther from coal seam, the time lag is relatively long, the damage degree is smaller, and the recharge of underground reservoir is weaker. The mixed aquifer provides the most abundant water supply to underground reservoir

(3) According to the numerical simulation results, the mine water inflows of different models are calculated. Combining the actual occurrence of Bulianta aquifer (type III aquifer), the rationality of the simulation results is verified. On this basis, the recharging of underground reservoirs by three types of aquifers is analyzed, which shows that mixed aquifers have the strongest recharging capacity, followed by lower aquifers, and upper aquifers with the weakest recharging capacity

(4) In order to ensure that the water supply of underground reservoirs is within a safe and reasonable range, based on the storage capacity of the underground reservoir, a preliminary method is proposed for the water supply control of the underground reservoir, including grouting, blocking of the main water-conducting fissures, and hole drilling (pipes) to divert or inject water into the aquifer

Data Availability

The raw data required to reproduce these findings cannot be shared at this time as the data also forms part of an ongoing study.

Conflicts of Interest

The authors declare that they have no conflicts of interest.

Authors' Contributions

Mingbo Chi and Zhiguo Cao contributed to the conceptualization. Mingbo Chi contributed to the methodology. Yong Zhang contributed to the software. Mingbo Chi and Quansheng Li contributed to the formal analysis. Baoyang Wu contributed to the investigation. Bao Zhang contributed to the resources. Yang Yi contributed to the data curation. Xiaoqing Liu and Mingbo Chi contributed to the writing—original draft preparation. Quansheng Li contributed to the writing—review and editing. Mingbo Chi contributed to the funding acquisition. All authors have read and agreed to the published version of the manuscript.

Acknowledgments

The research is financially supported by the National Natural Science Foundation (52004011) and the National key R & D plan (2016YFC0501100, 2016YFC0501104).

References

[1] Q. Wang, W. Li, T. Li, X. Li, and S. Liu, "Goaf water storage and utilization in arid regions of Northwest China: a case study of Shennan coal mine district," *Journal of Cleaner Production*, vol. 202, pp. 33–44, 2018.

[2] D. Gu, "Theory framework and technological system of coal mine underground reservoir," *Journal of China Coal Society*, vol. 40, no. 2, pp. 239–246, 2015.

[3] N. Uddin and M. Asce, "Preliminary design of an underground reservoir for pumped storage," *Geotechnical & Geological Engineering*, vol. 21, no. 4, pp. 331–355, 2003.

[4] D. Gu and J. Zhang, "Modern coal mining affected to underground water deposit environment in West China mining area," *Coal Science and Technology*, vol. 40, no. 12, pp. 114–117, 2012.

[5] M. Chi, D. Zhang, L. Honglin et al., "Simulation analysis of water resource damage feature and development degree of mining-induced fracture at ecologically fragile mining area," *Environmental Earth Sciences*, vol. 78, no. 3, p. 88, 2019.

[6] Z. Li, J. Xu, S. Yu, J. Ju, and J. Xu, "Mechanism and prevention of a chock support failure in the longwall top-coal caving faces: a case study in Datong coalfield, China," *Energies*, vol. 11, no. 2, p. 288, 2018.

[7] L. Zhao, C. Sun, P. Yan et al., "Dynamic changes of nitrogen and dissolved organic matter during the transport of mine water in a coal mine underground reservoir: column experiments," *Journal of Contaminant Hydrology*, vol. 223, article 103473, 2019.

[8] R. Stone and D. F. Snoeberger, "Cleat orientation and areal hydraulic anisotropy of a Wyoming coal aquifer," *Groundwater*, vol. 15, no. 6, pp. 434–438, 1977.

[9] X. H. Xie, B. Y. Su, Y. F. Gao, and X. B. Duan, "Numerical study on water inrush above a confined aquifer in coal mining using hydro-fracturing," *Chinese Journal of Rock Mechanics and Engineering*, vol. 24, no. 6, pp. 987–993, 2005.

[10] D. Zhang, G. Fan, Y. Liu, and L. Ma, "Field trials of aquifer protection in longwall mining of shallow coal seams in China," *International Journal of Rock Mechanics and Mining Sciences*, vol. 47, no. 6, pp. 908–914, 2010.

[11] Q. Zhang, S. Luo, L. Zhao et al., "Effect of Darcy flux on the release of dissolved organic matter and nitrogen from coal gangue in a coal mine underground reservoir: column experiments," *Chemical Geology*, vol. 545, article 119652, 2020.

[12] X. Kong, Z. Xu, R. Shan, S. Liu, and S. C. Xiao, "Investigation on groove depth of artificial dam of underground reservoir in coal mines," *Environmental Earth Sciences*, vol. 80, no. 6, pp. 1–17, 2021.

[13] Q. Yao, C. Tang, Z. Xia et al., "Mechanisms of failure in coal samples from underground water reservoir," *Engineering Geology*, vol. 267, article 105494, 2020.

[14] M. D. Kozar, M. C. KJ, J. Q. Britton, and B. M. Blake Jr., *Hydrogeology, Groundwater Flow, and Groundwater Quality of an Abandoned Underground Coal-Mine Aquifer, Elkhorn Area, West Virginia*, West Virginia Geological and Economic Survey, 2017.

[15] T. Roje-Bonacci and O. Bonacci, "The possible negative consequences of underground dam and reservoir construction and operation in coastal karst areas: an example of the hydroelectric power plant (HEPP) Ombla near Dubrovnik (Croatia)," *Natural Hazards and Earth System Sciences*, vol. 13, no. 8, pp. 2041–2052, 2013.

[16] B. F. Wang, B. Liang, J. G. Wang, K. M. Sun, and H. B. Chi, "Experiment study on rock bulking of coal mine underground reservoir," *Rock and Soil Mechanics*, vol. 39, no. 11, pp. 4086–4092, 2018.

[17] A. Royer-Lavallée, C. M. Neculita, and L. Coudert, "Removal and potential recovery of rare earth elements from mine water," *Journal of Industrial and Engineering Chemistry*, vol. 89, pp. 47–57, 2020.

[18] H. H. Hannan and L. Broz, "The influence of a deep-storage and an underground reservoir on the physicochemical limnology of a permanent Central Texas river," *Hydrobiologia*, vol. 51, no. 1, pp. 43–63, 1976.

[19] F. Wang, N. Liang, and G. Li, "Damage and failure evolution mechanism for coal pillar dams affected by water immersion in underground reservoirs," *Geofluids*, vol. 2019, 12 pages, 2019.

[20] S. J. Schatzel, C. O. Karacan, H. Dougherty, and G. V. R. Goodman, "An analysis of reservoir conditions and responses in longwall panel overburden during mining and its effect on gob gas well performance," *Engineering Geology*, vol. 127, no. 3, pp. 65–74, 2012.

[21] Federation W E, APH Association, *Standard Methods for the Examination of Water and Wastewater*, American Public Health Association (APHA), Washington, DC, USA, 2005.

[22] I. A. Wright, B. McCarthy, N. Belmer, and P. Price, "Subsidence from an underground coal mine and mine wastewater discharge causing water pollution and degradation of aquatic ecosystems," *Water, Air, & Soil Pollution*, vol. 226, no. 10, p. 348, 2015.

[23] L. Ma and R. F. Spalding, "Effects of artificial recharge on ground water quality and aquifer storage recovery," *Journal of the American Water Resources Association*, vol. 33, no. 3, pp. 561–572, 1997.

[24] R. Zhang, Z. Jiang, H. Zhou, C. Yang, and S. Xiao, "Groundwater outbursts from faults above a confined aquifer in the coal mining," *Natural Hazards*, vol. 71, no. 3, pp. 1861–1872, 2014.

[25] H. Song, J. Xu, J. Fang, Z. Cao, L. Yang, and T. Li, "Potential for mine water disposal in coal seam goaf: investigation of storage coefficients in the Shendong mining area," *Journal of Cleaner Production*, vol. 244, article 118646, 2020.

[26] A. H. Wilson, "The stability of underground workings in the soft rocks of the coal measures," *International Journal of Mining Engineering*, vol. 1, no. 2, pp. 91–187, 1983.

[27] A. Mortazavi, F. P. Hassani, and M. Shabani, "A numerical investigation of rock pillar failure mechanism in underground openings," *Computational Geosciences*, vol. 36, no. 5, pp. 691–697, 2009.

[28] H. Wang, D. Zhang, X. Wang, and W. Zhang, "Visual exploration of the spatiotemporal evolution law of overburden failure and mining-induced fractures: a case study of the Wangjialing Coal Mine in China," *Minerals*, vol. 7, no. 3, p. 35, 2017.

[29] P. Huang and J. Chen, "Recharge sources and hydrogeochemical evolution of groundwater in the coal-mining district of Jiaozuo, China," *Hydrogeology Journal*, vol. 20, no. 4, pp. 739–754, 2012.